UNIVERSITY OF SOUTHAMPTON

Faculty of Engineering and the Environment

Skin Stiffener Debonding of Top-hat Stiffened Composite Structures

by

Joanne Emma Yetman

ITDC EngD Thesis

May 2016

[BLANK PAGE]

UNIVERSITY OF SOUTHAMPTON

ABSTRACT

FACULTY OF ENGINEERING AND THE ENVIRONMENT

Engineering Doctorate

Skin Stiffener Debonding of Top-hat Stiffened Composite Structures

by Joanne Emma Yetman

Top-hat stiffened plates provide an efficient structure for engineering applications. During service debonding between the stiffener and the plate is a common failure mechanism. Therefore, an extensive understanding of the residual strength is required to rapidly and efficiently determine precautions to be taken to ensure the safety of the structure. Critical assessment of necessary repairs reduces the through life costs and in design damage assessment can lead to optimisation through tolerance of common damage incidents. Research on damaged stiffened structures to date is primarily focused on airframe applications and considers open sections with co-cured stiffeners which are not typical of marine structures. These studies have shown that debond size and location have a significant effect on the damage mode of the panel. However, they do not consider the interaction of failure modes or ultimate failure. Typical marine composite joints are manufactured by post-curing sub-components using a chopped strand mat layer at the interface. To predict failure of these joints requires accurate assessment of the material and fracture properties and a consistent set of data which is lacking in the literature. Therefore, the research in this thesis considers the damage tolerance of top-hat stiffened panels containing a debond between the stiffener and plate through numerical and experimental work. The focus of the work is post-cured top-hat multi-stiffened panels used in large marine applications manufactured from heavy weight glass vinylester woven roving.

An automated tool using non-linear finite element analysis capable of modelling debond damage and assessing the ultimate and the residual strength of the panel is verified. A parametric study investigating panel topology, damage parameters and stiffener type show the complexities of the damage case. Results show that top-hat stiffened panels exhibit a trend between ultimate strength and the debond size with crack initiation not necessarily propagating as geometric imperfections accelerate buckling but can provide an arrest point for crack propagation. Nominal lateral pressures are shown to significantly increase the damage tolerance. Full characterisation of typical materials is conducted experimentally providing a complete data set of mechanical characterisation and fracture data for both co-cured interfaces, typical of mid-laminate debonds and sub-component joints. Tensile, compressive, shear and flexural tests are conducted and a model for the non-linearity of the woven roving in tension and shear is proposed. The fracture results show the post-cured joint exhibits a 20% increase in mode I and II strain energy release rates. The experimental data is used in a number of studies to further verify and optimise the finite element model. Mode I and II tests are simulated to ascertain the cohesive element interface strengths and Turon's interface parameters. The material data is shown to give accurate results for the structural response, crack initation and debonding of an as built large scale top-hat stiffened panel which is tested experimentally under four point bend. Therefore, the effect of skin-stiffener debonding has been investigated for top-hat stiffened panels, providing improved characterisation of the material and interfaces and guidance on the damage tolerance to damage and design parameters.

[BLANK PAGE]

Contents

[BLANK PAGE]

List of Figures

[BLANK PAGE]

Author's Declaration

I, Joanne Emma Yetman, declare that this thesis entitled:

Skin Stiffener Debonding of Top-hat Stiffened Composite Structures

and the work presented within are both my own and have been generated by me as the result of my own original research.

I confirm that:

- This work was done wholly or mainly whilst in candidature for a research degree at the University of Southampton;
- Where any part of this thesis has previously been submitted for a degree or any other qualification at this University or any other institution, this has been clearly stated;
- Where I have consulted the published work of others, this is always clearly attributed;
- Where I have quoted from the work of others, the source is always given. With the exception of such quotations, this thesis is entirely my own work;
- I have acknowledged all main sources of help;
- Where the thesis is based on work done by myself jointly with others, I have made clear exactly what was done by others and what I have contributed myself;
- Parts of this work have been published as:
  - Davies, J.E., Sobey, A.J., Blake, J.I.R., Shenoi, R.A., Assessment of Damaged Composite Structures, MTPC 2012, Glasgow. Conference Proceedings
  - Davies, J.E., Sobey, A.J., Blake, J.I.R., Shenoi, R.A., Residual Capability of Damaged Composite Ship Structures, RINA-The Damaged Ship 2013, Croydon. Conference Proceedings
  - Davies, J.E., Sobey, A.J., Blake, J.I.R., Shenoi, R.A., Residual Capability of Composite Stiffened Marine Structures after Non-Critical Damage, International Conference on Composite Structures 2013, Porto. Conference Proceedings
  - Davies, J.E., Sobey, A.J., Blake, J.I.R., Shenoi, R.A., Damage Tolerance of Stiffened Composite Structures, |International Conference of Composite Materials 2013, Montreal. Conference Proceedings
  - Yetman, J.E., Sobey, A.J., Blake, J.I.R. and Shenoi, R.A., 2015. Investigation into skin stiffener debonding of top-hat stiffened composite structures. Composite Structures, 132, pp.1168-1181.

Signed: .....

Date:.....

[BLANK PAGE]

Acknowledgements

The author would like to thank Dr Adam Sobey, Prof. Ajit Shenoi and Dr. James Blake for their advice, support and time during this work. The author would also like to acknowledge the use of the IRIDIS 3 High Performance Computing Facility, and associated support services at the University of Southampton in the completion of this work.

Finally, the author would like to thank the UK Ministry of Defence and Lloyd's Register EMEA for their sponsorship and continued support and without whom this research would not have been possible. In particular the author would like to thank Mr Colin Snell, Mr Paul James, Mr Mike Mogford and Mr Ben Cuckson for their time, input and support of the work throughout.

[BLANK PAGE]

Abbreviations

2D	Two-Dimensional
3D	Three-Dimensional
DCB	Double Cantilever Beam
CAI	Compression After Impact
CLPT	Classical Laminate Plate Theory
ENF	End Notch Failure
ESL	Equivalent Single Layer
FEA	Finite Element Analysis
FEM	Finite Element Method
FF	Fibre Fracture
FORM	First Order Reliabiltiy Method
FRP	Fibre Reinforced Plastic
FSDT	First Order Deformation Theory
GRP	Glass Reinforced Plastic
HLU	Hand Lay-Up
IFF	Inter Fibre Fracture
LVI	Low Velocity Impact
LW	Layer-Wise
MCMV	Mine Counter Measure Vessel
MoD	Ministry Of Defence
RTM	Resin Transfer Moulding
SERR	Strain Energy Release Rate
SORM	Second Order Reliabiltiy Method
SRMH	Single Role Mine Hunter
SSDT	Second Order Deformation Theory
TSDT	Third Order Deformation Theory
VCCT	Virtual Crack Closure Technique
WWFE	World Wide Failure Exercise
XFEM	Extended Finite Element Method

[BLANK PAGE]

Nomenclature

Latin Symbols

a	Crack length
B	Panel breadth
C_d	Damage elasticity matrix
d	Damage degradation factor
d_v	Regularised damage degradation factor
E	Young's modulus
E_f	Young's modulus of fibres
F_{xy}	Tsai-Wu interaction factor
G	Strain energy release rate
G_c	Critical strain energy release rate
G_T	Total strain energy release rate
h	Thickness of sublaminate
k	Shear correction factor
K	Stress intensity factor
K_c	Critical stress intensity factor
K'	Initial interface stiffness
L	Length of plate
L_c	Characteristic length
L_{cz}	Cohesive zone length
L_e	Mesh size in the direction of crack propagation
M	cohesive model parameter
$m_{\sigma f}$	mean stress magnification factor for the fibres in the 2 direction
N_e	Number of elements in the cohesive zone
P	Applied load
$p_{\perp\perp}^{(-)}$, $p_{\perp\parallel}^{(-)}$	Puck's inclination parameter
$R_{\perp\perp}^{A}$	Puck's fracture resistance of the action plane
S	Failure stress
t_0	Interfacial strength
t	Thickness of plate
U, u	Displacement
x,y,z	Global coordinate system
X,Y,Z	Material coordinate system

Greek Symbols

β	Material interface index
δ	Displacement
ζ	Oscillatory index
ε, γ	Normal and shear strain
η	Viscosity parameter
η_{BK}	Benzeggagh-Kenane material parameter
τ	Traction component at interface
ν	Poisson's ratio
ν_f	Poisson's ratio of fibre
σ	Stress
σ_{1D}	Stress value for linear degradation
Δ	Relative displacement

Subscripts

1,2,3	Material coordinates (fibre, transverse in-plane and transverse normal direction)
C	Compressive
T	Tensile
eq	Equivalent
o	Initial failure
f	Final Failure
I,II,III	Mode I, II, III

Superscripts

o	Initial value
*	Largest value during loading history

1 Introduction

1.1 Damage Tolerance of Composite Structures

Composite construction has been widely adopted in engineering structures due to the ability to uniquely tailor the material properties for the application e.g. weight reduction due to specific strength characteristics, aesthetics, maintainability, corrosion resistance and signature performance. In comparison to steel, composite structures experience limited increase in maintenance costs over a 20-year life cycle and are therefore beneficial in reducing down-time, maintenance and repair [1]. However, composite construction has not yet gained broad acceptance and one of the key drivers is the lack of understanding of the damage characteristics. Top-hat stiffeners are used extensively in the aerospace, civil and marine industries as they provide increased torsional rigidity compared to open section stiffeners providing increased resistance to buckling modes. However during service debonding between the stiffener and the plate is a common failure mechanism.

Following major damage events rapid assessment of the integrity of the damaged structure is critical in making decisions and taking precautions to ensure safety of the structure and it's users. An appreciation on the affect of damage in a specific structure type and a guide to the reliability of the structural integrity within a scope of realistic damage parameters would give a guide to the severity of the situation during different loading conditions.

Repairing de-bonded stiffeners becomes difficult in the vertical plane where resin drainage and cloth sag become a concern. This repair becomes costly and complex due to the need for highly skilled operators and the possible need to remove the structure from service for repair work to take place. By characterising the damage or delaminations and assessing their effect within panels and top-hat stiffeners, we can assess the residual capabilities of the panel and therefore critically assess the need for repairs and maintenance on naval composite vessels.

During the design of a composite structure it is imperative to consider the effect of defects and damage. To avoid both catastrophic failure or an overly conservative design philosophy, leading to inefficient use of materials and excess weight, these effects must be incorporated during the design phase. In industry the effect of delaminations in a simple composite structure is often approximated by means of empirical formulae, for example Schoeppner and Abrate [2] determine a delamination threshold load which applies only to simple structures. For more complex structures or different lay-ups material specific tests must be conducted; the common procedure in industry to deal with the effect of low velocity impacts at the design stage is to conduct compression tests to determine the compressive strength after impact which verifies the damage tolerance and residual capabilities of the structure. The compression after impact tests are specific to the part of the structure in which they are tested and not a general material parameter. The behaviour is heavily dependent on the loading conditions and therefore a number of tests should be conducted which is costly.

Therefore, there is a need for in-depth guidance on the residual strength of damaged structures and the effect of damage parameters is required on the strength to ensure rapid decisions can be made in damage situations, ensure maintenance and repair is carried out efficiently and the design of the structure is optimised with minimal experimental tests.

1.2 Assessment of Damage in Ships

This work is sponsored by Lloyd's Register and the UK MoD and damage is considered in the context of the UK MoD response to damage in surface ships.

Glass reinforced plastic, GRP, is currently used in over 100 mine counter-measure vessels in around 20 navies throughout the globe for its low magnetic signature characteristics. In this thesis, the problem of damage within composite stiffened structures is discussed using current UK MoD composite vessels as a guide. There are currently two classes of composite RN mine hunters in service; the Hunt Class mine counter measure vessels (MCMV) and the Sandown Class Single Role Mine Hunters (SRMH). The Hunt and Sandown class are constructed from single skin E-glass polyester hulls stiffened with longitudinal and transverse top-hat frames and girders with bulkheads secured to the deck and hull using "tee-joint" connections. A typical arrangement is illustrated in Figure 1. In recreational marine applications top-hat-stiffened single-skin topology is common and FRP hull sailing yachts have been constructed to lengths greater than 70m.

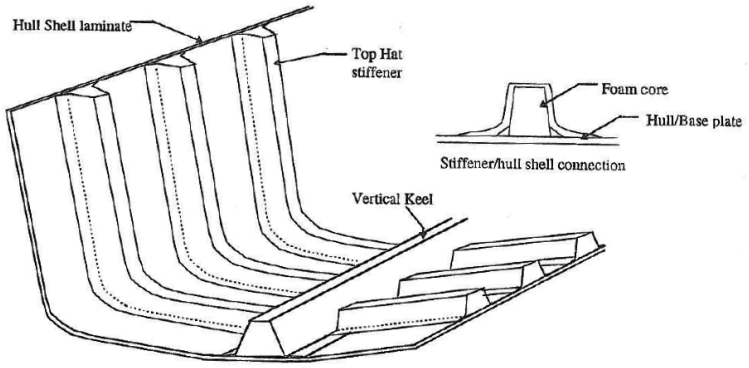

Figure 1: Schematic of structural connections in a GRP monocoque design

Marine structures are subjected to a variety of load conditions including both in-plane and out-of-plane quasi-static and dynamic forces. Hogging and sagging loads on the hull girder lead to compressive and tensile load which is generally in-line with the major stiffener direction, whilst out-of-plane hydrostatic and slamming loads occur in addition to structural loads and point loads for equipment. Whilst hogging and sagging loads on the hull girder are most likely to cause damage in the deck and keel, impact damage which is more commonly observed, occurs along the hull side. Damage can occur in both naval and commercial composite vessels through accidental collisions with other ships or wharves, by striking submerged objects or by severe wave slamming during high speed operations in heavy seas.

For MoD composite vessels, the large lamina thickness ensures a high hull girder stiffness, the primary loads on the hull girder are not considered critical. The secondary and tertiary structure will form the basis of a structural analysis as the connections create areas of stress concentrations and are critical in assessing the structural performance in the vessel. Particularly under wave slamming impact loading or under shock, the strength of the structure is dependent on the response of the bonded connections. Debonding of structural boundary angles and top-hat stiffeners is routinely observed by ship surveyors, as shown by Trask [3], however the cause of damage and

associated damage type is not yet documented in detail.

To illustrate the context of a post-damage decision figure 2 shows a methodology proposed by Cripps et al. [4] for damaged ships based on the Royal National Lifeboat Institution's experiences. The same methodology is used for metallic or composite ships from first report of damage through to return to service.

The practicality in applying this methodology to the in-service fleet rests upon the ability to access and identify post incident damage in-situ. Cabin outfit, equipment and fittings mean access to a damaged zone can be limited and the 'report of damage received' (action-1) prior to 'classifying initial damage' (action-5) may be reported as a worst-case estimate prior to the 'detailed survey at a designated location' (action-11).

The critical questions posed in the methodology are;

- how to determine the classification of damage?
- whether the damaged vessel may be moved?
- whether a cost effective repair can be made?

Rapid assessment of the integrity of the damaged vessel is critical in making these decisions and ensuring the safety of the crew and vessel. The UK MoD, following a minor damage incident, utilise the naval guidelines for 'maintenance and repair' of single skin composite vessels in line with Ministry of Defence Standard 02-752 Parts 1 and 2. Historically, standards required all delaminations to be repaired, which was costly and time consuming. This has subsequently been revised following research conducted for the third issue of the defence standard in-line with the Mine Warfare Fleet working towards a damage tolerance procedure. Current repair and survey guides are based on ship zoning diagrams and repair decision making trees; the extent of the damage is determined via methods outlined in Def Stan 02-752 Part I, where the defects are identified, the 'Ship Zoning Diagram', shown in figure 3, is used to outline the severity of damage in that area and the decision matrix outlines whether the damage needs to be repaired or subject to a 'mark and monitor' strategy. For typical damage type, a repair procedure is outlined in Def Stan 02-752 Part II.

A research program which updated the Def Stan was conducted by DERA in 2000 and published an acceptable limit to delamination of 300 mm diameter as the minimum size of defect which warrants structural repair rather than cosmetic repair or monitoring [3]. An abridged version of the delamination and debonding decision matrices for panels and top-hat stiffeners is illustrated in figure 4. It is worth noting that delaminations and stiffener de-bonding have the same decision matrix irrespective of zone. However, delaminations contained in the stiffener table and web are subject to a mark and monitor strategy where defects are less than 300mm diameter in the green and yellow zones.

Trask [3] produced a significant body of work on the intact response and failure modes of stiffened structures in the form of representative stiffened elements and larger structural elements under out-of-plane loads. It goes some way to confirm, experimentally, that a 300mm delamination does not affect the structural performance of the current fleet under-current working loads. However, the full effect of delamination damage on marine stiffened structures is still largely unknown; this is due to the lack of modelling capability and the limit on damage configurations tested

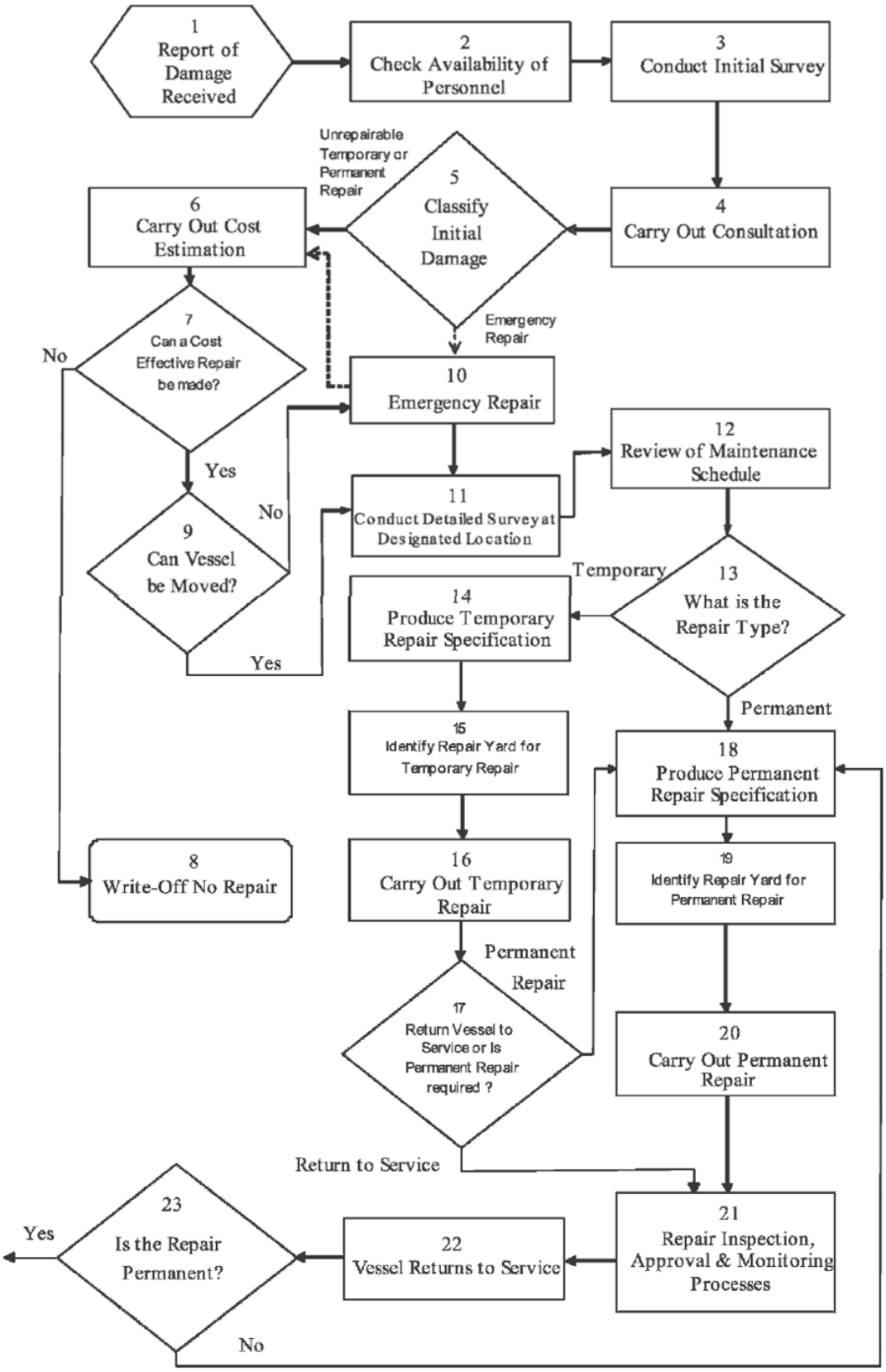

Figure 2: Generic Post-damage Decision Tree, Cripps et al. [4]

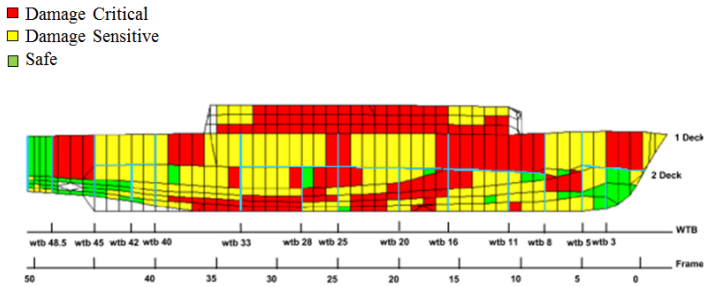

Figure 3: Ship zoning diagramTrask [3]

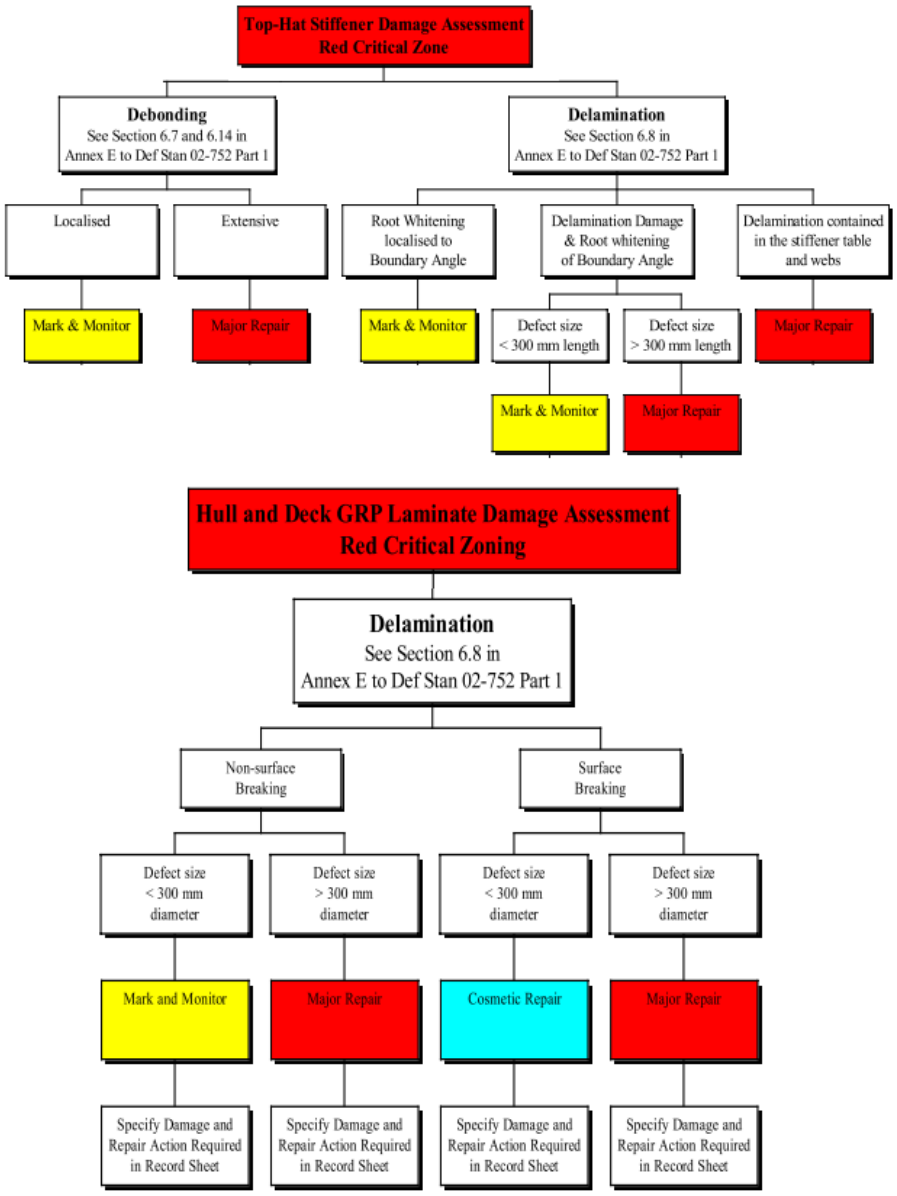

Figure 4: Repair approach for damage contained in red critical structural zones, Trask [3]

experimentally. The effect of delaminations under the stiffener, rather than within the bay, has not been investigated but has been shown by Meeks et al. [5] and Wiggenraad et al. [6] to have a far greater impact on the residual capability of the structure. Therefore, following a damage incident, whether minor or major, there are limited guides as to the residual strength and capabilities of the vessel. The MoD strategy looked at creating a damage tolerance approach and therefore, the inclusion of minor damage within the structure needs to be characterised along with it's effect on the capability of the vessel.

1.2.1 Case Study

One of the major incidents faced by UK MoD MCMV's was the grounding of HMS Grimsby off the coast of Norway in March 2006. She suffered areas of damage including known and suspected structural failure, water ingress and external hull damage. Both preliminary calculations and finite element analysis were carried out by QinetiQ [7] in order to determine her residual structural capability and determine the damage response process.

In the first phase damage was represented simplistically with de-bonded stiffeners removed entirely, delaminated side shells were thinned where abrasions occurred and transverse bulkheads removed where damage to boundary angles was suspected. In the second phase, following a more detailed survey report, de-bonded stiffeners were assessed against the hydrostatic pressure they support, neglecting the composite action between the stiffener and the shell, and the plates under fractured stiffeners were assessed as un-stiffened.

This incident highlighted the lack of knowledge on the damage response of composite naval vessels and the lack of readiness for a damage incident from a structural perspective. The main research tasks highlighted to overcome this shortfall as shown by Arason et al. [7] were:

- *"The characterisation of the likely properties of the GRP-material as a function of the operational history of each vessel*

- *Provision of a summary of possible failure mechanisms and corresponding simplistic assessment criteria*

- *Development of structural models to assess these mechanisms collectively"*

1.3 Research Objectives

Composite vessels commonly incur structural damage through impact however, as highlighted by the HMS Grimsby grounding situation, limited information is available on the residual strength of a damaged vessel. Composite joints

are critical in assessing the structural performance in the vessel and delamination and debonding damage are some of the most commonly observed damages. Following a damage incident there are limited guides as to the residual strength and capabilities of the vessel; there is a lack of extensive knowledge on how to assess and characterise damage, it's progression and how to survey, repair and design against it. For major damage incidents this is critical in deciding the appropriate course of action and ensuring the safety of both the crew and the vessel. Whilst for minor damage incidents assessment of the damage tolerance allows efficient maintenance and repair decisions to be made minimizing costs due to the need for highly skilled operators and the possible need to remove the vessel from service. The MoD strategy looked at creating a damage tolerance approach and therefore, the inclusion of minor damage within the structure needs to be characterised along with it's effect on the capability of the vessel. At the design stage, assessment of the effect of defects and damage leads to an optimised design which both avoids catastrophic failure and provides an efficient use of materials and therefore optimised weight and fuel efficiency or load carrying capacity.

1.3.1 Problem Statement

There is a need to assess, macroscopically, the effect of varying degrees of damage, the relationship between the type and extent of the damage and the residual strength of stiffened structures under realistic operational loads.

1.3.2 Research question

Following a damage incident, causing delaminations and associated damage within a composite top-hat stiffened plate, what are the residual capabilities of the stiffened plates under quasi-static loads?

1.3.3 Research Aim

The aim of this thesis is to generate a methodology to assess the performance capability of damaged joints and panels. An increased understanding of the effects of likely damage on the residual strength of a stiffened panel will guide post-damage decisions and also aid the design process of composite ships. Currently a conservative philosophy is applied to the design of stiffened composite panels due to the unknown effects of defects and damage. Therefore, guidance on the effect of defects and damage within the composite structure may be incorporated stochastically during the design phase to improve the design.

1.3.4 Research Objectives

In order to investigate the research question a number of objectives and sub-objectives are proposed:

[1] To conduct a comprehensive literature review in the following areas; experimental data and fracture properties, modelling methods for composite structures, modelling of damage initiation and progression within such structures and the effect of delaminations and debonds within composite structures.

[2] To identify the current state of the art in assessing the residual capabilities of composite stiffened structures.

[3] Development and verification of a finite element model capable of representing idealised delamination damage within a composite structure;

(a) verification of crack initiation and propagation by experimental data available in the literature.

(b) Verification of structural response of intact stiffened elements under in-plane compressive loads by experimental data available in the literature.

(c) Verification of progressive damage subroutine.

[4] Assessment of the effect of critical parameters on damage mechanisms and residual capability

(a) Sensitivity analysis investigating the effect of damage parameters on residual capabilities considering:

i. debond size and location,

ii. panel topology,

(b) comparison between stiffener section types between open and closed section stiffeners,

(c) comparison between combined loading configurations.

[5] Experimental assessment of the mechanical and interface properties of typical marine laminates and interfaces.

(a) Experimental assessment of the mechanical properties of heavy weight marine composites.

(b) Experimental assessment of the crack initiation and propagation through representative stiffened top-hat structures.

(c) verification and comparison of numerical model with experimental data

1.3.5 Research Scope

Due to the complexity of the problem, the scope of this project is defined to exclude:

- dynamic loading
- fluid-structure interaction
- modified stiffened structures including rivets
- metallic composite connections
- torsional and shear loading

As shown previously the MoD vessels are subjected to low velocity impact (LVI) loading commonly causing delaminations within the laminate and within a stiffened structure. However, in this thesis the damage response of the structure under an LVI is not considered; the post impact response of witnessed and proposed LVI damage under quasi-static loading is investigated. Stiffened structures are considered under quasi-static loads representing those

applied during use, however, the full fluid-structure interaction is not considered here. During the design and build of the Hunt Class McAdams a number of post build modifications were implemented including the addition of rivets securing the stiffener flange to the hull. Structures including such additions are not included in this analysis due to their unique nature. The loading conditions considered are limited to out-of-plane and in-plane loads and therefore neglects any torsional or shear loading.

1.3.6 Research Novelty

The novel contribution of this work is to efficiently model the effect of simulated debond damage on the ultimate strength of top-hat stiffened panels and multi-stiffened panels assessing the effects of damage and design parameters on the residual strength. The effect of typical marine interfaces is also assessed, which is lacking the literature, through an experimental program. Typical materials are fully characterised providing a complete data set of mechanical characterisation and fracture data for both co-cure interfaces, typical of mid-laminate debonds, and post-cured interfaces, which use an interface chopped strand mat layer at the interface, typical of sub-component joints. A four point bend test is conducted and the model is validated against this experimental data, verifying the properties represent those of an as built large scale structure. An assessment is also conducted on the effect on non-linearities on the flexural properties of DCB and ENF coupons and the assessment of interface properties for accurate modelling of post-cured glass vinylester laminates. A tool is therefore developed to allow further analysis and optimisation of typical marine top hat stiffened panels during both design to aid a damage tolerant design and for assessment in damage scenarios.

1.4 Publications

Conferences

- Davies, J.E., Sobey, A.J., Blake, J.I.R., Shenoi, R.A., Assessment of Damaged Composite Structures, MTPC 2012, Glasgow
- Davies, J.E., Sobey, A.J., Blake, J.I.R., Shenoi, R.A., Residual Capability of Damaged Composite Ship Structures, RINA-The Damaged Ship 2013, Croydon
- Davies, J.E., Sobey, A.J., Blake, J.I.R., Shenoi, R.A., Residual Capability of Composite Stiffened Marine Structures after Non-Critical Damage, International Conference on Composite Structures 2013, Porto
- Davies, J.E., Sobey, A.J., Blake, J.I.R., Shenoi, R.A., Damage Tolerance of Stiffened Composite Structures, |International Conference of Composite Materials 2013, Montreal

Papers

- Yetman, J.E., Sobey, A.J., Blake, J.I.R. and Shenoi, R.A., 2015. Investigation into skin stiffener debonding of top-hat stiffened composite structures. Composite Structures, 132, pp.1168-1181.

- Yetman, J.E., Sobey, A.J., Blake, J.I.R. and Shenoi, R.A., 2016. Fracture investigation of post-cured woven glass vinylester interfaces. Composites Part A: Applied Science and Manufacturing - under preparation

1.5 Report Structure

A literature review is presented in section 2 determining the state of the art in modelling and experimental testing composite stiffened panels and the inclusion of both simulated and impact delamination damage within composite structures. The literature review is then summarised and section 3 presents an outline of the research methodology. The modelling methodology is outlined in section 3.4 and verified in section 4 which presents a number of verification and parameter optimisation studies. The parametric analysis on the damage tolerance of generic top-hat stiffened panels is presented in 5. The mechanical characterisation and fracture properties are determined in section 6 along with four point bend tests on a top hat stiffened structure. The numerical analysis of this work is presented in section 7 to determine the key modelling parameters and further verify the model. A final study is conducted to compare the damage tolerance of top hat stiffened panels to debond damage using the experimentally determined properties and compared to the full study using assumed parameters from the literature. The key conclusions are discussed in section 8 with a discussion on future work.

2 Literature Review

Chapter 1 discussed that marine vessels are commonly subjected to low velocity impact, LVI, loading commonly causing delaminations within the laminate and within a stiffened structure. Composite joints are critical in assessing the structural performance in the vessel and that delamination and debonding damage are some of the most commonly observed damages. A greater understanding of the residual capability of the structure can both inform post damage decisions during major incidents, make maintenance and repair decisions more efficient and improve the design of the structure by avoiding catastrophic failure and improving the efficiency of use of materials.

To determine the response of stiffened structures and ultimately the ship response, a multi-scale analysis is required, as illustrated in figure 5. On the first level the material is characterised to determine ply stiffness through in-plane compression and tensile testing; the fracture toughness is determined through a number of mode and multi-mode tests. On the second level this data is used on larger scale models; some authors use 'representative stiffened elements' to show the effect of in-plane loads on the flange skin interface and to determine the load path through the structure. Single stiffeners are investigated to determine the stiffener response and damage progression subjected to in-plane and out-of-plane compressive loads in the pre-buckled and post-buckled regime. Multi-stiffened panels are required to replicate the skin-stiffener interaction during failure and the resulting damage mode interaction. Once this response is understood, grillage models replicating ship sections may be modelled to replicate the response under real loads interpreted from full ship data.

In this thesis heavy weight glass vinylester composites are investigated as they are used extensively in engineering applications with the majority of composite used in industry being glass woven roving and or mat layers [8] as they provide a balance between performance and cost. Vinylester provides higher fracture strain than typical polyesters and hence produces composites with superior mechanical properties, impact resistance, and fatigue life. For large engineering structures composite joints between plates, stiffeners and other sub-components are often post-cured due to the scale of the production process and typical interfaces contain a chopped strand mat (CSM) layer. Debonding of sub-component parts is a common failure mode of these types of structures however the characterisation of these typical post-cured interfaces is not well understood.

In this section the literature is critically reviewed and the state of the art is established in three sections. Section 2.1 summarises the material data available for input to the model for typical marine composites established in level one of the multi-scale analysis of the multi-scale analysis and section 2.2 discusses modelling damage and fracture in composites also referring to level one. Section 2.3 reviews the literature associated with modelling and testing of the structural response of stiffened composite laminates which is discussed as representative stiffened elements, stiffened panels and finally grillages; level two to four of the multi-scale analysis.

2.1 Experimental Characterisation

In this section the literature is reviewed for the mechanical characterisation and fracture interface properties of heavy weight woven glass vinylester for co-cured and post-cured interfaces. The literature on the assessment and

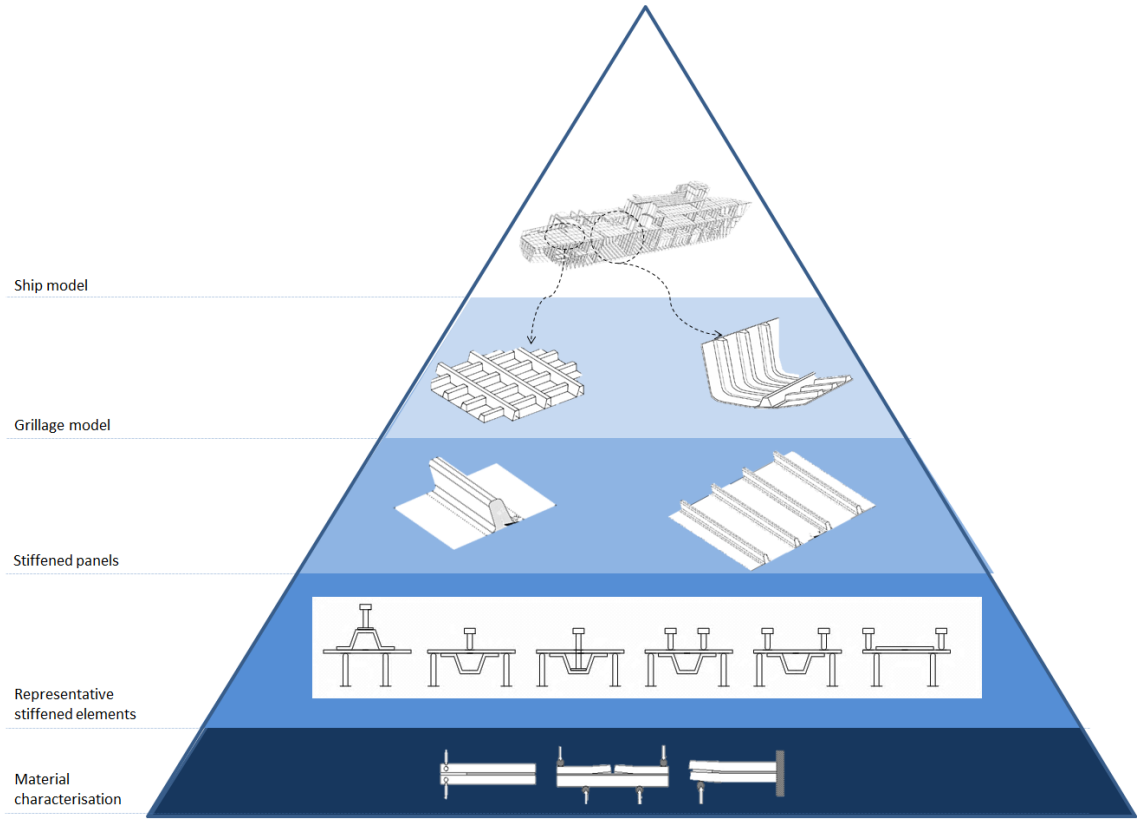

Figure 5: Multi-scale analysis of composite stiffened structures

failure of woven composites is divided into micro, meso and macro scale approaches. In this study a macro scale approach is adopted to assess the global failure mechanisms, therefore this review concentrates on the failure modes observed and the application of macro scale properties of woven composites.

Many papers outline material properties for heavy weight glass vinylester and the material data available in the literature is outlined in table 1. Dharmawan et al. [11] investigated the mode I, II and mixed mode fracture of plain weave glass vinylester composites but the manufacturing method is not defined in the paper. Compston [12] investigated 638gsm woven roving using both a standard (Dow Derakane 411-45) and modified vinylester (Dow Derakane 8084) and compared the results to comparable UD samples, all samples were fabricated by hand in a wet lay-up. Blake et al. [10] conducted mode I, II and mixed mode tests on E-glass fibre with a toughened vinylester resin matrix typical of the marine industry using a heavy woven fabric and compared a number of data sets available in the literature. These authors have characterised the fracture properties of glass vinylester of varying weave structure, weight and composition however the associated mechanical characterisation is lacking in these papers. Dharmawan has quoted elastic properties for the material in other papers but no experimental source is cited for these properties [14, 15, 11]. Shivakumar [9] has determined the material properties for 610gsm woven E-Glass with an unbalanced construction of 59% and 41% in the warp and fill directions. The panels were manufactured via VARTM using Derakane 510a-40 for work characterising impact but omits fracture information.

In these studies the non-linearity of the woven samples are not discussed. Zhou and Davies [16] conducted

material tests on thick glass woven roving polyester laminates typical of the marine industry and highlighted the non-linearities present tension and shear. The fabric was slightly unbalanced with approximately 30% more fibres in the 0° direction. In compression Zhou and Davies [16] showed a linear response however the tensile characterisation tests showed an initial linear stress-strain curve followed by a second linear region with reduced stiffness following the 'knee'. Zhou and Davies [16] found that the knee occurs at a stress approximately 18% of the ultimate load and coincides and perhaps coincidentally, at the typical tensile stress of polyester. This knee effect is also observed by other authors; Cox [17] describes this effect in 3D composites as the 'hardening phase' which is attributed to 'inelastic' straightening of the in-plane tows. Under in-plane shear the stress-strain curves exhibit a non-linear behaviour due to matrix yielding caused by the 'scissoring' action of the fibres. This effect is comparable to the matrix shearing that occurs in unidirectional coupons, however, an additional non-linear component at the later stages of loading is attributed to the straightening out of the crimped fibres. Zhou's tensile and shear constitutive curves are shown in figure 6. Welsh et al. [18] investigated 510gsm plain weave glass vinylester composite under biaxial tests and established an in-plane bi-axial failure envelope. Welsh also identified a shift in the overall stiffness under tensile load representing a 'knee' and quoted the initial and final stiffness to be 27.4 and 19.2GPa i.e. a reduction of 29%.

The interface properties of woven fabrics has been investigated by many authors. Funk and Deaton [19] showed that the mode I interlaminate fracture toughness increased from between two and eight fold greater for a woven fabric compared to a unidirectional composite for T300 carbon fibre/934 epoxy. However, the toughness depends on the weave structure and fibre stacking method. Another important factor in this apparent increase is the inherent roughness of woven laminates with the topology dependent on the fabric thickness as well as the weave structure. This roughness leads to interlaminar resin-rich areas which allow larger plastic yield zones to develop ahead of the crack tip [20, 21]. Dharmawan et al. [22] showed that for woven DCB samples the mode I fracture toughness is dependent on the thickness of the specimen below 10mm. Therefore, the manufacturing method (layup), specimen thickness, weave structure, fabric weight and fibre volume fraction have an impact on the fracture toughness. Specific tests are necessary to quantify these values for the thickness, weave structure and fibre volume fraction typical of a marine manufacturer.

The interface properties of glass Vinylester woven roving are assessed by a number of authors.Mouritz et al. [13] conducted mode I tests on post-cured alternating plies of 600 g/m^2 plain woven roving & 300g/m^2 chopped strand mat. The fibreglass preforms were infused with a vinylester resin (Dow Derakane 411-45) using vacuum assisted resin transfer moulding. However, the results for this data are unclear in the work presented. Aside from this work quantifying the effect of the chopped strand mat on a co-cured interface, fracture toughness is not well documented in the literature for mode I and not investigated for mode II crack opening. Authors who have investigated debonding of composites components, discussed in section 2.3.3, Yap [23], Wiggenraad et al. [24], Meeks et al. [5], Orifici et al. [25], Suh [26] have investigated the effect of stiffener skin debonding for co-cured and post-cured manufacture and conducted multi-scale analyses neglecting the CSM layer which can be present stiffener-plate joints. Kim et al. [27] investigated the effect of the joining method between the stiffener and the plate for carob epoxy pre-preg panels in

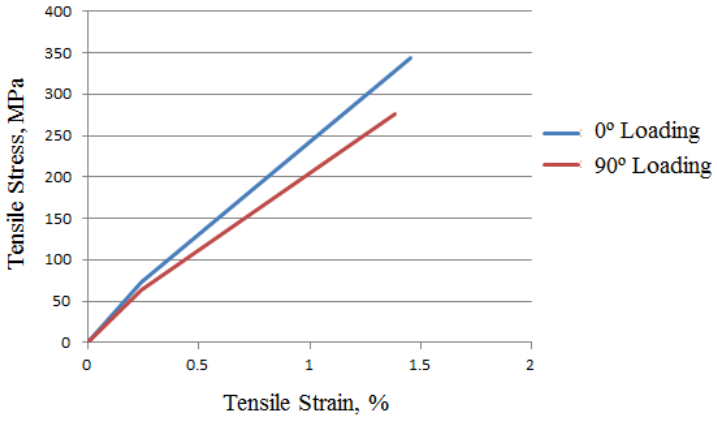

(a) Woven Roving Tensile Stress Strain Relationship

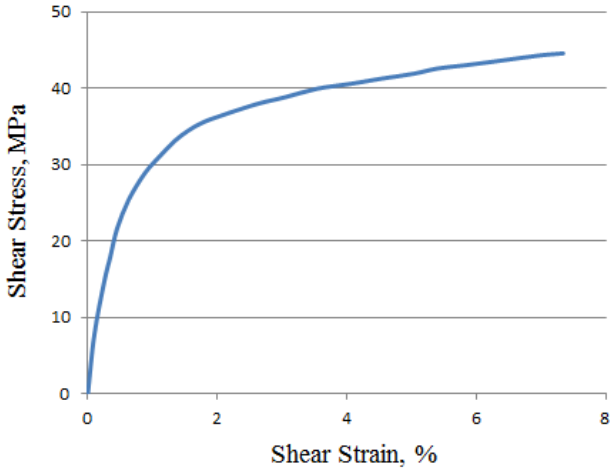

(b) Woven Roving Shear Stress Strain Relationship

Figure 6: Woven Roving Stress Strain Relationships (adapted from Zhou and Davies [16])

the context of the aerospace industry and showed that bonding post-cured plate and stiffeners reduced the pull off strength of the stiffener by 60% compared to the co-curing the specimen.

It is shown that the interface and mechanical properties are dependent on the specific material, layup and manufacturing configuration, therefore material data must be quite specific to the configuration in question. It is shown in table 1 that the data available for E-glass woven fabrics with a vinylester resin that there is significant variation between both the mechanical and fracture properties recorded and is likely to be due to differences in the test and material configurations. It is also shown that for woven fabrics prior to initial failure a non-linear response is required for tensile and shear loading to represent the straightening of the fibre tows and the 'scissoring' action of the fibres respectively. When modelling such structural interfaces a complete data set is required, drawing upon multiple and non-similar sources can lead to significant errors due to the variation in manufacturing methods, fibre volume fraction, weave structure, fabric weight and sample thickness.

Therefore, this literature review has identified a gap in the research in the assessment of complete data set including fracture properties is lacking for both mechanical and fracture properties and the fracture properties of

post-cured interfaces.

2.2 Modelling Damage and Fracture in Composites

LVIs can cause a number of failure modes; matrix crushing, local fibre breaking at the impact surface, matrix cracking, back-face ply splitting and fibre breaks and multiple delaminations. Demuts et al. [28] showed that induced low velocity impact can reduce the tensile strength of a coupon by as much as 25% and the compressive strength by more than 60% with little or no visible external damage. Numerous studies have investigated associated damage with LVI tests and the effect of lay-up, stacking sequence, impact energy, impact speed, boundary conditions, pre-loading, damage geometry and other parameters [29, 30, 31, 32, 33, 34, 35]. In this thesis the post impact response of LVI damage under quasi-static loading is investigated to ascertain the remaining structural capability. This analysis allows an understanding of the strength after impact during continued use and allows efficient operational, maintenance and damage incident decisions to be made. Following a major damage incident this analysis helps to answer the questions posed during damage response; determine the classification of damage, whether the damaged vessel may be moved and does the repair need to be immediately repaired.

Laminates containing delaminations investigated under compressive in-plane loads display a complex response involving a combination of local buckling of the delaminated region, global buckling of the laminate, damage initiation and propagation. Therefore an in-depth understanding is required of the response of intact laminate structures, strength based failure initiation and propagation, delamination initiation and propagation and the interaction between these mechanisms. For fibre-matrix composites the failure modes can often be complex; localised micro-cracks and fibre breakages accumulate altering the constitutive properties of the localised region, altering the load path which results in progressive damage across the structure. Many laminates may carry higher loads following initial damage to the structure and a progressive damage model is required to fully understand the remaining capability of the structure. Therefore, this section outlines the state of the art in modelling the response of intact laminate structures, strength based failure initiation and propagation, modelling cracks in composite materials, the effect of delaminations within a laminate and modelling realistic delamination damage.

2.2.1 Mechanics of Composites

In order to model the structural behaviour of composite laminates numerous theories have been developed to investigate the response at an appropriate level of detail: micro-mechanical, ply level or laminate level.

At a micro-mechanical scale the fibre and the matrix are modelled separately with different constitutive relationships allowing modelling of fibre pull out, weave structure, crack propagation and fracture at a fibre, matrix scale. Material variation, flaws, inclusions and cracks may be modelled as seen in microscopic 3D images and for woven laminates the individual tows may be modelled [36, 37]. These models are only feasible for micro analysis rather than large scale structures therefore ply level or lamina level models are required. These treat the fibre matrix composite as a homogeneous anisotropic material by defining material directions parallel to the fibre direction (1-direction), perpendicular to the main fibre directions (2-direction) and through the lamina thickness (3-direction).

The ply's constitutive behaviour is determined by material coupon tests. A laminate level model considers a number of stacked plies in the through thickness direction with the perfect bond condition assumed between the individual plies and the interface is neglected.

For the majority of laminate structures the laminate thickness is small in comparison to the lateral span. Therefore, a three dimensional structure may be represented as a two dimensional structural model, eliminating the thickness component by integrating along the thickness. A number of theories are proposed in this form that satisfy the basic requirements for the stress, strain and displacement field over the laminate thickness. Laminate plate theories broadly fit into two categories; equivalent single layer theories, which assume a single displacement field over the entire thickness of the laminate, or layer wise theories, where a separate displacement field is used for each layer.

Equivalent single layer theories are extensions of approaches established for homogeneous structures to allow for multiple layers within the laminate. A single displacement field is assumed across the thickness of the laminate. The simplest theory is classical laminate plate theory (CLPT) based on Kirchoff plate theory which neglects shear deformation effects and assumes that plane sections remain in plane under bending deformation. The through thickness stresses are neglected in the initial calculation which can assume an overly stiff structure. However, through thickness stress may be estimated by post-processing the in-plane stresses using equilibrium conditions allowing increased accuracy in displacement and stress.

First-order shear deformation theories (FSDT), based on Reissner-Mindlin kinematic models, allow rotation of the through thickness normal under bending and therefore assumes a linear displacement field across the thickness of the laminate therefore, the through thickness shear stresses are discontinuous across the ply boundaries. FSDT may be used for thin and moderately thick laminates to provide approximate solutions. However, thin plate assumptions are also dependent on the ratio of orthotropic properties, with increasing error as the transverse elastic flexibility constants increase relative to the in-plane constants [38]. The transverse shear stiffness may be corrected through an energy equivalence procedure whereby the strain energy calculated by the FSDT is corrected by a 'shear correction factor' which equates the strain energy to that predicted by full 3D elastic theory.

For increased accuracy on local effects, including inter-laminar stress distributions between layers and delaminations, higher-order shear deformation theories are required allowing for additional degrees of freedom in representing the through thickness displacement field and therefore allowing warping of the cross-section. Reddy [39] provides a simple higher-order theory which accounts for a parabolic variation of the transverse shear strains through the thickness without the need for shear correction coefficients.

Layer-wise theories use a separate displacement field for each ply and may be used to increase the accuracy of the stress distribution. The previously discussed theories all have equivalent single layer theories. Layer-wise models may more accurately predict inter-laminar stresses but are more computationally expensive as the number of layers increases. Layer-wise theories can be a good compromise compared to full three dimensional continuum-based theory which can predict the inter-laminar stress of a composite structure but are extremely computationally expensive.

Laminate plate theories may be implemented through finite element methods. Finite element methods introduce a piece-wise approximation to the governing equations. By dividing the whole domain into elements, equations are solved for each element and assembled in order to generate a global response of the structure. Shell elements represent an equivalent single layer approach, whereby the model is generated in a two dimensional geometry and the equivalent properties are assigned to the areas. It is then possible to post process the through thickness properties. Standard element formulations available in Abaqus allow for use of CLPT, FSDT and SSDT theory with or without post processed equilibrium based through thickness stresses. Solid elements with linear or quadratic formulation may be used to replicate a layer wise approximation for first order or second order deformation theory respectively, where an element per ply is used for meshing. As the number of elements increases through the thickness of the laminate the result increases in accuracy tending towards the full three dimensional continuum based theory. Although, the accuracy of the solution is dependent on maintaining a balanced proportionality of the element dimensions and therefore for an element per ply mesh the lateral mesh discretisation is of the order of the laminate thickness which can lead to computationally expensive models.

The relative accuracy of different laminate theories is dependent on the complexity of the lay-up, structural configuration, loading conditions, failure modes and failure criterion used and therefore the compromise between computational efficiency and accuracy must be made for each specific case. In this work FSDT and SSDT equivalent layer approaches are considered to produce an efficient and accurate model. These are compared to layer-wise approaches to ensure the accuracy and convergence of the model where complex loading and failure is observed.

2.2.2 Strength Based Failure Criteria

Many strength based failure criteria exist in a range of complexity from simplistic independent criteria to more complex criteria based on physical or phenomenological models which identify the failure mode and take into account the material non-linearity for pre and post initial failure response.

Initial failure is termed when the fibres fracture, (FF) or macroscopic cracks appear in the laminate, termed Inter Fibre Fracture (IFF). Micro-damage can occur prior to the 'initial failure'. In the curing process of a laminate structure, residual stresses are introduced due to the differing thermal expansion coefficients of the fibre and the matrix. These residual stresses cause flaws that, along with inherent variation and other micro structural defects and inclusions, lead to local fibre-matrix debonding and micro-cracking within the matrix. At relatively low loads these micro-cracks form and propagate causing a reduction in the stiffness and strength of the localised area and a non-linearity in the constitutive relationship.

Criteria are selected as a trade off on their proven accuracy in given load conditions and failure modes and the necessary material characterisation requirements. Recent and on-going work from the World Wide Failure Exercise (WWFE), [40, 41, 42, 43, 44] analyses failure criteria and compares them to experimental results to provide a summary of the strengths and weaknesses of each failure criterion.

The World Wide Failure Exercise (WWFE) has highlighted that no single criterion currently results in an accurate prediction of failure for all possible conditions. During the WWFE Part A, [40], 14 contributors analysed

different cases of biaxial failure envelopes and stress/strain curves and were compared, whilst part B [42] compared these failure criteria against experimental data. The exercise showed that some theories lack flexibility and others require further development and that even familiar investigations resulted in large differences in the final strength predictions of the laminates. Part B looked to identify the strengths and weaknesses of 19 different criteria and five were identified as promising however, the final fracture strength was only accurate to within 50% for 75% of cases.

The five approaches ranked highest [44], presented here are:

- Puck and Schürmann [45] - Puck is a phenomenological model and is based on the Coulomb-Mohr hypothesis of brittle fracture. Puck was the first author to separate failure modes of fibre failure, FF, and inter-fibre failure, IFF, and treats the failure modes separately; fibre failure is a result of tensile and compressive stresses parallel to the fibre direction and inter-fibre failure, the result of normal stresses perpendicular to the fibre direction and shear stresses. Puck also categorises three modes of matrix cracking depending on the angle of the fracture plane and the lamina and the load that causes fracture. The theory is based on a non-linear stress and strain up until fracture identifying the onset of micro damage and incorporating this influence on the material stiffness by means of weakening factors prior to IFF or FF failure. Continuous degradation is represented after the onset of failure by means of a weakening factor on the stiffness of the laminate.

- Tsai [46] - Tsai employs the Tsai-Wu interactive failure criterion, assuming linear elastic material properties and reduced matrix stiffness to account for degradation after initial failure. This criterion does not explicitly identify failure mechanisms. Tsai uses an interaction criterion, F_{12} to account for the interaction of in-plane stresses. Tsai recommends that for most materials F_{xy} equals -0.5.

- Zinoviev [47] - The Zinoviev failure criterion is a development on the maximum stress theory, where linear elastic material behaviour is assumed until initial failure and the progressive damage is predicted by the degradation of material properties. Zinoviev states that the theory may be used for predicting the failure envelope for multi-layered composites under a variety of loading conditions.

- Cuntze [48] - Cuntze's failure criterion is similar to Puck's, considering three dimensional failure mechanisms and in applying a non-linear analysis to predict progressive failure, however Cuntze assumes an interaction between failure modes due to probabilistic effects. Puck and Cuntze produced the highest number of accurate predictions and were capable of capturing the more general features of the experimental results.

- Bogetti [49] - Bogetti uses a three dimensional form of the maximum strain failure criterion which incorporates non-linear material behaviour prior to the failure strain and degradation of properties during a progressive failure analysis.

The theories of Puck (or Cuntze) and Tsai-Wu are recommended to be used together for predicting the response of unidirectional laminate under combined loading taking the most conservative estimate. Puck's theory is recommended for estimating the strength of multi-directional laminates whilst, Zinoviev's theory is recommended for use in predicting the deformation of laminates along with a non-linear method such as Puck or Cuntze. The Puck,

Tsai-Wu and Zinoviev theories are shown in table 2 and are illustrated using self developed code in figures 7 and 8 for first ply failure using the WWFE load cases 1 and 3 for longitudinal versus transverse loading and transverse versus shear loading respectively and verified against the work of Soden [50].

In longitudinal and transverse loading it can be seen from figure 7 that both the Tsai-Wu and Puck criteria yield the most conservative results for different loading segments. For this material the Tsai-Wu criterion yields significantly increased strength in the negative quadrant compared to the Puck and Zinoviev criteria. In this case the Puck criterion yields the most conservative results. For longitudinal and shear loading it can be seen from figure 8 that for this material the Tsai-Wu and Puck criteria yield similar results and that a combination of the Puck and Zinoviev criteria yield the most conservative assessment.

It is shown for this material that no one criterion yields a conservative response in all loading conditions. The accuracy of the Puck and Tsai-Wu criterion for a specific material are dependent on the material parameters used; Tsai-Wu's interaction parameter, Puck's inclination and degradation factors, the fibre modulus and Poisson's ratio. As these parameters are only established in the literature for specific materials and without detailed experimental results a near approximation is often used. To account for the inaccuracies in these assumptions, and to ensure a conservative criterion the minima of the three criterion are used for the parameters chosen, a combination of the Tsai-Wu, Puck and Zinoviev criteria is deemed as the conservative yielding failure envelopes as shown in figures 9 and 10.

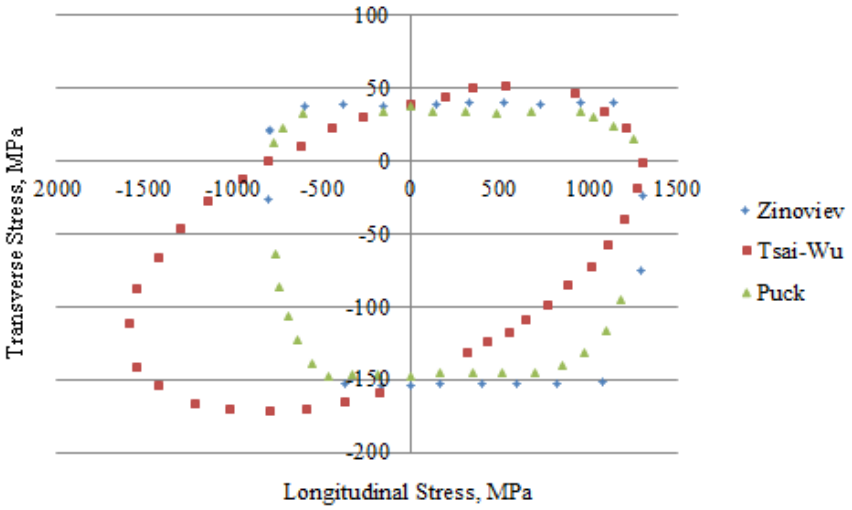

Figure 7: Comparison of failure criterion longitudinal and transverse failure envelopes

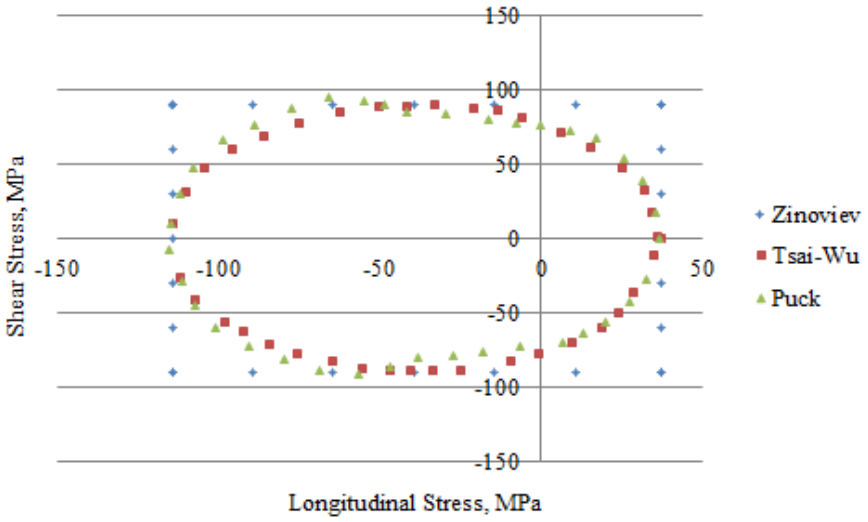

Figure 8: Comparison of longitudinal and shear failure envelopes

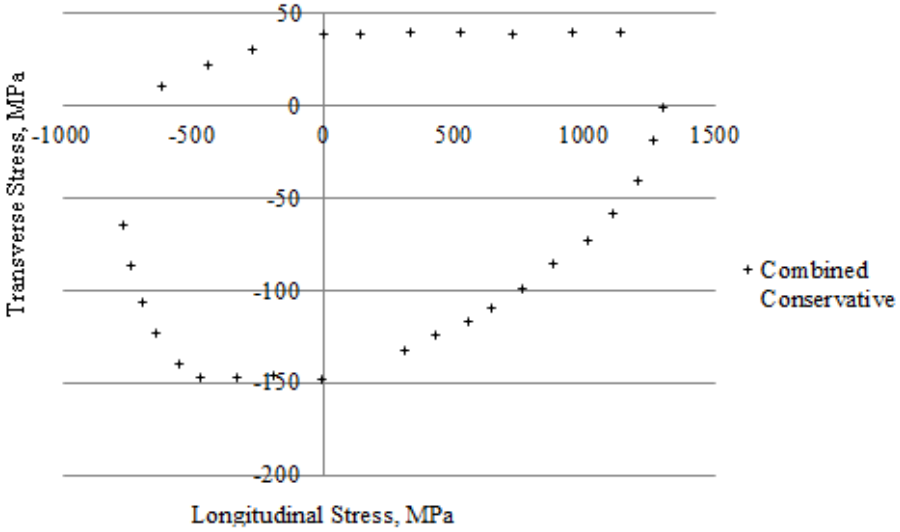

Figure 9: Conservative longitudinal and transverse failure envelope

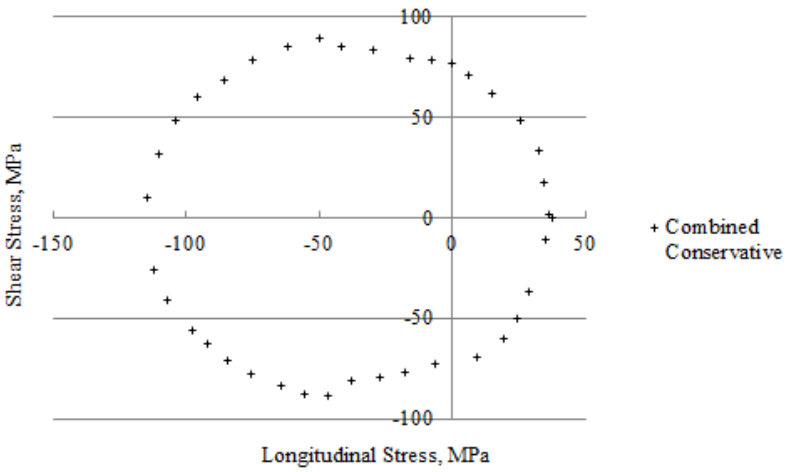

Figure 10: Conservative criterion longitudinal and shear failure envelope

For this research for multi-directional composites a UMAT code has developed from the work of Misirlis [51] using additional failure criteria as advised by the WWFE; the Tsai-Wu, Zinoviev and Puck failure criteria are combined to form a conservative criterion as described in section 2.2.4.

Strength based criteria have also been proposed for delamination initiation. Orifici et al. [52] reviewed delamination initiation failure criteria showing that these all use a combination of through thickness tensile and shear stresses whilst a few also consider the in-plane shear. A comprehensive review of such criteria compared to mixed mode experimental data is lacking in the literature and are not fully compared or verified. Therefore, the most commonly used criterion is adopted as part of this research; the quadratic nominal stress criterion [53] as shown in equation 1.

$$\left(\frac{\sigma_3}{S_{33T}}\right)^2 + \left(\frac{\sigma_{23}}{S_{23}}\right)^2 + \left(\frac{\sigma_{31}}{S_{31}}\right)^2 \geq 1 \tag{1}$$

2.2.3 Failure Criterion for Woven Roving

The failure criterion discussed in section 2.2.2 are discussed with regard to their application to unidirectional lamina or multidirectional laminates composed of numerous layers of angled unidirectional plies. In the marine industry alternative fibre distributions are also commonly used such as woven roving and chopped strand mat. The validity of these failure criteria for these types of composites is not usually discussed when used with such weave structures. Therefore, this section compares the constitutive equations, material non-linearities and the initial and progressive damage of plain woven roving, typical of the marine industry.

The literature on modelling and failure of woven composites is divided into micro, meso and macro scale approaches. In this study a macro scale approach is adopted to assess the global failure mechanisms, therefore this review concentrates on the failure modes observed and the application of macro scale failure criterion to woven composites.

Welsh et al. [18] investigated 510gsm plain weave glass vinylester composite under biaxial tests and established an in-plane bi-axial failure envelope. The authors conducted a multi-continuum theory to simulate and predict failure in bi-axial failure. Similar data is presented by Owen and Rice [54] for bi-axial tests on plain weave glass polyester for longitudinal and transverse stresses however as Fujii et al. [55] presents the experimental response for combined shear and longitudinal loading for plain weave glass polyester for the positive quadrant this data is chosen for further analysis.

The experimental biaxial data of Owen and Rice [54] on plain weave glass polyester for longitudinal and transverse stresses are compared here using user code to the failure criteria discussed in section 2.2.2 and illustrated in figure 11 and 12. Figure 11 compares the Tsai-Wu, Zinoviev and Puck criteria where the Tsai-Wu criterion uses the interaction factor, F_{xy} equal to -0.5 as recommended by the author for use with 'most materials'. The experimental data exists for only positive longitudinal stress. The response is symmetric, about the $\sigma_x = \sigma_y$ plane however, the negative loaded quadrant is not available. For the data present it can be seen that for a conservative estimate Puck provides good agreement under positive load, whilst providing a non conservative result for negative transverse loading. Tsai-Wu provides good agreement under negative transverse loading and a poor, unconservative, result under positive loading.

The effect of Tsai-Wu's interaction factor is assessed in figure 12. It can be seen that by increasing the interaction factor to -0.15 the Tsai-Wu criterion can provide good correlation with the experimental data, although a completely conservative result can not be achieved in both the positive and negatively loaded quadrants.

Fujii et al. [55] presents the experimental response for combined shear and longitudinal loading for plain weave glass polyester for the positive quadrant. The experimental ply failure stress is compared to the Tsai-Wu, Puck and Zinoviev failure criteria in figure 13. As expected the Zinoviev criterion gives an unconservative result for the majority of data points. The Puck failure criterion is illustrated using the parameters advised by the associated guidance paper for unidirectional laminates [56]. This parameter selection significantly alters the shape and therefore fit of the Puck failure criterion curve. In particular, reducing the inclination parameters could provide a far closer fit. However, without the data set for the negative quadrants the accuracy of the fit in this area cannot be assessed. In this case the Tsai-Wu criterion with an interaction factor of -0.15 gives reasonable agreement to the experimental final strength data. As the Tsai-Wu failure criterion provides good agreement for the experimental data provided and is the most conservative in the negative normal stress quadrant, it is deemed the most appropriate criterion in this case.

The experimental data for the 'knee', or first yield point for the woven material is also compared to the Tsai-Wu criterion which is assessed at 18% and 25% percent of the ply failure stresses in figure 14. Owen and Rice [54] suggests from the tensile tests that the 'knee' occurs at 18% of the ply failure stress, however the experimental data of Fujii et al. [55] for the biaxial normal-shear stress shows a closer fit is obtained from 25% of the ply failure. Although Fuji and Owen and Rice investigated plain weave glass polyester the longitudinal tensile failure stresses of the two materials vary significantly suggesting the laminates differ either in fibre volume fraction or the balance of materials in the longitudinal and transverse directions therefore it is suggested that the first yield point is lamina

specific.

In summary it is shown that for this data good accuracy can be achieved for the combined longitudinal-transverse and longitudinal-shear loading by modifying Tsai-Wu's interaction factor to -0.15 and that the initial yield during tensile loading can be represented by 25% of the Tsai-Wu ply failure stress. Therefore for this research the Tsai-Wu criterion is chosen for woven composites using an interaction factor of -0.15. During compressive loading a linear constitutive model is used unless otherwise stated.

	Interface	1	2 (warp/weft)	3	4	5	6	7	Units
Tensile Modulus		14910	29200/23900						MPa
Poisson's Ratio		.119	0.16/0.14						
Compressive Modulus		14910	31900/26900						MPa
Compressive Strength		171.5	363.4/336.4						MPa
Shear Modulus		2.1	4.5/4.3						GPa
Shear Strength		23.2	47.3						MPa
Flexural Modulus					24200				MPa
Co-Cured Mode I Initiation Strain Energy Release Rate	WR				0.577	0.227	0.239	0.69	kJ/m2
Co-Cured Mode I Propagation Strain Energy Release Rate	WR			0.804	1.210	0.988	0.739	0.68	kJ/m2
Co-Cured Mode II Strain Initiation Energy Release Rate	WR			0.627		1.152	0.724		kJ/m2
Co-Cured Mode II Propagation Strain Energy Release Rate	WR				4.550	5.461	4.102		kJ/m2
Co-Cured CSM Mode I Initiation Strain Energy Release Rate	CSM							0.67	kJ/m2
Co-Cured CSM Mode I Propagation Strain Energy Release Rate	CSM							0.70	kJ/m2
Co-Cured CSM Mode II Strain Initiation Energy Release Rate	CSM								kJ/m2
Co-Cured CSM Mode II Propagation Strain Energy Release Rate	CSM								kJ/m2
Post-cured Mode I Initiation Strain Energy Release Rate	CSM								kJ/m2
Post-cured Mode I Propagation Strain Energy Release Rate	CSM								kJ/m2
Post-cured Mode II Initiation Strain Energy Release Rate	CSM								kJ/m2
Post-cured Mode II Propagation Strain Energy Release Rate	CSM								kJ/m2

Table 1: Summary of Experimentally Determined Material Properties

(1) Gurit supplied material data E-glass 600gsm balanced woven roving with a Scott Bader vinylester resin manufactured by resin infusion

(2) Shivakumar [9] tested E-glass woven roving with a Dow Derakane 510A-40 brominated vinyl ester manufactured via VARTM

(3) Blake et al. [10] tested 800gsm woven E glass with a toughened Derakane 8084 matrix

(4) Dharmawan et al. [11] tested 800gsm woven E glass with a Derakane 411-350 matrix, data averaged if from multiple sources.

(5) Compston [12] tested Derakane 8084 using an E-glass woven 638gsm manufactured by hand lay up

(6)Compston [12] tested Derakane 411-45 using an E-glass woven 638gsm manufactured by hand lay up

(7) Mouritz et al. [13] tested alternating plies of 600 g/m^2 plain woven roving & $300 g/m^2$ chopped strand mat infused with a vinylester resin (Dow Derakane 411-45) using vacuum assisted resin transfer moulding.

Table 2: WWFE failure criterion

Failure Theory	Failure Mode		Failure Criterion	Condition for validity
Puck	Fibre Failure	Tensile	$\frac{1}{\varepsilon_{1T}}(\varepsilon_{11}+\frac{\nu_{f12}}{E_{f1}}m_{\sigma f}\sigma_{22})=1$	$\sigma_{11}>0$
		Compressive	$\frac{1}{\varepsilon_{1c}}\lvert(\varepsilon_{11}+\frac{\nu_{f12}}{E_{f1}}m_{\sigma f}\sigma_{22})\rvert=1$	$\sigma_{11}<0$
	Inter Fibre Failure	Mode A	$\sqrt{\left(\frac{\sigma_{21}}{S_{21}}\right)^2+\left(1-p\frac{S_{22T}}{S_{21}}\right)^2\left(\frac{\sigma_{22}}{S_{22T}}\right)^2}+p^{(+)}_{\perp\parallel}\frac{\sigma_2}{S_{21}}=1-\lvert\frac{\sigma_{11}}{\sigma_{1D}}\rvert$	$\sigma_{22}\geq 0$
		Mode B	$\frac{1}{S_{12}}\left(\sqrt{\sigma_{12}^2+\left(p^{(-)}_{\perp\parallel}\sigma_2\right)^2}+p^{(-)}_{\perp\parallel}\sigma_2\right)=1-\lvert\frac{\sigma_{11}}{\sigma_{1D}}\rvert$	$\sigma_{2<0}$ and $0\leq\lvert\frac{\sigma_{22}}{\sigma_{21}}\rvert\leq\frac{R^A_{\perp\perp}}{\lvert\sigma_{21c}\rvert}$
		Mode C	$\left[\left(\frac{\sigma_{21}}{2(1+p^{(-)}_{\perp\perp}S_{21})}\right)^2+\left(\frac{\sigma_{22}}{S_{22C}}\right)^2\right]\frac{S_{22C}}{-\sigma_2}=1-\lvert\frac{\sigma_{11}}{\sigma_{1D}}\rvert$	$\sigma_{2<0}$ and $0\leq\lvert\frac{\sigma_{12}}{\sigma_{22}}\rvert\leq\frac{\lvert\sigma_{21c}\rvert}{R^A_{\perp\perp}}$
Tsai-Wu	$\left(\frac{1}{S_{11T}}-\frac{1}{S_{11C}}\right)\sigma_{11}+\left(\frac{1}{S_{22T}}-\frac{1}{S_{22C}}\right)\sigma_{22}+\left(\frac{1}{S_{11C}S_{11T}}\right)\sigma_{11}^2+\left(\frac{1}{S_{22C}S_{22T}}\right)\sigma_{22}^2+(\frac{2F_{12}}{\sqrt{S_{11T}S_{11C}S_{22T}S_{22C}}})\sigma_{11}\sigma_{22}+\frac{1}{S_{12}^2}\sigma_{12}^2\geq 1$			
Zinoviev	Fibre Failure	Tensile	$\frac{\sigma_{11}}{S_{11T}}\leq 1$	$\sigma_{11}>0$
		Compressive	$\frac{\sigma_{11}}{S_{11C}}\leq 1$	$\sigma_{11}<0$
	Matrix Failure	Tensile	$\frac{\sigma_{22}}{S_{22T}}\leq 1$	$\sigma_{22}>0$
		Compressive	$\frac{\sigma_{22}}{S_{22C}}\leq 1$	$\sigma_{22}<0$
	Shear Failure	Shear	$\frac{\sigma_{12}}{S_{12}}\leq 1$	

where Puck's inclination parameters and strength parameters are defined by $p^{(+)}_{\perp\parallel}=-(\frac{d\sigma_{21}}{d\sigma_{22}})_{\sigma_{2=0}}$ of $(\sigma_{22},\sigma_{12})$ curve, $\sigma_2\geq 0$; $p^{(-)}_{\perp\parallel}=-(\frac{d\sigma_{22}}{d\sigma_{21}})_{\sigma_{2=0}}$ of $(\sigma_{22},\sigma_{12})$ curve, $\sigma_2\leq 0$; $p^{(-)}_{\perp\perp}=p^{(-)}_{\perp\parallel}\frac{R^A_{\perp\perp}}{S_{21}}$; and $R^A_{\perp\perp}=\frac{S_{22c}}{2(1+p^{(-)}_{\perp\perp})}=\frac{S_{21}}{2p^{(-)}_{\perp\parallel}}\left(\sqrt{1-2p^{(-)}_{\perp\parallel}\frac{S_{22c}}{S_{21}}}-1\right)$; $\sigma_{12c}=S_{21}\sqrt{1+2p^{(-)}_{\perp\perp}}$ and F_{12} is Tsai-Wu's interaction parameters

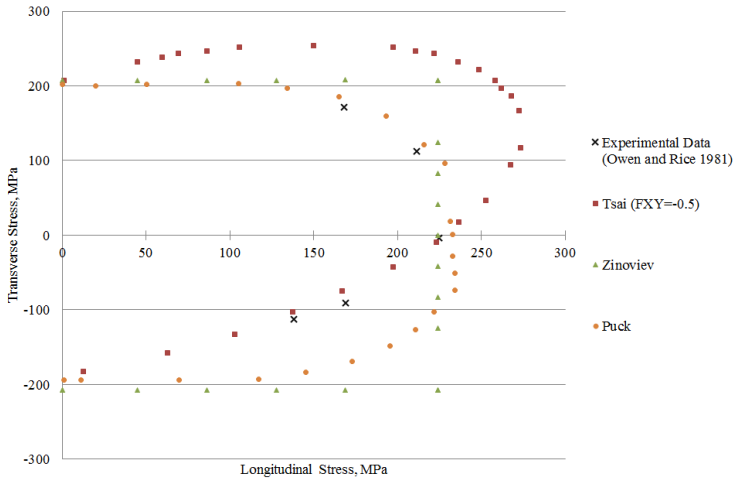

Figure 11: Biaxial Stress Failure Envelope; Comparison of Failure Criteria for Woven Glass Polyester

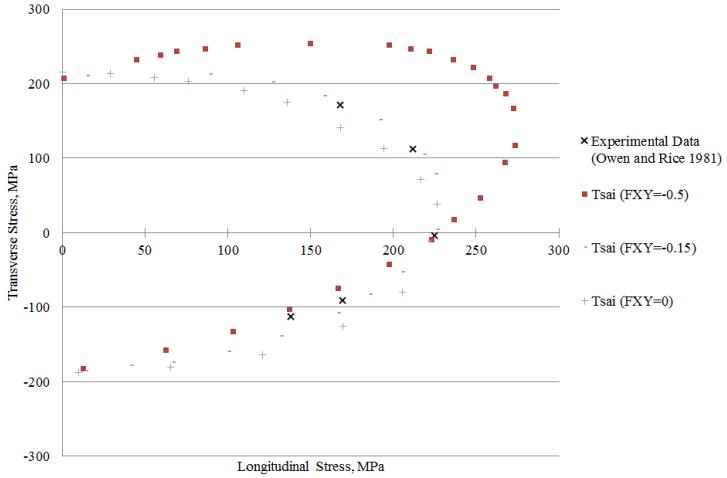

Figure 12: Biaxial Stress Failure Envelope; Comparison of Tsai-Wu Interaction Factor for Woven Glass Polyester

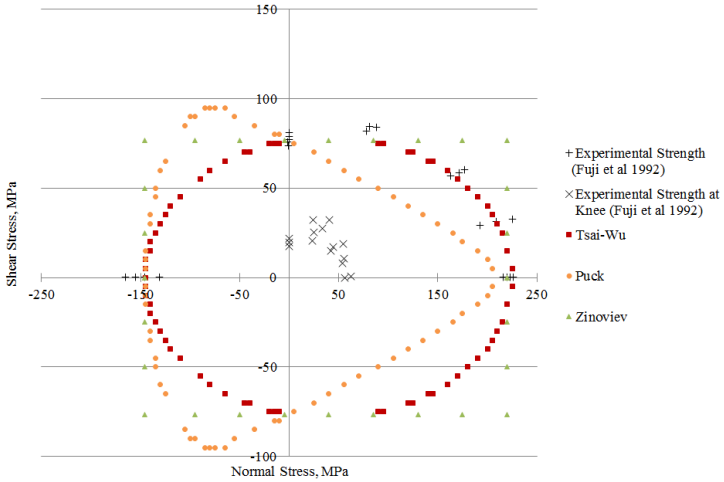

Figure 13: Biaxial Stress Failure Envelope; Shear Transverse Stress Map for Woven Glass Polyester

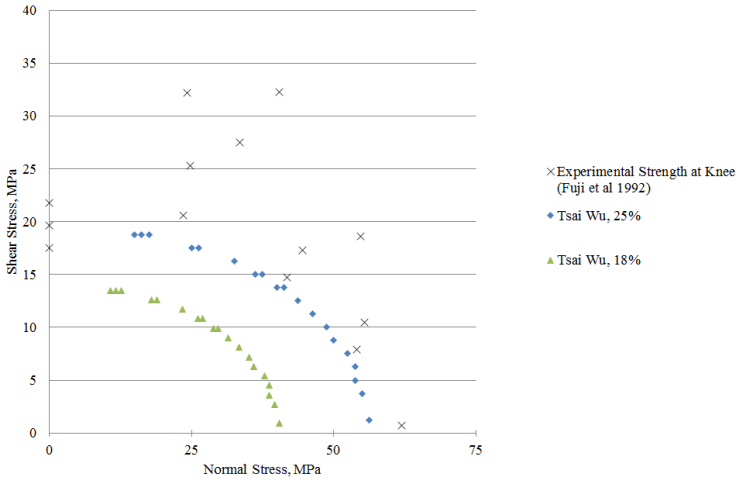

Figure 14: Biaxial Stress Failure Envelope; Shear Transverse Stress Map

2.2.4 Progressive Damage Approaches

For fibre-matrix composites the failure modes can often be complex; localised micro-cracks and fibre breakages accumulate altering the constitutive properties of the localised region and altering the load path resulting in damage progressing across the structure. Many laminates may carry higher loads after initial damage occurs as the load path is altered and can be capable of reducing stresses within the structure. Therefore, a progressive damage approach is required to fully understand the ultimate strength of a structure. A number of progressive damage approaches have been developed to simulate the damage evolution post first-ply-failure by degrading the material properties of the regions which exceed the failure criteria with appropriate properties. The progressive damage methodology and a review of such techniques is discussed here.

Prior to damage initiation the element integration point stiffness matrix is linear elastic, however once the failure criterion is exceeded for that element the stiffness matrix is then degraded accordingly. The stress, σ, strain, ε, relationship post-damage initiation is governed by equation 2;

$$\sigma = C_d \varepsilon \tag{2}$$

Where C_d represents the damaged elasticity matrix.

A number of degradation models are proposed, including the 'Total Discount Approach', where the strength and stiffness of failed plies are reduced to zero; the 'Gradual Degradation Method', where the stiffness reduction depends on the failure mode, as used in work by Chang and Chang [57]; and the 'Gradual Degradation Method', where continuum damage models are used to predict progressive damage and the associated drop in stiffness and damage accumulation is predicted by damage evolution laws. The total discount approach is the most conservative, whereby the element stiffness is degraded to zero in every direction, whereas for the limited discount approach the stiffness reduction is dependent on the failure mode.

For the limited discount approach and residual property method the 2D damaged elasticity matrix, C_d, has the form;

$$C_d = \frac{1}{D}\begin{bmatrix} (1-d_1)E_1 & (1-d_1)(1-d_2)\nu_{21}E_2 & 0 \\ (1-d_1)(1-d_2)\nu_{12}E_2 & (1-d_2)E_2 & 0 \\ 0 & 0 & (1-d_6)GD \end{bmatrix}, \tag{3}$$

where $D = 1-(1-d_1)(1-d_2)\nu_{12}\nu_{21}$ and d_1, d_2 and d_6 reflect the current state of the fibre, matrix and shear degradation factors respectively which are defined as either compressive (d_{1c}) or tensile components (d_{1t}) dependent on the current failure criterion used and on the loading as shown in equation 4.

$$
\begin{aligned}
d_1 &= \begin{matrix} d_{1t} & if & \sigma_{11} \geq 0 \\ d_{1c} & if & \sigma_{11} \leq 0 \end{matrix} \\
d_2 &= \begin{matrix} d_{2t} & if & \sigma_{22} \geq 0 \\ d_{2c} & if & \sigma_{22} \leq 0 \end{matrix} \\
d_6 &= 1 - (1 - d_{1t})(1 - d_{1c})(1 - d_{2t})(1 - d_{2c})
\end{aligned} \tag{4}
$$

In a limited discount approach the damage variables are degraded to zero, or may be reduced to a nominal positive value e.g. 1e-6. In a gradual degradation method the stiffness reduction is controlled using a softening material model which can be based on irreversible thermodynamic considerations. The gradual reduction of the stiffness properties is initiated at the equivalent failure stress, $\sigma_{o,eq}$ and displacement, $\delta_{o,eq}$ and is usually implemented by a linear softening or exponential softening technique, as shown in figure 15. The stiffness is decreased to zero at displacement,$\delta_{f,eq}$. The area enclosed by the constitutive curve is associated with the strain energy of complete rupture and/or mapped to experimental constitutive data. Matzenmiller et al. [58] suggested the use of a linear softening material model which is based on the rate-dependent constitutive model and used experimental data to show that the collapse strain lies within the range of two to four times the initial failure strain.

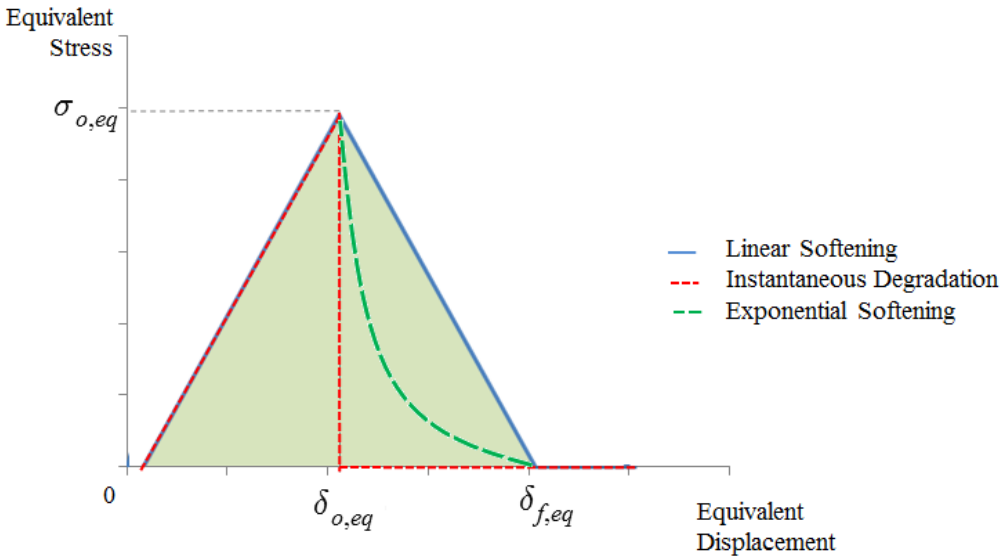

Figure 15: Stress displacement relationship for linear softening degradation model

All of the WWFE criteria discussed in section 2.2.2 include limited discount approaches. Tsai-Wu's failure criterion uses an instantaneous degradation scheme whereby the transverse modulus, Poisson's ratio and shear modulus are degraded to nominal values following failure initiation. As Tsai-Wu's criterion does not differentiate between failure modes the degraded properties are dependent on the transverse strains; a compressive transverse strain inhibits microcrack growth and therefore fibre failure is assumed. Under tensile transverse strain matrix

Table 3: Comparison of progressive damage modes of failure

	Zinoviev	Puck	Tsai-Wu
Fibre fracture	$E_1 = 0$	$E_1 = 0$	$E_1 = 0.01E_1^0$
Inter Fibre Fracture: $\sigma_2 > 0$	$E_2 = d_Z E_2^0$, $G_{12} = d_Z G_{12}^0$	$E_2 = d_P E_2^0$, $G_{12} = d_P G_{12}^0$,$\nu_{12} = d_P \nu_{12}$	$E_2 = 0.15E_2^0$, $G_{12} = 0.15G_{12}^0$
Inter Fibre Fracture: $\sigma_2 < 0$	$G_{12} = d_Z G_{12}^0$	$G_{12} = d_P G_{12}^0$,$\nu_{12} = d_P \nu_{12}$	$G_{12} = 0.01G_{12}^0$,$\nu_{12} = 0.01\nu_{12}$,$E_1 = 0.01E_1^0$ $E_2 = 0.01E_2^0$,

failure is assumed to have initially failed and on a second iteration where the failure criterion is exceeded, the fibre is assumed to have failed. For fibre failure the longitudinal, transverse and shear moduli and the Poisson's ratio are degraded, for matrix failure the transverse and shear moduli are degraded to nominal values. The Puck and Zinoviev progressive damage methodologies associate the degradation factors with the failure modes as shown in table 3 where E_1, E_2, G_{12}, ν_{12} are the secant modulus and E_1^0, E_2^0, G_{12}^0, ν_{12}^0 are the initial material properties. Puck's degradation factor, d_P, is a function of stress, calculated by iterating the degradation factor until the failure criterion equals zero. For each failure mode the degradation factors are set to equally reduce the appropriate material properties as shown in table 3. Zinoviev's degradation factor is a function of strain $d_Z = E_1[\frac{\varepsilon_2^*}{\sigma_2^*} + \frac{\nu_{12}^2}{E_1}]$ where σ_2^* and ε_2^* represent the largest stress and strain values during the history of the loading. Therefore the stress at initial failure and the strain at ultimate failure are both required to implement the failure criterion.

When using progressive damage methodology within the finite element method it is necessary to introduce a characteristic length to alleviate mesh dependency so the stress-strain relation is expressed as a stress displacement relation as shown in figure 15. The characteristic length, L_c, represents the length of a line across an element with a linear node function or half the same length for an element with quadratic function.

Constitutive models with strain softening behaviour can also lead to numerical convergence issues in implicit solvers. These difficulties can be overcome by use of a viscous regularisation scheme which causes the tangent stiffness matrix of the softening material to be positive for sufficiently small time increments, as shown by equation 5;

$$\dot{d_v} = \frac{1}{\eta}(d - d_v), \tag{5}$$

where η is the viscosity parameter, d is the degradation factor and d_v is the regularised degradation factor.

To ensure an analogous strain energy released by the damage evolution for each material direction the viscous parameter may be calculated by equation 6,

$$\eta_{2T} = \frac{\eta_{1T} S_{2T} E_1}{S_{1T} E_2} \tag{6}$$

Applying a viscous regularisation scheme slows the rate of increase of damage, leads to an increased fracture energy and therefore increases the likelihood of a non-conservative result. It must be ensured that the viscosity parameter is small compared to the characteristic time increment to improve the rate of convergence and remove

convergence difficulties without compromising the result.

Progressive damage methodologies have been shown to successfully replicate experimental tests using finite element methods with developed user subroutines for Abaqus, ANSYS or LS-Dyna. For example, Reddy and Reddy [59] presented a progressive failure model based on the Tsai-Wu criterion with a limited discount approach and instantaneous degradation following failure for a layer wise plate theory for a three point bend specimen including geometric non-linearity. Padhi et al. [60] developed a progressive damage subroutine for Abaqus and compared a number of failure criteria using instantaneous degradation and a limited discount approach. This work used FSDT to model a plate subjected to transverse pressures and was compared to experimental tests with good correlation. Blake [61] used Padhi's progressive damage subroutine to successfully replicate the static structural response on a tee joint containing viscoelastic inserts. As fibre-matrix composites tend to be relatively weak in transverse shear there is a need to accurately predict the peak transverse shear strain to simulate damage progression. Models using FSDT were shown to predict slower damage accumulation and yield significantly higher failure loads compared to the layer-wise model.

2.2.5 Modelling Cracks in Homogeneous Materials

Modelling damage in the form of cracks or delaminations requires either a damage mechanics, fracture mechanics or combined approach. Damage mechanics approaches investigate stress and strain at the interface, whilst fracture mechanics approaches equate the strain energy release rate to the fracture toughness of the material. Fracture mechanics approaches are the most widely used approach and have currently achieved the most success however, more recently, there has been an increase in the use of a combined cohesive element approach.

An overview of fracture mechanics theory is presented here in relation to the following discussion, however the fundamental principals are reported in Appendix B.

In the 1920's Griffith [62] proposed his linear elastic fracture mechanics theory for crack propagation, whereby a crack extension occurs when the energy available is large enough to overcome the resistance of the material. Irwin defined the strain energy release rate (SERR), G, as the amount of energy released if the crack were to advance by one unit length. When the strain energy release rate is greater than the surface energy of the material, the crack will advance. At the moment of crack propagation the strain energy release rate is equal to the critical strain energy release rate, G_c. The stability of crack growth can be calculated by computing the energy release rate, G, at different crack lengths, a, and calculating the derivative of the energy release rate with respect to the crack length.

Irwin [63] utilised linear elastic theory to develop the stress intensity approach. At the crack tip the stress intensity factor, K, determines the magnitude of the elastic stresses. Irwin [63] also showed that his critical stress intensity factor, K_c, is equivalent to the Griffith-Irwin energy balance approach.

Linear elastic fracture mechanics is only applicable with a small plastic zone ahead of the crack tip. Rice [64] proposed the J-integral approach based on the linear elastic energy approach whereby the plastic response is modelled as a non-linear elastic response. As plastic deformation is irrecoverable it is required that no unloading may occur. The J-integral is a path independent line integral measuring the magnitude of the singular stresses and

strains in the region of the crack tip and is equivalent to the strain energy release rate when subjected to monotonic loading under quasi-static loading.

For isotropic homogeneous materials there are three well defined and independent modes of crack propagation; mode I caused by in-plane normal stresses, mode II caused by in-plane shear stress and mode III caused by transverse shear stresses. These failure modes are illustrated in figure 16. Each mode has an associated stress intensity factor and strain; K_I, K_{II}, K_{III} respectively for modes I, II and III. These stress intensity factors may be expressed in terms of the principal stresses.

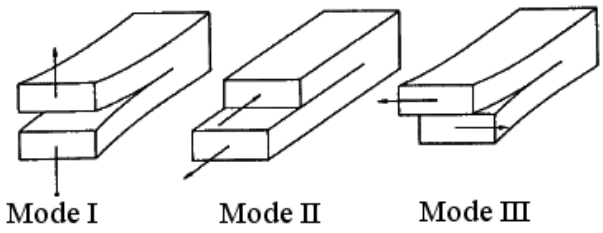

Figure 16: Crack propagation modes

The fracture toughness for each mode may be determined from standardized test methods; the double cantilever beam specimen for mode I, the end notched flexure or end-loaded split test specimen for mode II and a edge crack torsion test for mode III.

For crack propagation under mixed-mode loading, a number of mixed-mode failure criteria exist which determine the relationships between modes. The relevance of such failure criteria may be determined from mixed-mode bending tests for modes I and II, however, no such mixed mode test exists incorporating mode III loading. Reeder [65, 66] performed mixed mode bending tests to assess a number of failure criteria compared to experimental data. He concluded that different composite materials respond differently and that no one failure criterion will be the most accurate for all materials, and that practical material characterization tests are required in pure mode and mixed-mode for each material. The choice of failure criterion is based on the number of curve fitting parameters used, how well the criterion fits a variety of material responses and ease of use. The bilinear criterion [67], linear interaction criterion [68] or the Benzeggagh-Kenane criterion [69] (B-K) are recommended and have recently been used by many researchers when modelling delaminations. The Benzeggagh-Kenane criterion with a single parameter is shown to deliver adequate accuracy of mixed mode fracture for a wide range of composite materials and is recommended by the ASTM standards [70]. The Benzeggagh-Kenane criterion for crack propagation is shown for the 2D case and 3D case in equations 7 and 8 respectively, where η is a semi-empirical exponent applied to delamination initiation and growth. For the 2D case $G_T = G_I + G_{II}$ and for the 3D case $G_T = G_I + G_{II} + G_{III}$.

$$G_{IC} + (G_{IIC} - G_{IC})(\frac{G_{II}}{G_T})^{\eta} \geq G_T \tag{7}$$

$$G_{IC} + \left((G_{IIC} - G_{IC}) \frac{G_{II}}{G_T} + (G_{IIIC} - G_{IC}) \frac{G_{III}}{G_T} \right) \left(\frac{G_{II} + G_{III}}{G_T} \right)^{\eta - 1} \geq G_T \tag{8}$$

The energy of crack propagation may be calculated from analytical or numerical models by a number of methods the most common being a form of the virtual crack closure technique and the equivalent domain integral. These more popular techniques in a three dimensional formulation are available as an intrinsic feature of Abaqus finite element software.

The equivalent domain integral method uses the J-integral formulation where the surface integrals are transformed into integrals over a domain or volume. This allows modal decomposition utilising one analysis step and eliminates the need for orthogonal elements to the crack front.

The Virtual Crack Closure Technique (VCCT) is a term used in the literature to refer to a number of techniques whereby the crack extends by a small amount and the energy dissipated during the crack extension is equal to the work required to close the crack to the original length. Therefore, the SERR may be calculated from nodal forces and displacements in the region of the crack tip. A number of variations on this method exist, where the strain energy release rate is calculated either by closing the original crack (crack closure method), extending the crack by a small amount (crack extension method) or a combination. The crack extension method allows a comparison of the the total SERR as a function of the direction of virtual extension and therefore allows the crack extension direction to be predicted by means of a minimum energy approach. This method requires two analyses to compare the SERR before and after crack advancement, however, the 'Modified Virtual Crack Closure Technique' eliminates the need for a second analysis by assuming that additional crack advancement does not alter the state of the crack. Therefore, the virtual crack extension is assumed to require the same energy needed to close a crack of the same length behind the crack tip and may be calculated in a single analysis but the modified virtual crack closure integral may only be used if the elements in the region of the crack tip have the same dimension in the crack growth extension.

The approach and application of the VCCT is discussed in great detail in a review paper presented by Krueger [71]. These fracture mechanics methods requires an initial delamination to be present and cannot be used to predict the onset of a delamination. It is computationally efficient when the mesh is sufficiently refined and the elements in the region of the crack tip have the same dimension in the crack growth direction as the SERR may be calculated using one analysis. For reasonably behaved SERRS and in two dimensional analyses, Raju et al. [72] suggested element size should be taken as 0.25 - 0.5 of the ply thickness. A commonly adopted industry practise is that the finite element size at the crack tip is standardized to a half ply thickness and displacement and forces at the node nearest to the singularity are used for the modal energy release rate calculation. However, modelling the crack growth at the scale of the crack tip may not be physically correct due to the micro-mechanical behaviour at the crack tip.

The VCCT is capable of assessing the static modal components of the SERR but independently cannot predict follow and determine the crack propagation path as it assumes self-similar crack growth. In order to model crack progression whilst using the VCCT or the J-integral approach a nodal release algorithm is required, however determining the crack propagation direction and finding the true energy minimum, requires an adaptive meshing

algorithm is required which can be extremely costly and complex.

Node release patterns can be used to monitor crack propagation either based on experimentally observed crack propagation paths or through iterative calculation where the the region around the interface where delaminations are expected are divided into a number of double nodes, one on the upper surface and one on the lower. One such method, proposed by Chen et al. [73] is based on the responses of the unit load on the potential cracks, the nodal forces and displacements for the evaluation of strain-energy release rate are solved by a series of linear equations without re-analysing the finite element model during crack growth. Zheng and Sun [74] used the J-integral approach to predict delamination propagation paths and variation of strain energy release rate along a crack front with good agreement to 3D finite element models and also with experiments with delamination due to impact loading.

Moes et al. [75] have developed a computationally more efficient method; the extended finite element approach (XFEM) utilising an FEM process which enriches the solution space for elements whose domain contains the material interface. This allows a crack path to be followed without the need for re-meshing. However, the geometry of the crack front does not always match the element boundary therefore, the domain form of the J-integral must be utilised rather than a VCCT or crack extension technique. The XFEM technique is available as an intrinsic feature of finite element software however in it's current form it is not possible to assess the J integral at material or part boundaries, i.e. at a ply interface. Nagashima et al. [76] discusses the use of the XFEM approach and shows that this methods requires increased computation time to solve the system equations compared to conventional FEM.

2.2.6 Modelling Cracks at a Bi-Material Interface

When a crack initiates between the plies of the laminate this is termed a delamination and is effectively a crack problem. Whilst the bounding plies are similar in material and orientation the problems may be simplified to that of a homogeneous material, however, modelling laminates of multiple, different plies and orientations complicates the modelling of the crack problem significantly at the bi-material interface.

Williams (1959) showed that the stresses at a radial distance, r, from the crack tip possess singularities of the type $r^{-1/2\pm i\zeta}$, where ζ is the oscillatory index. The oscillatory index is a bi-material constant dependent on the elastic moduli of the two interface materials and is defined by Suo [77] as;

$$\zeta = \frac{1}{2\pi}\ln(\frac{1-\beta}{1+\beta}), \tag{9}$$

where β is dependent on the elastic properties of and stresses in the materials above and below the interface.

The imaginary part of the exponent leads to violent oscillations in the immediate vicinity of the crack tip. Due to the oscillatory nature of the stresses and displacements the mixed mode ratio is undefined as the extension length tends to zero although the total SERR is well defined [78, 72]. Empirical parameters are often used to model crack propagation and damage in bi-material interfaces however their physical significance is often dubious. Test methods may be used to determine, so-called, material properties for energy dissipation under pure mode loading, however incorporation of these parameters into complex composite structures and loading conditions contains assumptions and cumulative errors and must be verified by rigorous characterisation on a multi-scale approach. Micro and

meso scale models can be used to equate these parameters to physical mechanisms taking place in real composite structures and to determine their dependencies on micro and macro parameters.

A number of techniques exist to overcome this complexity and allow mixed mode separation; utilising characteristic lengths to identify parameters used for mode separation, a number of non-singular field approaches removing the oscillations in the vicinity of the crack tip and modelling the crack in the interface layer between plies. The details of these are summarised below:

Due to the oscillatory nature of the near tip stresses the mode mix is dependent on the distance relative to the crack tip in which the mode mix is defined. This characteristic length must therefore be defined to determine the mode mix calculated from virtual crack closure technique in numerical models. Raju et al. [72] showed, using elements at the crack tip of the order of a quarter to half of the ply thickness, the individual modal components of the energy release rate agreed well with more detailed calculations including a resin-rich layer between the plies. Beuth [79] proposes a method whereby the crack extension is normalised with respect to the characteristic length. This characteristic length is considered to be the dominant length scale determining the size of the oscillatory zone.

A number of 'non-oscillatory' strain energy release rate components are derived by eliminating the oscillatory term. One such method is the so-called '$\beta = 0$' approach whereby the classical square root singularity is recovered by simply neglecting the oscillatory function as defined by Hutchinson and Suo [80]. Some authors suggest altering 'less significant' material properties so that $\beta = 0$. Typically the Poisson's ratio is changed and it is assumed that this does not significantly affect the physics of the problem, although there is currently no consistent procedure for altering the material properties. These 'non-oscillatory' strain energy release rate components have been shown to have relatively poor predictive capabilities [81].

To alleviate the need for such mesh refinement at the crack tip a number of crack tip elements are suggested [82, 83, 84] where mode separation is achieved by equating the total energy release rate from classical plate theory to that from the 3D near-tip solution. The method requires two supplementary finite element solutions, in which the VCCT was employed. Yang et al. [84] used the modal components of the energy release rate with respect to a finite crack extension with a crack tip extension of 0.1% of the crack length. These methods utilise classical laminate plate theory and neglect the transverse shear stresses which could become significant in increasingly complex structures and loading behaviours and lead to an underestimation of the strain energy release rate. A number of theories have since attempted to extend this theory to include, by first order approximations, the transverse shear. However, these elements require a detailed three dimensional study of the near-tip solution and for increasingly complex structures and loading behaviours this would need to be conducted for each scenario.

Alternative methods include the J integral, XFEM and cohesive element methods.Sukumar et al. [85] shows that the J integral remains globally path independent for bimaterial interface crack problems when there exists no material inhomogeneity in the direction parallel to the crack. Nagashima et al. [76] presents a review of XFEM for bimaterial interface showing that various methods for evaluating the stress intensity factors related to bimaterial interface cracks have been developed. The XFEM technique applies an enrichment function to describe the displacement field near a crack is determined according to the asymptotic solution of a homogeneous crack and

is therefore not specific to the bi-material interface. There are also problems, as previously discussed if the crack is located on the interface of two materials.

At a bi-material interface the crack may be considered to lie between the plies in a resin rich interface, as seen in micrographs of composite laminates, then the crack problem becomes that of a homogeneous isotropic material on the neighbouring surfaces. However, as with the VCCT method the assumption also leads to a self-similar trajectory for crack propagation which may bound the true stress intensity factor. Should the crack deflect into the neighbouring plies the calculation of the true value of K is increasingly complex. In order to remove this assumption involves conceptual difficulties along with mathematical mechanics subtleties.

Cohesive or interface elements, based on a Dugdale-Barenblatt [86] type cohesive zone look to model the region between the interface plies. The interface is assumed to be attached by 'springs' which dissipate energy during micro-cracking and once this energy is equivalent to the fracture toughness then cracks form. This method combines a fracture mechanics and damage mechanics approach; cohesive elements use a strain softening constitutive model in the interface process zone ahead of the crack tip and relate displacement continuities with traction vector at the process zone to the fracture toughness and crack surface area, as shown in figure 17.

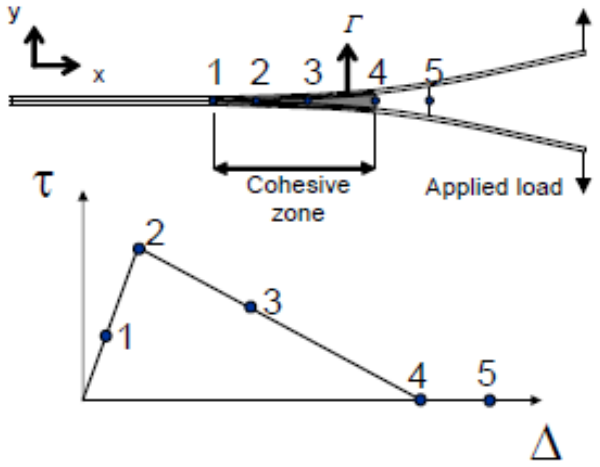

Figure 17: Cohesive zone ahead of crack tip

Cohesive elements are a convenient method for calculation providing a prediction of both delamination onset and growth without the need for intervention during the analysis. The constitutive model must be consistent with allowing all the energy dissipation at the crack tip to be equal to the fracture toughness for each fracture mode and respective shear stress,

$$\int_0^{\Delta_{if}} \tau_i d\Delta_i = G_{ic}$$

τ_i, traction component at interface,

Δ_{if}, relative displacement corresponding to complete decohesion,

Δ_i, relative displacement,

G_{ic}, critical strain energy release rate.

For mixed mode cracks, the damage activation criteria must take into account all the traction tensors.

Many constitutive models have been proposed, as shown in figure 18, with the most common being a linear strain softening behaviour.

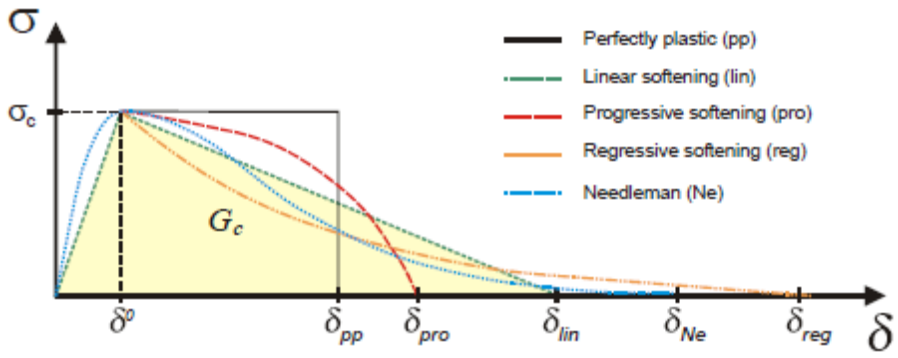

Figure 18: Constitutive strain softening equations

The cohesive element constitutive equation assumes linear elastic behaviour with interfacial initial stiffness, E, until the damage initiation strain, ε_o, is reached followed by linear evolution of damage until the failure strain, ε_f, is reached. Where the tractions integrated to complete failure represents the fracture energy release rate, G_c.

For thickness, T, the traction-separation relationship is related to the stress-strain relationship by 10 and 11.

$$K = K'T \tag{10}$$

$$\varepsilon_n = \frac{\delta_n}{T}, \varepsilon_s = \frac{\delta_s}{T}, \varepsilon_t = \frac{\delta_t}{T} \tag{11}$$

The interfacial initial stiffness, K', and failure strain, ε_o, must be defined to allow for numerical stability and to ensure suitable accuracy and efficiency. The interfacial stiffness must be high enough to prevent artificial compliance from being added to the model by the cohesive elements although if too high this may lead to numerical instability. Turon et al. [87] proposed a relationship for mode I opening, shown by equation 12, that ensures that the bulk modulus is much larger than the initial stiffness of the cohesive element:

$$K_3 \geq \alpha \frac{E_3}{h}, \tag{12}$$

where E_3 and h are the through thickness dimension and through thickness stiffness of the bulk material respectively and α is a parameter which must be set much greater than unity ($\alpha \gg 1$). Turon et al. [87] suggests that $\alpha = 50$ which results in a loss of stiffness of less than 2% for most problems.

The length of the cohesive zone, l_{cz}, is defined as the distance behind the crack tip where the maximum cohesive traction is obtained, δ_f. It has been shown that for delaminations in slender bodies that the cohesive zone length is a material and structural property [88] and that for a polymeric composite is less than 1 or 2 mm .

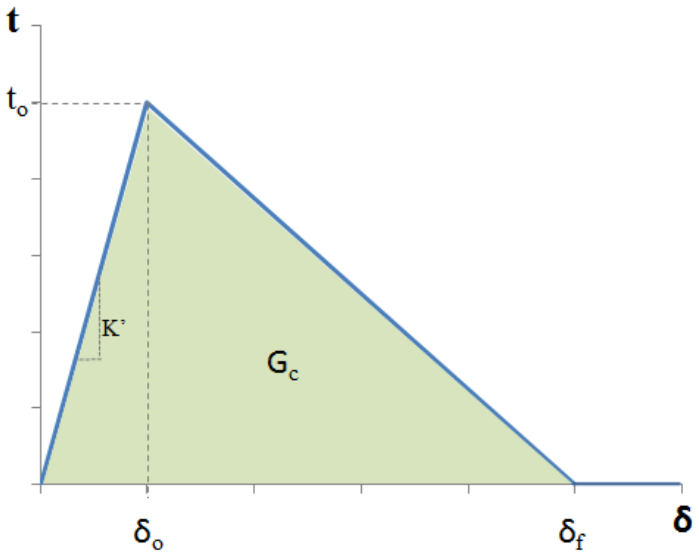

Figure 19: Constitutive linear softening relationship

	M
Hui et al. [89]	0.21
Irwin and G [90]	0.31
Dugdale [86], Barenblatt [91]	0.4
Rice [92], Falk et al. [93]	0.88
Hillerborg et al. [94]	1.00

Table 4: Interface Parameters in the Literature

As summarised by Turon et al. [87] all of the models in the literature to describe the cohesive zone length, l_{cz}, have the form:

$$l_{cz_i} = ME_2 \frac{G_{c_i}}{t_{o_i}^2}, \tag{13}$$

where M is the interface parameter which depends on the cohesive model which is normally close to unity and E_2 is the transverse modulus of orthotropic material. The interface parameter is quantified by many authors, as shown in table 4 with significant variation but Turon et al. [87] states this is normally close to unity.

For accurate representation of the tractions ahead of the crack tip using finite element methods requires a fine discretisation is required with sufficient elements within the cohesive zones. Turon et al. [87] suggests that a minimum of 3 elements are required to accurately represent the cohesive zone. Therefore, this method becomes impractical for large structures due to the computational efficiency.

Alfano and Crisfield [95] showed that the damage initiation strain does not have a strong influence on the predicted results and that reducing the damage initiation strain can improve the rate of convergence. As reducing the damage initiation reduces the length of the cohesive zone the size of elements required in the cohesive zone also reduces. The fracture process ahead of the crack tip can be accurately modelled with a reduced damage initiation

strain however, the stress distribution in the region of the crack tip may be altered. Turon et al. [87] suggests that the interface strength can be calculated from the following equation:

$$t_{o_i} = \sqrt{\frac{ME_2Gc_i}{N_e l_e}}, \tag{14}$$

where l_e is the mesh size in the direction of crack propagation and N_e is the number of elements in the cohesive zone. By this method the cohesive zone length may be artificially increased therefore increasing the cohesive element size in the vicinity of the crack tip and improving the efficiency of such models.

In summary the issue of mode separation is much discussed and debated and not likely to be solved in the near future. The use of characteristic lengths or finite crack extension methods have proven to be a practical solution as long as the sensitivity of the model is shown with regard to changing modelling parameters. Fracture mechanics approaches have largely proven to be effective in characterising delamination growth and whilst the plane in which the crack propagates is known it provides superior computational efficiency. Cohesive elements are gaining popularity and have the advantage of a relatively elegant solution to the bi-material problem by providing a prediction of both delamination onset and growth without the need for intervention during the analysis. Therefore cohesive elements provide a convenient method for calculation as mesh refinement and efficiency issues can be over-come by Turon's relationship however, this requires extensive testing in determining the material properties necessary for the analysis.

In the context of this work the cohesive element method using linear degradation is chosen to model crack propagation to allow for debond initiation between the supporting stiffeners where Turon's method is used to improve the efficiency of the model. Where the crack lies on the stiffener plate interface the propagation path is assumed to occur within this interface and therefore the XFEM method is not required. Where crack initiation and crack propagation are analysed a combination of a strength based criterion and the modified VCCT method or the cohesive element method are compared and discussed further in section 4.3.

2.2.7 Modelling Delaminations in Laminates

Multiple researchers have investigated the effect of modelling delaminations with finite element techniques within composite plates. Research has mainly focused on delaminated plates subjected to in-plane compression. Three types of buckling are apparent as summarized by Hwang [96]; local buckling of the delamination region, mixed mode buckling (a combination of local and global buckling) and global buckling, as illustrated in figure 20. Local buckling (figure 20a) refers to buckling of only the delaminated plies, global buckling (figure 20c) refers to buckling of the bulk laminate where the delamination does not affect the mode shape and mixed mode buckling (figure 20b) refers to buckling of the bulk laminate and delaminated plies forming independent mode shapes. Local buckling or mixed mode buckling may occur prior to global buckling resulting in a reduction in the ability to withstand compressive loads. Kutlu and Chang [97] showed that the distribution, size and location of embedded delaminations play a critical role in determining the mode of buckling and collapse load of the plate and that the inclusion of residual stresses improves the reality of the model.

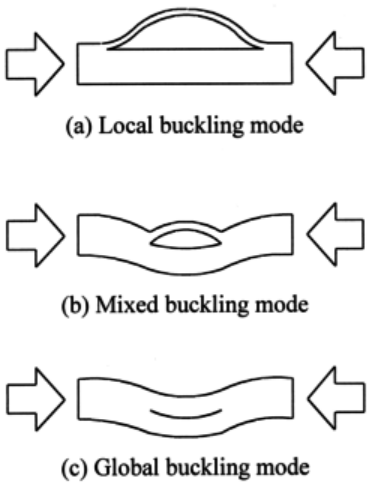

Figure 20: Buckling mode shapes of delaminated plates, Hwang [98]

A number of researchers have investigated through-width delaminations as a simplified analysis of more realistic embedded delaminations. In realistic structures delaminations are rarely through width and occur in more complex structural configurations although these studies highlight some of the key factors affecting delamination propagation.

Chai and Babcock [99] propose 'thin film' modelling for buckling of delaminated plate by assuming that the thickness of the damaged area is small compared to the delaminated ply thickness and therefore, neglecting bending deformation in the undamaged laminated segments. Whitcomb [100] modelled 'thin film' delaminations using beam theory and normalised finite element results using VCCT. From this parametric study Whitcomb showed that small changes in flexural stiffness or delamination length resulted in large changes in the the SERR for modes I and II. It was shown in the same paper that an initial imperfection had a significant influence on mode I but not on mode II and that the ratio of G_I/G_{II} decreases monotonically with applied load and magnitude of the initial imperfection. The effects of bending-extension moments were neglected in this study. Larsson [101] showed that the thin film approximation is satisfactory, and slightly conservative, for delamination thicknesses that are less that 25% of the total laminate thickness. For thin film delaminations it is shown that the presence of the delamination has negligible effect on the critical instability load. However, for longer delaminations there are two possible scenarios; if the fracture toughness of the material is sufficiently small, delamination growth occurs under constant axial load and the growth is therefore catastrophic, else the growth behaviour is governed by the initial delamination length. Thin film models are good for assessing general trends but are limited in modelling realistic damage situations on complex structures. More general models have been developed relaxing the assumptions of the thin film approximation.

Delamination buckling models require a rigorous ply-level model with a crack propagation analysis investigating the interaction of the instability behaviour and delamination growth. Simple models whilst most widely researched, typically assume through-width delamination. The behaviour of plates containing a through-width delamination

under compressive loading are shown to be dependent on two non-dimensional parameters the crack length compared to the length of the plate, a/L, and the thickness of the thinner sub-laminate compared to the total thickness of the plate, h/t [102]. It is also concluded that delamination growth strongly influences the local, mixed and global buckling behaviour and that ignoring delamination growth may not be conservative [102].

Many authors have investigated the effect of embedded delaminations within a laminate and have shown that the stability of the laminate containing an internal delamination is strongly dependent on its shape. Whitcomb [103] conducted a parametric study using a 3D non-linear Finite Element model and the VCCT to investigate the effect of delamination shape, size and the strain level for the interior delamination. The laminate was assumed to be quasi-isotropic and in latter models included contact constraints which prevents material overlapping [104]. It was concluded that in general there is a large gradient in the SERR along the delamination front and the mode mix is highly dependent on the location along the interface, delamination shape and applied load. It is proposed that the delamination would grow forming an ellipse with the major axis perpendicular to the load direction for an isotropic material. The author also found that the mode III fracture mode was significant, although this may only be for this specific experiment. Larsson [101] was the first to include contact at the crack interface and showed the SERR differed by up to 20% by including neglecting contact considerations in the analysis. The analysis found that in general as contact is dependent on the buckling shapes of the sub-laminates that contact, if not considered, forms an underestimate of the SERR and that in modelling a single delamination in place of multiple delaminations the SERR is non-conservative.

Nilsson et al. [105] experimentally and numerically investigated embedded delaminations at different depths. Results showed that initially delaminated panels failed below the global buckling load of the undamaged panel and failed by compression. A finite element model accounting for contact between plies and using the VCCT and a moving mesh scheme to follow crack propagation with good agreement to the experimental results. Riccio and Pietropaoli [106] numerically investigated embedded delaminations illustrating the improved accuracy obtained in using a progressive damage technique and modelling the crack propagation using the modified VCCT and nodal release method.

2.2.8 Summary

This section has summarised the state of the art in damage identification and prediction, as well as the modelling of cracks and delaminations. A number of methods for composite laminates are assessed in terms of their computational efficiency and accuracy. Equivalent single layer theories are the most computationally efficient and may provide suitable accuracy for plate structures, however, for increased accuracy of thick laminates and to establish local effects, including inter-laminar stress distributions between layers and delaminations, higher-order shear deformation or layer-wise theories are required. It is shown by the World Wide Failure Exercise that no single strength based failure criterion currently results in an accurate prediction of failure for all possible conditions. Therefore, the WWFE recommendations will be used by combining the top-rated failure criterion, Puck, Zinoviev and Tsai-Wu. A study is conducted showing that for glass polyester woven roving good accuracy can be achieved for the combined longitudinal-transverse and longitudinal-shear loading by modifying Tsai-Wu's interaction factor to -0.15. Full progressive damage model allows modelling of the ultimate strength of a laminate with the state of the art criteria allows the degradation of specific material properties depending on the failure mode. Degradation can either be instantaneous or a linear degradation method which is associated with the strain energy to failure of the specific material. A number of crack propagation methods are discussed including the VCCT, cohesive element and XFEM methods. Whilst the VCCT method can provide an efficient technique the cohesive elements provide a convenient method for calculation by providing a prediction of both delamination onset and growth without the need for intervention during the analysis. For delaminations within laminates complex buckling configurations arise in the form of local, global and mixed mode buckling. When modelling delaminated laminates under compressive loads the interaction between these buckling effects and delamination growth is critical in determining the damage mode and residual capability. It has been shown that detailed modelling is required including contact analysis to accurately assess such failure modes and ultimate strength.

2.3 Analysis of 'Top-Hat' Stiffened Panel

In the marine, aerospace and civil industries stiffened shell laminates are increasingly used in the primary structure. A number of stiffener cross sections are utilised in this application as shown in figure 21. The stiffener arrangement transmits the shear stresses from the shell and frame flanges under local bending either from hydrostatic or concentrated loads. The top-hat or omega stiffener configuration offers increased torsional stiffness due to it's closed profile and is used extensively in marine applications and increasingly in aerospace applications. Elaldi [107] showed that the structural efficiency of a top-hat stiffened panel was 25% greater than that of a J-stiffened panel showing the potential for weight saving.

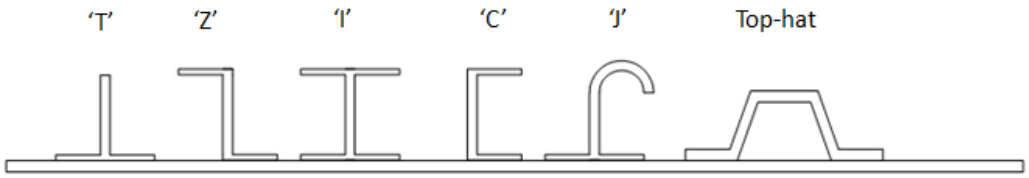

Figure 21: Stiffener cross-sections

Commonly top-hat stiffeners are used for longitudinal and transverse stiffening of marine structures; the SRMH and McAdams stiffeners are fabricated by draping a woven roving reinforcement over a shaped foam core with the flanges of the stiffener being post-cured onto the laminate plate. Typical configurations are shown in figure 21 showing the difference in design of the internal fillet radius and the ply dropped edge of the flange.

Typically, top-hat stiffeners are subjected to in-plane tensile and compressive loading resulting from hull girder bending and out-of-plane loads due to the hydrostatic loading on the hull, wave slamming and impact loads. The intact and damaged properties of stiffened composite laminates have been studied in varying load scenarios and boundary conditions and a review of this work is outlined in this section within the context of the multi-scale analysis mentioned previously.

2.3.1 Representative Stiffened Elements

In order to model delamination between bonded structures, Minguet and O'Brien [108] proposed a 'non-specific coupon' to examine the flange/ skin interface when tested under three or four point bend. These coupons consist of a bonded skin and flange assembly as shown in figure 22.

Figure 22: Non-specific coupon configuration, Minguet and O'Brien [108]

Krueger et al. [109] used these non-specific coupons experimentally and numerically under uni-axial and biaxial loading showing that failure initiated in the flange near the tip causing a partial debond. Non-linear three dimensional finite element using VCCT showed good agreement with experimental findings however, it was shown that

two dimensional analyses failed to allow changing failure patterns across the width of the specimen. This non-specific coupon approach was also used by Camanho et al. [110] to verify the cohesive elements who also showed that neglecting residual thermal stresses leads to a 4.8% over prediction of the debond load for carbon epoxy coupons. Krueger and Minguet [111] verified the use of a shell/3D modelling technique for representing non-specific flange/ skin coupons using multi-point constraints to enforce appropriate translation and rotations at the shell-solid interface.

A number of authors have investigated stiffened structural elements, investigating the in-plane response of composite stiffeners. Early studies investigating in-plane loads showed the stiffener plate interface is relatively strong compared to the rest of the stiffener section although there is a lack of continuity of fibres across the joint, the over laminate is susceptible to failure by delamination or peel as a mode of failure [112]. Along this interface voids or geometric imperfections make the joint increasingly sensitive to delamination failure. Shenoi [113] studied the top-hat stiffener joint under out-of-plane loads with finite element analysis determining load transfer paths and failure mechanisms. Junhou [114] presented a comprehensive review of FRP marine joints and conducted experimental studies on top-hat stiffeners. Three experimental load configurations are suggested; the three point bend, reverse three point bend and pull off as shown by configurations a-c in figure 23. The three point bend saw initial failures observed at the fillet-overlaminate interface followed by progressive delaminations in the over-laminate due to excessive inter-laminar stresses. Failure of the panel skin occurred during the reverse three-point bend test. Complete de-bonding of the over-laminate from the base panel was observed during the pull-off test. Phillips et al. [115] conducted numerical analysis on these three testing configurations to determine internal load transfer characteristics and failure mechanisms. It is suggested that the delamination of the over-laminate in the curved region close to the fillet was due to high through thickness stresses. Li et al. [116] examined fracture behaviour in marine T shaped stiffeners, utilising the VCCT and highlighted the sensitivity of the SERR at the crack tip on skew loading. Orifici et al. [117] examined the skin-stiffener interface of T-shaped stiffeners under symmetric and antisymmetric in-plane loads to represent the post-buckled configuration. Cohesive elements were used to analyse the interface with good agreement with experimental failure and damage progression. Bertolini et al. [118] investigated top-hat stiffeners in a four point bend test as illustrated in configurations d and e of figure 23. By varying the width of the internal rollers of the four point bend test it is possible to modify the debond location and associated loading to cause de-bonding at the internal and free edge of the flange-skin interface. Numerical modelling showed the importance of including the resin fillet which led to a 61% error on the failure load when neglected from the model and demonstrates the accuracy of an iterative fracture mechanics approach for replicating crack propagation.

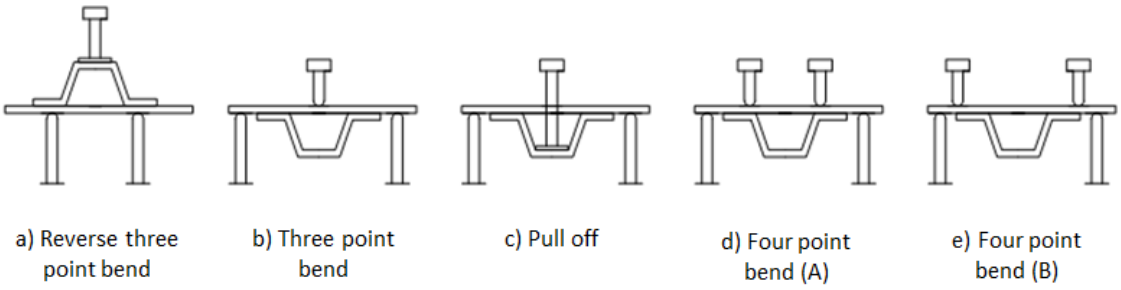

Figure 23: Load configurations for top-hat stiffener tests

2.3.2 Single and Multi-stiffened Panels

There are a wide variety of modelling techniques available to assess the response of composite stiffened panels balancing the accuracy required and computational expense of the analysis. During the preliminary design phase, simplistic methods are invaluable for design optimisation however, for post-damage evaluation the analysis method requires suitable accuracy to replicate the damage and progression of damage until ultimate collapse. Structures loaded in compression typically experience buckling, where the structural deformation forms a minimum energy deformation configuration. For stiffened structures this can lead to complex deformation configurations which cause and interact with failure mechanisms of the plate and stiffener. Therefore, the buckled and post-buckled configurations of stiffened plates must also be modelled with sufficient accuracy to account for their part in damage progression. This section presents an overview of analytical and numerical techniques with a discussion on their accuracy and computational expense followed by a review specific to failure mechanism of composite stiffened panels

The following section outlines the literature investigating modelling and experimental work on intact stiffened and multi-stiffened panels under different loading conditions.

Eksik [119] conducted experimental and numerical studies on top-hat shaped GRP beams under out-of-plane loads. Two types of top-hat composite beam have been tested under four-point bending loads until failure. The failure sequence observed was: matrix cracking, root whitening and delamination at the web-flange corner and finally depending on the layup, failure with fibre matrix breakage and/or catastrophic shear failure. Eksik et al. [120, 119] furthered this work by investigating the response of top-hat stiffened panels under hydrostatic pressure both experimentally and in a linear finite element model using solid elements. Strength and failure mode are investigated identifying critical regions of damage and damage propagation is identified by means of increasing failure stresses with good correlation with experimental testing. Similarly, Bertolini et al. [118] investigated top-hat stiffened panels under a three point bend configuration, again illustrating the need for accuracy in modelling the stiffener geometry and resin fillet

Structures loaded in in-plane compression typically experience buckling, where the structure forms a minimum energy deformation configuration. The buckling modes of stiffened structures becomes increasingly complex compared to that of a homogeneous isotropic laminate and critical in assessing the damage progression under compressive loading.

Smith [121, 122, 123] comprehensively investigated the buckling effects on composite top-hat stiffened panels in a number of published works including specific tests representing the MoD MCMV deck structure. The damage mechanism for the deck structure showed that prior to overall grillage buckling, buckling in the plate between stiffeners was observed with no damage or change in stiffness in the post-buckled state. At increasing loads, cracking and whitening under the flanges of the longitudinal stiffeners was observed and the final failure was sudden and explosive involving fracture of the entire cross section [122]. This work investigates intact grillage structures showing the effect of bay buckling as part of the collapse process causing a loss of effective width and an increase in stress in the stiffener and stiffener-laminate joint.

For stiffened panels loaded a number of failure modes have been identified:

[1] Local buckling of a stiffener or skin between stiffeners

[2] Column-like inter-frame buckling

[3] Stiffener tripping, lateral-torsional buckling of a stiffener

[4] Overall grillage buckling

Stiffener tripping is usually associated with open section stiffeners such as tee shaped stiffeners as closed stiffener sections, such as top-hat stiffeners, have a high torsional stiffness preventing tripping.

Smith [123] examined compressive buckling of transversely stiffened panels showing failure by inter-frame modes as illustrated in figure 24. The three modes labelled a to c involve the bending of the shell, which is restrained by the flexural action of the stiffeners web and table, by the torsional stiffness of the frame and bending of the shell with a modal half wave length equal to the frame spacing respectively. More commonly the stiffeners are aligned with the loading direction to prevent lateral-torsional instability and panel buckling.

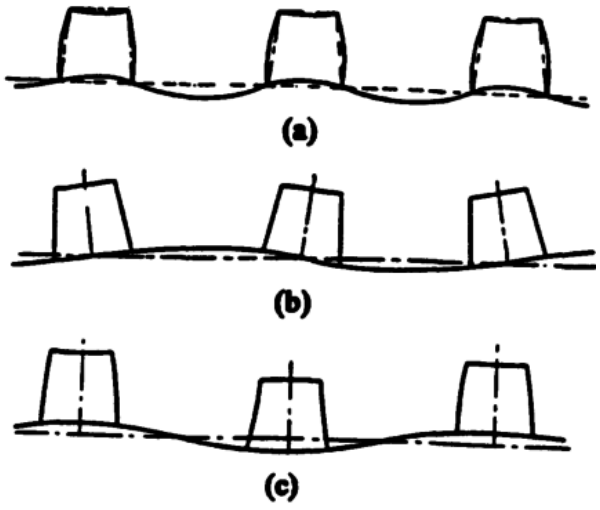

Figure 24: Inter frame buckling modes for top-hat stiffened panels, Smith [123]

Simplistic buckling analyses assume that buckling loads occurs at a bifurcation buckling analyses where a laminate or sub-laminate remains flat until the bifurcation limit is reached. At the bifurcation limit the equilibrium state of the laminate becomes unstable causing an abrupt movement to a post-buckling equilibrium state. A laminate with off axis layers, containing a symmetric and central delamination, will lead to bending-extension coupling in the sub-laminate. This coupling, under in-plane compressive loads may lead to large lateral deflections from the onset of loading and remain stable, hence a bifurcation analysis is no longer appropriate. To investigate the post-buckled region a full non-linear solution should be obtained.

Numerous authors have modelled the post-buckled response of stiffened plates by non-linear finite element techniques and shown good to excellent predictions of structural stiffness, especially prior to global buckling, and the buckling load and displacement[124, 125, 126, 127, 117, 128, 129].

Ko and Jackson [130, 131] conducted a buckling analysis on a top-hat stiffened panel subjected to in-plane compression and shear loading showing that the buckling load was several times higher than the ultimate failure load. They also showed that the classical shear buckling theory for a flat plate was useful for predicting the local buckling load of the stiffened panel. Kong et al. [126] investigated blade stiffened, I stiffened and top-hat stiffened panels numerically. The model was verified against experimental data for a multi-stiffened blade and I stiffened panels. Kong manufactured the stiffeners from continuous fibres and therefore neglected stiffener debonding as a mode of failure. He investigated the effect of stacking sequence and showed that the post-buckled compressive strength was dependent on the bending stiffness in the loading direction and the bending stiffness in the transverse direction. By comparing the stiffener shapes he concluded that the torsional stiffness of the stiffener influenced the post-buckled compressive strength more than the buckling load.

Falzon and Steven [132] showed that for stiffened panels with a large skin bay and a high width to skin-thickness ratio a Maguerre type Rayleigh-Ritz energy method is an efficient and accurate tool to adequately capture mode transition in the deep buckling range. However this can only be applied to simple load cases by investigating the plate between stiffeners. Falzon [133] showed that an explicit dynamic finite element model could also capture the mode switch where the mass and damping matrices are approximated by the tangent stiffness. The static solution is recovered when the time dependent vectors go to zero. The model is shown to accurately capture the load at which the mode switch occurs. In the majority of applications, particularly in the marine industry, panels with a high width to skin-thickness ratio would not be used therefore the modelling accuracy of the deep post-buckled response is not of concern unless such mode-switches are observed experimentally.

Much research has been conducted in the context of the aerospace industry where there is an increased application of lightweight fibre reinforced structures. Recent programs namely GARTEUR POSICOSS and COCOMAT [134, 135], are a series of programs that look to exploit the strength reserves of composite fuselage and are investigating the post-buckled response until ultimate collapse [135, 134]. Bisagni [136] showed through post-buckled optimisation that allowing skin buckling within the structure as part of the considered safe zone can save 18% weight of the stiffened structure for T-shaped stiffened carbon epoxy panels. This material exploitation is based on the high fatigue tolerance of the composite material used.

The POSICOSS program developed two types of tools; fast relatively basic and suitable for the design process [137, 138, 139] and accurate but more computationally expensive tools for final certification [140], both were verified against experimental response of carbon epoxy composites stiffened by T-shaped stiffeners.

Experimentally Bertolini et al. [141] investigated a seven point bend test, five point supports and two load points, as presented by Wiggenraad [142], which is said to replicate the deformations witnessed in post-buckling. The point supports can be varied to study symmetric and antisymmetric buckling. Numerical modelling using the Benzeggagh-Kenane failure criterion and the VCCT successfully identified the onset of de-bonding within the scatter of the experimental results. The global-local modelling approach reduced computational time from 24 hours, for the required high mesh refinement for convergence on a full solid element model, to 20 minutes for a shell-solid model demonstrating the efficiency and accuracy of the method for a more complex model. The same authors also investigated a stiffened panel containing three top-hat stiffeners under uni-axial compression and subjected to shear loading. Non-linear numerical models were generated to follow damage progression and post-buckled behaviour using a global-local model as discussed previously, with the local model representing approximately a quarter of the stiffened plate. The initial buckling load and damage progression prediction is thought to be adequate, within 15% given the dependency on the plate thickness and possible variation within the panel. Similarly, Orifici et al. [143] investigated the global-local approach post-buckled response in a strength based analysis for T-shaped stiffened panels containing multiple stiffeners. The model is verified using a multi-scale analysis which investigates stiffened structural elements, single stiffened panels and multiple stiffened curved panels.

Perret et al. [128, 144] investigated multi-stiffened top-hat panels manufactured using liquid resin infusion under compressive in-plane loads for aircraft applications both experimentally and numerically. This showed that for liquid resin infusion and a co-cured stiffener the integration between plate and stiffener is much greater and prevents stiffener debond as a mode of failure.

Faggiani and Falzon [145] used genetic algorithms to optimise the design of I-stiffened panels in terms of ply orientations to minimise the total damage at the stiffener plate interface in the post-buckled regime. Falzon uses a global-local model to model the post-buckled response and delamination initiation and propagation. Falzon showed that the optimised panel was able to decrease the total damage by 41% which is attributed to the delayed mode jump from five to six half waves as node and anti-node lines provide a sudden increase in skin-stiffener interface damage.

2.3.3 Damaged Stiffened Structures

Much attention has been paid to the intact response and damage progression under quasi-static loads however, there is far less literature on the response of a stiffened panel containing initial damage.

Mid-bay delaminations have been investigated by a number of authors. Sumpter [146] investigated the effect of circular delaminations positioned in the plate between two top-hat stiffeners and loaded in compression. The delaminations ranged from 50 to 300 mm and were manufactured with delaminations placed between every ply through the width. The results showed little dependency on the delamination diameter. Failure was localised to

the centre of the panel and spread rapidly and in a catastrophic manner. For the smallest delamination size the stiffener delaminated prior to the delamination propagating. Fatigue testing was also conducted and it was found that the failure mode was slightly more diffuse in this case compared to the quasi-static compression test but was again believed to be independent of the delamination size. Falzon [147] investigated the effect of circular cut outs in the bay of top-hat stiffened panels both numerically and experimentally. Falzon showed that the buckling load was reduced by the presence of the hole but also concluded that the ultimate collapse load was largely unaffected by the presence of the cut-out with both panels failing by local buckling of the stiffener. Non-linear finite element models were shown to have good correlation in the pre-buckling and initial post-buckling region for both damaged and undamaged panels but as discussed previously failed to capture the buckling mode transition of the skin. Wiggenraad et al. [6] investigated the damage tolerance of impacted multiple I-stiffened panels experimentally and numerically. The delamination growth was seen to be controlled by the buckling modes within the skin and is therefore dependent on the impact location. Modelling was conducted by non-linear finite element models using a fracture mechanics approach with re-meshing to follow crack propagation. Design optimisation was conducted based on conservative modelling assumptions showing the penalty for increased damage resistance for 35J impact loads which leads to an increase in panel weight of 16-28%. However, the model was restricted to bay delaminations due to the constraints of the software. Riccio et al. [148] proposed a linear numerical approach to simulate the delamination growth initiation in stiffened composite panels. The model is intended to be efficient for design and optimisation purposes. The model is restricted to bay delaminations which are relatively shallow delaminations with a delaminated sublaminate depth of 15% of the total laminate thickness.

The effect of stiffener de-bonding has been investigated numerically and experimentally on I stiffened structures by the following authors. Gadke et al. [149] numerically investigated the effect of stiffener debonds in a single blade stiffened panel. A linear eigenvalue analysis was conducted using a shell model and the VCCT to assess the affect of a full width debond and it's length on the initial buckling load. Gadke investigated the effect of the geometric and lay-up sequence on the damage tolerance and load carrying capacity showing that geometric parameters could significantly affect the damage tolerance however where the damage tolerance was improved the load carrying capacity was decreased. Altering the plate lay-up to include more ± 45 layers has shown to increase both the damage tolerance and load carrying capacity. Wiggenraad et al. [6] also experimentally investigated impact under the I-stiffened foot and showed that these impacts were shown to be driving the design and therefore the skin-stiffener interface was critical when considering damage resistance. Suh [26] investigated both experimentally and numerically the compression after impact tests of fully, partially and non stitched and co-cured I stiffened plates. The impact damage was applied directly to the stiffener and showed that selective partial stitching deflected the crack in the stiffener and suppressed delamination in the flange. Suh was able to model the damage stiffeners with reasonable accuracy using a non-linear shell model and accounting for the damage within the stiffener by areas of reduced stiffness from experimental observations. Yap [23, 150] considered a curved T-stiffened panel experimentally and using a non-linear finite element model utilising shell elements and a fracture mechanics approach to investigate the critical parameters affecting crack growth within the stiffener and plate. Both mid plate delaminations and stiffener-

plate debonds were considered in parametric studies investigating size, shape and location of the delamination. This study showed that the sequence of global and local buckling affects the debond growth and that, depending on the buckling mode shape, this may lead to crack propagation or crack closure depending on location. It was concluded that mid laminate delamination damage did not affect the post-buckled shape of the panel as debonded stiffeners did. This work may act as a guide to trends of damage variables for this specific type however it does not capture the ultimate failure of the panel and interaction of damage modes as damage criterion and crack propagation are omitted from the study. Meeks et al. [5] conducted a fractographic analysis of T-stiffened multi-stiffener panels tested in compression for both intact, and initially damaged panels. This work highlighted the complex three dimensional nature of skin-stiffener detachment and suggests that a 3D analysis is required to characterise damage, as it is observed that the crack growth direction under the stiffener foot was seen to be parallel to the fibre direction rather than perpendicular to the stiffener length. The location of impact damage has shown to be critical with that in the skin bay between the stiffeners resulting in a 7% reduction in panel strength whilst defects underneath the stiffener foot led to the greatest reduction in strength of 23%. The location of the damage was again deemed critical due to the location of the buckling nodes and anti nodes. Suemasu et al. [151] numerically studied the effect of a partial debond on a blade stiffened panel using a global local approach. Suemasu showed that if the debond area was located at the edge of the flange no noticeable reduction in compressive buckling load was found until the the debond area represented half a wavelength of the buckling mode. However, the buckling load dropped significantly when multiple delaminations were present which were small in comparison to a half wavelength of the buckling mode. Suemasu used a full solid model to represent the stiffened panel and compared the compressive buckling load, however the model omitted fibre, matrix damage or crack propagation. Orifici et al. [25] investigated a single co-bonded T-stiffened panel under compressive loading for both intact and pre-damaged panels. Numerical models demonstrated the global-local approach, discussed previously, using Hashin's degradation model and following crack propagation by means of the VCCT and re-meshing algorithm. As an extension of this work, Lauterbach et al. [152], used the same model to conduct a parametric study on skin-stiffener bond parameters again highlighting the criticality of the debond location relative to the post-buckle deformation shape. Vescovini et al. [153] developed a global-local approach using a simplified model for analysis of debonding of top-hat stiffened panels. Verscovini examines a carbon epoxy top-hat stiffened panel and develops a simplified approach assuming symmetry of the buckled mode shape, that the stiffener web to plate interface provides a fixed constraint. The models are shown to provide reasonable accuracy but is limited in use due to the symmetry constraints preventing modelling of asymmetric buckling modes and failure and lack of feedback in the global local approach. Therefore the interaction between crack propagation and changes to the panels buckling mode are not captured. The ultimate strength and therefore residual strength can also not be ascertained by this method. More recently Bisagni and Dávila [154] investigated a single co-cured top-hat stiffened panel experimentally and numerically showing that minor imperfections due to manufacturing and residual thermal strains can result in large differences in the post-buckled response. An attempt was made to simulate the measured imperfections although the exact post-buckled response could not be matched for the panels tested. Bisagni also investigated the effect of a simulated debond with the aim

of producing verification data for future modelling and assessing the effect of two sizes of simulated damage. It was shown that significant variation was observed between results and that with a limited number of tests in the study strong trends into the damage tolerance could not be identified although a dependence between global panel and local buckling, material failure and stiffener debonding was observed. Wang et al. [155] conducted experimental testing on co-cured I-stiffened multi-stiffened panels and compared an intact panel to an impacted panel at the edge of the stiffener. It was shown that although buckling occurred in the region of the debond no crack propagation was observed with shear and compression failure at the impact site leading to ultimate collapse. Modelling work was conducted but omitted debonding as a failure mechanism.

2.3.4 Summary

In this section the literature has been assessed relating to the analysis of top-hat stiffened panels at different scales. The research conducted to date is summarised in table 5 for experimental testing and table 6 for numerical modelling . The simulation and experimental findings on the intact response and progression of damage following a prior damage incident is displayed in reference to a multi-scale analysis as illustrated in figure 5. It is not possible to test for embedded delaminations for representative stiffened elements, therefore these sections are omitted.

It is shown by Bisagni and Dávila [154] that the testing of top-hat stiffened panels in compression are sensitive to a number of varying factors including the imperfection scale, manufacturing tolerance and boundary conditions. Bertolini et al. [141] verified their model using a multi-scale approach comparing experiments and numerical models with good correlation. Therefore, to provide a comprehensive understanding of the complexities of the variables in damaged stiffened panels in compression requires a verified model where the effects of design, manufacturing and damage can be assessed. It is shown that a finite element approach is required to assess delamination and progressive damage which can accurately assess the displacement and stress field in both the stiffener and the plate. The intact and damaged post-buckled response can be well captured by a non-linear finite element model with the exception of dynamic mode switching which is observed experimentally. A global-local model of damaged plates has been shown to replicate stiffened panel behaviour for the tested configurations however, these models are restricted to modelling debonds in the initially damaged area and don't account for debond initiation elsewhere in the panel and therefore could provide non-conservative results.

Table 5 shows that many authors have investigated the damage progression of intact structures with good correlation to experimental results however, there is still limited research conducted on the residual capabilities of structures containing prior delaminations. Falzon [147] and Sumpter [146] showed that mid bay delaminations and holes had minimal affect on the ultimate collapse load of a stiffened structure, however it has been shown by other authors Wiggenraad et al. [6] and Meeks et al. [5] that delaminations present under the stiffener where shown to have a significant affect on the ultimate strength of the panel. It is also shown by parametric studies that delamination and debond size and location has a significant affect on the damage mode of the panel Yap [23, 150], Suemasu et al. [151] and Gadke et al. [149] however, these studies are based on either a non-linear shell model or a linear eigenvalue analysis and do not consider the interaction of failure modes as they omit any material failure or damage

Table 5: State of the Art Summary; Experimental

		Representative Stiffened Elements			Single Stiffened Panels		Multi-stiffened Panels	
		Representative flange	Open Section Stiffener	Top-Hat Stiffened	Open Section Stiffener	Top-Hat Stiffened	Open Section Stiffener	Top-Hat Stiffened
Experimental	Intact Response	Krueger et al. 2000	Orifici et al. 2008a Li et al. 2006	Junhou et al. 1996 Bertolini et al. 2008	Orifici et al. 2008c, 2008d	Eksik et al. 2004, 2007a, 2007b Bertolini et al. 2008, 2009	Orifici et al. 2008c Zimmerman et al. 2006 Elaldi et al. 2008, 2009	Elaldi et al. 2008, 2009 Falzon et al. 2001 Bertolini et al. 2009 Smith et al. 1985 Perret 2011
	Simulated Delamination				Orifici et al. 2008d Bisagni et al. 2014	Bisagni et al.2014	Yap et al. 2002 Orifici 2007	Sumpter 1996
	Impact Damage					Rousseau et al. 1999	Meeks et al. 2005 Wiggenraad 1996, 2002 Wang 2015	

Table 6: State of the Art Summary; Modelling

		Representative Stiffened Elements			Single Stiffened Panels		Multi-stiffened Panels	
		Representative flange	Open Section Stiffener	Top-Hat Stiffened	Open Section Stiffener	Top-Hat Stiffened	Open Section Stiffener	Top-Hat Stiffened
Modelling Damage Progression from 'Perfectly' Intact	Shell Model	Krueger et al. 2007 Camanho et al. 2008	Orifici et al. 2008a Li et al. 2006	Shenoi et al. 1995 Philips et al. 1999 Bertolini et al. 2008	Orifici et al. 2008c, Suh et al. 2003	Bertolini et al. 2008 Eksik et al. 2004, 2007a, 2007b	Zimmerman et al. 2006 Orifici et al. 2008c	Bertolini et al. 2009
Modelling Damage Progression from Initial. Delamination	Shell model				Orifici et al. 2008d Lauterbach et al. 2010 Suh et al. 2003 Gadke at el 1996	Verscovini et al. 2010 Bisagni and Davila 2014	Meeks et al. 2005, Wiggenraad et al. 2002 Yap et al. 2002, 2004 Riccio et al. 2010 Suemasu et al. 2006 Wang et al. 2015	NONE

propagation. Bisagni and Dávila [154] also highlighted the sensitivity of such panels to imperfections in the plate and stiffener on the buckling mode and damage tolerance.

Research on damaged stiffened structures to date is primarily focused on airframe applications considering stiffeners with open cross sections and investigated co-cured or co-bonding methodologies which are not typical of marine structures. Top-hat stiffeners have been shown to have increased torsional rigidity in comparison to I-stiffeners or T-stiffeners and have been shown to have an increased structural efficiency when compared to J-stiffened panels. However, the damage response of such panels is not well understood.

Therefore, this literature review has identified a gap in the research in modelling debond damage in multi-stiffened top-hat panels and more generally a parametric study is lacking that assesses the the residual strength and ultimate strength of debonded stiffened panels.

2.4 Summary of State of the Art

This section summarises the state of the art in modelling damaged composite structures as reviewed in the previous literature.

As part of a post-damage research methodology, there are a number of critical questions posed during damage vessel assessment in order to make key decisions on recovering and or repairing the vessel:

- how to determine the classification of damage?
- Whether a cost effective repair can be made?
- Whether the damaged vessel may be moved?

Therefore, an understanding of the residual capability of the structure is critical in accurately and safely determining the most appropriate cause of action. It is shown that the UK-MoD's post-damage procedure contains no readily available guidelines as to the residual capability of the structure following a major damage incident as highlighted by the Grimsby damage incident.

The state of the art for generating numerical models to simulate damage incidents has advanced significantly allowing delamination within laminates to be modelled more efficiently and accurately. Finite element methods are one of the most powerful analyses for structural composites, particularly in establishing response of structures containing discontinuities. For complex problems, such as, delaminations in larger structures, a local-global modelling approach is commonly used and can be shown to be computationally effective and an accurate compromise however this model type neglects debond initiation away from the simulated damage and can provide non-conservative results. The problem posed in this thesis, modelling delaminations in larger structures, is modelled using equivalent layer approximations, implemented through shell elements which approximate the displacement and stress field with a suitable accuracy and is verified in section 4.

Inclusion of strength based failure criteria allows the prediction of failure initiation and progressive degradation of laminate composites. A combination of top-rated failure criteria, such as Puck, Zinoviev and Tsai-Wu are

recommended to predict the response of the lamina, final strength of multi-directional laminates or deformation. These will be used in the following research for multidirectional laminates. Therefore, a model using a combination of appropriate failure criteria or a combined criterion as recommended by the WWFE will be used to model the damage case. It is shown that for woven fabrics that a non-linear response is required, prior to initial failure, for tensile and shear loading to represent the straightening of the fibre tows and the 'scissoring' action of the fibres respectively. It can also be shown that for glass polyester good accuracy can be achieved for the combined longitudinal-transverse and longitudinal-shear loading by modifying Tsai-Wu's interaction factor to -0.15 and that the initial yield during tensile loading can be represented by 25% of the Tsai-Wu ply failure stress. Progressive damage methods have been shown to successfully model the ultimate strength of composite structures. The state of the art methodologies allow improved accuracy allowing for degradation of specific material properties depending on the failure mode and the associated material properties of the failed element are commonly degraded based on either an instantaneous degradation method or a linear degradation method. The linear softening constitutive equation is associated with the strain energy to failure of the specific material. This has been shown to be within the range of two to four times the initial failure strain. A comparison of degradation models should be made, where data is available, to ensure a conservative estimate of the ultimate strength of composite panels is made when compared to experimental data. Without experimental data instantaneous degradation is assumed to ensure a conservative result.

Crack or delamination propagation may be characterised using fracture mechanics principles to calculate the strain energy release rate. The VCCT method is verified and used extensively in the literature however cohesive elements are gaining popularity as they provide a convenient method for calculation by providing a prediction of both delamination onset and growth without the need for intervention during the analysis. Cohesive elements have the advantage of a relatively elegant solution to the bi-material problem and as mesh refinement and efficiency issues can be over-come by Turon's method providing an efficient solution. The Benzeggagh-Kenane mixed-mode criterion has been shown to give adequate accuracy to determine crack propagation under mixed mode loads for a wide range of composite materials. Therefore, the cohesive element method using linear degradation is chosen to model crack propagation to allow for debond initiation between the supporting stiffeners where Turon's method is used to improve the efficiency of the model. Where the crack lies on the stiffener plate interface the propagation path is assumed to occur within this interface and therefore the XFEM method is not required. Crack initiation and crack propagation are analysed using the modified VCCT method and the cohesive element method and compared and discussed further in section 4.3.

For delaminations within laminates complex buckling configurations arise in the form of local, global and mixed mode buckling. When modelling delaminated laminates under compressive loads the interaction between these buckling effects and delamination growth is critical in determining the damage mode and residual capability. It has been shown that detailed modelling is required including contact analysis to accurately assess such failure modes and ultimate strength. The distribution, size and location of embedded delaminations are critical parameters in determining the structural response and multiple delaminations must be modelled accurately in order to provide a

non-conservative estimate of strength.

The literature review highlights limited knowledge in experimental testing of simulated damage in top-hat single and multi stiffened panels with available experimental results showing sensitivity to a number of parameters. Testing has also highlighted that the most economical way to understand the complexities of many variables in damaged stiffened panel in compression requires a verified model where the effects of design, manufacturing and damage variables can be assessed.

Many authors have investigated the damage progression of intact structures with good correlation to experimental results however, there is still limited research conducted on the residual capabilities of structures containing delaminations from prior damage. Research on damaged stiffened structures to date is primarily focused on airframe applications and considering stiffeners with open cross sections and investigate co-cured or co-bonding stiffeners which are not typical of marine structures. Top-hat stiffeners have been shown to have increased torsional rigidity in comparison to I-stiffeners or T-stiffeners and have an increased structural efficiency when compared to J-stiffened panels. However, the damage response of such panels is not well understood.

Any simulation and modelling is inherently only as accurate as the input material data allows. Analysis of the material data available in the literature for heavy weight glass vinylester woven roving typically used in large marine applications shows that a complete data set of mechanical and interface properties is lacking and that there can be significant variation between results from different manufacturing methods, component materials, layups and weave structures. Typical marine sub-component joints commonly use an interface layer of chopped strand mat between the initially cured plate and post-cured sub-component. These joints are not well characterised in the literature although it is shown that the chopped strand mat layer can have significant affect on the interface properties.

Therefore, this literature review has identified a gap in the research in modelling debond damage in multi-stiffened top-hat panels and more generally a parametric study is lacking that assesses the residual strength and ultimate strength of debonded stiffened panels. A gap in the research is also identified in the generation of a complete set of data for both mechanical and fracture properties, and the fracture properties of post-cured interfaces, for a given manufacturing method and material type.

2.5 Research Novelty

The novel contribution of this work is to investigate the effect of simulated debond damage on the ultimate strength of top-hat stiffened and multi-stiffened panels. Modelling and experiments are performed to assess the effects of damage and design parameters on the residual strength. In addition to generic topologies and material properties typical marine interfaces are also assessed. Typical materials are fully characterised which provides, for the first time, a complete data set of mechanical characterisation and fracture data for both co-cure interfaces, typical of mid-laminate debonds, and post-cured interfaces, which use an interface chopped strand mat layer at the interface and are typical of sub-component joints. A four point bend test is conducted and the model is validated against this experimental data, verifying the properties represent those of an as built large scale structure. An assessment is also conducted on the effect on material non-linearities on the flexural properties of DCB and ENF coupons and

the assessment of interface properties, for accurate modelling of post-cured glass vinylester laminates. A parametric study is performed, using FEA, on top-hat stiffened panels, to determine how the crack characteristics and changes to the stiffener topology affect the rate of growth. A methodology is therefore developed to allow further analysis and optimisation of typical marine top hat stiffened panels to aid a damage tolerant design and for assessment in damage scenarios

3 Methodology

3.1 Introduction

Chapter 1 highlighted a need for a greater understanding of the residual capabilities of a damaged stiffened structures following an incident causing delamination and associated damage. Composite joints are critical in assessing the structural performance of the vessel where delamination and de-bonding damage are some of the most commonly observed faults. In this thesis the quasi-static response is considered due to the complexity of the mechanical response under high strain-rate loading and the lack of maturity of research in this area. This research which will give an increased understanding of the critical parameters affecting the residual capability of the damaged structure. The literature review has shown that state of the art modelling of stiffened composite structures which contain delamination and debonds, can accurately and computationally efficiently simulate the effect of delaminations utilising progressive damage algorithms and a fracture mechanics approach for crack propagation [156, 118, 23, 150]. The current research is concentrated on the effect of co-cured open-section stiffeners commonly used in the aerospace industry, and the response of damage in the region of closed section, top-hat stiffeners are not well understood.

Assessment of the material data available for such a study has highlighted there is a lack of data and consistency of data for heavy weight glass vinylester composite materials. There is a lack of consistent data for both mechanical and interface properties and that the variation in material and manufacturing parameters can have a marked effect on the interface parameters. It is also clear that there is a lack of data on the interface properties for post-cured joints which are common in large composite structures where sub-components, such as stiffeners, are infused onto a cured plate. These joints commonly have a chopped strand mat interface at the post-cured interface although there is no data available for mode I and II interface data for such a joint.

The work in this thesis examines the effect of debond damage within post-cured top-hat stiffened panels, typical in the marine industry, and compares the design, manufacturing and damage parameters on the ultimate strength and residual capabilities of damaged structures. A model is verified to assess the effect of debond damage in top-hat multi-stiffened panels and used in a parametric study to assess the residual and ultimate strength of damage cases. Experiments are conducted to improve the material and fracture properties and material models used in modelling such a problem. This section presents the proposed methodology in order to answer the research question posed in section 1.3.2.

3.2 Research Methodology

In order to further understanding on progressive collapse and damage tolerance of composite stiffened structures the following strategy is outlined.

Having established the current state of the art in the field, the next stage of the research is the development of an appropriate model capable of simulating the response of damage stiffened panels where FEA has been chosen as an appropriate method. The model is verified against experimental data available in current literature in section 4 for crack propagation and the response of delaminations in composite panels and the intact response of top-hat

stiffened panels under compressive in-plane loads.

Following the verification of the model the progressive collapse mechanisms are investigated examining the effect of delamination size, location and the topology of the stiffened panel in section 5. This model simulates idealised delaminations, where a delamination exists between plies or at the stiffener-plate interface with no associated damage. The damage tolerance and modelling requirements for different stiffener sections are also compared. This sensitivity analysis provides a guide to the critical damage parameters affecting the damage mechanism and residual capability, investigates how the stiffener type and design dimensions affect the damage tolerance and allow a comparison between typical stiffener configurations. This work draws conclusions which can provide guidance for damage vessels and develops a design tool to aid a damage tolerant design.

Experimental tests are conducted investigating crack initiation and propagation at the flange/plate interface to verify the material properties for marine lay-ups which are discussed in section 6. Material characterisation tests are conducted to provide both mechanical properties and assessment of the fracture properties for mid-laminate delaminations and debonding of post-cured joints. Larger tests on stiffener sections are also conducted

In section 7 the improved material properties are used in a number of case studies to improve and verify the modelling technique and conducts a further parametric damage tolerance study for the experimentally determined properties. The four point bend tests conducted on stiffener sections are compared to the verified FEA model and characterisation data to verify that the coupon tests represent as-built stiffened structures typical of composite ships. A final study is conducted using the verified model and experimentally determined material parameters to assess the damage tolerance of typical multi-stiffened panel. This allows comparisons to be made between the assumed and tested material properties.

3.3 Reference Panel Description

A reference panel is considered to investigate the effect of debond damage in sections 5, 6 and 7. A triple stiffened panel is considered to assess the debonding of the supporting stiffeners as a failure mode. The dimensions and boundary conditions are shown in figure 25. The panel is loaded in longitudinal compression with the loaded and reaction ends of the panel fully clamped. The panel is loaded under displacement control to determine the ultimate load. The panel is considered to be part of a larger grillage and therefore symmetric boundary conditions are applied to the unloaded transverse edges. The panel dimensions are chosen to represent a generic stiffened panel representing a half scale bulkhead panel in a marine structure. A layup is considered using glass vinylester balanced woven roving with the fibre direction aligned with the stiffeners. The table of the stiffeners is reinforced with an additional central unidirectional glass vinylester ply. The material properties are shown in Table 7 and are taken from manufacturer's data or approximate values taken from the literature. Material properties are expressed in the directions 1, 2, 3 which refer to the longitudinal, transverse and through thickness material directions respectively.

The critical strain energy release rates are taken from the mixed mode test data of Dharmawan et al. [11]. The Benzeggagh-Kenane exponent is calculated at 1.17 using the least squares fitting method forcing a (0,0) intercept through this data as shown in figure 26. This gives an R^2 value of 0.9242 showing a linear approximation is

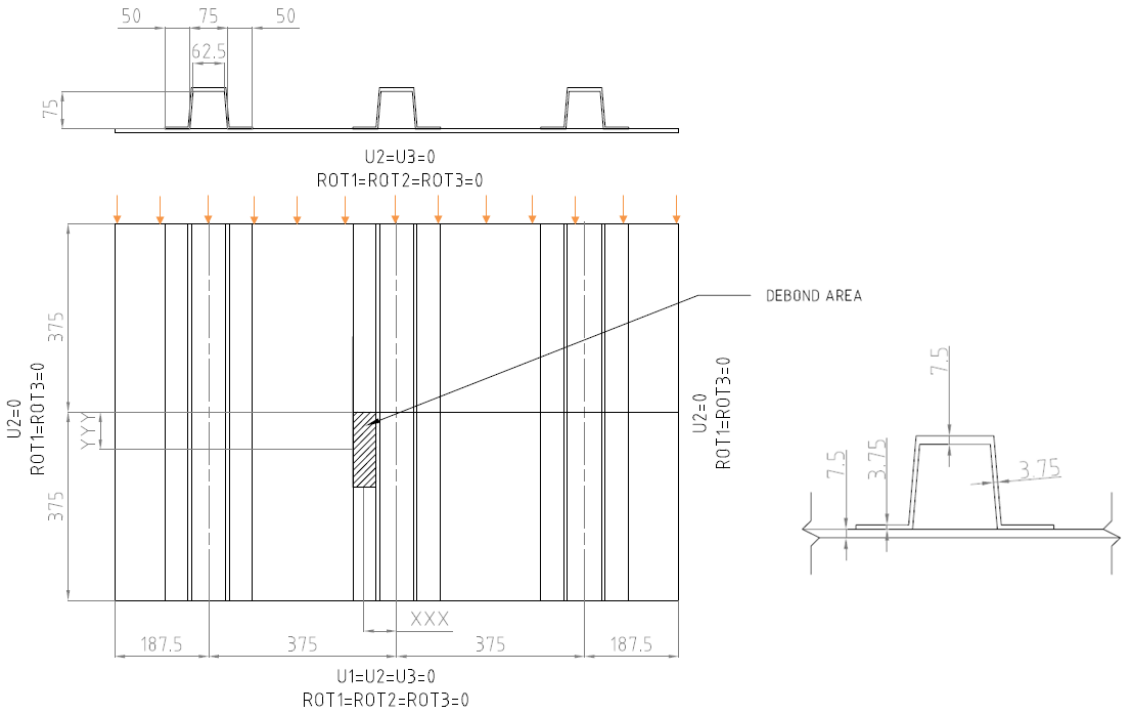

Figure 25: Panel Dimensions Configuration A

reasonable for this data.

The shear interface strengths are taken as a conservative value of 23.2MPa which represents the lower range of material parameters reported by Juntikka and Olsson [157] (20-85Mpa) and the material properties reported for room temperature cure by Compston et al. [158]. Compston et al. [158] reports an increase in interlaminar shear strength to 50MPa and therefore an increase of 115% from a room temperature cure.

The normal interface strength is taken as the transverse strength of the unidirectional laminate as the tensile failure of the fibre-resin interface represents the mode of failure in this test. In this case the tensile resin strength is not used as the fibre-resin interface strength is key in this failure mode which is better represented by a transverse tensile test on a uni-directional coupon.

Table 7: Material Properties

Property	Units	WRE580	UE500
Young's Modulus, E_{11}	MPa	14910	26790
Young's Modulus, E_{22}	MPa	14910	5850
Young's Modulus, E_{33}	MPa	5850	5850
Shear Modulus, G_{12}	MPa	2110	2200
Shear Modulus, G_{13}	MPa	2110	2200
Shear Modulus, G_{23}	MPa	2110	2200
Poisson's Ratio, ν_{12}	-	0.119	0.272
Poisson's Ratio, ν_{13}	-	0.408	0.058
Poisson's Ratio, ν_{23}	-	0.408	0.058
Tensile Strength, S_{11T}	MPa	223.7	482.0
Compressive Strength, S_{11C}	MPa	171.5	308.0
Tensile Strength, S_{22T}	MPa	223.7	17.6
Compressive Strength, S_{22C}	MPa	171.5	87.8
Shear Strength, S_{12}	MPa	23.2	24.2
Interface Strength, X_N	MPa	17.6	
Shear Strength, $X_{T(ILSS)}$	MPa	23.2	
Mode I Critical SERR, G_{IC}	kJ/m^2	1.21	
Mode II Critical SERR,G_{IIC}	kJ/m^2	4.55	
Benzeggagh-Kenane exponent, η_{BK}	-	1.17	

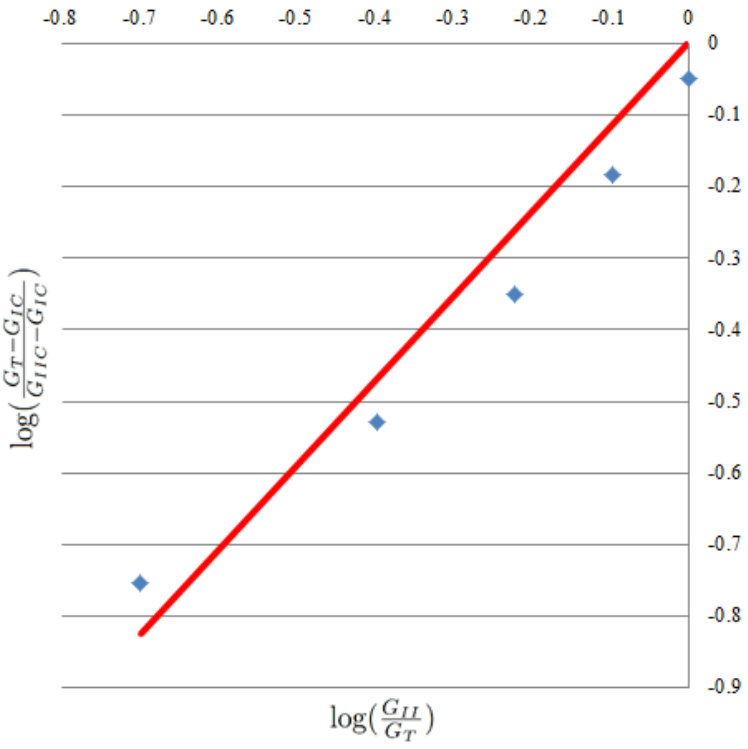

Figure 26: Assessment of Benzeggagh-Kenane Exponent using Mixed Mode Test Data

3.4 Modelling Methodology

A comparison of methods is discussed in section 4 comparing the VCCT and cohesive element methods in terms of accuracy and efficiency. The details of the final methodology used in sections 5 and 7 is presented here.

A shell element model minimises the computational time whilst providing an accurate assessment of the buckled and post-buckled response of the stiffened plate. The stiffeners and plate are connected to the cohesive elements by multi-point constraints, restricting the degrees of freedom of the plate nodes to that of the connected flange nodes. To initiate the post-buckled state an imperfection is seeded onto the structure using the primary buckled mode of the intact case found via Eigenvalue analysis as illustrated in figure 27. The 'nominal' imperfection is represented by an out-of-plane deflection equivalent to 0.1% of the plate thickness and similarly a 'forced' imperfection is equivalent to 10%. This nominal imperfection is used as it does not affect the overall buckled and post-buckled mode shape. The forced imperfection is observed in large scale manufacture as measured by Smith [123] therefore the effect of a forced imperfection is assessed on the damaged response.

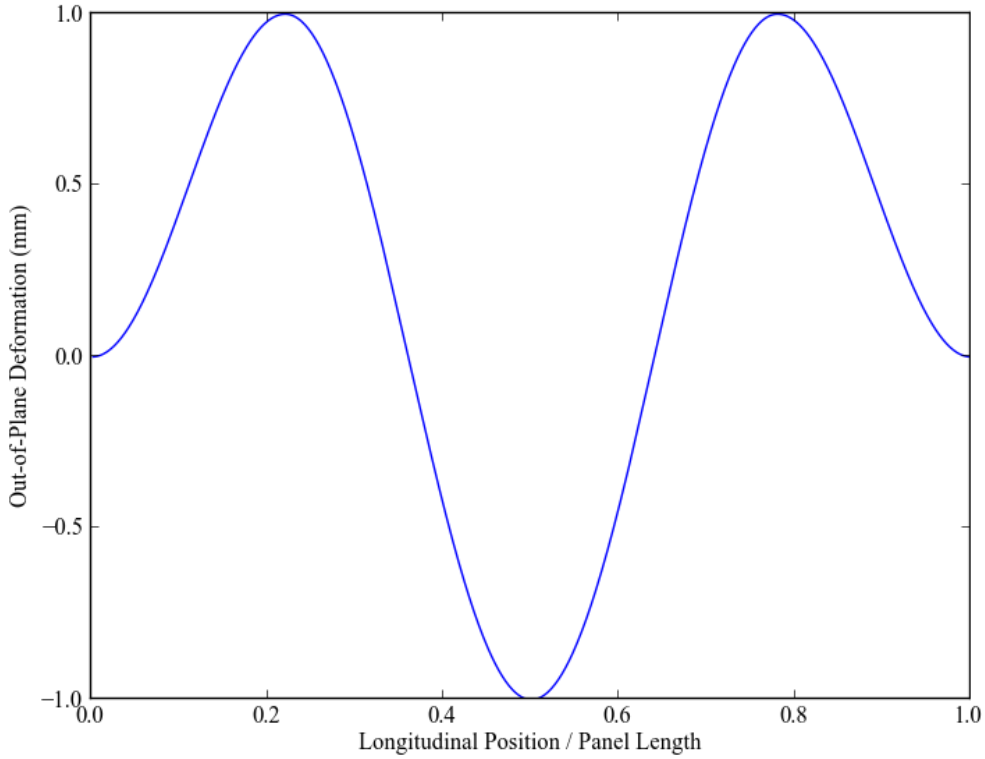

Figure 27: Applied Imperfection

A non-linear analysis is then conducted using a UMAT user defined material to implement the strength based progressive damage. The shell section transverse shear stiffnesses are calculated from equations 15 by averaging the section properties, where t is the thickness of the section,

$$k_{44} = \frac{5}{6} G_{23} t$$

,

$$k_{55} = \frac{5}{6} G_{13} t, \tag{15}$$

$$k_{45} = 0.$$

This UMAT code is developed from the work of Misirlis [51] using additional failure criteria as advised by the WWFE; the Tsai-Wu, Zinoviev and Puck failure criteria are combined to form a conservative criteria as described in section 2.2.4. Following the onset of failure the material properties of the affected element are instantaneously degraded to 1% of the nominal value depending on the failure mode as shown in table 8.

Table 8: Progressive Damage Degradation Factors

	Properties post failure
Fibre fracture	$E_1 = 0.01$
Inter Fibre Fracture: $\sigma_2 > 0$	$E_2 = 0.01E_2^0$, $G_{12} = 0.01G_{12}^0$
Inter Fibre Fracture: $\sigma_2 < 0$	$G_{12} = 0.01G_{12}^0$

Due to the strain softening constitutive model a viscous regularisation scheme is required to avoid numerical convergence issues. An artificial Duvaut and Lions [159] viscous model is used which causes the tangent stiffness matrix of the softening material to be positive for sufficiently small time increments, as shown by equation 16,

$$\dot{d_v} = \frac{1}{\eta}(d - d_v) \tag{16}$$

Where η is the viscosity parameter, d is the degradation factor and d_v is the regularised degradation factor.

To ensure an analogous strain energy released by the damage evolution for each material direction the viscous parameter is calculated by equation 17,

$$\eta_{2T} = \frac{\eta_{1T} S_{2T} E_1}{S_{1T} E_2}. \tag{17}$$

The crack propagation is assessed using a linearly degrading cohesive element with traction separation curve as shown for a single mode in figure 19. G_c is the critical strain energy release rate, K_i the interfacial initial stiffness and t_o is the interfacial strength.

A comprehensive review of damage initiation criteria compared to mixed mode experimental data is lacking in the literature. Therefore, the most commonly used criterion is adopted to assess the location and load at which the

debond initiates; the quadratic nominal stress criterion [53] as shown in equation 18. The Hashin [53] criterion is implemented via a user subroutine, UVARM, and used to assess the location and time step in which the delamination or debond initiates.

$$\left(\frac{\sigma_3}{S_{3T}}\right)^2 + \left(\frac{\sigma_{23}}{S_{23}}\right)^2 + \left(\frac{\sigma_{31}}{S_{31}}\right)^2 \geq 1 \tag{18}$$

Under mixed mode loading the Benzeggagh-Kenane criterion [69] is used to assess the mixed mode failure criterion. The Benzeggagh-Kenane criterion for crack propagation is shown in equation 20, where η_{BK} is a semi-empirical exponent applied to delamination initiation and growth and the total strain energy release rate, G_T, is given by equation 19.

$$G_T = G_I + G_{II} + G_{III} \tag{19}$$

$$G_{IC} + \left((G_{IIC} - G_{IC})\frac{G_{II}}{G_T} + (G_{III} - G_{IC})\frac{G_{III}}{G_T}\right)\left(\frac{G_{II} + G_{III}}{G_T}\right)^{\eta_{BK}-1} \geq G_T \tag{20}$$

To conduct the parametric study the model is generated in Abaqus using python script commands. The stiffener geometric parameters are illustrated in figure 28a and include; stiffener and plate dimensions, number of stiffeners and stiffener position, material properties, layup details, input for failure criteria, boundary conditions and loading. The internal and external radii of the stiffener are considered to allow accurate representation of debond initiation from the interior flange edge.

The optimisation and verification of this modelling methodology is discussed in chapter 4. This verified model is then used to assess the sensitivity analysis of damage and manufacturing parameters in sections 5 and 7.

3.5 Experimental Characterisation

An analysis of the material data available in the literature for heavy weight glass vinylester composites typical of the marine industry is discussed in section 2.1. It is shown that there is a lack of consistent mechanical and fracture data and that interface properties are dependent on many material and manufacturing properties. Therefore a complete set of experimental tests is conducted to provide the mechanical and fracture properties required for modelling debond and delamination damage in top-hat stiffened plates typical of the marine industry.

Post-cured joints are common in large composite structures where a sub-component, such as a stiffener, is post-cured onto an initially cured plate. For such structures a chopped strand mat layer is commonly used at the interface to aid adhesion. The interface properties of such a structure are lacking in the literature and therefore both co-cured and post-cured mode I and II interface properties are determined experimentally and compared. This allows improved modelling of such structures containing both delamination and debond damage.

The experimental tests conducted in section 6 are summarised in table 9 outlining the guiding standard, minimum number of tests and properties acquired.

This experimental data is used to improve the modelling capability in section 7 where the characterisation data

Test	Standard	Minimum Number of Tests	Properties Acquired
Tensile	BS ISO EN 527-4:2009	5	Poisson's Ratio, Tensile Modulus
Compression	BS ISO EN 14126:1999	5	Compression Modulus, Compressive Strength
Shear	BS ISO 14129:1997	5	Shear Modulus, Shear Strength
Flexure	BS ISO 14125:1998	5	Flexural Modulus
Mode I Co-cured	BS ISO EN 7991:2001	4	Critical strain energy release rate for initiation and propagation, R curve
Mode II Co-cured	ASTM D7905/D7905M-15	5	Critical strain energy release rate for initiation and propagation, R curve
Mode I Post-cured	BS ISO EN 7991:2001	4	Critical strain energy release rate for initiation and propagation, R curve
Mode II Post-cured	ASTM D7905/D7905M-15	5	Critical strain energy release rate for initiation and propagation, R curve
Four Point Bend on Post-cured Top-hat Stiffened Section	-	3	Load deflection response, crack initiation and propagation

Table 9: Outline of Experimental Tests

is compared to appropriate models and optimise the cohesive element response to determine the key modelling parameters.

A final set of experiments is conducted to verify that the coupon tests used to characterise the material are representative of a large top-hat stiffened structure and to further verify the model. A four point bend tests is conducted on a stiffener built to the same dimensions as the reference panel discussed previously. The inner rollers are positioned on the inside edge of the flange edge as shown in figure 29. This configuration reduces the stress at the center of the specimen compared to a three point bend configuration and is designed to initiate failure at both the inner and outer flange edges. The specimens are cut from a larger sample of the order of 1.5m by 1.5m and two sets of specimens are cut from two different stiffeners on the panel. Comparison of these stiffeners gives an indication of the variation during manufacture. It is noted that figure 29 illustrates the as built material properties.

3.6 Model Optimisation and Verification Based on Experimental Tests

In section 7 the improved data set is used in a number of case studies to improve and verify the modelling technique and compare the repose to the assumed properties available in the literature. The four point bend tests conducted on stiffener sections are compared to the verified FEA model and experimentally determined characterisation data to verify the coupon tests represent as-built stiffened structures typical of composite ships. Finally an assessment is made on the damage tolerance of de-bonding of top-hat stiffened structures utilising the methodology outlined in section 3.4 and material properties and modelling parameters determined in section 3.5. This allows comparisons to be made between the damage tolerance of top-hat stiffened panels with the assumed properties analysed in section 5 and the experimentally determined material properties.

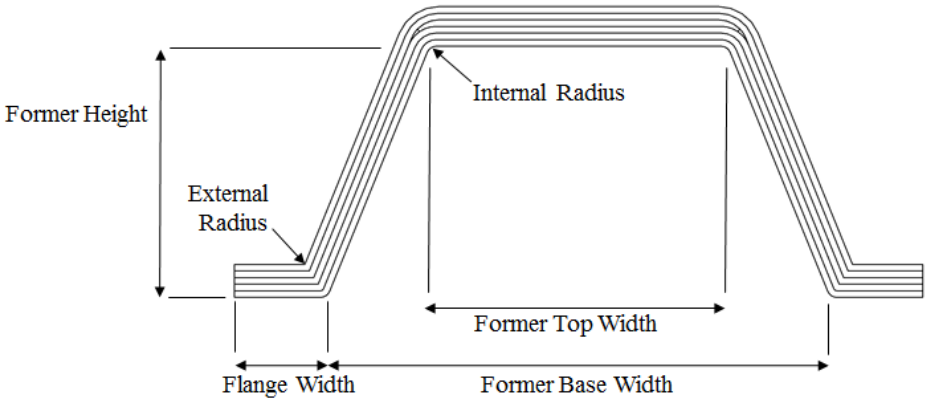

(a) Stiffener Modelling Dimensions

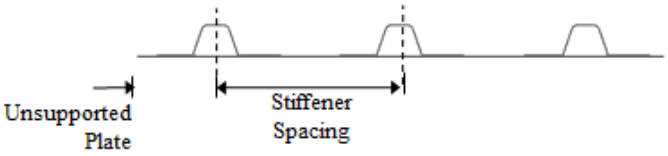

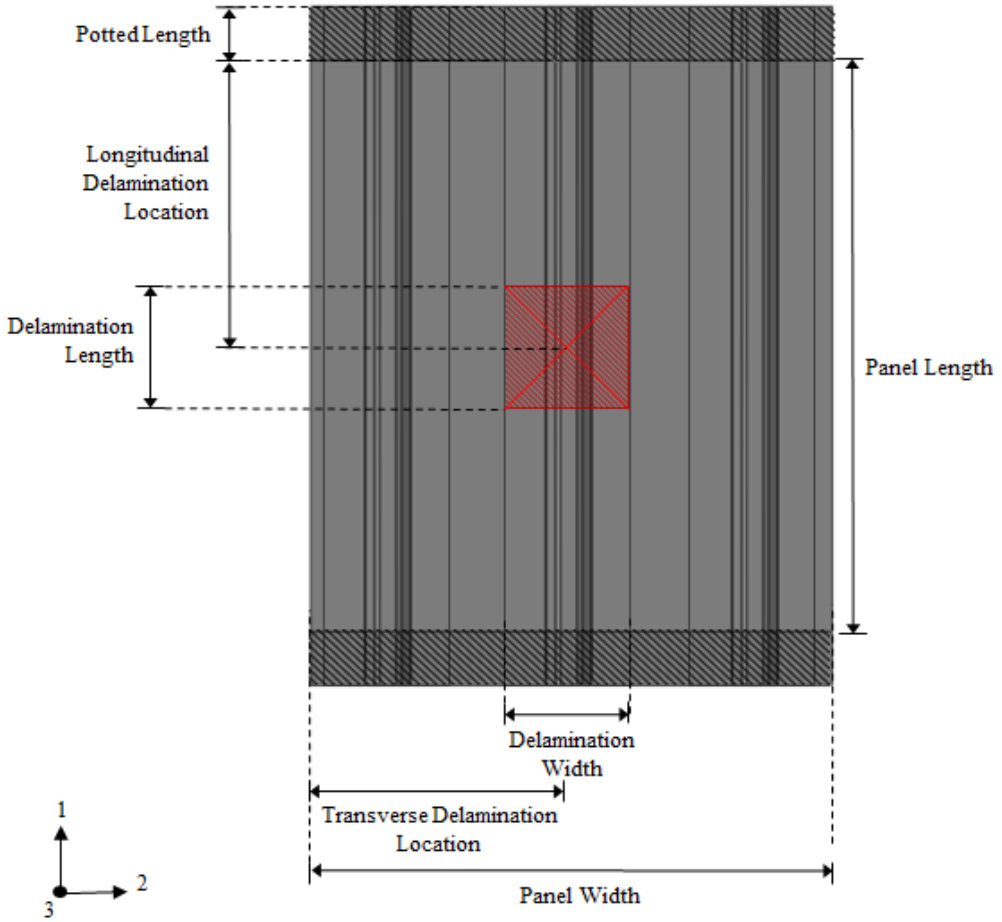

(b) Stiffener Layup

Figure 28: Stiffener Details

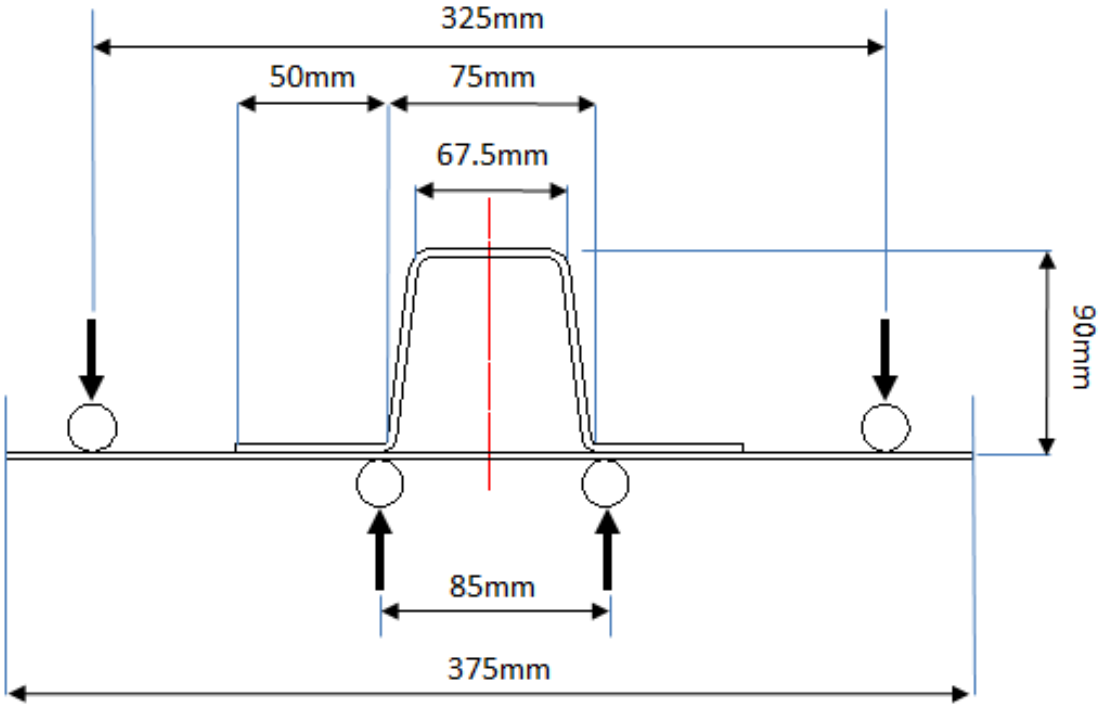

Figure 29: Four Point Bend Test Configuration

4 Model Verification

To verify the model and methodology, solutions are compared to selected experimental and analytical results available in the literature. Due to the complexity of the damage mechanisms in a debond damaged multi-stiffened top-hat panel the model is verified incrementally. The elements to be verified and analysed are shown in figure 30 along with verification studies and sections in which they are reported. A number of tests on rectangular plates loaded in uniaxial compression conducted by Starnes [160] are used to verify the buckled and post-buckled response and to compare a number of failure criteria previously discussed in section 2.2.4. The buckled and post-buckled response of multi-stiffened structures is verified against experimental work of Kong et al. [126]. The VCCT and cohesive element crack propagation methods are verified against experimental results of mode I and mode II tests and compared in terms of computational time and accuracy to determine the method for the final analysis. The inclusion of delaminations in composite structures is verified against through width delamination tests conducted by Kutlu and Chang [161] and embedded delamination tests conducted by Nilsson et al. [105]. The elements are combined to test the damage progression in top-hat stiffened composite structures are verified against full scale tests conducted by Smith and Dow [122] on a MCMV deck structure. The damage tolerance model defined in section 3.3 and the imperfection sensitivity are assessed and the VCCT and cohesive method are compared. A final study is conducted on the reference panel described in section 3.3 in both the intact and debonded state to compare the VCCT and cohesive element method and assess the mesh convergence and the effects of implied imperfections.

	Buckling of Rectangular Plates	Buckling of Blade Stiffened Plates	Mode I And II Crack Propagation	Through Width Delaminations	Embedded Delaminations	Damage Evolution of Top-hat Stiffened Plates	Damage Tolerance Model Verification
Section	4.1	4.2	4.3	4.4	4.5	4.6	4.7
Assessment of Mesh Convergence	✓	✓	✓	✓	✓	✓	✓
Assessment of Panel Buckling	✓	✓		✓	✓	✓	
Comparison of Failure Criteria	✓	✓					
Comparison of Progressive Damage Parameters	✓						
Assessment of Crack Propagation			✓	✓	✓	✓	
Comparison of Crack Propagation Methods			✓	✓			✓
Assessment of Applied Imperfection				✓	✓	✓	✓
Assessment of Turon's Method			✓	✓			
Assessment of Debond Buckling				✓	✓		

Figure 30: Summary of Verification Cases and Verified Elements

4.1 Buckling of Rectangular Plates in Compression

To verify the buckled and post-buckled response and to compare a number of failure criteria and progressive damage methodologies the FEA model is compared to the experimental work of Starnes [160] on compressive loading of flat

rectangular FRP plates.

Table 10: Buckling of Rectangular Plates; Lamina Properties

(a) Elastic Properties

E_{11}	131000MPa
$E_{22} = E_{33}$	13000MPa
$G_{12} = G_{13}$	6400MPa
G_{23}	1700MPa
$\nu_{12} = \nu_{13} = \nu_{23}$	0.38

(b) Material Strength

S_{11T}	1400MPa
S_{11C}	1138MPa
S_{22T}	189MPa
S_{22C}	81MPa
S_{12T}	69MPa
S_{12C}	62MPa

Starnes [160] studied flat rectangular graphite epoxy plates loaded under in-plane compression. Specimens were fabricated from unidirectional Thornel 300 graphite fibre tape, pre-impregnated with 450K cure Narmco 5208 thermosetting epoxy resin. The plates are a 24 ply laminate of total thickness 3.36mm with the stacking sequence $[\pm 45/0_2/\pm 45/0_2/\pm 45/0/90]_s$. The average lamina properties were obtained experimentally as shown in table 10. Three rectangular plates are tested of length 508 mm and breadth, B, 102mm, 140mm, and 178mm respectively for panels C1, C2, and C3. The panels are held in a support fixture which clamps the longitudinal ends and leaves the unloaded edges of the plate simply supported, as shown in figure 31.

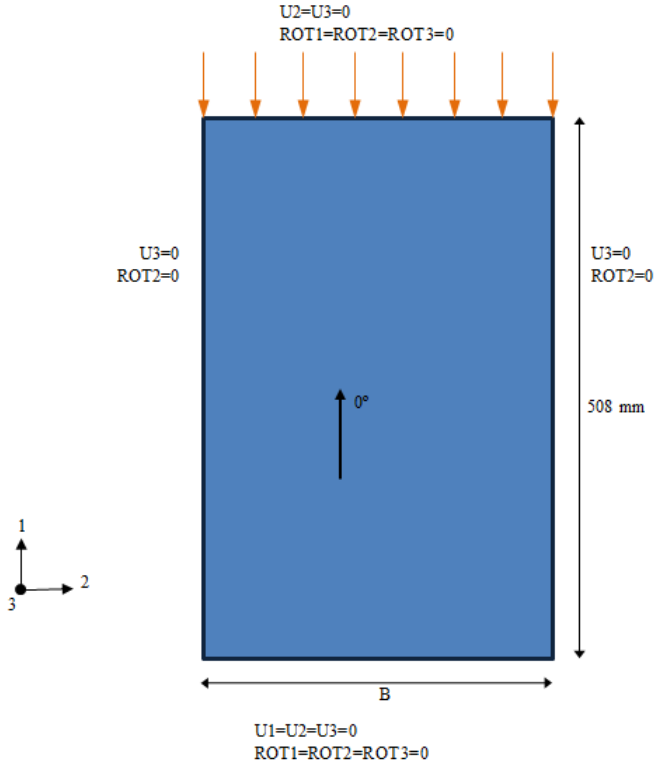

Figure 31: Model Configuration for Buckling of Rectangular Plates

The panel is modelled using the plane stress formulation, neglecting the through thickness stresses and is discritised with 8-node shell elements (Abaqus S8).

A non-linear finite element model is used with the Newton-Raphson method and an automatic incrementation scheme. For the initial imperfection the mode shape is taken of the first buckling mode generated from a linear eigenvalue analysis and is scaled so that the maximum out-of-plane displacement is 1% of the lamina thickness. The viscous parameter for the damage evolution parameter is initially chosen as 1E-6.

A mesh convergence study is conducted on panel C1 and the load shortening curves for a varying number of elements is presented in figure 32. The solution converges using 389 elements or an element size of 12mm when considering maxim load; an element size of 12mm is used for the remainder of this study. The convergence post initial failure is highly dependent on the time incrementation chosen due to the viscosity regularisation scheme and as the automatic time incrementation scheme is used a variation in the damaged response is observed. The effects of the viscous parameter, as described in section 2.2.4, using automatic time incrementation are compared in figure 33 where the percentage error of the maximum load is compared to the load using a viscosity parameter of 1E-7. The results are shown to converge with a viscous parameter lower than 1.0E-5. The right hand side of figure 33, shows the effect of the viscosity parameter on the computational time of the solver. The CPU time decreases linearly with the logarithmic decrease in the viscosity parameter. For large viscosity parameters the first ply failure is over predicted compared to the experimental results, therefore a balance between accuracy and efficiency must be drawn. In this case 1.0E-5 provides reasonable accuracy where the solution has converged to within 1% and provides a reasonable run time and is used for the remainder of this study.

Qualitatively the three panels yield the correct number of longitudinal half waves as reported by Starnes [160], as shown in table 11. The predicted buckled load is defined here as a change in stiffness of 5% compared to the initial stiffness.

The load shortening curves presented in figure 34 a, b and c, for panels C1, C2 and C3 respectively, compares the failure criteria discussed in section 2.2.4 to the reported experimental buckling load and final collapse load for panels C1 and C2 and the full experimental data for panel C3 as reported by Starnes [160].

Table 11: Experimental Data for Buckled Response for Buckling of Rectangular Plates

Specimen	Width, (mm)	Experimental Critical End Shortening, (mm)	Experimental Buckling Load, (kN)	Model Buckling Load, (kN)
C1	102	1.5	65	66.0
C2	140	.8	49	51.9
C3	178	.5	40	42.9

Figures 34 a, b and c and the data presented table 11 show that the buckled and post-buckled response of the panel is accurately modelled; the initial stiffness, global buckling load and post-buckled stiffness show good

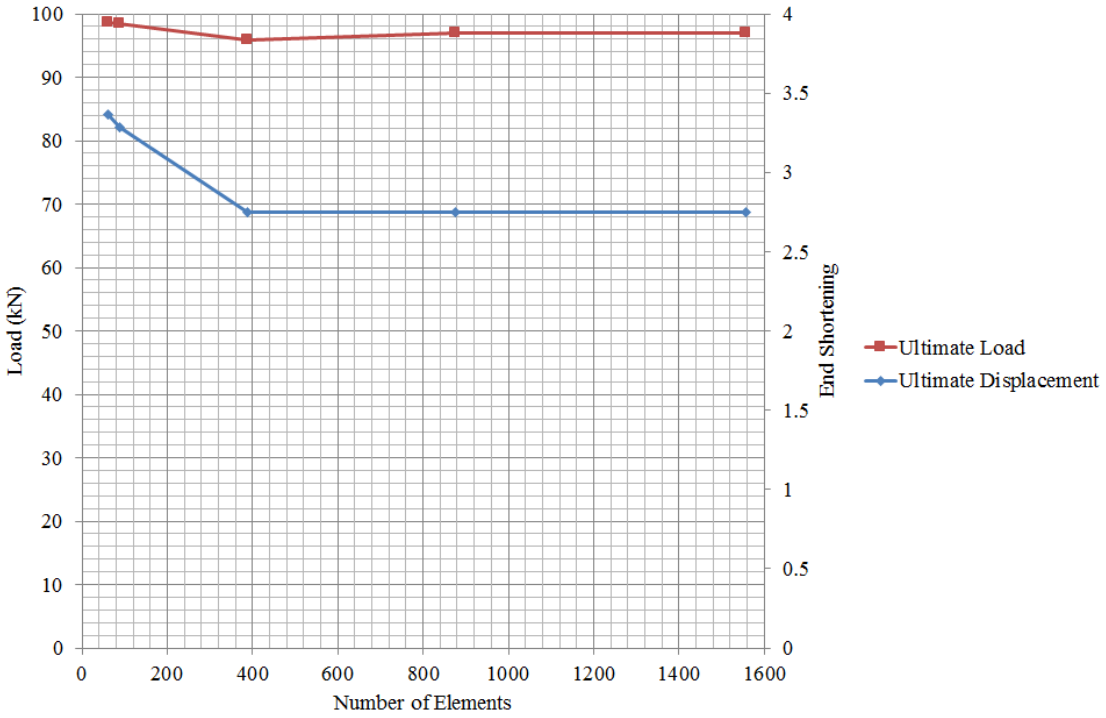

Figure 32: Buckling of Rectangular Plates; Convergence Study

agreement with the experimental results for all three panels. The load-shortening curves are used to compare the failure criteria; the Abaqus implementation of Hashin's 1980 theory is compared to a user defined UMAT code using the World Wide Failure Exercise recommended criteria, as discussed in section 2.2.4. The Abaqus progressive damage subroutine uses the Hashin [53] failure criterion with a linear softening constitutive model where the ultimate collapse strain is defined as twice the initial failure strain for the transverse and shear modes of failure, as recommended by Matzenmiller et al. [58]. For failure in the longitudinal direction no residual strength of the material is apparent therefore instantaneous collapse is assumed i.e. the collapse strain is equal to the initial failure strain. In the UMAT code the elements of the stiffness matrix are instantaneously degraded following initial failure of each integration point by each mode. The recommended failure criteria by the WWFE are compared along with a conservative criterion combining all of the criteria. In the case where an instantaneous degradation model is used the Zinoviev criterion is equivalent to a maximum stress criterion. The Hashin [53] failure criterion is also compared using both instantaneous and linear degradation to compare the effect of the degradation models. The load shortening curves are presented in figure 34 and the ultimate failure loads are compared to the experimental results in table 12.

Comparison of the Hashin 1980 criterion using the two degradation models shows that the additional strength of the material post initial failure provided by the linear degradation model increases the ultimate failure load error by 6.2%, 8.4% and 8.0% respectively for panels C1, C2 and C3 leading to an increasingly non-conservative result. The UMAT Hashin criterion under compressive loads replicates the Maximum Stress failure envelope for

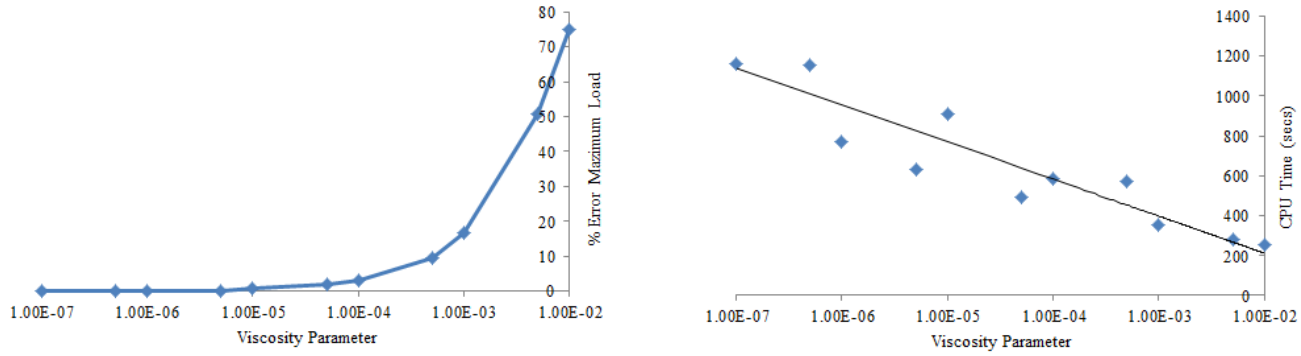

Figure 33: Buckling of Square Plates; viscous regularisation versus computational time

longitudinal and transverse loading and therefore these results are similar and lead to a error of between -1.5 to 7.1% for the three panels and provide a non-conservative estimate for 2 out of the 3 panels. As the complexity of the failure criterion increase the failure modes are more accurately captured and the ultimate failure load becomes increasingly conservative, as seen in the longitudinal, transverse and shear loading failure envelopes presented in section 2.2.4. The Tsai-Wu criterion also yields non-conservative results, as expected from the negative quadrant of the longitudinal and tensile stressed failure envelope whereas the Puck and Combined Conservative failure criterion yield the most conservative results for all three tested panels. The most critical attribute for the failure criterion is to generate conservative results for each case modelled. The Tsai-Wu and Maximum stress criterion yield accurate results for Panel C1 but non-conservative results for panels C2 and C3, up to 7%. Conversely the Puck criterion and the Combined Conservative failure criterion, yields accurate results for Panels C2 and C3 and conservative results for Panel C1 with an error of 9%. Therefore, the Combined failure criterion is shown to be the most conservative for these cases.

The model has shown excellent correlation to the post-buckled response of composite laminate plates closely matching the initial stiffness and global buckling load for a number of experimental tests. The effect of the degradation model has been assessed and it is shown that a linear degradation model provides unrealistic residual capability of the material, for this case, and therefore an instantaneous reduction method is identified as being the most conservative method. The World Wide Failure Exercise recommended failure criteria are compared showing that for this case the Puck or a combined conservative criterion are required for the most accurate results and a conservative estimate for all cases.

Table 12: Comparison of Failure Criterion and Experimental Results for Buckling of Rectangular Plates

	Panel C1 (102mm wide)		Panel C2 (140mm wide)		Panel C3 (178mm wide)	
	Failure Load, kN	Error on Failure Load	Failure Load, kN	Error on Failure Load	Failure Load, kN	Error on Failure Load
Experimental Failure Load, kN	98	(-)	92	(-)	98	(-)
Abaqus Hashin 1980 with Linear Degradation: Failure Load, kN	102.5	4.6%	106.4	15.6%	111.6	13.9%
UMAT Hashin 1980 with Instantaneous Degradation: Failure Load, kN	96.5	-1.5%	98.2	6.7%	103.3	5.4%
UMAT Maximum Stress: Failure Load, kN	97.1	-0.9%	98.5	7.1%	103.4	5.5%
UMAT Tsai-Wu: Failure Load, kN	97.3	-0.7%	98.8	7.4%	102.9	5.0%
UMAT Puck: Failure Load, kN	89.2	-9.0%	91.3	-0.8%	96.4	-1.6%
UMAT Combined Conservative: Failure Load, kN	89.2	-9.0%	91.3	-0.8%	96.4	-1.6%

Figure 34: Comparison of Failure Criteria for Buckling of Rectangular Plates

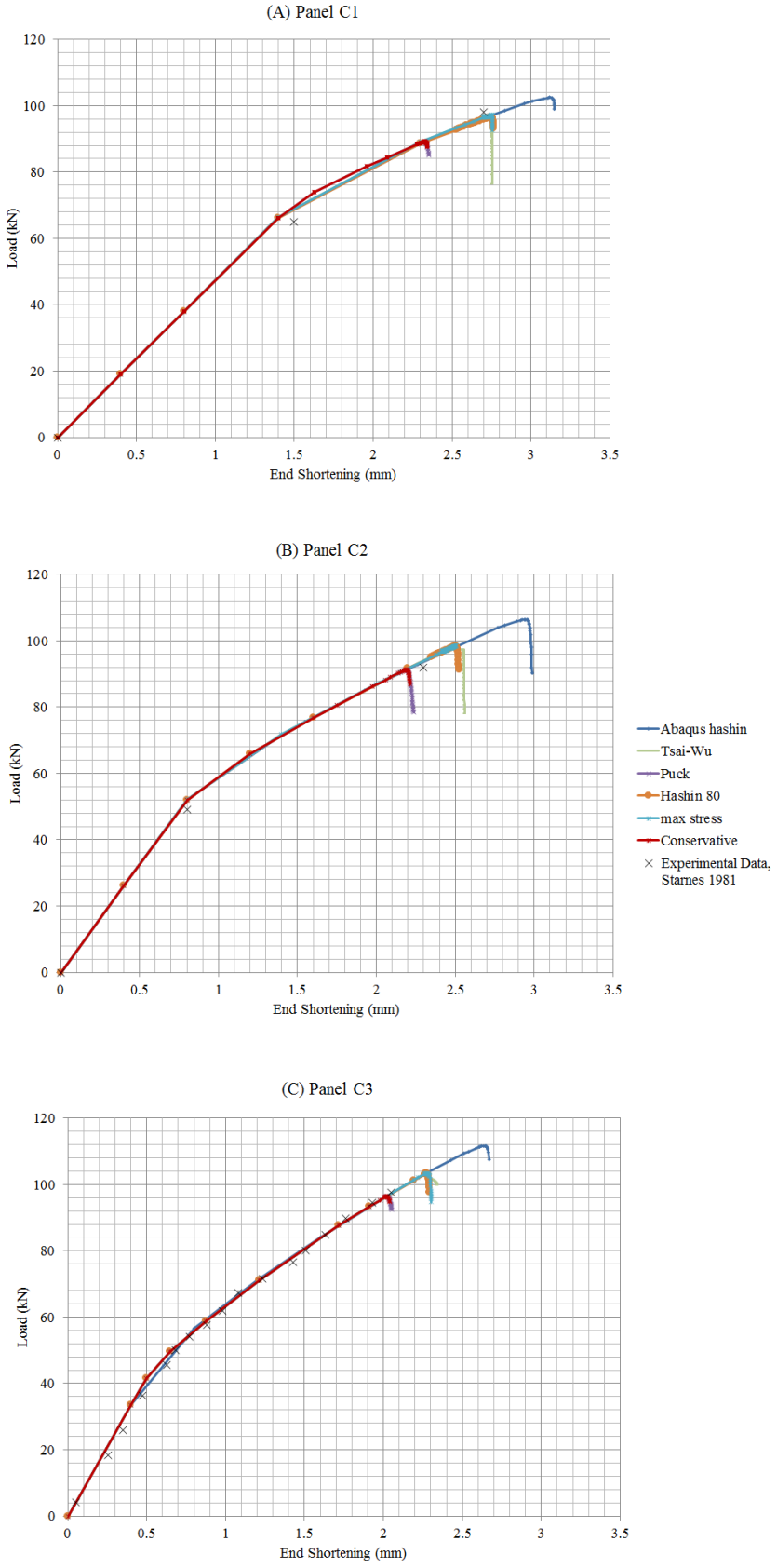

4.2 Buckling of Blade Stiffened Plates

In this study the buckled and post-buckled response of stiffened structures is verified against experimental work of Kong et al. [126] who studied a composite panel stiffened by two longitudinal blade stiffeners under in-plane compressive loading as shown in figure 35. The panels are fabricated from graphite epoxy prepreg with material properties, as quoted by Kong et al. [126], shown in table 13. The stiffeners have a layup sequence of $[0/90/45/0/-45]_s$ and the skin of $[0/90/\pm 45/]_s$. The panel is clamped along the loaded edges and is unconstrained on the unloaded edges. The loaded edges are potted in casting resin and machined flat and normal to the loading direction, as indicated by the shaded region in figure 35. The modelled boundary conditions are also shown in figure 35 to replicate the experimental setup.

Table 13: Lamina Properties

(a) Elastic Properties (b) Material Strength

E_{11}	130000MPa	S_{11T}	1933MPa
$E_{22} = E_{33}$	10000MPa	S_{11C}	1051MPa
$G_{12} = G_{13}$	4850MPa	S_{22T}	51MPa
G_{23}	3620MPa	S_{22C}	141MPa
$\nu_{12} = \nu_{13}$	0.31	S_{12T}	61MPa
ν_{23}	0.52	S_{12C}	61MPa

The panel is modelled using the plane stress formulation, neglecting the through thickness stresses and is discritised with 8-node shell elements with 6 degrees of freedom per node (Abaqus S8). For this analysis an arc length method is required to solve the non-linear problem. For the initial imperfection the mode shape is taken of the first buckling mode generated from a linear eigenvalue analysis and is scaled so the maximum out-of-plane displacement is 3% of the lamina thickness. The viscous parameter for the damage evolution parameter is initially chosen as 1E-6 using automatic time incrementation and increased until convergence is reached.

A mesh convergence study is conducted and illustrated in figure 36 where the ultimate load is compared for increasing number of elements. The figure shows that the model has converged to within 1% change in ultimate load for 1152 elements, an element size of 5mm. To ensure the deflection of the stiffeners is modelled correctly the load against lateral deflection of the stiffeners is also compared in figure 37. The central deflection of the stiffener is shown to have converged to less than 1% change in deflection for 1602 elements, a uniform element size of 4mm, which is used in the remainder of this study.

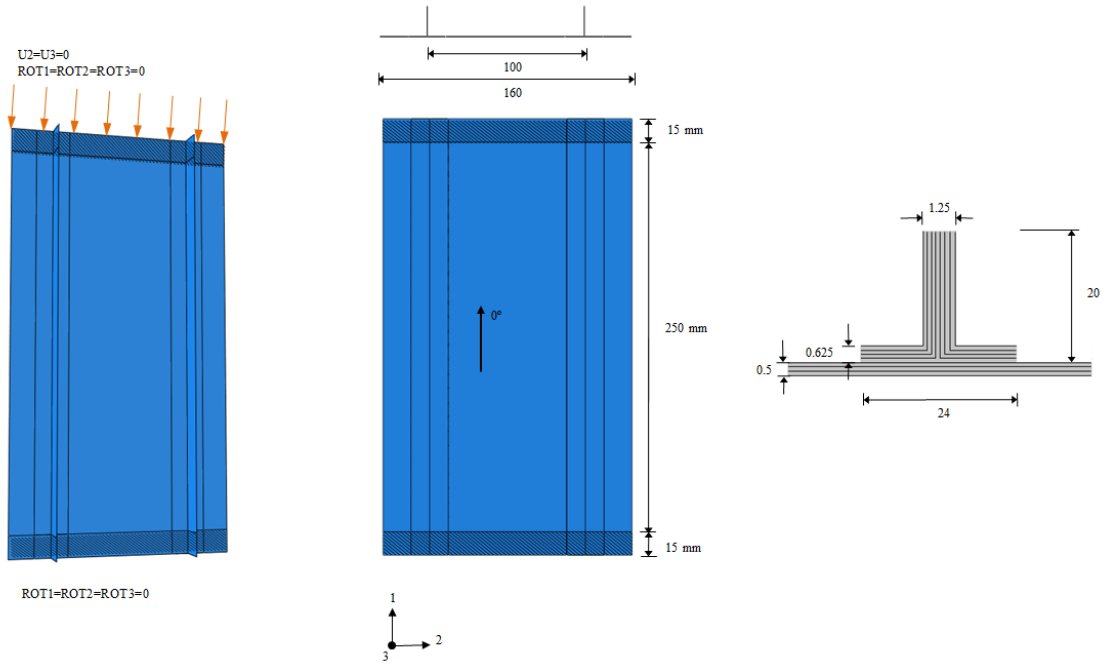

Figure 35: Buckling of Blade Stiffened Plates; Model Configuration

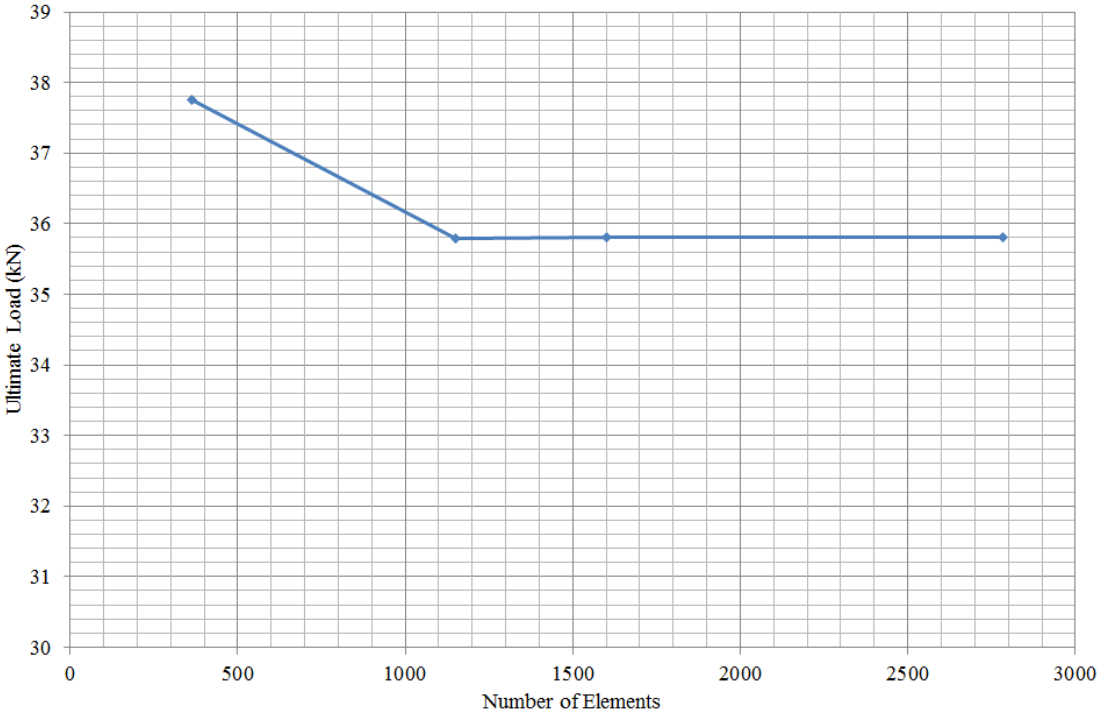

(a) Mesh Convergence; Ultimate Load

Figure 36: Buckling of Blade Stiffened Plates; Mesh Convergence of Ultimate Load

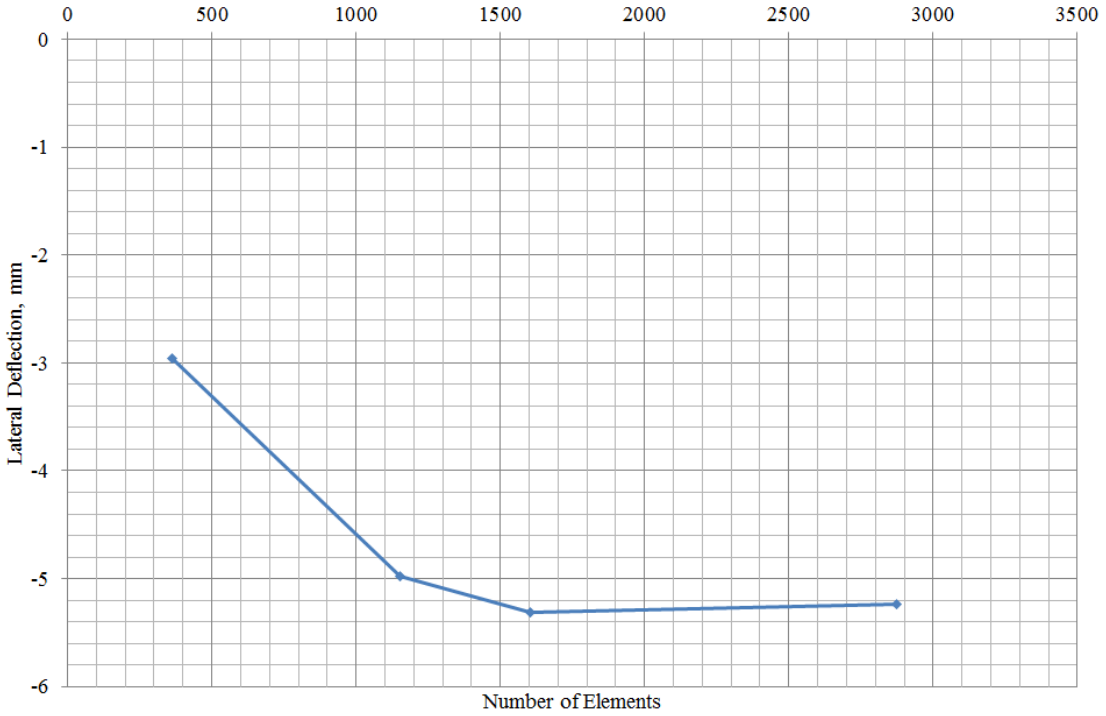

(a) Mesh Convergence; Lateral Deflection

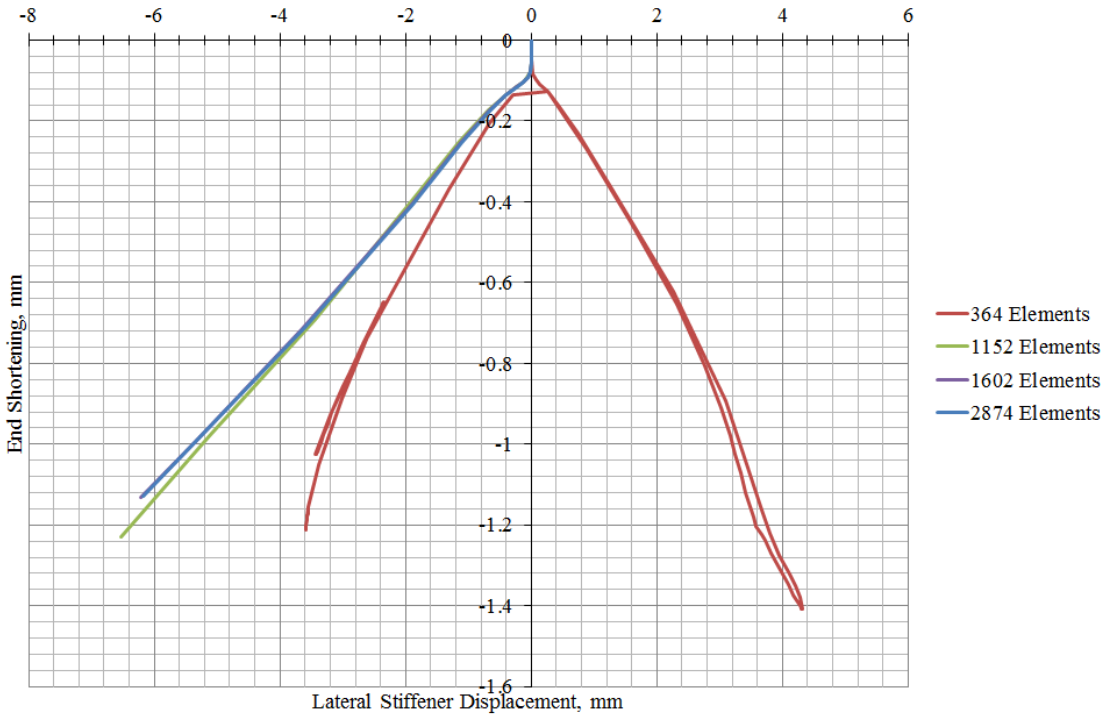

(b) Lateral Stiffener Displacement Curve

Figure 37: Buckling of Blade Stiffened Plates; Mesh Convergence of Lateral Displacement

The effect of the boundary conditions on the load-end shortening curves is assessed and shown in figure 38.

The potted boundary conditions, as described by Araico et al. [124] are compared to modelling the unpotted plate using both clamped and simply supported boundary conditions. The potted boundary allows a restricted degree of rotation, the initial stiffness more closely matches the simply supported case however in the post-buckled state it provides a compromise between the simply supported and clamped conditions. Without detailed experimental data at the boundary and on the as built material properties no further assessment can be made as to the suitability of these conditions. In this case for all three types of boundary conditions the initial stiffness is over estimated by the model suggesting that the elastic modulus of the material quoted by Kong et al. [126] is not necessarily representative of the as built structure. As the failure mode is strongly affected by the deformation of the stiffeners and the post-buckled state the boundary condition on the stiffener ends is critical in accurately modelling failure, therefore potted boundary conditions, as suggested by Araico et al. [124], are implemented as they are proven to be most accurate for a similar single stiffened model.

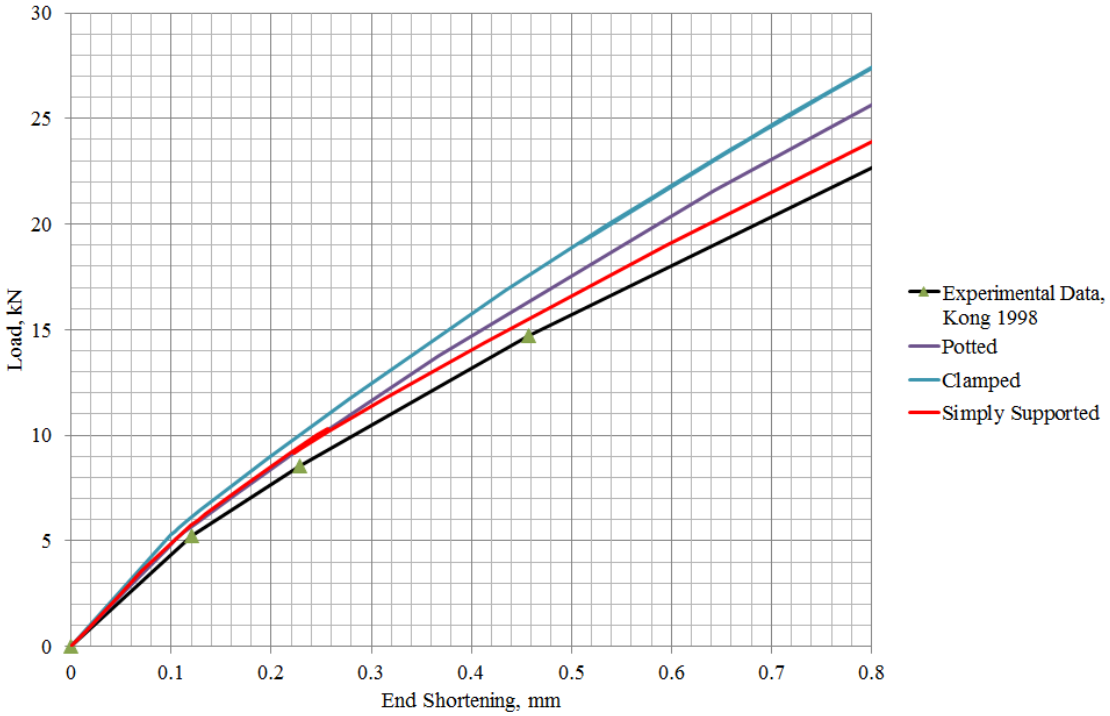

Figure 38: Buckling of Blade Stiffened Plates; Boundary Condition Study

Experimentally Kong et al. [126] observed that the panel buckled into two half sine waves at a load 4.89kN. Following initial buckling, the deformation of the panel increased, with significant bending and distortion of the stiffeners at a load of 15kN. Experimentally initial failure was detected by piezoelectric film sensors at 23.82kN, which represents matrix cracking. Final failure and collapse of the panel occurred at 26.80kN due to the large deformation of the stiffener as the load increased in the post-buckled range.

The deformation states captured by the numerical model are illustrated in figure 39. Qualitatively the model matches the experimental observations well. The buckling load occurred at a load of 5.8kN, where the panel buckled

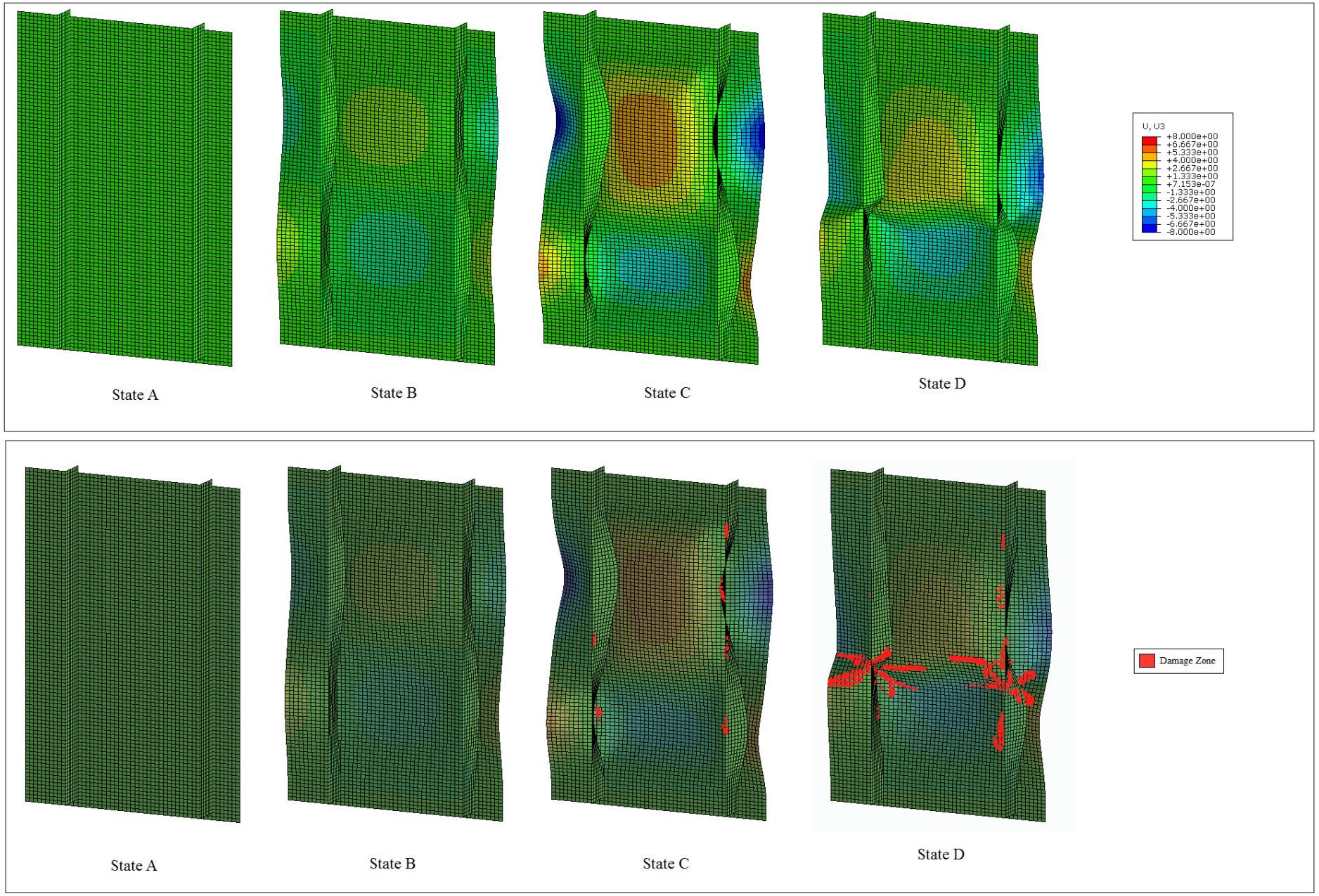

Figure 39: Buckling of Blade Stiffened Plates; Deformation States

into two half sine waves, state A. As the load increases the deepening of the buckling mode and the bending and deformation of the stiffeners is observed in state B. For all the failure criteria considered initial failure is detected in the flange of the stiffeners and plate beneath due to the excessive deformation of the stiffeners, as shown in state C. These failed regions develop gradually and final failure and collapse of the panel occurs due to collapse of the stiffeners, as shown in state D. Quantitatively the buckling load is overestimated by 20%, however as the the initial stiffness is also overestimated this suggests that the elastic modulus of the material quoted by Kong et al. [126] is not necessarily representative of the as built structure.

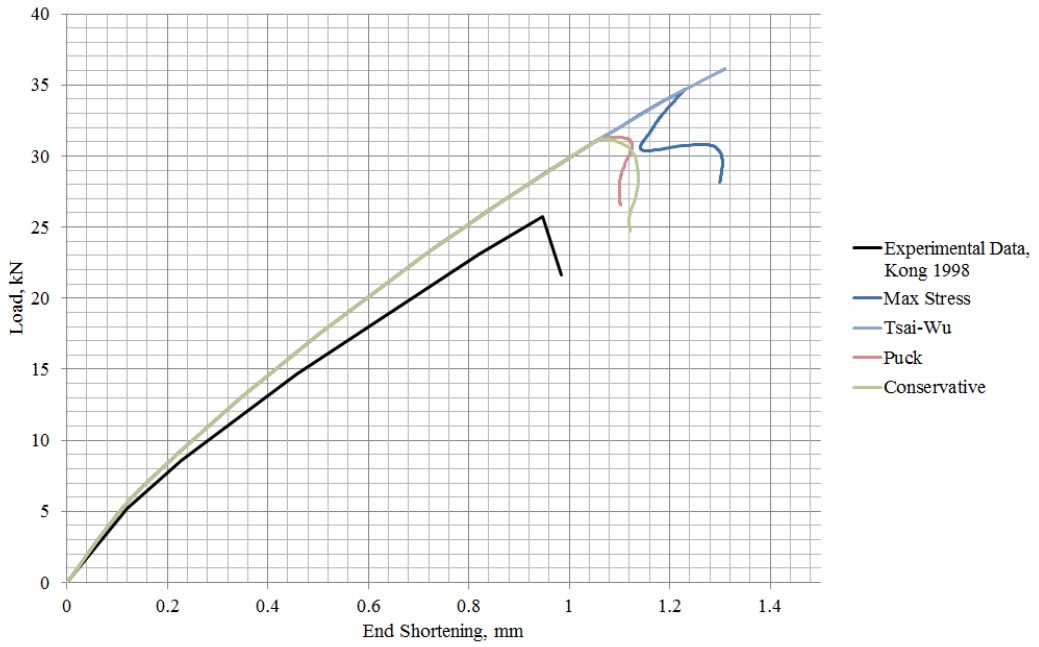

Figure 40: Buckling of Blade Stiffened Plates; Comparison of Failure Criterion

Using the potted boundary condition and a uniform mesh size of 4mm, the WWFE recommended failure criteria are compared to the experimental results, as shown in figure 40. Comparing the failure criteria, the load-end shortening curves show a similar trend to the rectangular plates. The maximum stress and Tsai-Wu criterion significantly over estimate the collapse load leading to non-conservative results. In this case the Combined Conservative failure criterion mimics the Puck failure criterion which yields the most conservative response. All four criteria initially yield a similar failure pattern; tensile matrix failure initiates and develops in the flange and plate underneath the stiffener flange due to the bending and deformation of the stiffener and plate as shown in figure 39. For the Maximum stress criterion compressive failure initiates on the boundary whereas for Puck compressive failure in the fibre direction develops on the transverse central axis leading to ultimate collapse of the stiffener. Without detailed observations from the experimental tests it is not possible to comment further on the validity of the failure modes and damage evolution.

The model has shown good correlation with the post-buckled response of blade stiffened composite plates. Qualitatively the model matches the experimental observations well, mimicking the failure modes observed. Quant-

itatively the model overestimates both the buckling load and final failure load. As the initial stiffness is also overestimated it is assumed that the material properties quoted by the author are not a true representation of the build quality and may in part account for this error. The effect of the boundary conditions is assessed showing that the potted conditions suggested by Araico et al. [124] provide a reasonable compromise between the simply supported and clamped boundary conditions. The World Wide Failure Exercise recommended failure criteria are compared showing that for this case the Puck criterion, as part of a combined conservative criterion, is required to yield the most accurate results. For future tests the combined conservative criterion is adopted.

4.3 Mode I and Mode II Crack Propagation

In this section the VCCT and cohesive element crack propagation methods are verified against experimental results of mode I, mode II tests and compared in terms of computational time and accuracy. The experimental results of mode I, mode II tests cases are used to verify the VCCT and Cohesive element method and optimisation of input parameters. Turon's method is assessed for increasing the model efficiency in sections 4.3.3 and 4.3.4

Mode I, Double Cantilever Beam, DCB, and mode II, End Notch Failure, ENF, specimens are modelled and compared to the experimental data of Reeder et al. [162] with additional data published on the experiments by Camanho et al. [163].

The model configuration, boundary conditions and load deflection configurations are shown for the DCB specimen in figure 41 and for the ENF specimen in figure 42. Models are generated using both a 3D model using C3D8 linear 8 noded brick elements and S4 shell elements with shell thickness offset from the central plane. Aside from the initial crack length, the same specimen properties and geometry are used for both the DCB and ENF specimens; each sublaminate is composed of 24-ply unidirectional AS4/PEEK (APC2) carbon fibre composite with material properties shown in table 14.

Table 14: DCB and ENF Material Properties

(a) Geometric Parameters

2L	102mm
B	25.4mm
h	1.56mm

(b) Material Properties

E_{11}	122700MPa
$E_{22} = E_{33}$	10100MPa
$\nu_{12} = \nu_{13}$	0.25
ν_{23}	0.45
G_{IC}	0.969 kJ/m^2
G_{IIC}	1.719 kJ/m^2

(c) Initial Crack Length

DCB: a	32.9mm
ENF: a	39.3mm

The Virtual Crack Closure Technique, as discussed in section 2.2.5, is based on the principles of linear elastic fracture mechanics. It is assumed that the strain energy released when a crack is extended by a certain amount is the same as the the energy required to close the crack by the same amount. Here the crack propagation is modelled by the Abaqus kinematically compatible nodal release sequence. A guide to the numerical implementation of the kinematically compatible nodal release method is outlined in Appendix C.

4.3.1 Mode I VCCT Method

A mesh convergence study for the DCB is conducted using a uniform mesh size over the specimen and is shown in figure 43. The initial stiffness has converged for 105 elements or an element size of approximately 5mm. However, the accuracy of the solution during crack propagation is also dependent on the element size and requires a further reduction in mesh size. As the nodal release method releases a single node pair ahead of the crack tip per increment, as the element size decreases the crack propagation curve smooths.

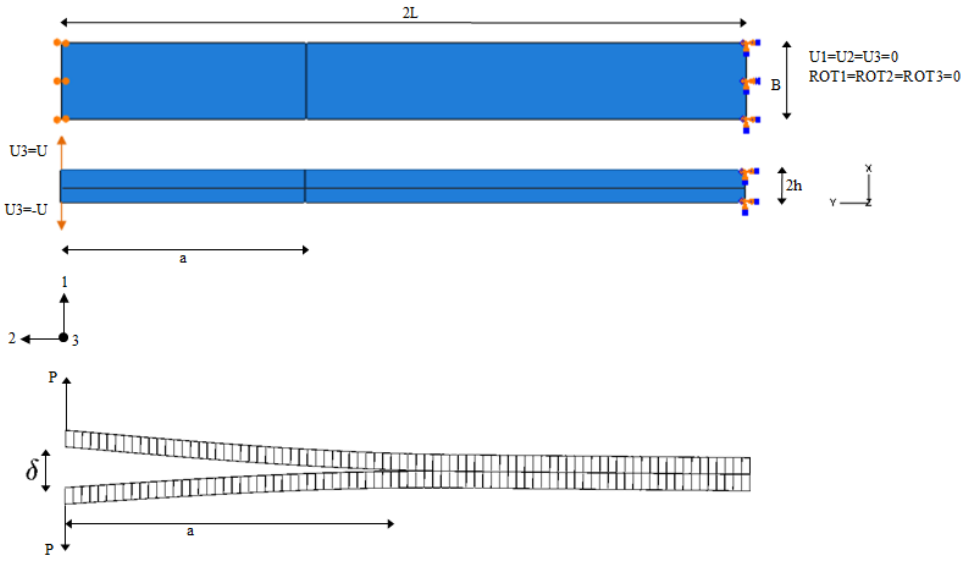

Figure 41: Double Cantilever Beam Configuration

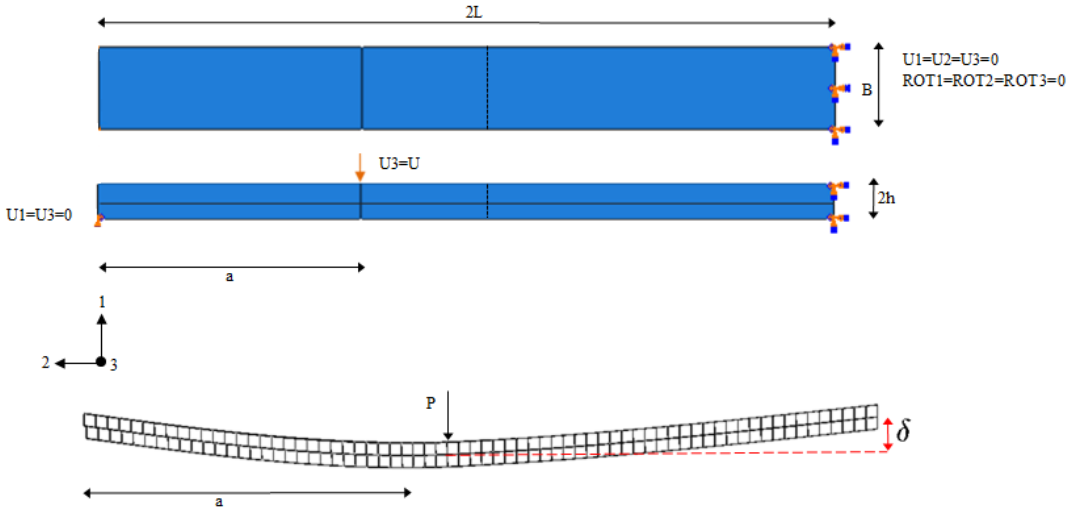

Figure 42: End Notch Failure Configuration

The accuracy of the solution can also be improved by the optimisation of a number of control parameters; in this case the release tolerance and contact stabilization parameter. The release tolerance controls the allowable tolerance of the strain energy release rate. If the strain energy release rate is exceeded a cutback operation is required which reduces the time increment and therefore increases the accuracy of the nodal release load and displacement but increases the computational cost. For this model the release tolerance has been reduced from the default value of 0.1 to 0.02 to ensure the solution has converged to within 1% change of the maximum load for a given element size. The contact stabilization parameter is also reduced to 1E-4 to remove any error introduced on the initial stiffness at low load.

Comparison of the VCCT to the experimental results shows good agreement in the initial stiffness however the load at which the crack propagates is underestimated by 8.8%. The experimental results shows a graduated change in stiffness during initial crack advancement, whereas, the VCCT shows a reduction in stiffness following the initial crack advancement at 142N. Both the under estimation in the critical strain energy release rate and this shape change may be due to an idealised fracture surface between the two laminates caused by lack of fibre bridging across the interface, however the idealised model provides a conservative estimate.

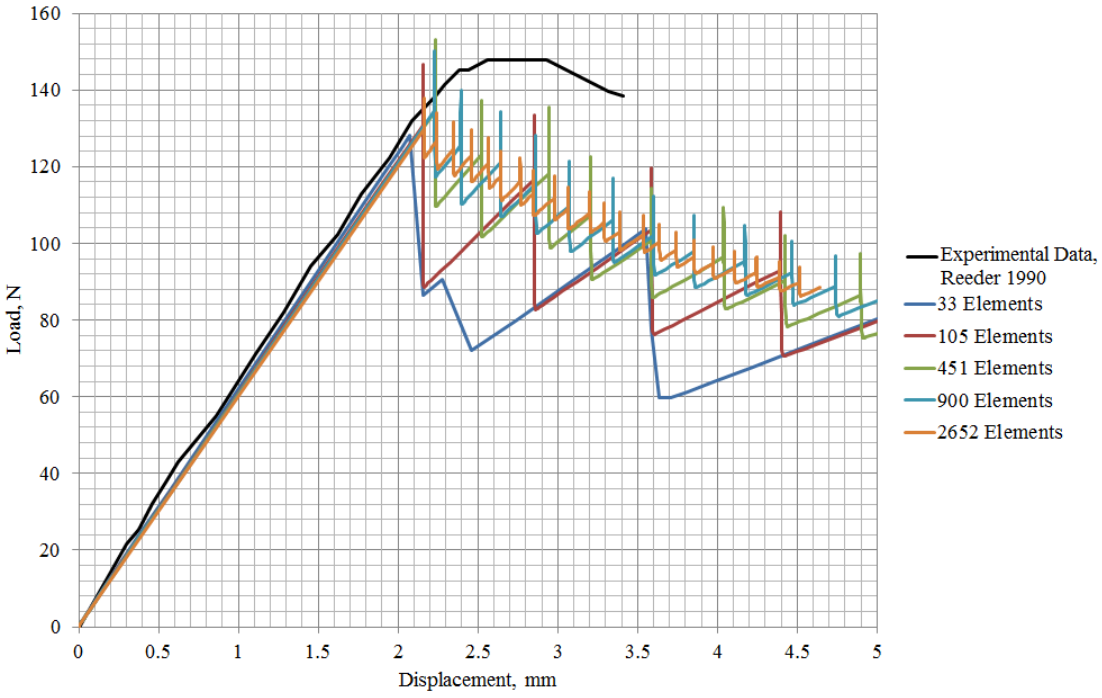

Figure 43: DCB VCCT Shell Element Convergence Study

4.3.2 Mode II VCCT Method

Similarly for the ENF, mode II test a convergence study was conducted. For mode II, shear crack opening, additional convergence parameters are required; convergence of the solution is aided by increasing the maximum number of cutbacks allowed for each increment and increasing the convergence criterion for the ratio of the largest residual to

the corresponding average flux normal for convergence to 1.0.

The load-displacement curves of the convergence study are presented in figure 44. This shows that with regard to stiffness the solution has converged for 2094 elements. When considering the maximum load, convergence is reached with 2094 elements, to within 5% change; however the solution has converged to within 1% for 5526 elements or an element size of 1.25mm. The converged solution is compared to the experimental results with reasonable agreement. The maximum load is over estimated by 12% however the experimental results exhibit a gradual reduction in stiffness rather than the sudden load drop of the numerical model. The gradual stiffness reduction may be attributed to the contact and fibre breakage between the plies as the crack propagates which is not accounted for by this model.

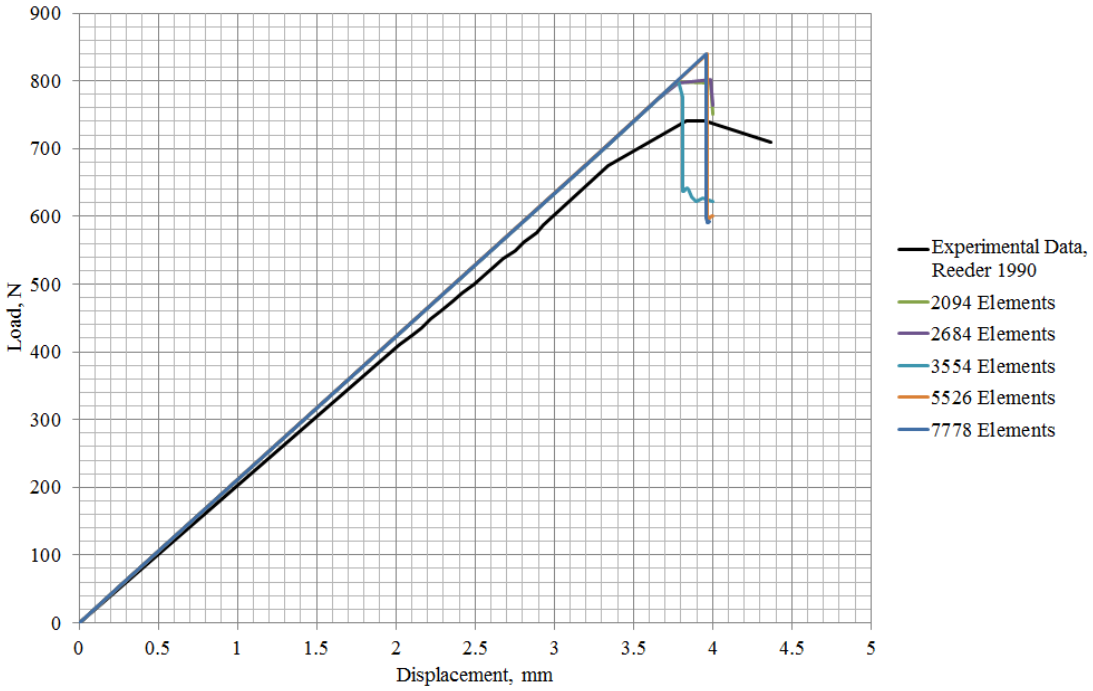

Figure 44: ENF VCCT Shell Element Convergence

4.3.3 Mode I Cohesive Element Method

Cohesive elements combine a fracture mechanics and damage mechanics approach, as discussed in section 2.2.6. The interface between adherends is modelled by a layer of cohesive elements which model the interface region ahead of the crack tip in this case with a linear strain softening constitutive model, and relates displacement continuities with a traction vector at the process zone to the fracture toughness and crack surface area.

For these models the cohesive elements are positioned between the upper and lower arms with an element thickness in the 1 direction of 0.01mm. The initial interfacial stiffness, cohesive element length and interfacial strengths for mode I and mode II are given in table 15 and calculated using the method outlined in section 2.2.6.

It has been shown that the cohesive zone length may be artificially increased by increasing the interfacial strength using the Turon et al. [87] relationship shown in equation 21. The method outlined by Turon et al. [87] is

summarised in appendix C and is used to determine the interface parameter.

$$t_{o_i} = \sqrt{\frac{ME_2G_{ic_i}}{N_e l_e}} \tag{21}$$

Initially a conservative model is used with a cohesive mesh size of 0.3mm which is assumed to be less than the materials cohesive length and the interface strength outlined in table 15. From this model the interface strength distribution is used to approximate the actual cohesive zone length. The out-of-plane traction against distance ahead of the crack tip is shown in figure 45 where the cohesive length is determined as 0.65mm from a linear approximation and therefore the interface parameter is 0.4. The effect of increasing the mesh size to improve efficiency is conducted by artificially increase the cohesive zone length and reduce the interface strength using Turon's relationship. For each model the shell element size used to mesh the DCB arms is set to the cohesive zone length. The modelling parameters are shown in table 16.

Table 15: Cohesive Element Properties

Parameter	Symbol	Value
Initial Normal Interfacial Stiffness	K_I	323000MPa
Initial In Plane Interfacial Stiffness	K_{II}	10100MPa
Element Thickness	T	0.1mm
Mode I Interfacial Strength	t_{o_I}	77.5MPa
Mode II Interfacial Strength	$t_{o_{II}}$	104.5MPa

The load deflection curves are shown for a quarter width model in figure 46 comparing the effect of increasing the cohesive zone length and the number of elements in the cohesive zone. It is shown that good agreement is achieved for each cohesive zone length for 2, 3 and 5 cohesive elements within the cohesive zone. The crack opening load and crack propagation curve is well estimated and comparable to the VCCT method. Similar undulations are seen in the load deflection curves during crack opening which are dependent on the outer shell element size which provide a slight overestimate on the crack opening load. A deviation is also observed in the initial stiffness as the first line of elements at the crack tip exceed the interface strength criterion and the stiffness begins to reduce. The deviation increases as the cohesive zone length increases and the interface strength decreases, however crack propagation is well modelled.

4.3.4 Mode II Cohesive Element Method

The same process is conducted for the ENF configuration. The traction ahead of the crack tip is examined for an cohesive element length of 0.3mm and an interface strength or 104.5MPa. The traction against distance ahead of the crack tip is shown in figure 47. It is shown that the tractions do not decrease linearly to zero at the crack

Table 16: Double Cantilever Beam Interface Strength (MPa) for Increasing Cohesive Zone Length

Adjusted Cohesive Zone Length	0.65mm	1.29mm	1.94mm
t_{o_I}	77.50	54.80	44.74

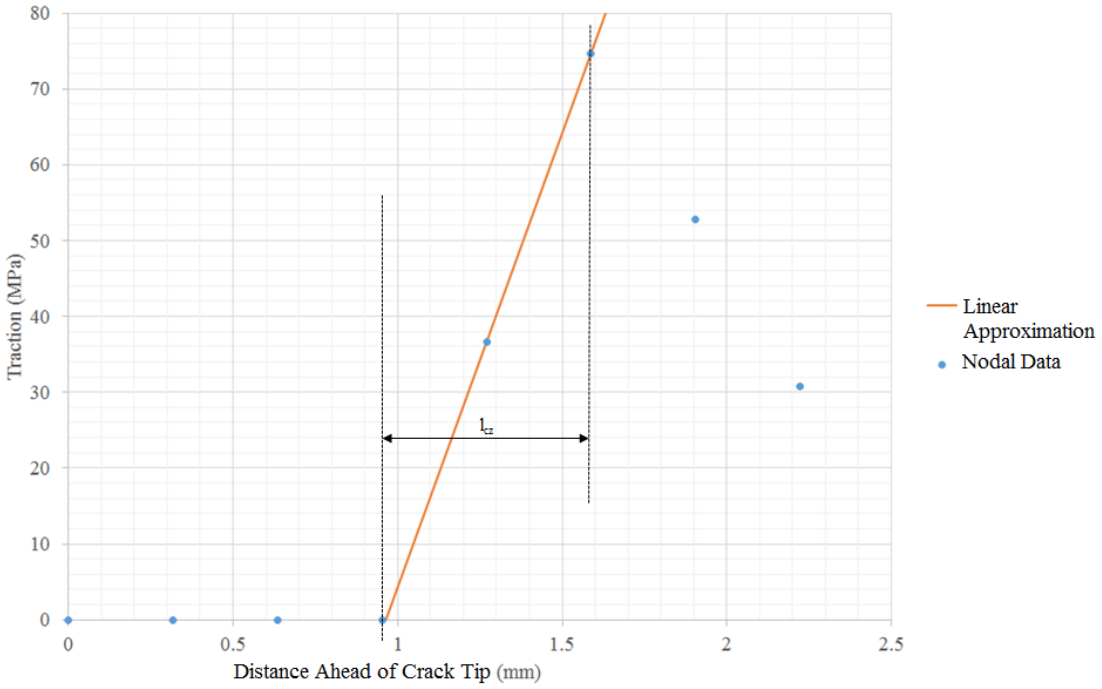

Figure 45: Double Cantilever Beam Traction Ahead of the Crack Tip

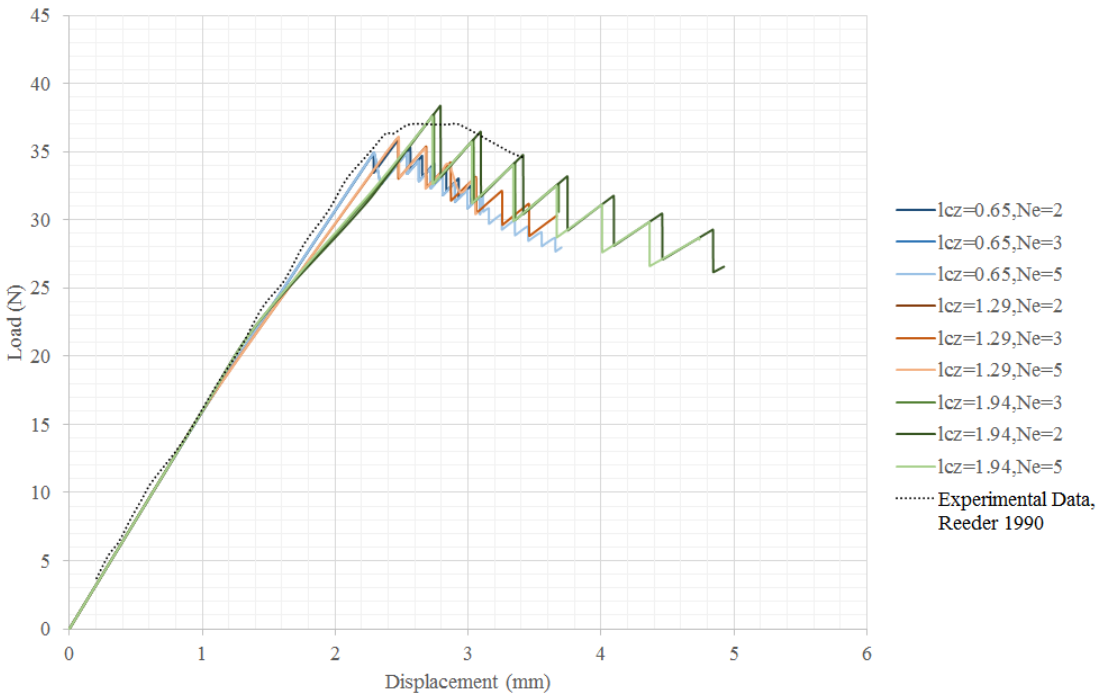

Figure 46: Double Cantilever Beam Load Displacement Curve for Artificial Cohesive Zone Lengths

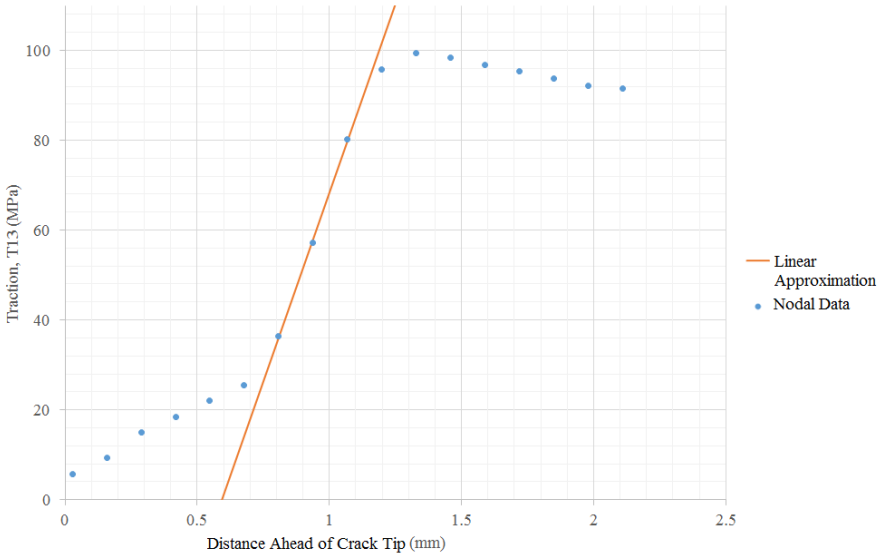

Figure 47: End Notch Failure Traction Ahead of the Crack Tip

tip therefore a linear approximation is used to estimate the cohesive zone length. The cohesive zone length is determined as 0.62mm and therefore the interface parameter is 0.61. The load displacement curves are compared for the cohesive element size and number of elements in the cohesive zone in figure 48. The results are also compared to the experimental data with good correlation. The ENF results show that for all models the stiffness is initially slightly overestimated but due to the linear softening of the cohesive zone there is a gradual change in stiffness of the model prior to crack propagation. This change in stiffness occurs well before the peak load and occurs due to the graduation in the stiffness followed by a drop in the load as the elements at the crack front reduce to zero stiffness and separates. The graduation in stiffness prior and post crack propagation replicates the experimental behaviour in this case however, the load at which the crack propagates is underestimated by the model by 10%. This is due to the energy release prior to crack opening.

The effect of artificially increasing the cohesive zone length on the applied load against roller deflection is shown in figure 48 for cohesive zone lengths and interfaces strengths as shown in table 17. It can be seen that there is less fluctuation in the results when compared to the mode I, DCB results. The results have converged for any number of cohesive elements within the cohesive zone length showing good approximations for 2, 3 and 5 cohesive elements. Increasing the mesh size of the shell elements on the sample arms produces a stepped response to the load displacement response creating a slight over estimation in the crack propagation load.

Table 17: End Notch Failure Interface Strength (MPa) for Increasing Cohesive Zone Length

Adjusted Cohesive Zone Length	0.60mm	1.20mm	1.80mm
t_{o_I}	98.9	70.0	57.1

4.3.5 Comparison of Methods

To compare the VCCT and cohesive element methods the converged solutions and experimental results for the DCB and ENF tests are shown in figure 49.

For the double cantilever model both methods exhibit a similar trend; the initial stiffness compares well to the experimental data and the load at crack advancement is reasonably estimated at 134N and 142N for the VCCT and cohesive methods respectively compared to the experimental results of 147N. The cohesive elements result in a slightly higher estimation of the maximum load although the discrepancy between the two methods may be attributed to the tolerance value used on the critical strain energy release rate used for the VCCT method. The stiffness reduction as the crack advances is matched by both methods however the experimental results show a graduated change in stiffness from stable crack growth.

For the end notch failure model a greater discrepancy between the two methods is apparent. The cohesive element method shows a gradual reduction in stiffness prior to crack advancement due to the stresses at the interface exceeding the interfacial strength which is comparable to the experimental results where a gradual reduction in stiffness associated with a build up of matrix cracking in the interface layer. The peak load is underestimated with a peak load at 700N compared to 742N experimentally. However the VCCT method stiffness remains linear and fails to account for a build up of damage at the interface; it overestimates the load at which the crack advances. Following crack advancement the VCCT method sustains a linear drop as predicted by the analytical solution to approximately 600N whereas the cohesive elements have a gradual drop which closely match the experimental case.

Therefore the study shows that good approximation for the crack propagation in modes I and II can be obtained from both methods. The cohesive element method is capable of modelling the gradual build up of matrix cracking and damage at the crack tip prior to crack advancement in mode II opening whereas neither method effectively captures the fibre bridging behind the crack tip under mode I opening in this case. It is shown that the Turon method can be used effectively to artificially increase the mesh size and provide reasonable solutions. Therefore, the cohesive element method is the method of choice for further studies.

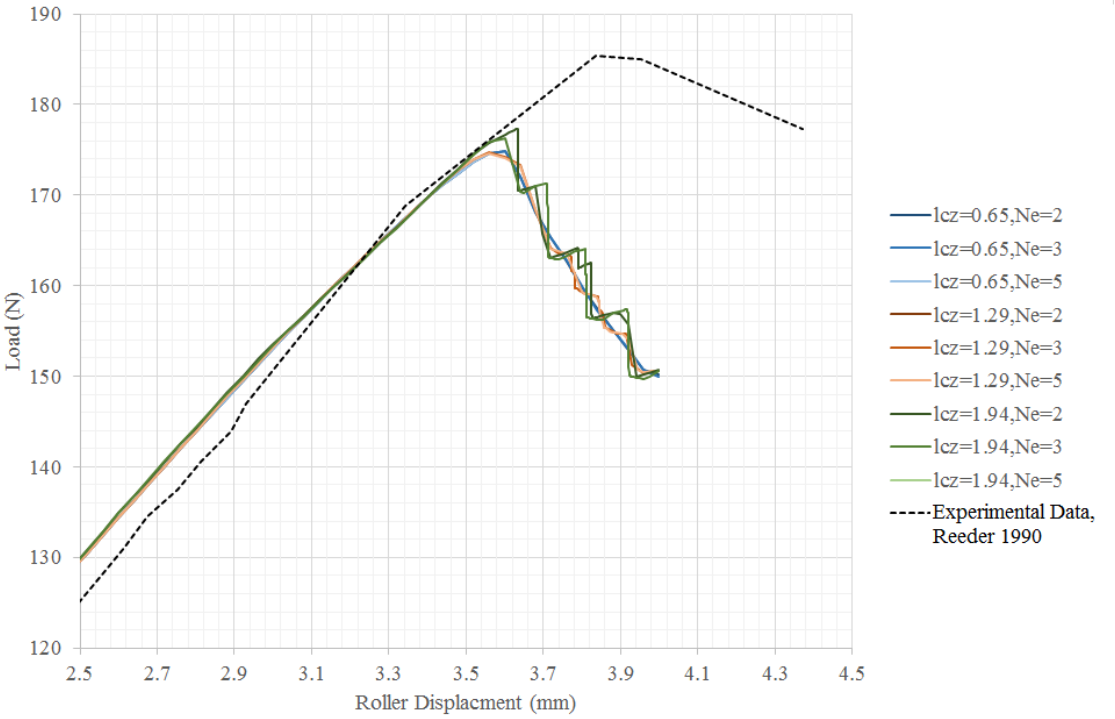

Figure 48: End Notch Failure Load Displacement Curve for Artificial Cohesive Zone Lengths

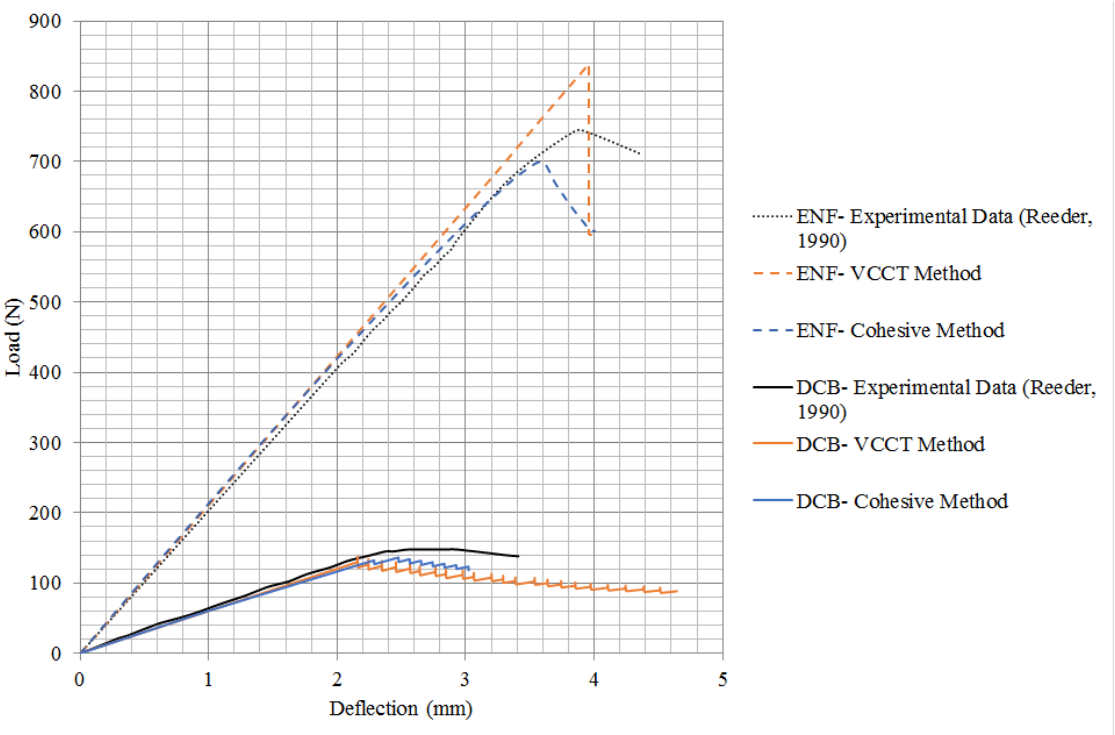

Figure 49: Comparison of VCCT and Cohesive Element Method; DCB & ENF

4.4 Through Width Delaminations

In this section the VCCT method and cohesive element models are assessed in their ability to follow combined crack propagation and buckling is verified against the experimental work of Kutlu and Chang [161] and the numerical work of Liu et al. [164] and Zhang and Wang [165]. Initially a mesh convergence study is conducted and an assessment is made on the effect of local, global and combined imperfections using the VCCT method. The cohesive element method is used and an assessment if made of the cohesive zone length and the interface parameters. Turon's method is used to assess to the accuracy of the model whilst improving it's efficiency. The VCCT and cohesive element method are compared to both the experimental data and other models available in the literature.

Kutlu and Chang [161] investigated composite panels containing through width delaminations subjected to compressive loading. The panels are manufactured from 20 plies of T300/976 graphite epoxy with material properties as shown in table 18.

Table 18: Buckling of Delaminated Coupons; Lamina Properties

(a) Elastic Properties

$E_{11}=$	139300MPa[(1)]
$E_{22}=E_{33}=$	9722MPa[(1)]
$G_{12}=G_{13}=$	5585MPa[(1)]
$G_{23}=$	3448MPa[(1)]
$\nu_{12}=\nu_{13}=$	0.29[(1)]
$\nu_{23}=$	0.40[(1)]

(b) Strength Properties

$S_{11T}=$	1517MPa[(1)]
$S_{11C}=$	1593MPa[(1)]
$S_{22T}=$	44.5MPa[(1)]
$S_{22C}=$	253MPa[(1)]
$S_{12T}=$	106.9MPa[(1)]
$S_{12C}=$	106.9MPa[(1)]

(c) Damage Criterion

$G_{IC}=$	0.088 N/m[(1)]
$G_{IIC}=$	0.315 N/m[(1)]
$\eta_{BK}=$	2 [(3)]
$E_f=$	230000MPa[(2)]
$\nu_{f12}=$	0.2[(2)]

[(1)] Kutlu and Chang [161]
[(2)] data for T300 Epoxy, Soden [166]
[(3)] Estimated from the Literature, Benzeggagh and Kenane [69]

Kutlu and Chang [161] tested a number of panels with delaminations inserted using Teflon layers of different lengths and positions between the plies as shown in figure 50. Strain gauges positioned on the outer most surfaces recorded the strain history as a function of applied load.

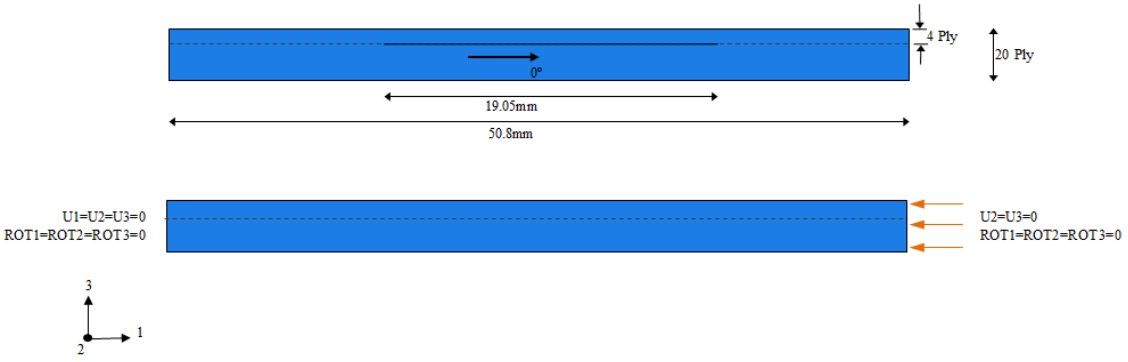

Figure 50: Buckling of Delaminated Coupons; Model Configuration

The panel is modelled using 4-node shell elements (Abaqus S4). The crack propagation is modelled using the Abaqus nodal release method using the VCCT and the Benzeggagh-Kenane criterion for mixed mode failure. The

nodes on the bond line are initially tied until the critical strain energy release rate is exceeded. As the mixed mode crack propagation data is not given by the authors the Benzeggagh-Kenane exponent is initially chosen as 2 which represents a typical exponent for composite materials.

As in the previous section a non-linear model is used with the Newton-Raphson method and an automatic incrementation scheme. The viscous parameter for the damage evolution parameter is chosen as 1E-6. A contact constraint is placed between the delaminated upper ply and the lower ply to prevent penetration of the plies. Small sliding is assumed with a surface to surface discretisation which applies an average contact condition over the region providing improved stresses at the contact surface. The UMAT subroutine is used to investigate fibre and matrix failure using the Combined Conservative failure criterion, as used in the previous sections. Throughout this investigation the applied load discussed is the load applied to the coupon ends, in this case modelled with a 10mm width.

4.4.1 Mesh Convergence

A mesh convergence study is conducted investigating the buckled response of the delaminated layer using the minimum imperfection required to cause a non-linear response; a maximum out-of-plane imperfection is initially chosen at 0.1% of the ply thickness. The local and global buckling loads are compared for increasing mesh density in figure 51. The model is shown to have converged with 2666 elements, equivalent to an element size of 1mm showing convergence of the ultimate load and global buckling load. An element size of 1mm is used for the VCCT models for the remainder of this study.

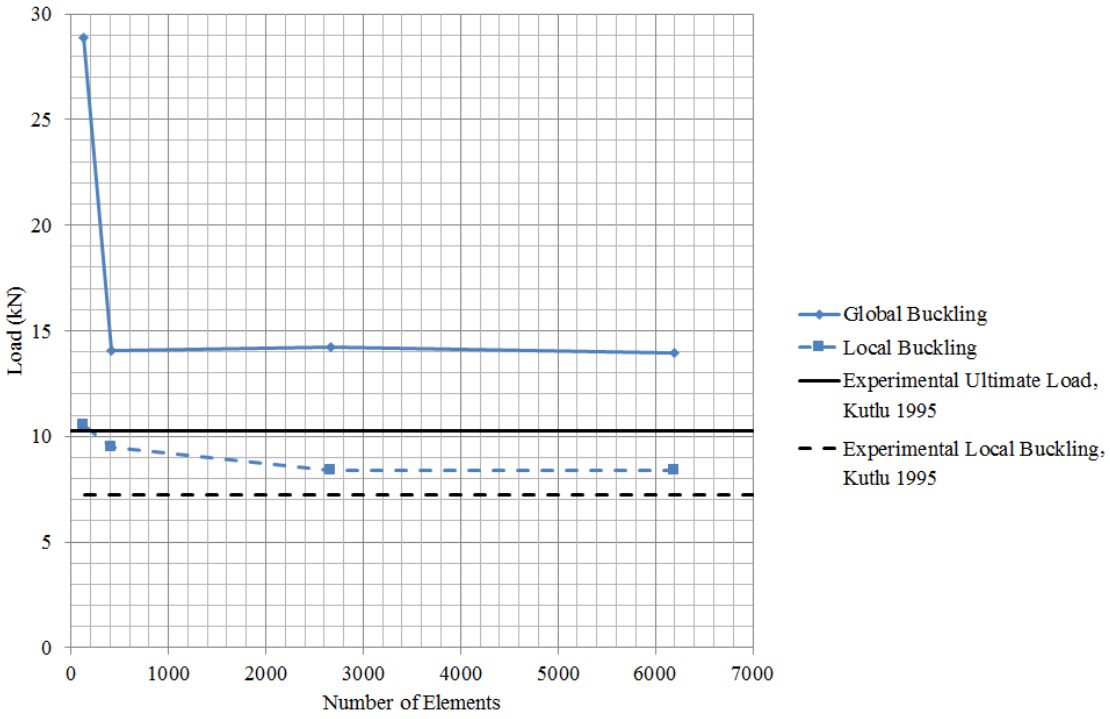

Figure 51: Buckling of Delaminated Coupons; Convergence Study

4.4.2 Assessment of Imperfection Sensitivity

The converged solution compared to the experimental results shows a significant over-estimation of the buckled load along with a discrepancy in the strain-load relationship during the transition to the buckled state. The Teflon insert thickness is quoted by authors of similar tests as 0.0254mm [167] which is approximately 5% of the upper lamina thickness and therefore cannot be assumed to be negligible. Due to the presence of the Teflon layer a significant imperfection is assumed between the lower and upper delaminating plies. Therefore the imperfection magnitude and shape is determined parametrically in a study comparing the imperfection shape as the first buckling mode generated from a linear eigenvalue analysis scaled by the upper laminate ply thickness, and a constant indent over the area of the Teflon layer. The results are shown in figure 52 and 53 in the form of the load strain graphs for a sinusoidal and indented imperfection respectively and compared to the experimental results. For each case the maximum out-of-plane imperfection is varied and scaled to a percentage of the upper laminate thickness. A minimum imperfection of 0.1% of the upper laminate thickness was required to initiate buckling.

For the sinusoidal imperfection the strain and load at which the crack propagates are reasonably captured by all three levels of imperfection. However, the initial stiffness is significantly affected by an imperfection of 5%, reducing the experimental fit. The critical buckling load, where the strain deviates from the initial linear state and where the strain becomes positive, is better captured by a 5% imperfection, or 0.0259mm maximum deflection.

For the constant indent imperfection the initial stiffness is significantly affected by an imperfection of 5-10%. The critical buckling load, where the strain deviates from the initial linear state and where the strain becomes positive, is most accurately modelled by 2% lamina thickness or 0.01mm imperfection, approximately half the Teflon insert thickness. The constant indent imperfection yields a closer fit to the experimental results for the transition to the buckled mode. Therefore a constant indent of 2% or 0.01mm is assumed for the remainder of this study.

In order to initiate a global buckled response the sensitivity of the model to a global imperfection on the lower laminate is assessed based on the first buckle mode shape and a linear indent over the Teflon layer, both with the maximum out-of-plane displacement scaled to a percentage of the lower laminate thickness.

A 0.1% global imperfection, the minimum imperfection required to initiate a global buckled response is compared to 0.2% and 0.5% in figure 54 for the front and back responses. An overall imperfection of the laminate first mode shape is applied to the coupon in the form, $\frac{1}{2}(1 - cos(\frac{2\pi x}{L})$, where x is the distance along the length of the coupon and L represents the length of the coupon. As global buckling could equally result in a positive or negative displacement the initial imperfection is applied and is seeded in the negative direction to ensure the model can be suitably compared to the experimental results. An indented imperfection with maximum out-of-plane displacement of 0.01mm is then additionally applied to the upper laminate over the Teflon, the delamination region. Figure 54 illustrates the effect of the combined imperfection on the front and back of the coupon. The results show that a global imperfection of 0.2% does not significantly reduce the global buckling load compared to an imperfection of 0.1% whereas for a global imperfection of 0.5% the failure mode changes; global buckling becomes the initial response, followed by delamination propagation, local buckling of the delaminated ply and ultimate collapse. This modified failure mode is not representative of the experimental results.

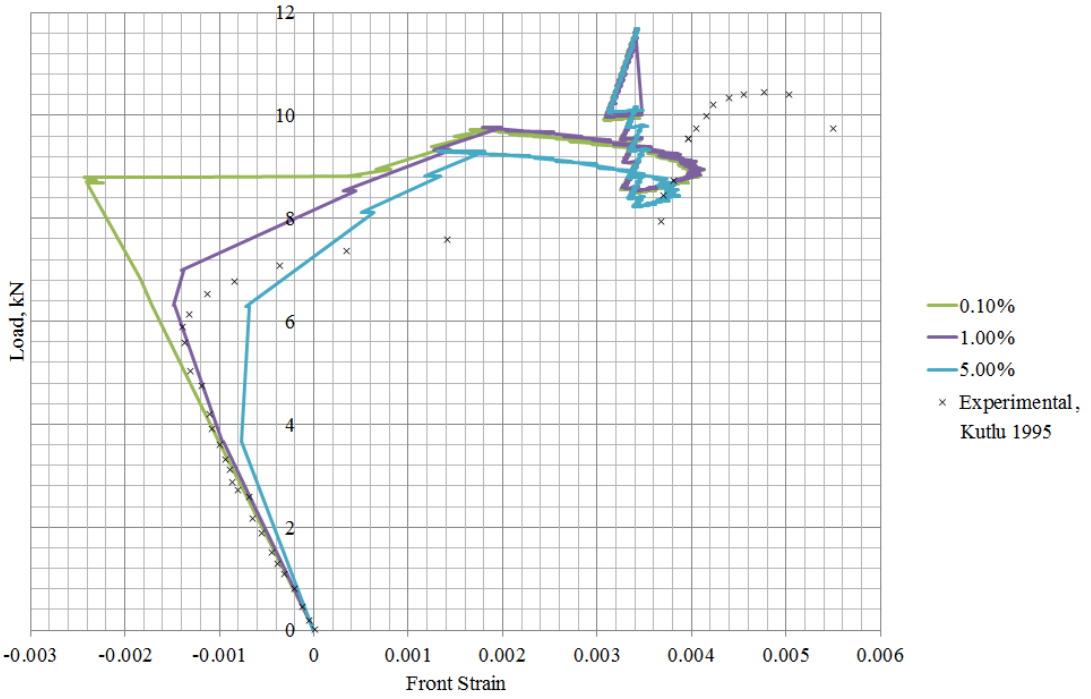

Figure 52: Buckling of Delaminated Coupons; Delaminated Ply Sensitivity to Sinusoidal Imperfections

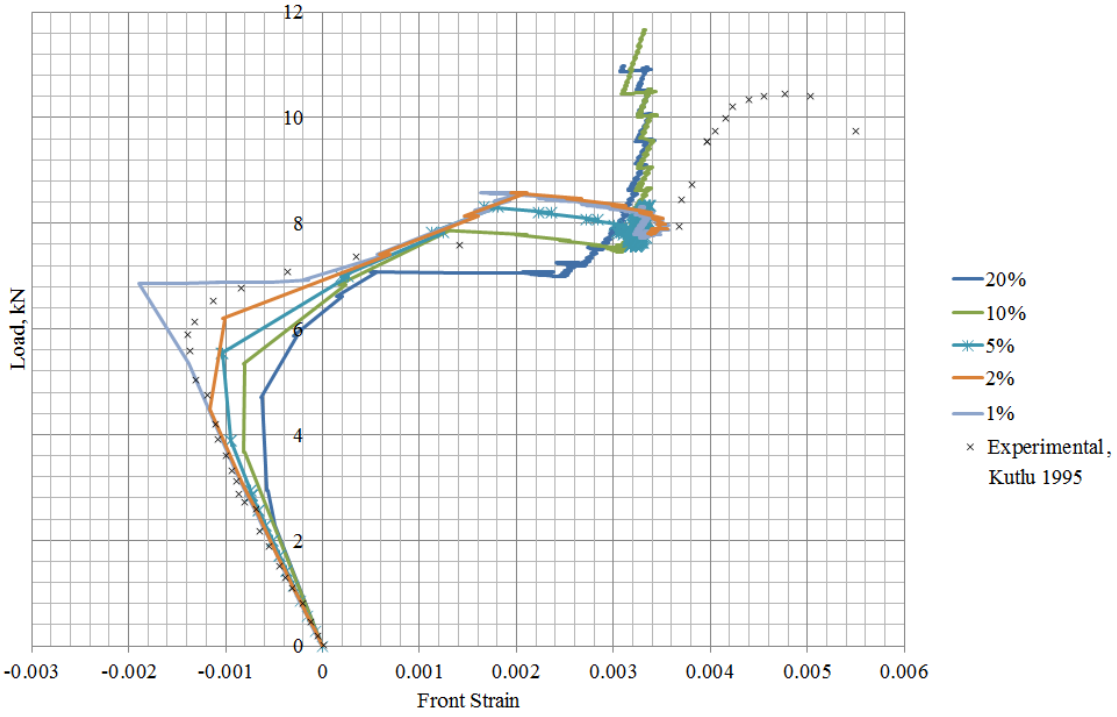

Figure 53: Buckling of Delaminated Coupons; Delaminated Ply Sensitivity to Indented Imperfections

A combined imperfection using a 0.1% global imperfection over the coupon and a constant indent of 2% or 0.01mm in the delamination zone is discussed with respect to the experimental results. The experimental results show that the test coupon initially buckles locally in the region of the delaminated layer and as the load increases the crack propagates in an unstable manner. Once the delamination approaches the clamped boundary the delamination growth ceases. The load is then increased in order to restart delamination growth and finally local failure develops near the clamped boundary due to local bending. The ultimate failure mode is fibre crushing near the clamped boundary induced by the global buckling mode.

Qualitatively the failure modes closely match those described by Kutlu and Chang [161] and are displayed in figure 55. The coupon compresses linearly prior to the buckling of the delaminated upper ply as shown in configuration A and B. Configurations C-E shows the unstable propagation of the crack, initiated by the buckling of the sublaminate, causing an increase in through thickness stress at the crack tip where the crack propagates under mixed mode driven crack propagation; $\frac{G_{II}}{G_T} = 0.8$. Once the crack reaches the clamped boundary the upper ply is fully delaminated and further load is sustained prior to the global buckling of the lower laminate as shown in configuration F. This global buckling instigates material failure in the region of the clamps, shown in configuration G, which leads to the ultimate collapse of the panel and failure of the center of the lower laminate, configuration H.

The load-strain responses shown in figures 54 show that up to a load of approximately 8kN the response of the model shows good correlation with the experimental results replicating the initial stiffness, buckling load of the delaminated ply and transition to the post-buckled state well. The front and back strains and load at which the crack begins to propagate is also captured well. However, the global buckled response and ultimate collapse is significantly over estimated by the model. This overestimation may be attributed to unrealistic boundary condition assumptions and imperfections or flaws within the material. The boundary is assumed to be ideally clamped whereas the experimental fittings are unlikely to restrict all rotations and would lead to higher deflection at the back of the laminate experimentally compared to the finite element model. Inclusion of imperfections or flaws within the material lead to areas of stress concentrations which may cause premature localised failure. This along with any asymmetry in the panel could lead to a reduction in the buckling load and ultimate failure.

4.4.3 Cohesive Model

The cohesive element method is compared. The cohesive element layer is modelled as 0.01mm thickness between two shell element plates using S8 quadratic elements. An imperfection is applied using a constant indent of 2% or 0.01mm in the delamination zone. A global imperfection is not assessed for this model due to the warping of the cohesive elements.

An initial model is created with a cohesive element length of 0.16mm and the cohesive zone length is measured at 0.43mm therefore giving the interface parameter as 0.92 and 0.26 for mode I and II respectively. A convergence study is conducted assessing the effect of the cohesive zone length which corresponds to the shell element size and the number of elements within the cohesive zone, Ne. The reported interface properties are used with a mesh size of 0.2mm to determine the cohesive zone length and an interface parameter of 0.5 which is estimated from the

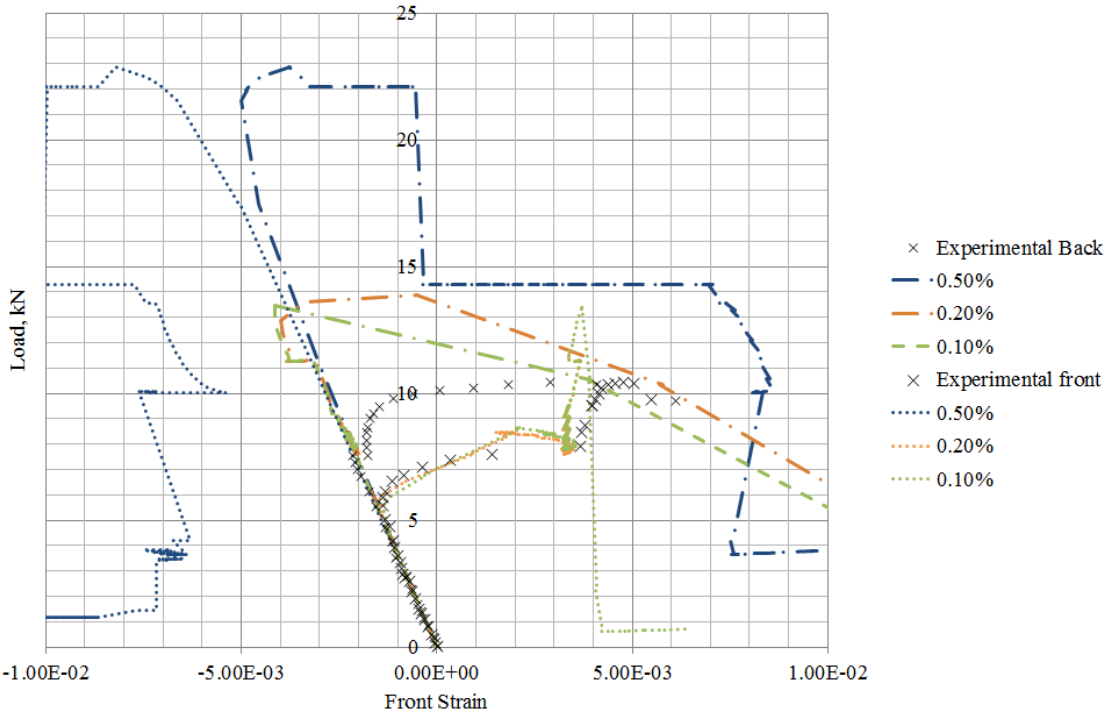

Figure 54: Buckling of Delaminated Coupons; Affect of Combined Imperfection on the Load Strain Response

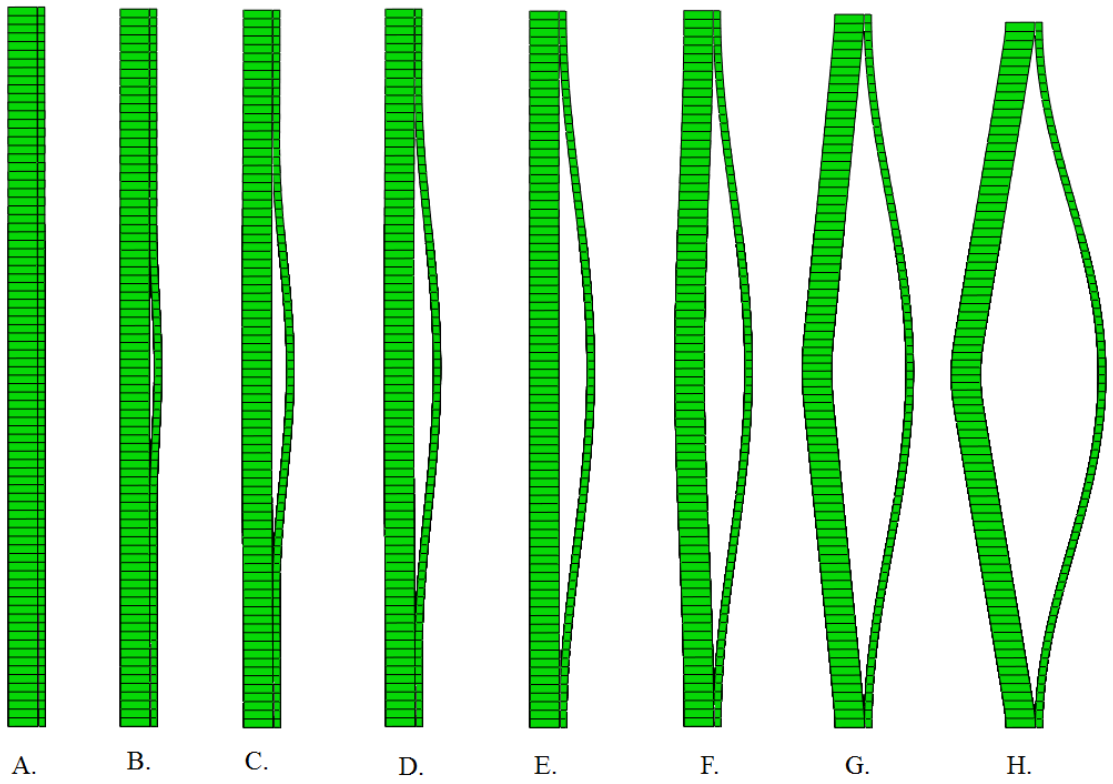

Figure 55: Buckling of Delaminated Coupons; Qualitative Failure Mode

Table 19: Cohesive Element Parameters

K_I=	938,217MPa$^+$
K_{II}=	9,722MPa$^+$
t_{OI}=	45MPa*
t_{OII}=	45MPa*

$^+$Calculated from Equation 12
* data from [168]

previous study. Figure 56 shows the strain response of the center of the plate on the upper and lower surfaces with increasing load. As the load strain response shows a number mechanisms the crack initiation and propagation point is used to assess the convergence for this case as the shell element sizes considered have been shown in the previous case to show convergence for the buckling response. Therefore the upper strain curves are discussed with respect to the change in stiffness during buckling as the strain moves from a compressive to tensile strain and significant crack propagation, which is shown by the steep increase in load from approximately 8kN with a relatively small increase in tensile strain. It is shown that the results become more conservative with a reduced cohesive zone length. Convergence of the initial stiffness, buckling load and during crack propagation is achieved for a cohesive zone size of 0.43mm as calculated. For all cohesive zone sizes there is good correlation with 2 and 3 elements in the cohesive zone for the initial stiffness, buckling point and during rapid crack propagation. However in the post-buckled response the initial crack propagation is affected by the number of elements in the cohesive zone where using 2 elements provides a non-conservative result. The model has converged for a cohesive zone size of 0.43mm and 3 elements within the cohesive zone.

The load strain curves for the front and back surfaces are compared to the experimental work and the previous VCCT method in figure 57 using a 2% imperfection. The front provides an improved match to the experimental data compared to the VCCT method. The initial stiffness is well matched by both models however the gradual change in strain during the upper plate buckling is more accurately captured by the cohesive model. This is due to the gradual change in stiffness of the cohesive elements prior to crack propagation which in this case may be realised as matrix cracking and build up of damage at the interface. In the post buckled state crack propagation occurs at lower loads for the experimental results and cohesive model compared to the VCCT model. The ultimate collapse is over estimated by both the VCCT and cohesive element models which may be due to a misrepresentation of the boundary conditions or premature failure of the back plate initiated by a material or geometric imperfection.

4.4.4 Comparison with Other Numerical Models

To further verify the model the results are compared to the numerical work of Liu et al. [164] and Zhang and Wang [165]. Liu et al. investigated the problem using a two dimensional in-plane finite element model similarly using the VCCT and nodal release method whereas Wang et al. used a layer wise B-spline finite strip method. These methods are compared to the current three dimensional shell element method for both VCCT and cohesive elements for the upper and lower laminate load-central deflection response in figure 59. The four models show reasonable overall correlation. The current shell models incorporate damage initiation and progression and this is illustrated

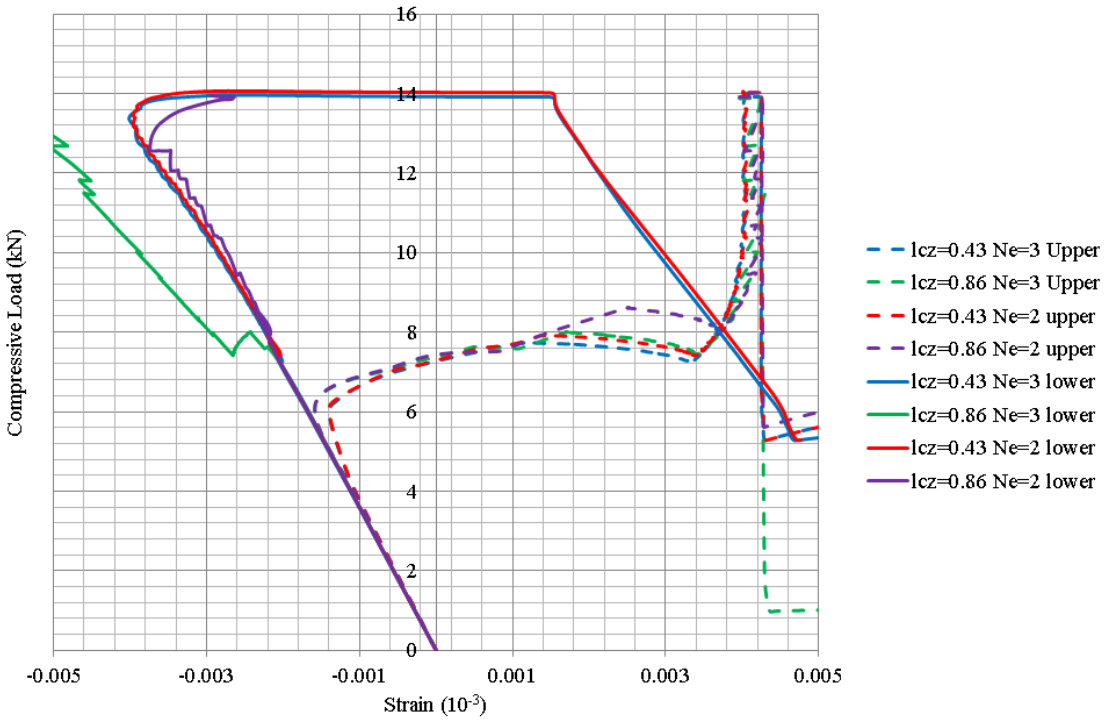

Figure 56: Buckling of Delaminated Coupons; Convergence of Cohesive Elements

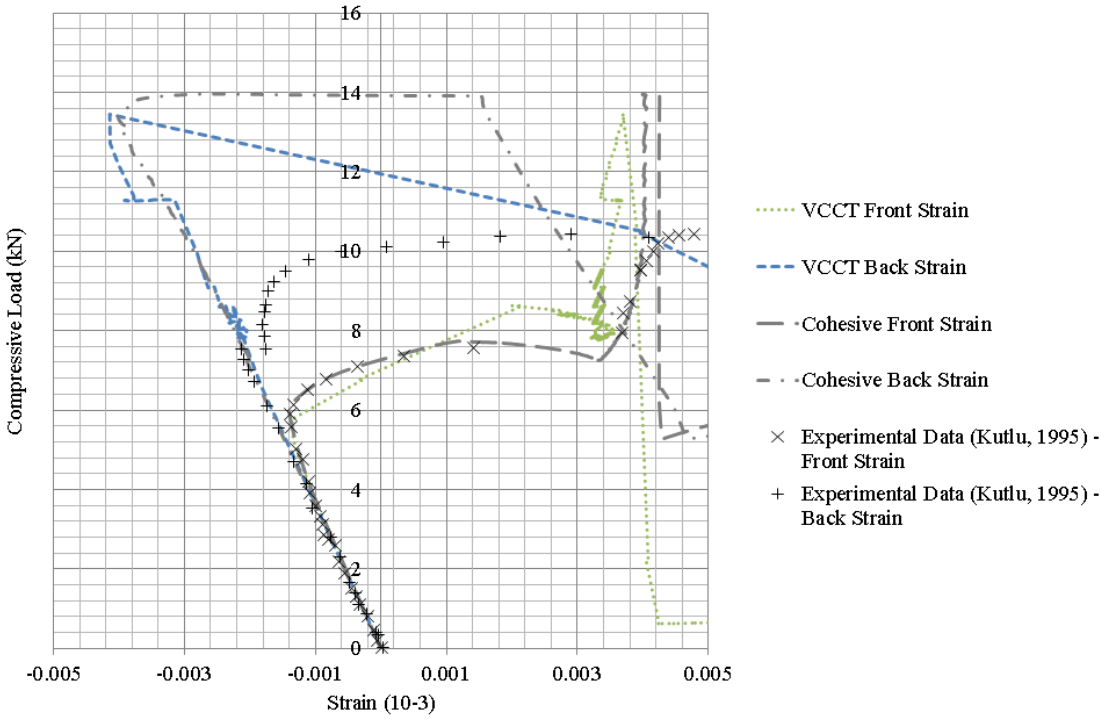

Figure 57: Buckling of Delaminated Coupons; Comparison of Modelling Technique

by the load drop during the global post-buckled response. The load-strain response shows the initial stiffness is well correlated, particularly between the 2D and shell finite element model. The 2D and VCCT shell finite element model provide a stiffer solution compared to the finite strip method. The buckling load is shown by a slight change in stiffness seen in the load-strain response shown in figure 58, for the VCCT model presented here this occurs around 7.2kN. The reduction in compressive load at a strain of approximately $2.5E^{-3}$ indicates the initiation of the unstable crack propagation which continues as the load increases to 12kN. The crack growth load deviates slightly between the current model and the finite strip and 2D finite element model which may be attributed to the mixed mode relationship used as the mixed mode data for this specific material is unavailable. Global buckling occurs around 12.8kN for the current model which is closely matched by the alternative models however, only the current model takes into account the damage progression leading to the ultimate collapse.

4.4.5 Summary

In this section the VCCT method and cohesive element model are assessed in their ability to follow combined crack propagation and buckling is verified against the experimental work of Kutlu and Chang [161] and the numerical work of Liu et al. [164] and Zhang and Wang [165]. Qualitatively the failure modes closely match those described by Kutlu and the initial stiffness, buckling load of the delaminated ply and transition to the post-buckled state are well captured by the model however, the global buckled response and ultimate collapse is significantly over estimated by the model. The sensitivity of the model to the imperfection shape and size is investigated comparing the first buckling mode generated from a linear eigenvalue analysis scaled by the upper laminate ply thickness, and a constant indent over the area of the Teflon layer as its thickness in this case is not insignificant when compared to the lamina thickness. It is shown that a constant indent of thickness approximately equal to half the Teflon thickness yields a close fit to the experimental results for the transition to the buckled mode. The effect of the global imperfection is investigated and is shown to improve the global buckling load however, the imperfection is shown to affect the failure mode and therefore not be representative of the experimental observations. The cohesive element model is shown to give an improved response in the buckled and post buckled response. It is assumed that matrix cracking during buckling and the early post-buckled response is present in the specimen and that the cohesive response is able to model it successfully. Compared to the numerical models of Liu et al. [164] and Zhang and Wang [165] the current three dimensional shell element method shows good overall correlation and therefore verifies the use of shell elements for modelling combined crack propagation and buckling problems. All four numerical models overestimate the global buckling load suggesting this overestimation may be attributed to unrealistic boundary condition assumptions and imperfections or flaws within the material.

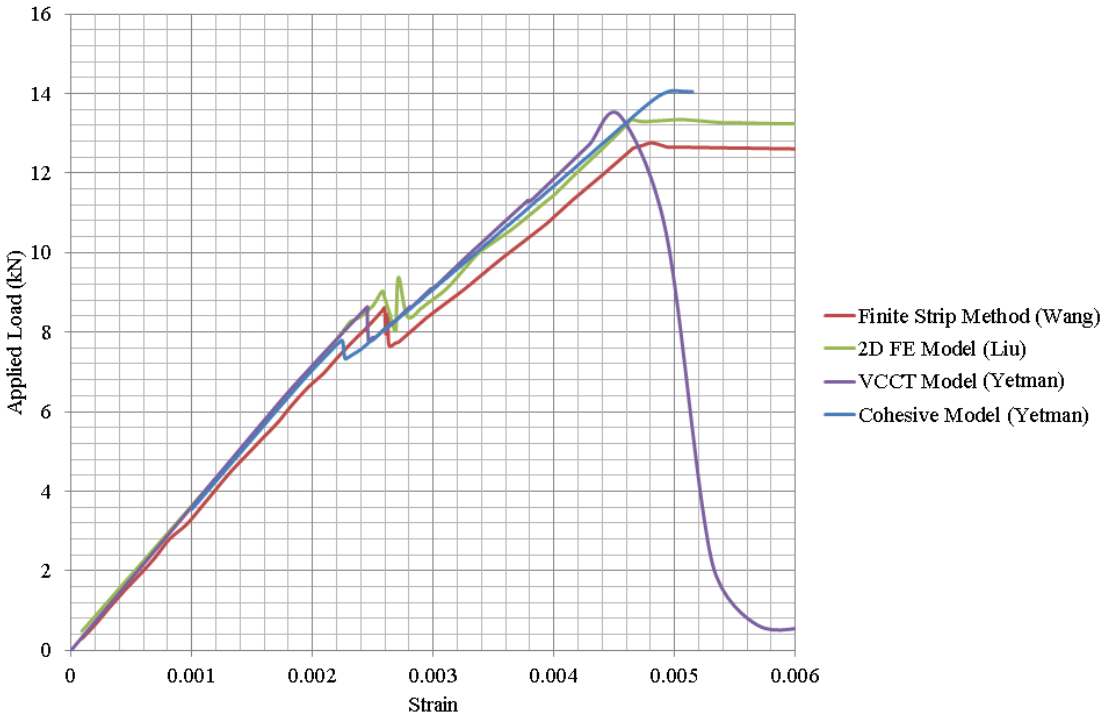

Figure 58: Load-Strain Response of Upper Ply

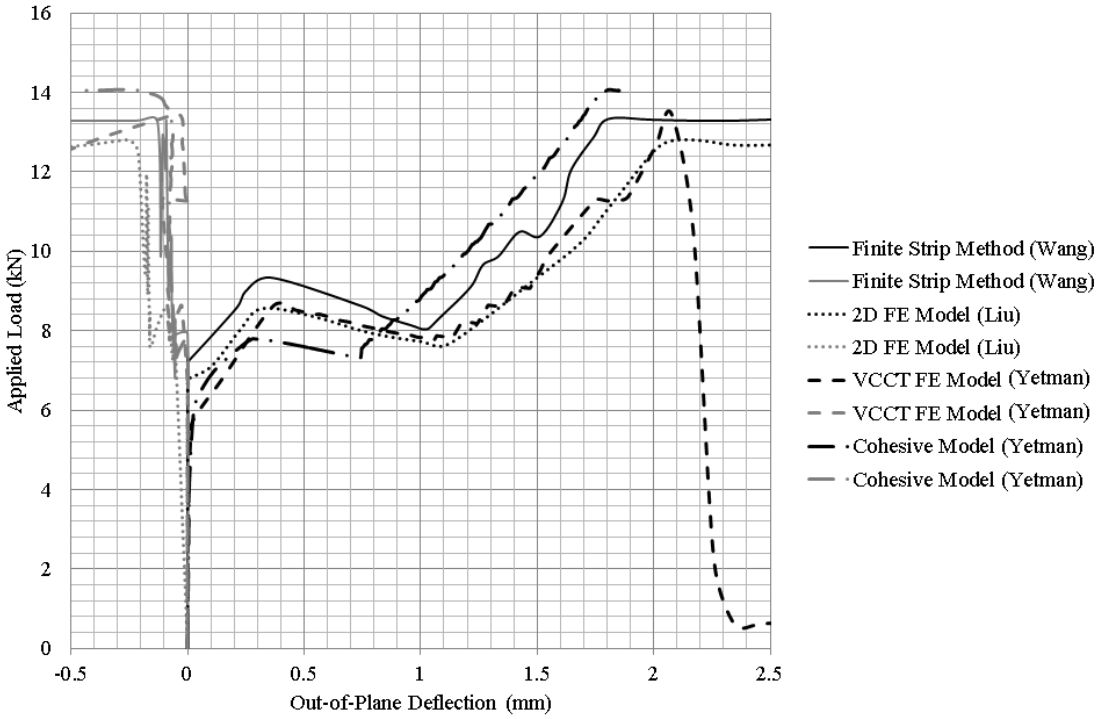

Figure 59: Load-Central Deflection Response of Upper Ply

4.5 Embedded Delaminations

The effect of embedded delamination is assessed using cohesive elements. Combined local and global buckling is assessed along with crack propagation. An assessment is made on the imperfection sensitivity and data is compared to the experimental work of Riccio and Pietropaoli [106]

Riccio and Pietropaoli [106] studied flat rectangular plates with embedded circular delaminations subjected to in-plane compressive loading. Specimens were fabricated from carbon epoxy, HTA/6373C, with material properties quoted by Riccio as shown in table 20. The plates are a 35 ply laminate of total thickness 4.55mm with the stacking sequence $[90/(0/90)_{17}]$ delaminations are inserted between the 90/0 plies at a depth of 3, 5 and 7 plies from the upper surface for panels A3, A5, and A7 respectively. The panels are held in a support fixture which clamps the longitudinal ends whilst the unloaded edges remain unsupported, as shown in figure 60.

Table 20: Buckling of Rectangular Plates; Lamina Properties

(a) Elastic Properties

E_{11}	146000MPa^{+}
$E_{22} = E_{33}$	10500MPa^{+}
$G_{12} = G_{13}$	5250MPa^{+}
G_{23}	3480MPa^{+}
$\nu_{12} = \nu_{13}$	0.30^{+}
ν_{23}	0.51^{+}

(b) Strength Parameters

S_{11T}	1730MPa^{+}
S_{11C}	1379MPa^{+}
S_{22T}	66MPa^{+}
S_{22C}	268MPa^{+}
S_{12T}	134MPa^{+}
S_{12C}	134MPa^{+}

(c) Fracture Criterion

G_{IC}	$0.20kJ/m^{2+}$
G_{IIC}	$0.57kJ/m^{2+}$
η_{BK}	2$^{\circledast}$
$t_{OI}=$	30MPa *
$t_{OII}=$	30MPa*

$^{\circledast}$Data from Benzeggagh and Kenane [69] for composite materials
$^{+}$Data from Kutlu and Chang [161]
* Data from Turon et al. [168]

A quarter model configuration is modelled with symmetry boundary conditions on the interior edges. The loaded edge is modelled using clamped conditions and the clamped plate held in the support fixtures is modelled restraining the out-of-plane displacement. The panel is modelled using the plane stress formulation, neglecting the through thickness stresses and is discritised with 4-node shell elements (Abaqus S4). A non-linear finite element model is used with the Newton-Raphson method and an automatic incrementation scheme. For the initial imperfection the mode shape is taken as the first buckling mode generated from a linear eigenvalue analysis and is scaled so the maximum out-of-plane displacement is a percentage of the upper lamina thickness. The first buckled mode shape is chosen as in this case the assumed Teflon insert thickness is small compared to the upper laminate ply thickness, 0.6%. The viscous parameter for the damage evolution parameter is initially chosen as 1E-6 using automatic time incrementation. The crack propagation is modelled using cohesive elements of 0.01mm thick and tied to the upper and lower plies. The UMAT progressive damage model using the combined conservative model is incorporated to capture the progression of damage. As the mixed mode crack propagation data is not given by the authors the Benzeggagh-Kenane exponent is chosen as 2.0 which represents a typical exponent for composite materials[69].

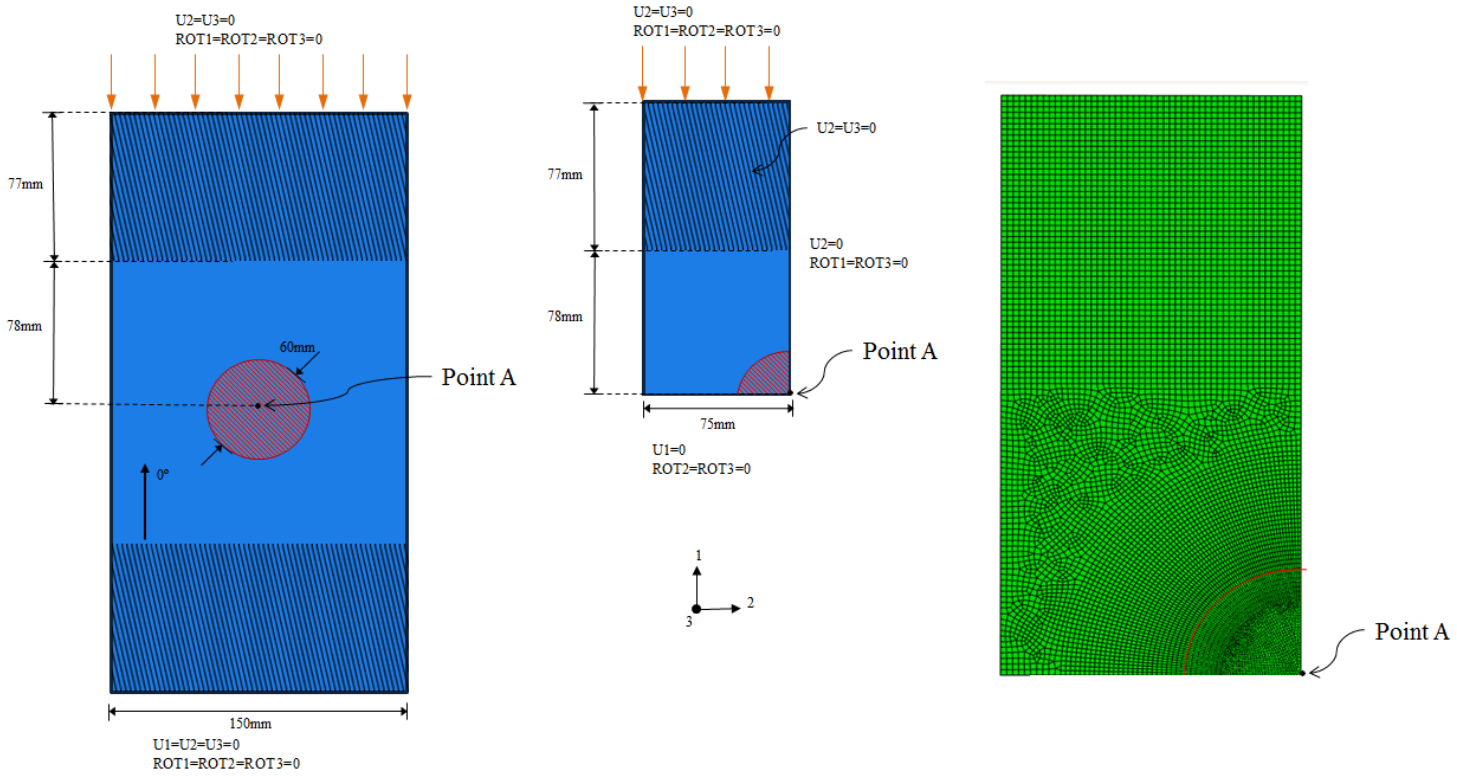

Figure 60: Embedded Delaminations; Model Configuration

The model mesh is shown in figure 60 ensuring the element size is uniform in the crack direction where the edge of the delamination zone is shown in red. An initial model is run with a cohesive element size of 0.2mm using the interfacial stiffness in table 20 and the cohesive zone length is measured as 0.58mm giving an interface parameter of 0.55 and 0.69 for the mode I and mode II data respectively.

A convergence study is conducted comparing the effect of increasing the shell element size, using Turon's relationship to calculated the interface strength and including 3 cohesive elements within the cohesive zone length whilst maintaining the general element distribution as shown in figure 60. For this study panel A3 is modelled and the initial imperfection is chosen so the maximum out-of-plane imperfection is 10% of the upper lamina thickness, 0.04mm. The out-of-plane displacements of the upper laminate at the center of the delaminated zone, illustrated as point A in figure 60, are compared for three mesh densities against applied load graphs in figure 61. It is shown that the mesh has converged for a shell element size of 3mm which corresponds to a cohesive element size of 1mm which is used in the rest of this study

The effect of the imperfection size is also investigated for the low load response in figure 62. The first buckling mode of the delaminated plate is scaled so the maximum out-of-plane imperfection is varied between 0.05mm and 0.1mm and are compared to the experimental results. It is shown that the imperfection affects the initiation of buckling of the delaminated ply with the increase in the out-of-plane displacement occurring at lower load for larger imperfections. The imperfection also has an effect on the deformation of the outer ply at increased load with the out-of-plane deformation reduces for increasing applied imperfections. The panel is modelled for a nominal imperfection where a maximum out-of-plane imperfection of 0.05mm is shown to have converged for the out-of plane deflection and the buckled load is converging imperfection of 0.05mm 50% leads to significant alteration of the laminate stiffness and displays a linear increase in the out-of-plane displacement showing no switch to a buckled configuration.

The results for the three panels are compared to the experimental results in figure 63. It is shown that reasonable correlation is achieved for the global buckling load and out-of-plane displacement of both the upper and lower plies. The local buckling point is reasonably well estimated for the three cases with the most error on panel A3. The local buckling load is dependent on the Teflon insert and any local imperfections in the panel and therefore the model provides reasonably good correlation. The post buckled response is well approximated given the offset in the initiation of local buckling. The global buckling loads are similar for each of the three panels both experimentally and numerically. This could be due to assumptions in the boundary conditions or the global imperfection of the plate. For each case delamination growth initiates at the center of the panel, on the symmetry line and propagates perpendicular to the loading direction, as reported by Riccio and Pietropaoli [106]. The crack propagates under mixed mode loading initially by a ratio of $\frac{G_{II}}{G_I+G_{II}} = 0.51$.

The models ability to follow the progressive collapse of an embedded delamination is verified against the experimental work of Riccio and Pietropaoli [106] using flat rectangular plates with embedded circular delaminations subjected to in-plane compressive loading. The effect of the imperfection size is investigated for the low load response. A minimum of 10% imperfection is required to initiate the post-buckled response which most closely matches

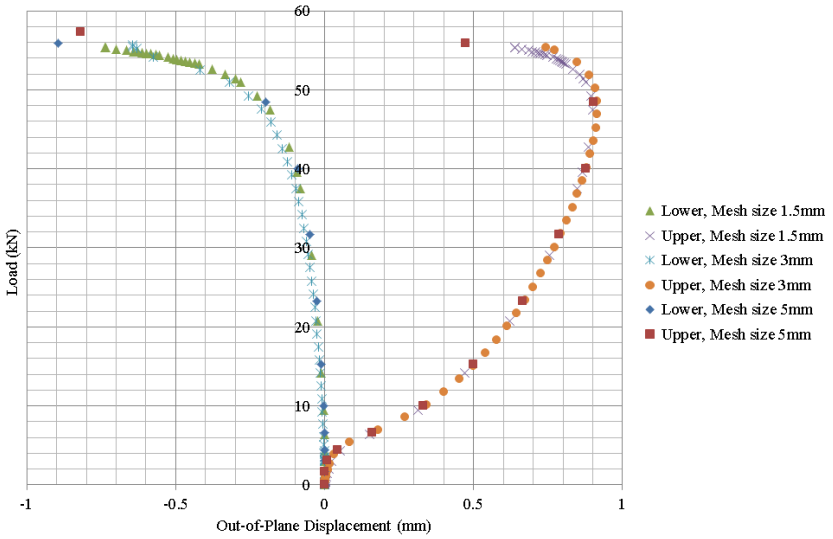

Figure 61: Embedded Delaminations; Mesh Convergence

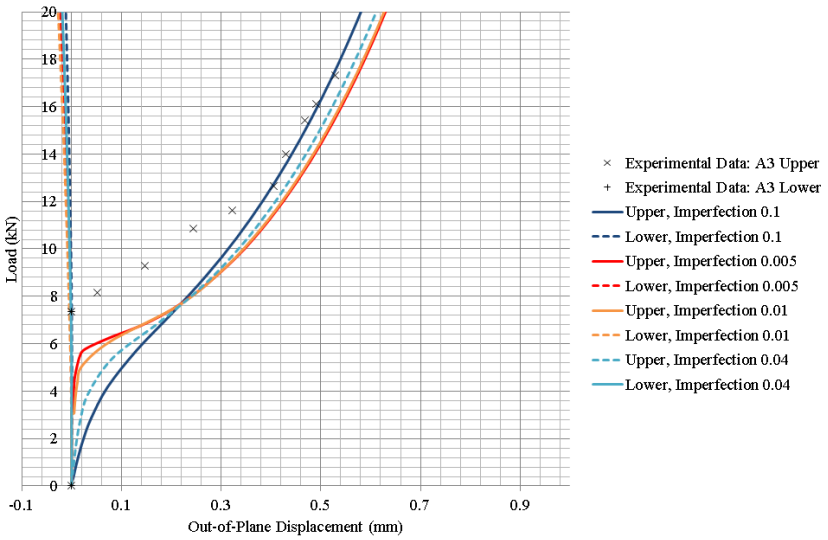

Figure 62: Embedded Delaminations; Imperfection Analysis

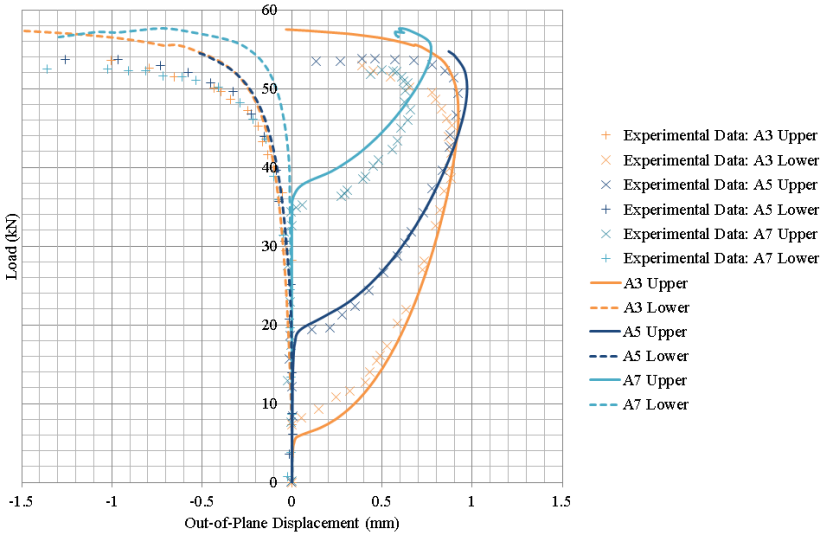

Figure 63: Embedded Delaminations; Comparison of Load-Deflection Response against Out-of-Plane Displacement and Experimental Data

the experimental results at low load. The local buckling load, post buckled response and the global buckling loads are predicted well and crack propagation is as described by the author.

4.6 Damage Evolution of Top-hat Stiffened Panel

In this section debond initiation is assessed for a top-hat stiffened panel which buckles under in-plane load. An imperfection sensitivity is conducted comparing nominal and realistic imperfections, as measured.

Smith and Dow [122] conducted tests on a large-scale, longitudinally and transversely top-hat stiffened panel representing a MCMV deck structure. The panel failed predominantly by stiffener debonding leading to catastrophic failure and is used to verify the global local methodology as discussed in section 3.4.

The ends and sides of the panel were reinforced by discontinuous steel pads bonded and bolted to the GRP. The test arrangement is illustrated in figure 64 and the dimensions of the longitudinal stiffener are given in figure 65. The structure is manufactured from glass polyester woven roving; the lamina properties given by Smith and Dow are given for the shell laminate, web and table of the longitudinals in table 21. The critical strain energy release rates are taken from experimental tests reported in academic literature Swift [169] and Morais and Silva [170]. In this case the Benzeggagh-Kenane criterion is used where the mixed mode parameter is taken as 1.5 which in the absence of mixed mode data is approximated from similar GRP materials.

The test results, as described by Smith and Dow [122], show that no significant deformations were observed up to a compressive stress of $40N/mm^2$ where the local buckling of the deck was observed. No observable damage, permanent distortion or loss of stiffness occurred until an average compressive stress of $50N/mm^2$. At this load cracking noises and whitening under the flange of the longitudinal stiffeners where recorded as the load increased. Final failure was sudden and explosive at $59.5N/mm^2$ as the entire cross section of the panel fractured about the mid-plane.

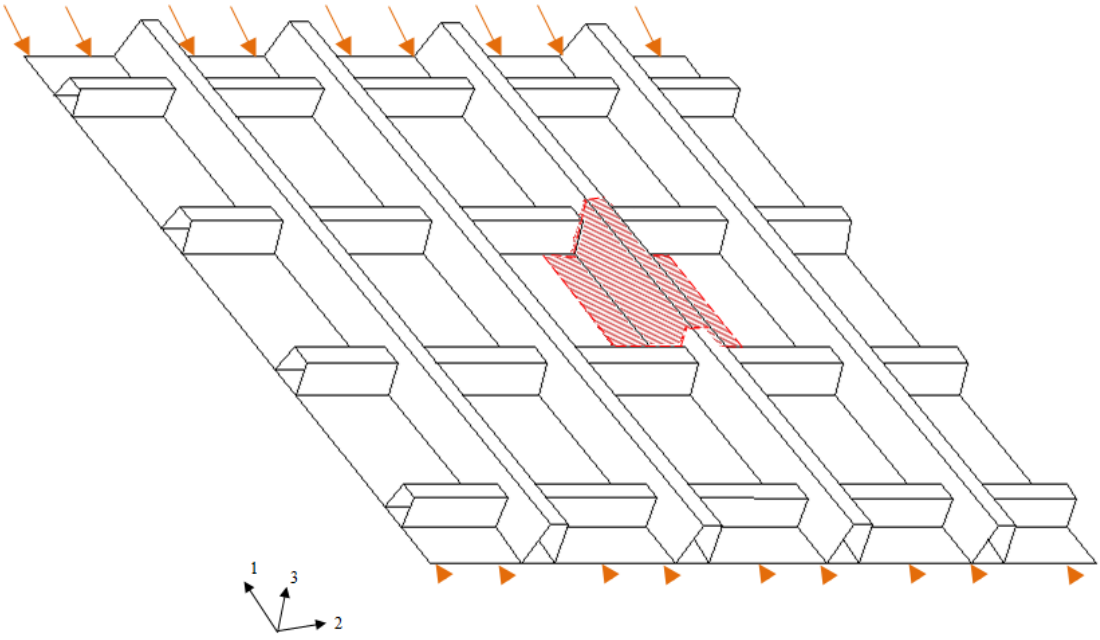

Figure 64: Damage Evolution in Top-hat Stiffened Plates; Test Configuration

Table 21: Damage Evolution in Top-hat Stiffened Plates; Lamina Properties

(a) Shell Laminate Material Properties[1]

E_{11}	15700MPa
$E_{22} = E3_3$	14800MPa
G_{12}	3400MPa
ν_{12}	0.120
$\nu_{13} = \nu_{23}$	0.127
S_{11T}	238MPa
S_{11C}	204MPa
S_{22T}	210MPa
S_{22C}	224MPa
$S_{12T} = S_{12C}$	277MPa

(b) Stiffener Table Laminate Material Properties [1]

E_1	21000MPa
$E_2 = E_3$	13800MPa
G_{12}	3400MPa
ν_{12}	0.100
$\nu_{13} = \nu_{23}$	0.152
X_T	238MPa
X_C	204MPa
Y_T	210MPa
Y_C	224MPa
$S_T = S_C$	277MPa

E_1	16600MPa
$E_2 = E_3$	15200MPa
G_{12}	3400MPa
ν_{12}	0.120
$\nu_{13} = \nu_{23}$	0.131
X_T	238MPa
X_C	204MPa
Y_T	210MPa
Y_C	224MPa
$S_T = S_C$	277MPa

(c) Stiffener Web and Flange Laminate Properties [1]

X_T	28MPa [2]
S_T	6MPa [2]
G_{IC}	$0.5kJ/m^2$ [3]
G_{IIC}	$2.0kJ/m^2$ [4]
η_{BK}	1.5[5]

(d) Interface Properties

[1]Smith and Dow [122], [2]Green and Bowyer [171], [3]Swift [169], [4]Morais and Silva [170],[4]Estimated from the literature

The panel is modelled as a single half length top-hat stiffener between transverse stiffeners in the central region of the panel, as shown in figure 64. Symmetric boundary conditions along the central plane and plate edges replicate the symmetry of the grillage structure and a clamped boundary condition is applied at the connection between stiffeners. The model is created using the methodology outlined in 3.4 and is meshed using 4-node shell elements (S4) and 3 cohesive elements within the cohesive zone length.

The sensitivity of the model to the magnitude of the imperfection is investigated for the model omitting crack propagation. Figure 66 shows the effect of the maximum magnitude of the imperfection compared to the experimental data for the applied load against the maximum out-of-plane deflection. It can be seen that an imperfection of 7.8mm (50% of the plate thickness) gives a significant alteration in the stiffness of the panel and does not buckle within the range displayed. Imperfections of 1.57mm (10% of the plate thickness) and 0.79mm (5% of the plate thickness) show a moderate agreement with the experimental data. Smith and Dow reported a measured local distortion of 1.5mm which agrees well with the findings of the imperfection sensitivity. For future models an imperfection of 10% is used.

A convergence study is conducted by reducing the shell element size where the the maximum out-of-plane deflection against applied load is compared and shown in figure 67. The cohesive zone length is measured for the

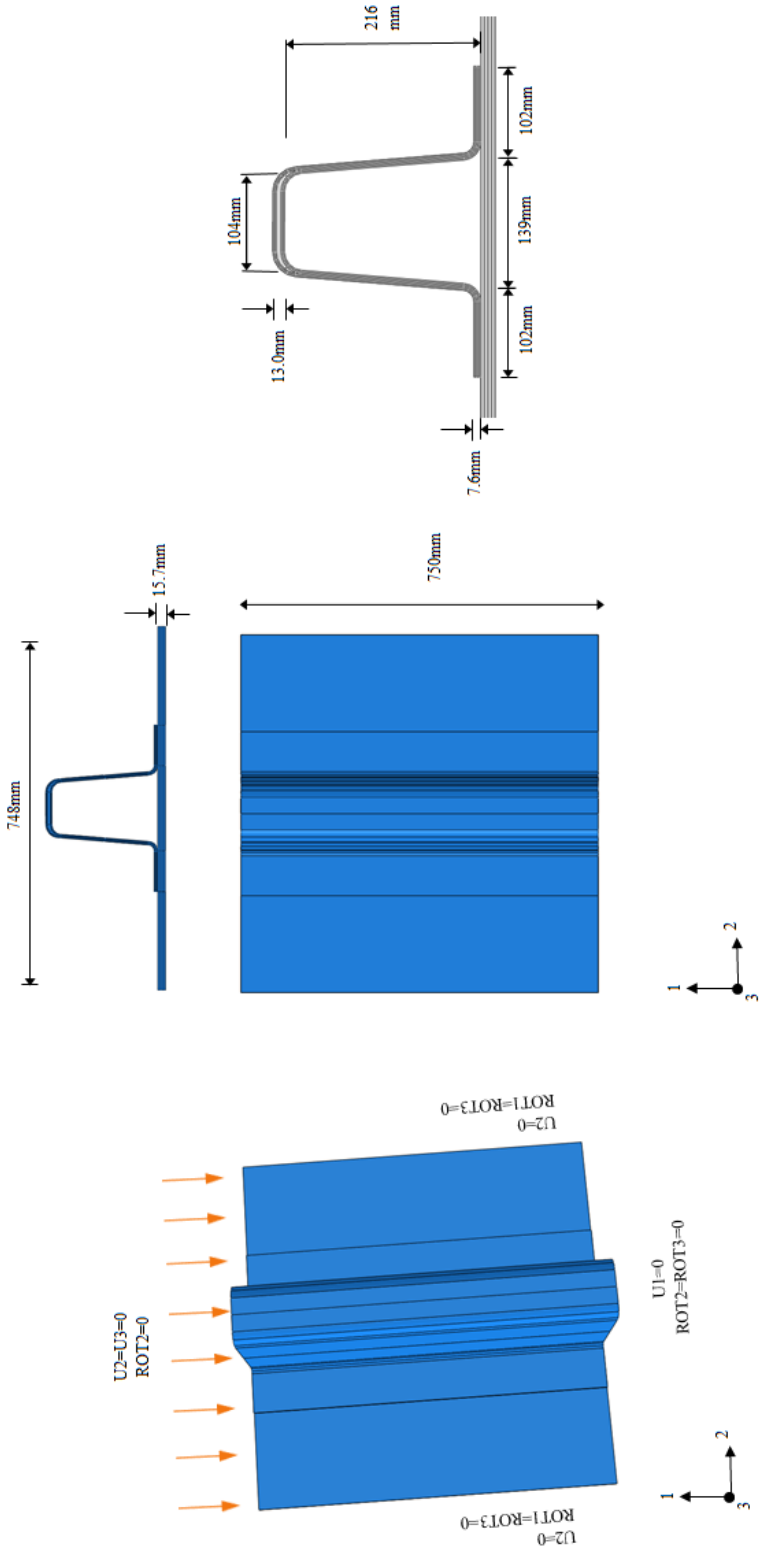

Figure 65: Damage Evolution in Top-hat Stiffened Plates; Model Configuration

smallest case at 5.9mm giving interface parameters of 0.6 and 0.01 respectively for mode I and mode II. The data is also compared to the experimental data reported by Smith and Dow [122]. The model is shown to converge for a shell element size of 5mm with a converged load deflection response and a 1% change in the ultimate load for a reduction in element size to 2mm.

Smith recorded the local buckling at a stress of $40N/mm^2$, or 740kN for the stiffener section modelled. The model captures the plate deformation moderately well as the plate buckles into three half sine waves with a negative deflection in the center of the plate, however the onset of buckling is gradual and therefore difficult to identify numerically. In the numerical model the grillage structure is modelled as a clamped plate. As the stiffener ends are constrained by transverse stiffeners the clamped condition will be overly constrained compared to the true boundary conditions allowing no rotation on the stiffener or plate at the fixed ends. It is assumed that a more accurate representation of the boundary conditions would result in a closer match to the experimental results in the buckled and post-buckled response.

Following the buckling load the model predicts no material failure prior to delamination initiation. At $50N/mm^2$ or 920kN Smith recorded cracking noises and whitening under the flange of the longitudinal stiffeners, and Smith recorded final failure as sudden and explosive at $59.5N/mm^2$ or 1090kN as the entire cross section of the panel fractured about the mid-plane. The cohesive element shows that the failure criterion initiates at a load of 62kN and the stiffness of the cohesive element is reduced by 95% at a load of 886kN and to 98% at a load of 1.1MN which is comparable to Smith's observations. However, the model predicts crack growth initiating at the center of the plate at the negative inflection point and progressing along the flange-plate interface which gradually reduces the load carrying capability whereas Smith et al. observed a residual capability following delamination propagation. This could be attributed to the boundary condition assumption or due to an assumption made in the material properties which are taken from multiple sources.

The damage progression in top-hat stiffened composite structures is used to verify the cohesive element methodology monitoring delamination initiation and propagation in a post-buckled structure against full scale tests conducted by Smith and Dow [122] on a MCMV deck structure. Qualitatively the failure modes closely match those described by Smith et al. and the initial stiffness, buckling load and plate deformation are reasonably captured by the model given the boundary condition assumptions. However the sensitivity to the initial imperfection is again highlighted although use of a measured imperfection is shown to aid modelling. The delamination initiation is well predicted however final failure and crack propagation could be improved with more accurate material properties and boundary assumptions.

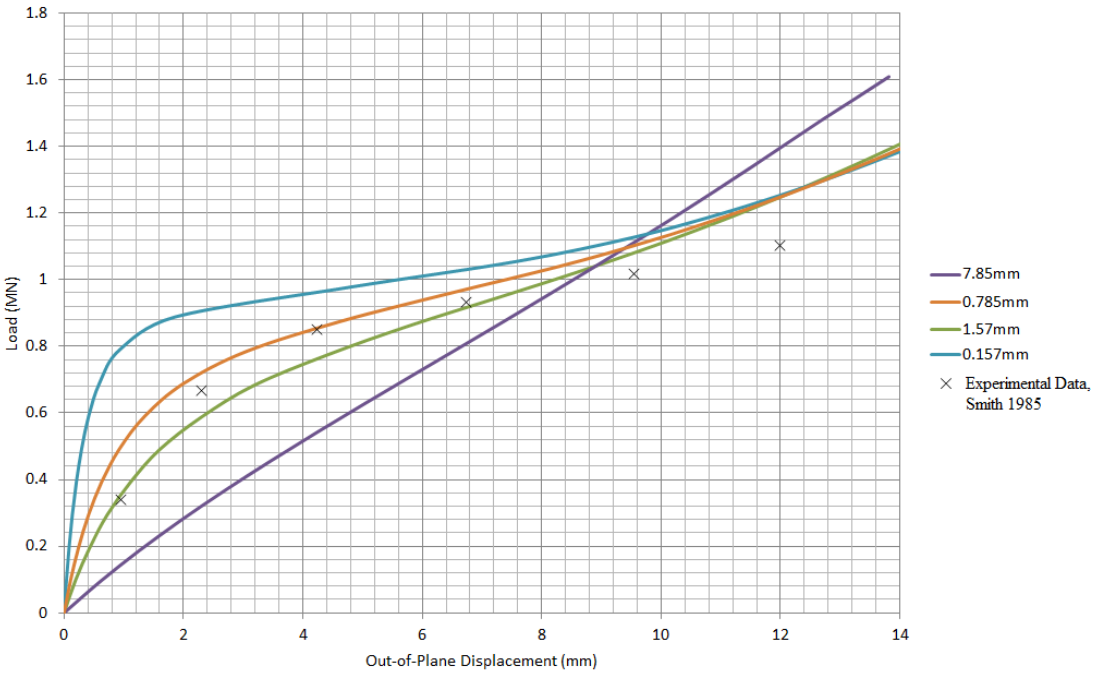

Figure 66: Damage Evolution in Top-hat Stiffened Plates; Imperfection Sensitivity

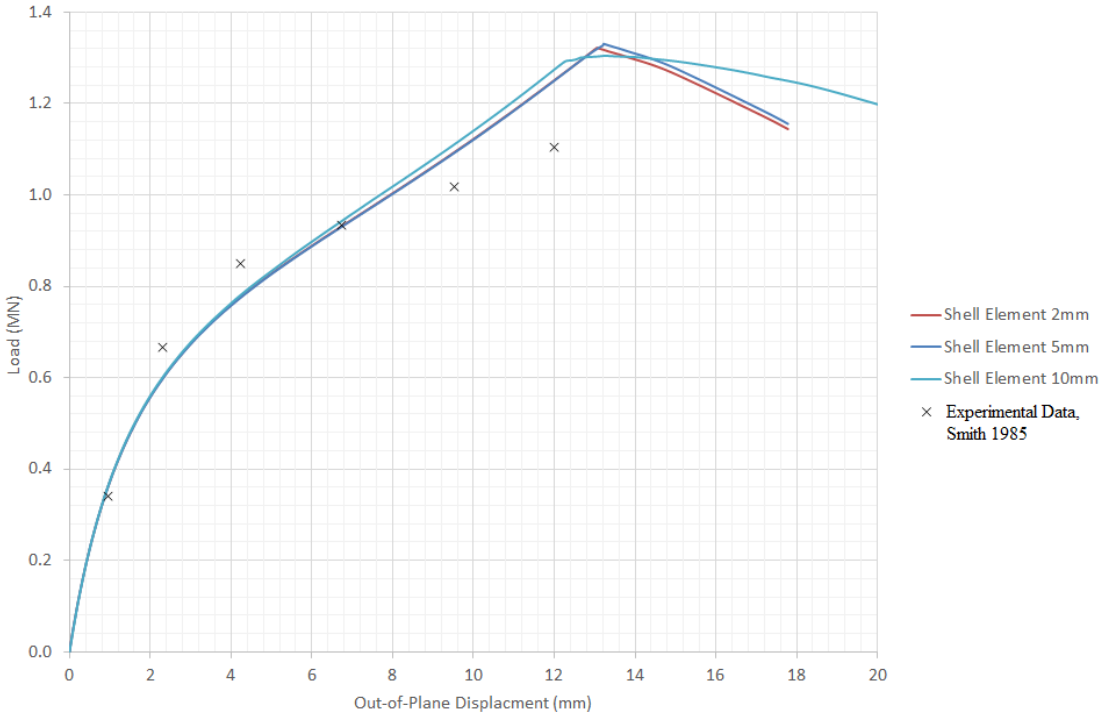

Figure 67: Damage Evolution in Top-hat Stiffened Plates; Convergence of Out-of-plane Displacement

4.7 Damage Tolerance Model Verification

In this section the reference panel, model and debond cases discussed in section 3.4 are verified. A mesh convergence study is conducted using both the VCCT and cohesive element method and both methods are compared to determine the most suitable methodology. An initial study is conducted to assess the effect of the imperfection on the model and determine the nominal and forced imperfection cases to be studied.

4.7.1 Convergence of VCCT Method

Convergence of the VCCT model is assessed using a number of damaged cases. Linear 4-noded shell elements, S4, are used for the VCCT technique. For larger debonds, greater than 13% of the panel length, the analysis has converged for a mesh size of 10mm corresponding to 560 elements in the debond area, as shown in figure 68. For smaller debonds, less than 13% of the panel length, a more refined mesh is required to capture buckling of the debonded flange, the radial nature of crack growth and clarity of the crack front. An element size of 5mm is chosen, equivalent to 2250 elements in the debond area as a compromise between efficiency and accuracy; the solution has converged to within 5% change in ultimate load and crack propagation load as shown in figure 69.

4.7.2 Convergence of full cohesive model

Table 22: Cohesive Element Properties

Parameter	Symbol	Value
Initial Normal Interfacial Stiffness	K_I	178000MPa
Initial In Plane Interfacial Stiffness	K_{II}	14910MPa
Element Thickness	T	0.01mm
Interface Strength	T_{0I}	17.6MPa
Interface Strength	T_{0II}	23.2MPa

For this model the cohesive elements are positioned between the stiffener flange and plate with an element thickness in the z direction of 0.01mm. The initial interfacial stiffness, interface strength and element thickness for mode I and mode II are given in table 22. Turon's method as verified in section 4.3 is used with assumed parameters determined for composite materials. In the absence of validating data the cohesive zone length is assumed to be 1mm and an interface parameter of 1.0 is used as recommended by Hillerborg et al. [94]. The outer shell element is set at the length of the cohesive zone length and the interface strength is established by Turon's relationship for each mesh size. To ensure convergence is achieved for crack initiation and propagation the convergence of the damaged case is assessed for a central debond of 350mm. The effect of decreasing mesh size on the ultimate load, damage initiation load, crack initiation load and buckling load is assessed for 2 and 3 elements within the characteristic length and illustrated in figure 70. Convergence is achieved for the damage initiation and buckling load for a shell size of 5mm or less. The ultimate load is shown to be converging and shows a 1.8% reduction from a shell element size of 5mm to 2.5mm. The crack initiation load shows more variation as the shell element size and therefore cohesive element size reduces. This variation is partly due to the measure used to determine the load at which the

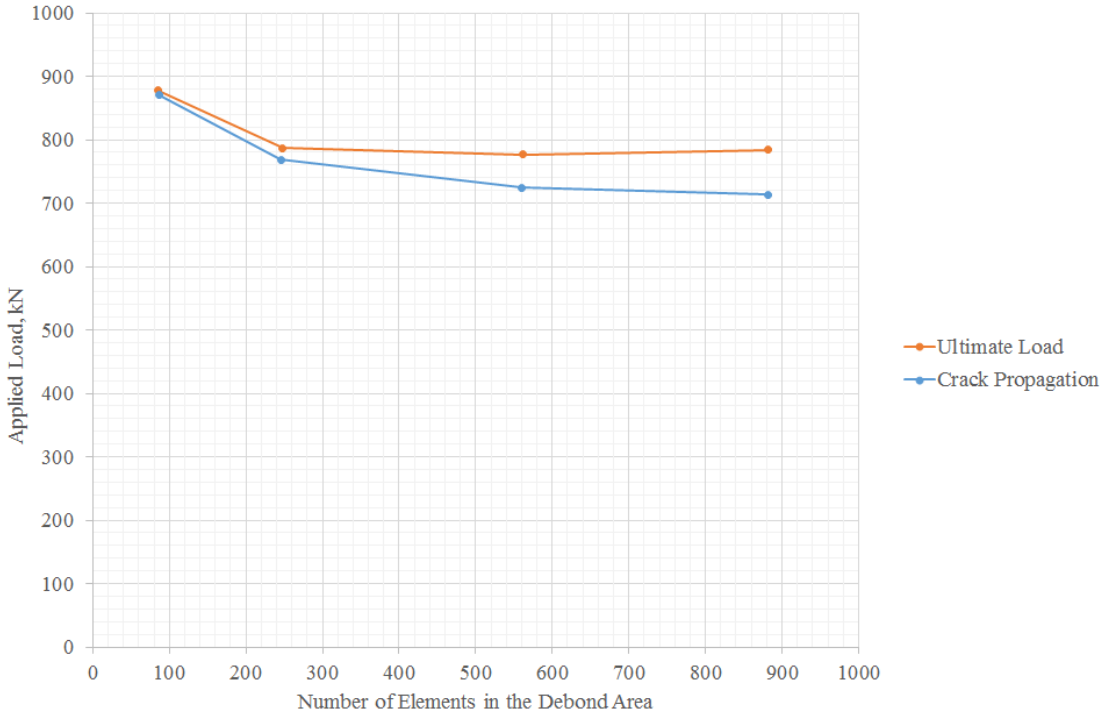

Figure 68: Mesh Convergence: 20% Debond Size

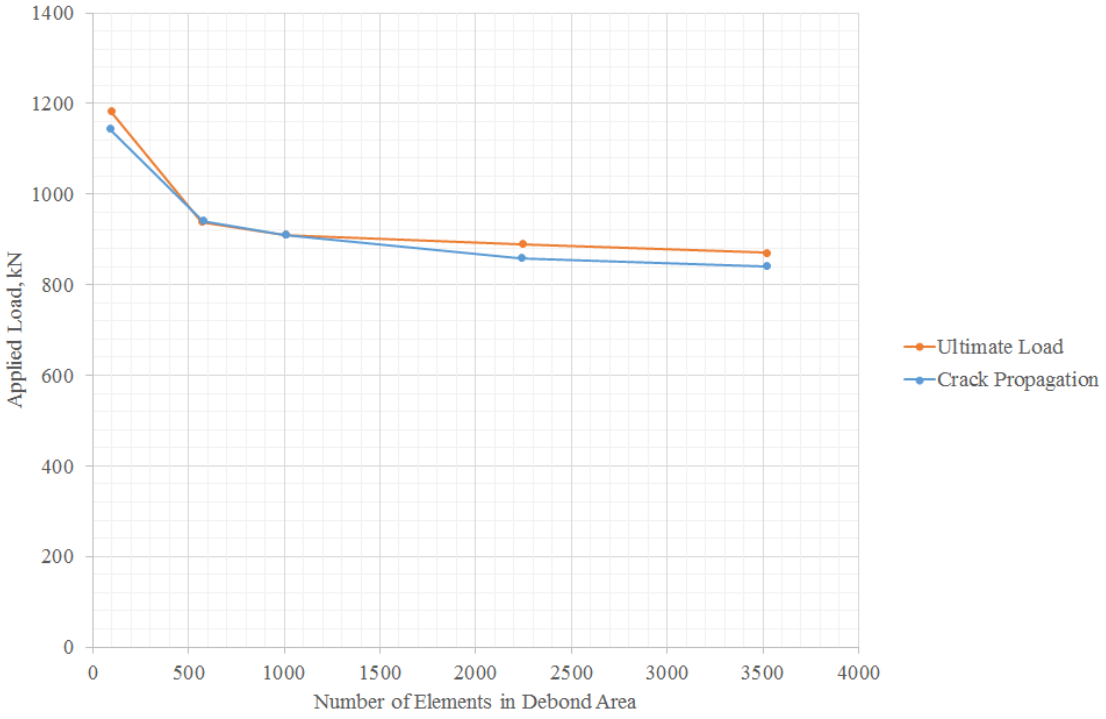

Figure 69: Mesh Convergence: 13% Debond Size

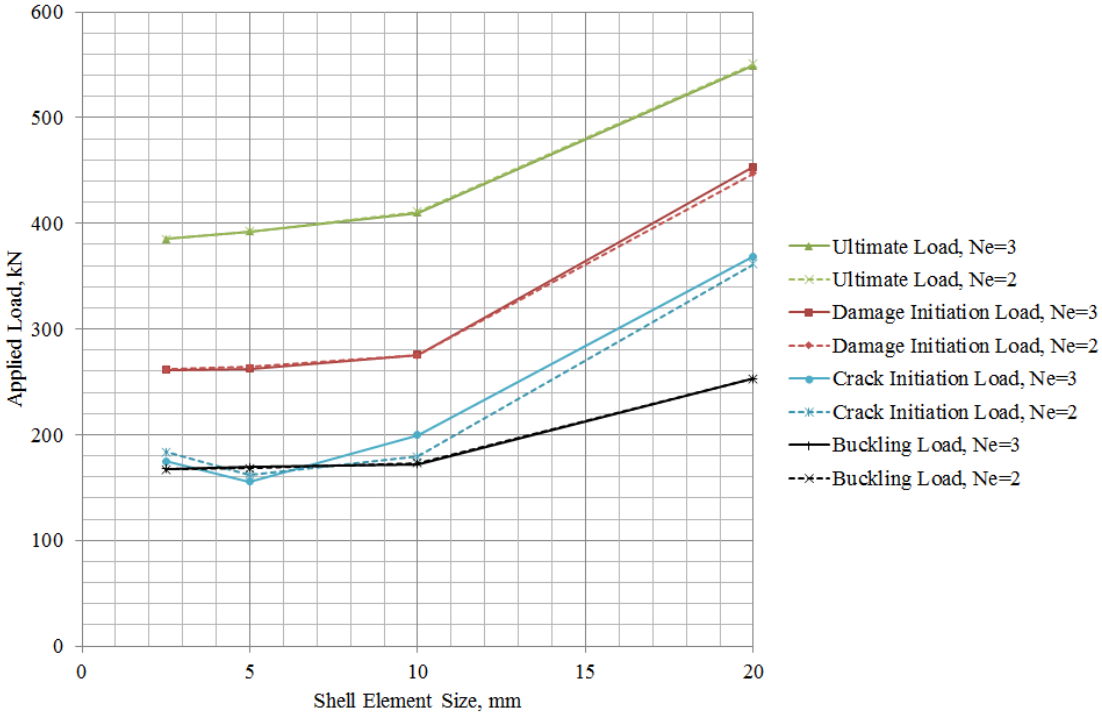

Figure 70: Convergence of 350mm Central Damage Tolerance Model

crack initiates; the load at which a single element reaches 99% degradation in stiffness. As the element size reduces, the area of the element over which the loading must be sufficient to initiate crack growth and therefore the load required also reduces. As the inside edge of the flange represents a stress concentration in this case it is unlikely that this measure would truly converge.

Therefore the degradation of the critical cohesive element, positioned at the inner flange corner, is compared for decreasing element size and for 2 and 3 elements within the cohesive zone in figure 71. From these curves the apparent increase in the crack initiation load from shell element size of 5mm to 2.5mm is due to the more gradual increase of the degradation factor between 0.95 and 1. The convergence of the crack initiation is apparent from these curves when considering the end shortening displacement at which the degradation factor approaches 1. Good convergence is seen from 5mm to 2.5mm for both 2 and 3 elements in the cohesive zone. Therefore the solution is judged to have suitably converged for an element size of 5mm with 2 cohesive elements within the cohesive zone. This shell element size is also shown in the previous convergence case to suitably account for the post-buckled response of the smallest damage size considered here.

4.7.3 Discussion of method

Figure 72 shows the end shortening curves for the intact case, 100mm and 300mm central debond cases for configuration A comparing the VCCT method and cohesive element method using a forced imperfection represents 10% of the plate thickness. It is shown that the stiffness and buckling load are the same for both methods. The

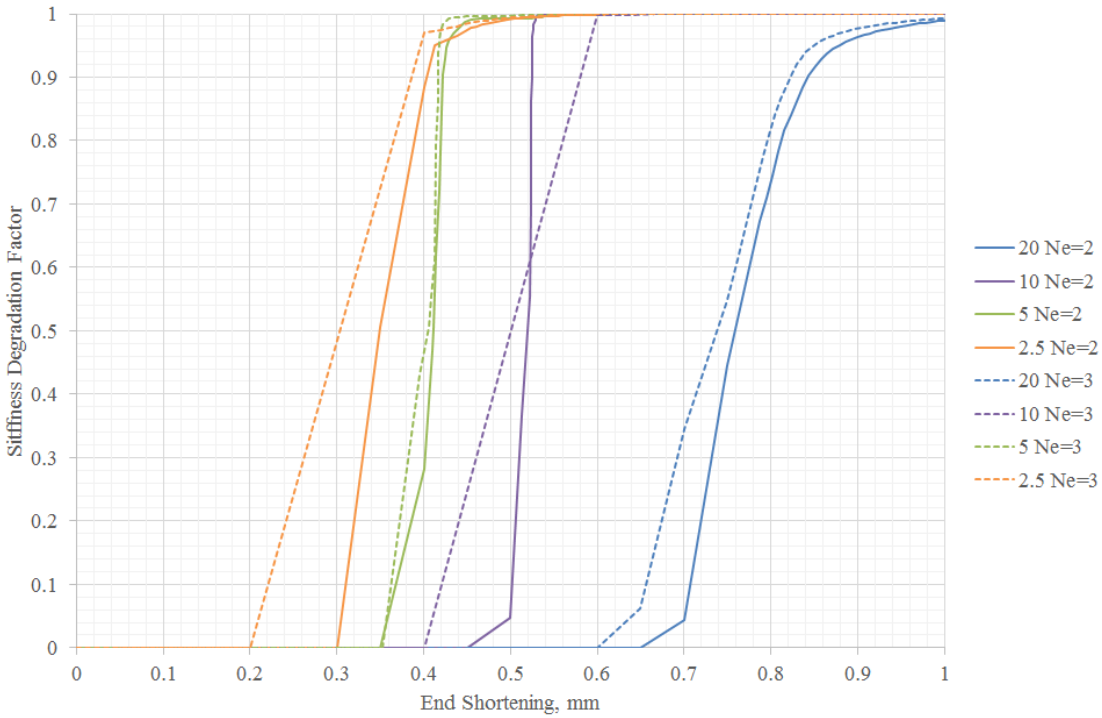

Figure 71: Convergence of Damaged Model - Stiffness Degradation of Cohesive Elements

cohesive element method shows a slight reduction in ultimate strength from 510kN to 503kN representing a 1.4% increase in ultimate strength in neglecting the degradation of the stiffener interface. The 100mm debond shows a 2.4% reduction in the first peak which represents the onset of unstable crack propagation using the cohesive element method although the ultimate strength shows less than a 1% change between methods. For increasing debond size, 300mm, a more significant change of 4.3% in ultimate strength is observed as the debond of the outer supporting stiffener becomes significant. The panel buckling load shown by the marked change in stiffness from the initial stiffness occurs at 224kN for the VCCT method and 164kN for the cohesive element method. This 26% reduction is from including matrix cracking and a degradation in stiffness at the interface prior to crack propagation. Crack propagation occurs at 224kN for the VCCT method and 121kN for the cohesive method and although a discrepancy may be expected due to the difference in scale of the mesh size there is a gradual transition which is captured by the cohesive elements which is lost by the VCCT method which may alter the failure mechanisms of the panel and the ultimate strength.

The cohesive elements are shown to capture debond initiation in the intact cases and in the supporting stiffener which cannot be determined by the standard VCCT model. It shows that it may have a significant affect on both the failure mechanisms and ultimate strength of the panel. A global-local model has been considered although determination of the characteristic length requires careful calibration in multiple loading condition and although a crack initiation load and location may be calculated the effect of this crack initiating on the ultimate strength may only be determined by a full analysis such as the cohesive element method. In order to assess the effect of design

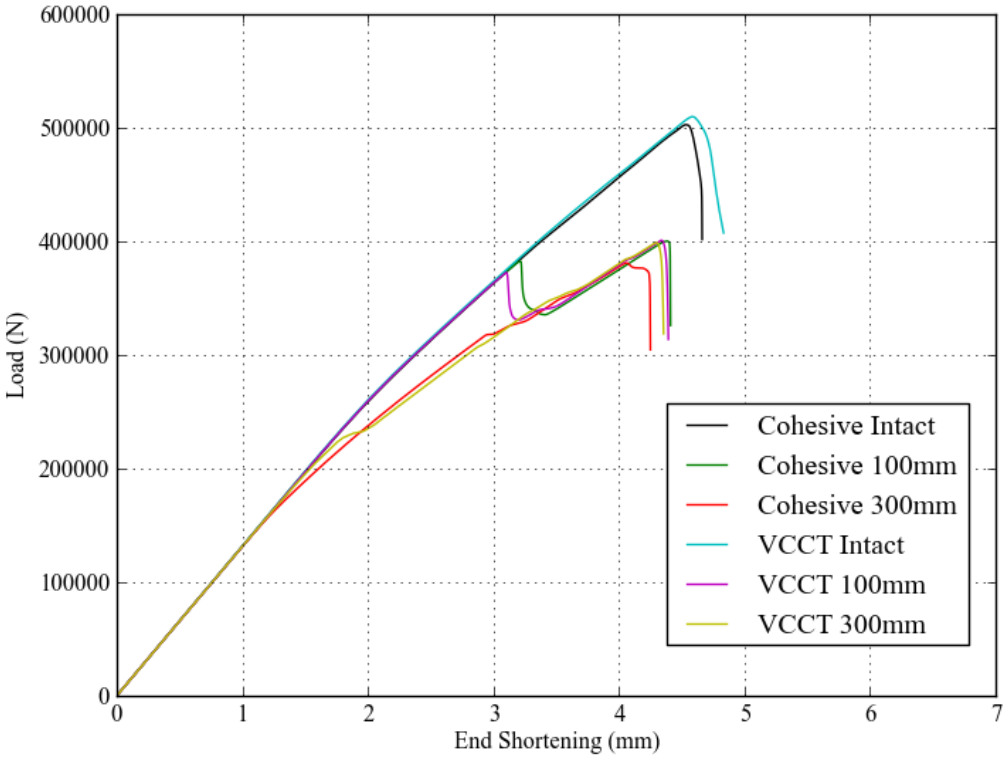

Figure 72: End Shortening Curve Comparing VCCT and Cohesive Element Method

and damage parameters on both the ultimate strength and failure mechanisms including further crack initiation the full cohesive method is chosen.

4.7.4 Imperfection Sensitivity

The effect of the scale of the imperfection is assessed for the smallest stiffener spacing considered, 275mm, as the eigenvalue analysis shows that multiple buckling modes are found within the shortest loading range. From the eigenvalue buckling analysis it is shown that the plate buckles into 3 half sine waves at 4.87mm end shortening and into an asymmetric four half sine waves at 5.26mm end shortening . Therefore to obtain the lowest energy configuration a switch between 3 and 4 half sine waves is expected and would be highly dependent on the imperfection scale, defects and mesh size. An imperfection of 3 half sine waves is applied to the model to assess the effects of the magnitude of the imperfection. Results for the buckling load and ultimate load are shown in figure 73 for increasing imperfection where the out-of-plane imperfection is scaled as a percentage of the plate thickness.

For large imperfections of the order of 10% plate thickness the plate does not buckle as the imperfection is large enough to define a 'buckled' plate shape without loading. An imperfection of 1% allows the buckling mode shape to switch between three and four half sine waves and is therefore not predetermined by the applied imperfection. Figure 74 shows the central out-of-plane deflection at increasing end shortening for scaled imperfections from 0.01-

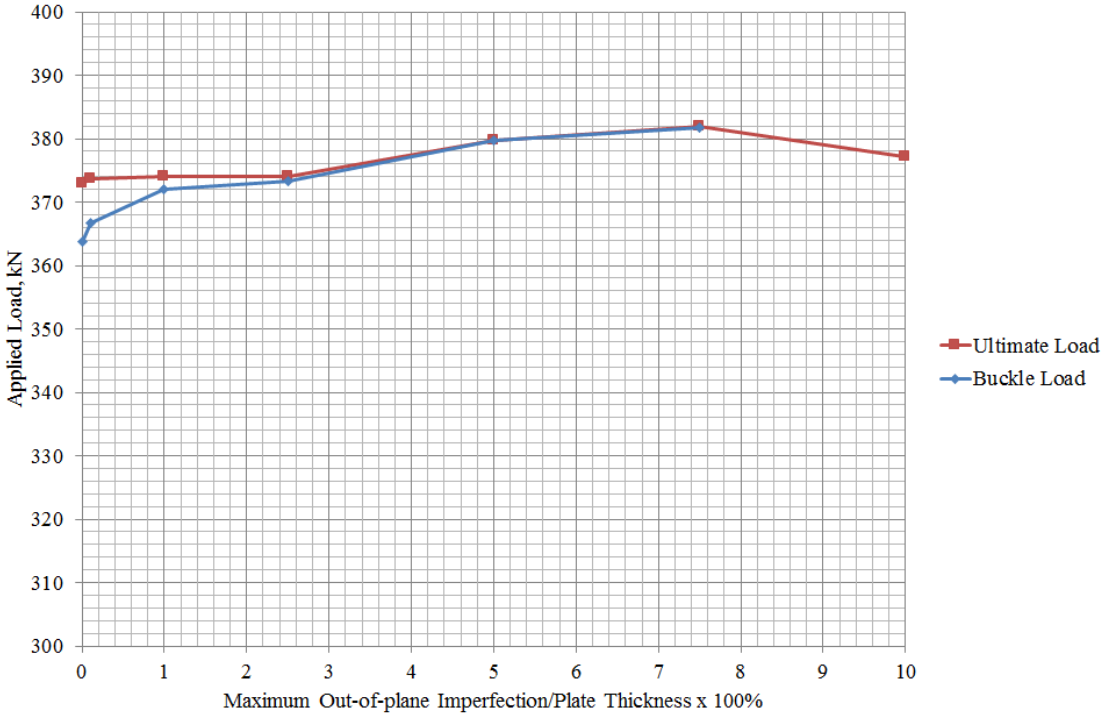

Figure 73: Effect of Imperfection Scale on Stiffener Spacing of 275mm

100%. Figure 74 shows that the reduction in the buckling load at 0.01% seen in figure 73 is due to the switch in the sign of the out-of-plane displacement in the first buckling mode. 0.1% and 0.01% show a negative central inflection whereas scaled imperfections greater than 1% show a positive central inflection.

An imperfection scaled at 0.1% of the plate thickness is shown to allow the panel to take the lowest energy configuration whilst still allowing buckling to occur therefore this is defined as a nominal imperfection for this configuration.

4.8 Summary of verification Cases

To verify the model and methodology, solutions from finite element models are compared to selected experimental, analytical and numerical results available in the literature.

A number of tests on rectangular plates loaded in uniaxial compression conducted by Starnes [160] are used to verify the buckled and post-buckled response and to compare a number of failure criteria. The model has shown excellent correlation to the post-buckled response of composite laminate plates closely matching the initial stiffness and global buckling load for a number of experimental tests. The effect of the degradation model is assessed showing the linear degradation model in this case provides unrealistic residual capability of the material and therefore an instantaneous reduction method is identified as being the most conservative method. The World Wide Failure Exercise recommended failure criteria are compared showing for this case that the Puck criterion or a combined conservative criterion are required to yield the most accurate results and a conservative estimate for two out of the

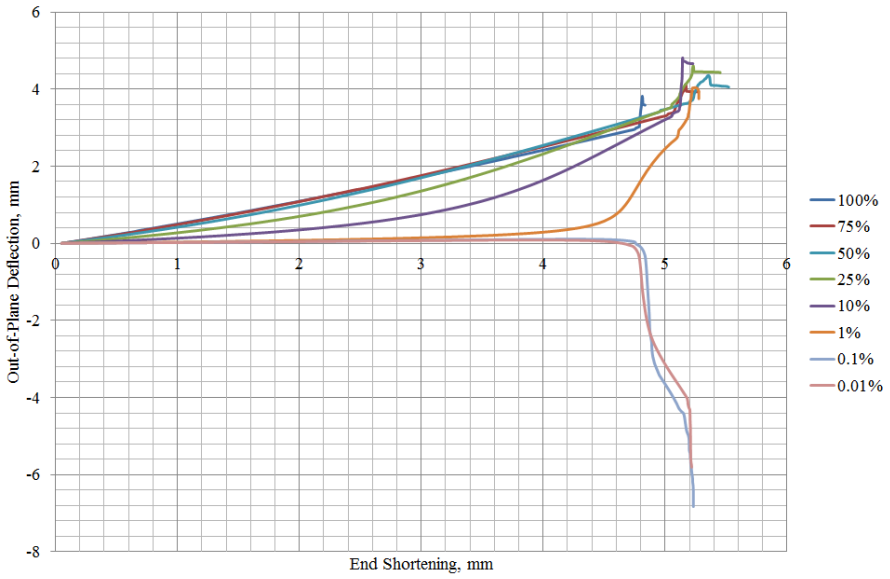

Figure 74: Effect of Imperfection Scale on Stiffener Spacing of 275mm, Out-of-plane Deflection

three results.

The buckled and post-buckled response of blade stiffened structures is verified against experimental work of Kong et al. [126]. The model has shown good correlation to the post-buckled response; qualitatively the model matches the experimental observations well, matching the failure modes observed. Quantitatively the model overestimates both the buckling load and final failure load by 20% and 18% respectively. As the initial stiffness is also overestimated it is assumed that the material properties quoted by the author are not a true representation of the build quality and may in part account for this error. The effects of the boundary conditions are assessed showing that the potted conditions suggested by Araico et al. [124] provide a reasonable compromise between the simply supported and clamped boundary conditions. The World Wide Failure Exercise recommended failure criteria are compared again showing that for this case the Puck Criterion, as part of a combined conservative criterion, is required to yield the most accurate results. For the buckled response of rectangular plates and stiffened plates the Puck Criterion yields the most conservative results, however, for future models the combined conservative criterion will be used to ensure that for the specific material parameters of the Puck and Tsai-Wu criteria that the most conservative result is used for each material.

The buckled and post-buckled response of top-hat stiffened structures is verified against experimental work of Falzon and Steven [132]. The model has shown reasonable correlation of the buckled and initial post-buckled response of top-hat stiffened composite plates. As the initial stiffness is overestimated it is assumed that the material properties quoted by the author are not a true representation of the build quality and may in part account for this overestimation. The importance of determining the build quality material properties of the structure is again highlighted showing the sensitivity of the model to the compressive modulus of the material which is not quoted by the author. The study highlights the models failure to correctly determine the mode switches in the

deep post-buckled state. However as there is a large skin bay with a high width to skin-thickness ratio between the stiffeners, which is not representative of stiffened structures used in load bearing situations, only the initial post-buckled state is compared which is achieved with reasonable agreement.

The VCCT nodal release method and the cohesive element method are verified against the double cantilever beam and end notch failure coupon tests conducted by Reeder et al. [162]. The study shows that reasonable approximation for the crack propagation in modes I and II can be obtained from both the VCCT method using shell and the cohesive element method. The cohesive element method is capable of modelling the gradual build up of matrix cracking and damage at the crack tip prior to crack advancement in mode II opening whereas neither method effectively captures the fibre bridging behind the crack tip under mode I opening in this case. The VCCT method is shown to be computationally efficient for a large mesh size however a global-local approach is required to capture crack initiation. This type of method requires a prior knowledge of the region in which the crack initiates or a number of local models. It is shown that the cohesive zone length can be artificially increased using the cohesive element method and therefore can be an efficient method for predicting delamination initiation and propagation. The cohesive zone model is therefore chosen for future work.

The model's ability to follow combined crack propagation and buckling is verified against the experimental work of Kutlu and Chang [161] and the numerical work of Liu et al. [164] and Zhang and Wang [165]. Qualitatively the failure modes closely match those described by Kutlu and the initial stiffness, buckling load of the delaminated ply and transition to the post-buckled state are well captured by the model however, the global buckled response and ultimate collapse is significantly over estimated by the model. The sensitivity of the model to the imperfection shape and size is investigated comparing the first buckling mode generated from a linear eigenvalue analysis scaled by the upper laminate ply thickness, and a constant indent over the area of the Teflon layer as the Teflon thickness in this case is not insignificant when compared to the lamina thickness. It is shown that a constant indent of thickness approximately equal to half the Teflon thickness yields a close fit to the experimental results for the transition to the buckled mode. The effect of the global imperfection is investigated to improve the global buckling load however, the imperfection is shown to affect the failure mode and therefore not be representative of the experimental observations. Compared to the numerical models of Liu et al. [164] and Zhang and Wang [165] the current three dimensional shell element method shows good overall correlation and therefore verifies the use of shell elements for modelling combined crack propagation and buckling problems. All three numerical models overestimate the global buckling load suggesting this overestimation may be attributed to unrealistic boundary condition assumptions, imperfections or flaws within the material. The boundary is assumed to be ideally clamped whereas the experimental fittings are unlikely to restrict all rotations and would lead to increased deflection of the back laminate experimentally compared to the finite element model.

The models ability to follow the progressive collapse of an embedded delamination is verified against the experimental work of Riccio and Pietropaoli [106]. The effect of the imperfection size is investigated for the low load response. A minimum of 10% imperfection is required to initiate the post-buckled response which most closely matches the experimental results at low load. The local buckling load, post buckled response and the global buckling

loads are predicted well and crack propagation is as described by the author. The delamination growth is modelled well; delamination growth initiates at the center of the panel, on the symmetry line, and propagates perpendicular to the loading direction, as reported experimentally. During global buckling the model predicts tensile matrix and shear failure in the lower ply of the delaminated layer however with a lack of information from the experimental test on the damage propagation this cannot be verified.

The damage progression in top-hat stiffened composite structures is used to verify the methodology monitoring delamination initiation and propagation in a post-buckled structure against full scale tests conducted by Smith and Dow [122] on a MCMV deck structure. A single stiffener located in the center of the grillage is modelled using symmetric boundary conditions and a clamped longitudinal edge. Qualitatively the failure modes closely match those described by Smith et al. and the initial stiffness, buckling load and plate deformation are reasonably captured by the model given the boundary condition assumptions. The delamination initiation is predicted at a comparable load to the experimental test however, the model predicts a rapid progression of damage with instantaneous crack growth down the length of the flange-plate interface which reduces the load carrying capability gradually whereas Smith et al. observed a residual capability following delamination propagation. This could be attributed to the boundary condition assumption or due to an assumption made in the material properties.

An initial study is conducted on the reference panel described in section 3.3. The converged mesh size is determined for the intact and damaged cases. An initial study has shown that neglecting debonding in the outer stiffeners shows significant deviation in the panel stiffness and failure mechanisms therefore the cohesive element method is confirmed as the most suitable method for the study as it is capable of capturing the additional debonding. An imperfection sensitivity is conducted to assess the effect of the magnitude of the scaled imperfection on the response of the stiffened panel. A nominal imperfection is defined which is shown to have minimal effect on the buckled mode shape and allows the panel to take the lowest energy configuration. This imperfection is compared to a forced imperfection which is applied to the panel to represent a maximum out-of-plane deformation of 10% of the plate thickness, as measured by Smith and Dow [122]. To allow comparison between damage cases a number of failure mechanisms are defined which determine the damage initiation, plate buckling, panel buckling and stiffener buckling.

Therefore, it has been shown that the proposed methodology in section 3.4 is capable of assessing the linear buckled and post-buckled response of composite and stiffened plates. A number of criteria recommended by the World Wide Failure Exercise have been compared and the instantaneous degradation method and the combined conservative criterion has been chosen as the preferred criterion as it guarantees the most conservative estimate for the cases tested. The crack propagation in mode I and mode II test coupons has been investigated and compared for two methods. The cohesive element model is shown to ba an efficient and accurate method where the cohesive zone length can be artificially increased by Turon's method and is capable of predicting both delamination initiation and propagation for large scale problems. This method has been shown to effectively model both through width and embedded delaminations correctly following the crack propagation direction and collapse mechanisms. The methodology proposed is shown to model the post-buckled response, delamination initiation and damage propagation

correctly identifying the failure modes of a top-hat stiffened panel and is shown to be accurate where the material and geometric properties of the problem are given.

5 Damage Tolerance Analysis

In this section the effect of debond damage between the stiffener and the plate is assessed for the generic top-hat stiffened panel defined in section 3.4. The failure mechanisms and ultimate load are defined to allow comparison between cases. The failure mechanisms and ultimate load are compared for varying debond sizes and locations along with the effect of the panel geometric properties such as stiffener spacing, plate thickness, stiffener height and the effect of imperfection scale. Two imperfection scales with the maximum out-of-plane deflection equivalent to 0.1% and 10% of the plate thickness, representing a 'nominal' and 'forced' imperfection, are compared for the reference case. The top-hat stiffener is compared to open section stiffeners and the effect of combined in-plane and lateral loads are considered.

For each study the intact case is used as the reference case for the analysis and the failure mechanisms are discussed with respect to failure maps. The load at which the failure mechanisms are shown is scaled by the ultimate load of the intact case and the debond length is scaled as a percentage of the panel length to allow an easy comparison. For clarity the deformations are scaled to 500% in all images presented in this chapter.

5.1 Defining Buckling and Failure Mechanisms

It is critical during the parametric study to allow comparison between damage cases therefore the failure mechanisms are defined including the onset of buckling, damage initiation, crack propagation and the ultimate load.

During buckling a bifurcation point is not present therefore, in order to assess the buckling point of the plate the deflection at the center of the plate is assessed and a criterion is chosen to determine the load at which buckling occurs. The out-of-plane deflection against the end shortening is compared for increasing debond size for a central debond and a nominal imperfection in figure 75. For the intact case the deflection curve shows the plate exhibits a linear increase in out-of-plane deflection until an end shortening of 1.8mm. Significant deviation is observed with a marked change in out-of-plane deflection from an end shortening of 1.8 to 2.1mm where the plate deflection changes dramatically. A similar trend is observed for the debond cases where the plate buckles in a negative inflection. Where the plate buckles to a positive inflection the buckling point is less clear. A marked deviation is observed by examining the change in out-of-plane deflection with end shortening for increasing debond size, shown in figure 76. As buckling represents an instability which is shown by a marked change in the out-of-plane deflection a change in out-of-plane deflection with end shortening of greater than 0.05 is chosen to represent the 'local plate buckling' point. This is illustrated by a five starred mark in figures 75 and 76. This estimate is shown to give reasonable results when considering both the out-of-plane deflection results for negative and positive buckled inflections.

In the following cases the out-of-plane deformation of the plate beneath the debond area is monitored and local plate buckling is termed when a marked deviation is observed, as discussed. As buckling may alternatively be defined as a marked change in stiffness the change in stiffness of the panel is also monitored and recorded when a 5% change is observed; this is termed panel buckling.

A similar analysis is conducted for the buckling point of the stiffener where the deflection of the central table

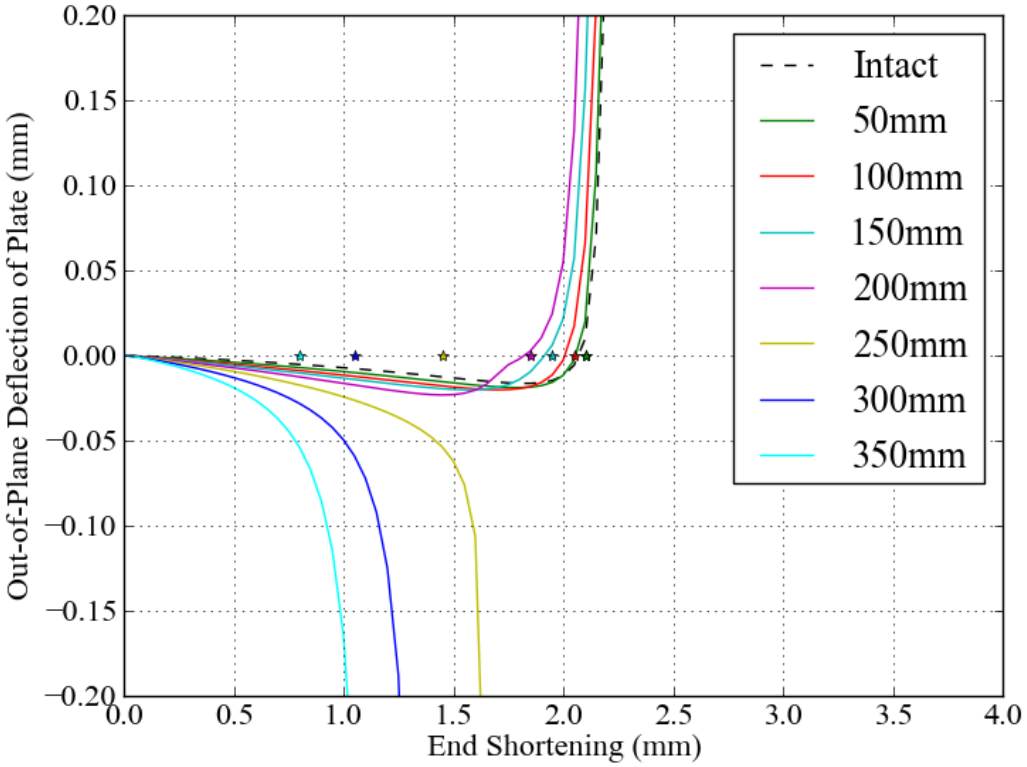

Figure 75: Out-of-Plane deflection of Plate for Increasing Central Debond for Nominal Imperfection

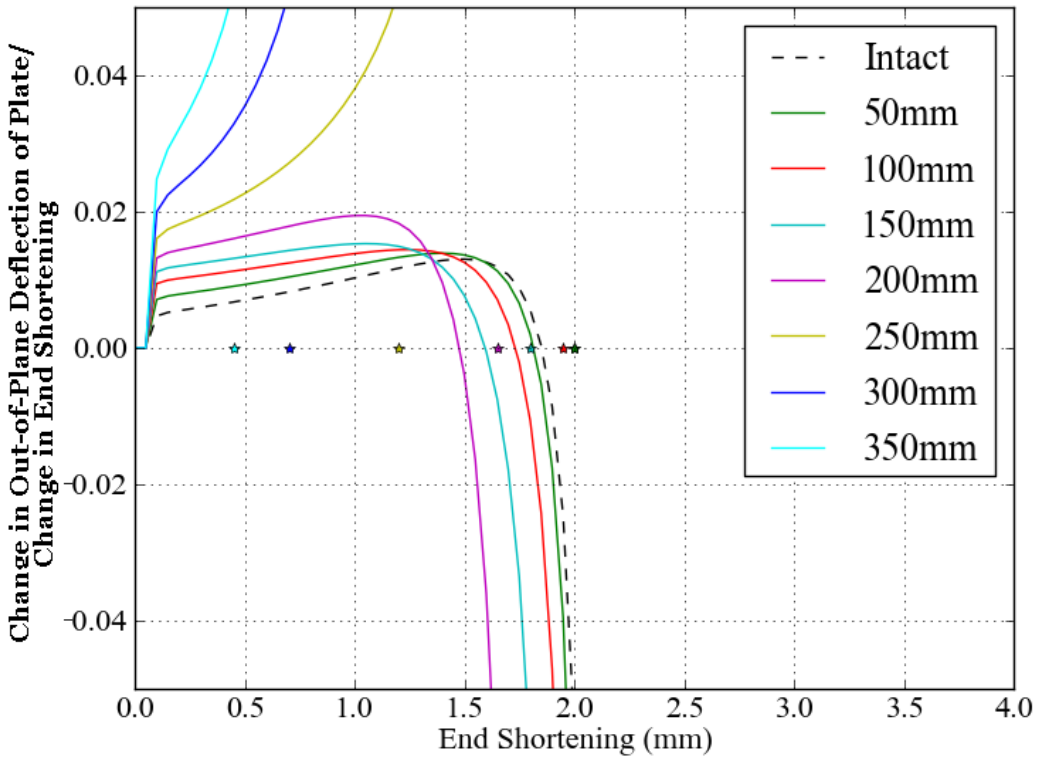

Figure 76: Change in Out-of-Plane Deflection of Plate/ Change in End Shortening for Increasing Central Debond for Nominal Imperfection

of the stiffener is assessed. The full analysis is reported in Appendix D. A change in out-of-plane deflection with end shortening of greater than 0.05 is also chosen to represent the stiffener buckling point. Therefore,a consistent method is used to define buckling both in the stiffener and the plate. This is illustrated by a the marked circles in figures 149 and 150 in appendix D. This estimate is shown to give reasonable results when considering both the out-of-plane deflection results.

Significant damage initiation is defined when 100 elements exceed the Tsai-Wu failure criterion. Crack growth is defined once a single element has fully degraded. The load deflection curve is monitored and the analysis is stopped when a 20% reduction in load is observed which is shown to correspond to gross failure of global buckling of the panel

5.2 Analysis of Debond Size

The effect of debond size is investigated for central debonds with initial size from 50mm (6.6%) to 350mm (47%) at 50mm spacings in panels with a nominal and forced imperfection. A nominal imperfection is defined here as a small imperfection used to initiate a post-buckled response. Therefore, the nominal imperfection analysis represents the response of idealistic manufactured panel. A forced imperfection is defined here as a larger imperfection at the scale of those measured experimentally [122], maximum out-of-plane deflection at 10% of the plate thickness, although implemented so as to maintain the first buckled mode.

5.2.1 Nominal Imperfection

The intact case failure mechanisms are shown in figure 77 and illustrated on the load deflection curve in figure 78; the plate buckles into three half sine waves with a positive inflection at the center of the plate, damage initiates on the anti-node line (a) and develops across the width of the plate (b), the debond develops on the anti-node line on the inner flange edge and propagates across the flange just prior to ultimate failure (c). Shear failure of the plate in the region of the anti-node lines, regions corresponding to zero out-of-plane deflection, is the dominant mode of failure for the intact case and small debonds. Crack propagation occurs at the ultimate load but follows a significant amount of shear damage in the plate and flange and is not considered to be the primary cause of ultimate failure.

The failure mechanism map is shown in figure 80 illustrating the change in ultimate strength, crack propagation, damage initiation, and panel, plate and stiffener buckling with increasing initial debond length. There is only minor deviation in the failure characteristics for debonds of 20% or less except for a gradual reduction in the local plate buckling load, from 50.9% to 45.9% at 30%, which has a nominal effect on the damage initiation and crack propagation.

At 26% initial crack length the debond approaches the length of the half sine wave buckled mode and there is a significant reduction in the crack propagation load from 99.9% to 78.2% with a reduction in the ultimate strength to 94.7%. The crack propagates from the inner flange edge which enhances the plate deformation and aids damage propagation in the center of the plate beneath the debond. The development of the crack and shear failure are illustrated in figure 79 where the colour scale illustrated the shear degradation factor (SDV11) and cohesive

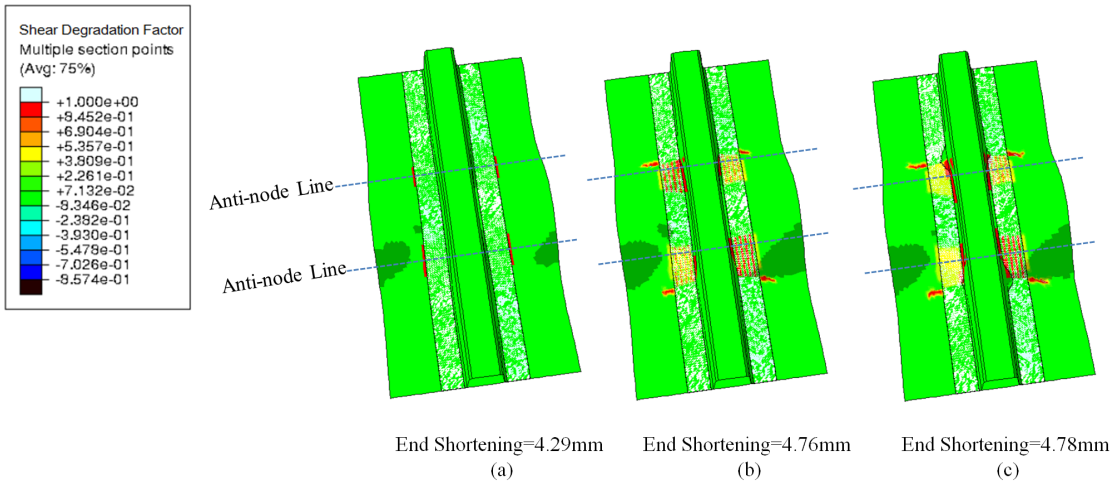

Figure 77: Shear Failure Development in the Intact Case with a Nominal Imperfection

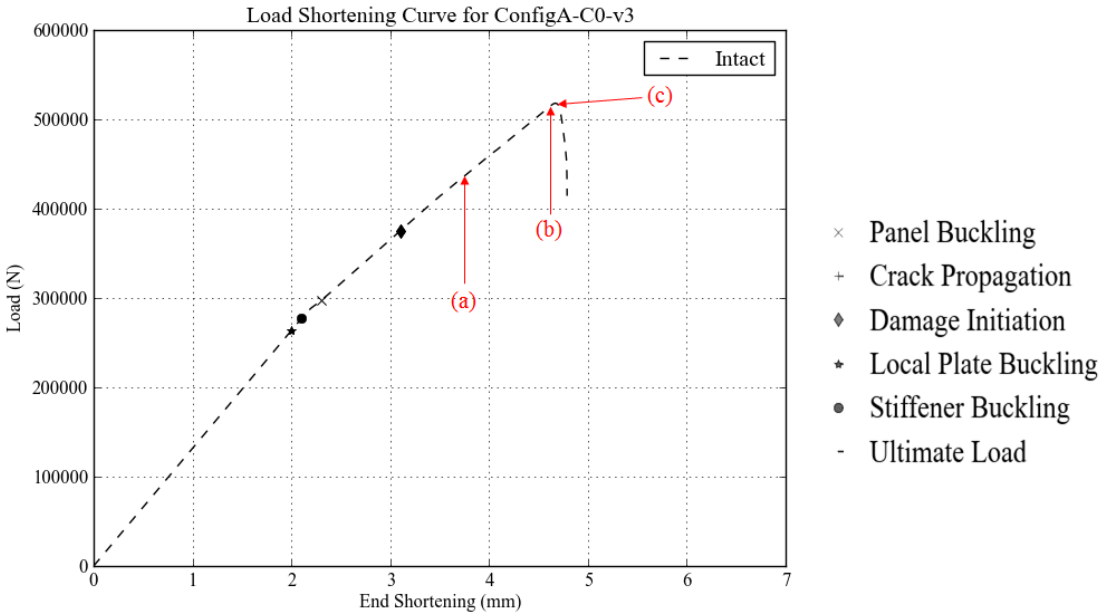

Figure 78: Load Deflection Curve for the Intact Case with a Nominal Imperfection

degradation parameter (SDEG). Crack propagation becomes dominant for debonds greater than 33%, which is greater than the length of the half sine wave inflection. Crack propagation occurs prior to the damage initiation load and is largely coincident with the stiffener buckling. This change in mechanism is caused by the inversion of the plate inflections, switching of the central inflection from positive to negative out-of-plane deflection. At this critical point the buckling mode shape shows a significant deflection beneath the debond and has altered the preferred buckling mode of the plate. Instead of a positive inflection in the region of the debond, which pushes the debonded plate and flange together preventing mode I crack growth, the negative inflection drives mode I opening at the crack tip. The untied flange also buckles away from the plate further enhancing the opening force. A reduction in stiffener buckling, significant crack growth and a significant reduction in the ultimate strength to 73-74% of the intact case is observed.

For debonds increasing beyond this critical point a plateau exists where the ultimate strength remains greater than 60% of the intact ultimate strength. Material failure is observed in the center of the flange and then on the anti-node line of the supporting stiffener. Ultimate failure is due to gross failure of the plate. The supporting stiffener is observed to debond only during the final collapse of the panel.

5.2.2 Forced Imperfection

The small realistic imperfection is compared to the first buckling mode shape which is scaled with the maximum out-of-plane deflection set to be 10% of the plate thickness. The effect of debond size for a centrally located debond is investigated. The failure mechanism map is shown in figure 81 for increasing debond size.

In contrast to the nominal imperfection case the intact case plate buckles into three half sine waves with a negative inflection at the center of the plate although the failure mechanisms are similar to the nominal case as shown in figure 82.

The failure maps for the nominal imperfection case show a distinct change in modes at the critical debond size, 27%-33%. However the forced imperfection shows a more gradual change in characteristics as the debond size increases with the critical point at which crack propagation becomes significant between 0% and 6% debond. The crack propagation load shows a marked reduction from the intact case and then a steady reduction for increasing debond size. The ultimate strength rapidly decreases from the intact case to 20% debonds plateauing at 73% for larger debonds. The damage initiation load reduces between 13% and 33% debond although there is then a gradual rise between 33% and 46% debond. This increase represents localised damage in the flange-plate interface at the crack front. For large debonds the crack propagates up to the anti-node lines and failure is observed on the anti-node line of the intact stiffeners and in the central plate. Following a significant amount of failure in these regions the previously intact stiffener then debonds centrally as shown in figure 84 although this occurs post ultimate load.

With a forced imperfection plate buckling occurs at much lower loads for all debond sizes compared to those with a nominal imperfection. This is due to the change in the central inflection beneath the unsupported stiffener

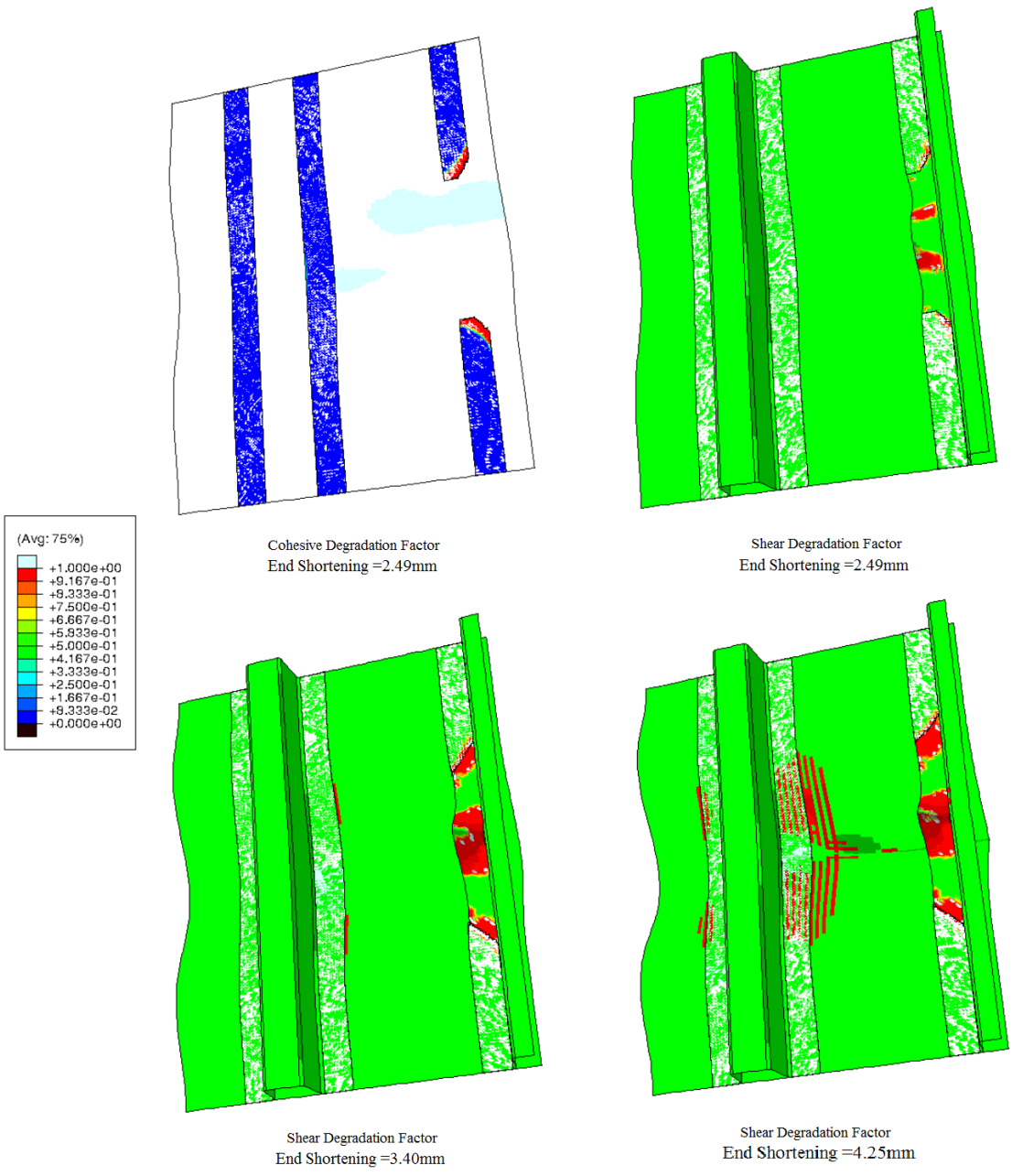

Figure 79: Failure Development with 250mm Central Debond and a Nominal Imperfection

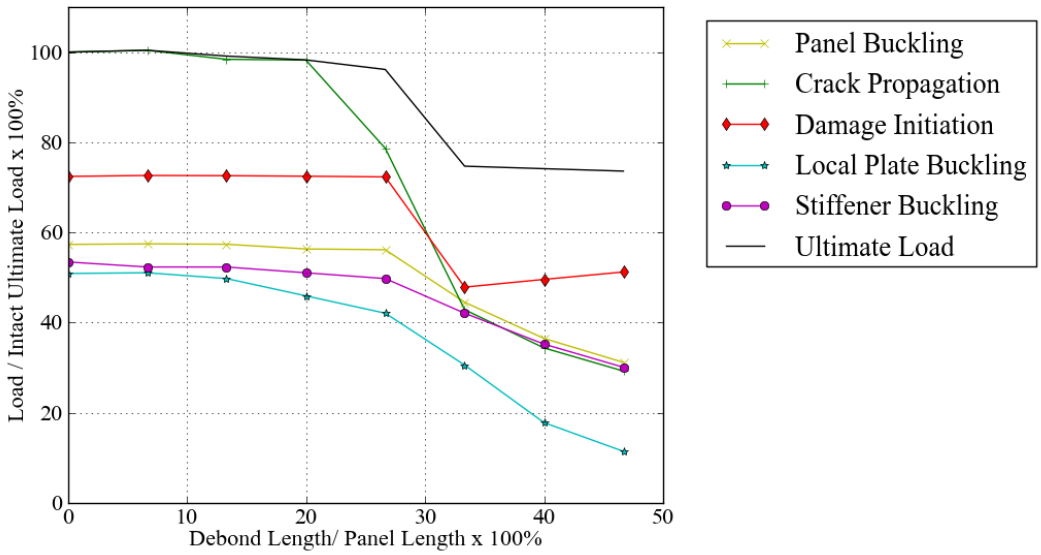

Figure 80: Failure Mechanism Map for Increasing Central Debond Size With Nominal Imperfection

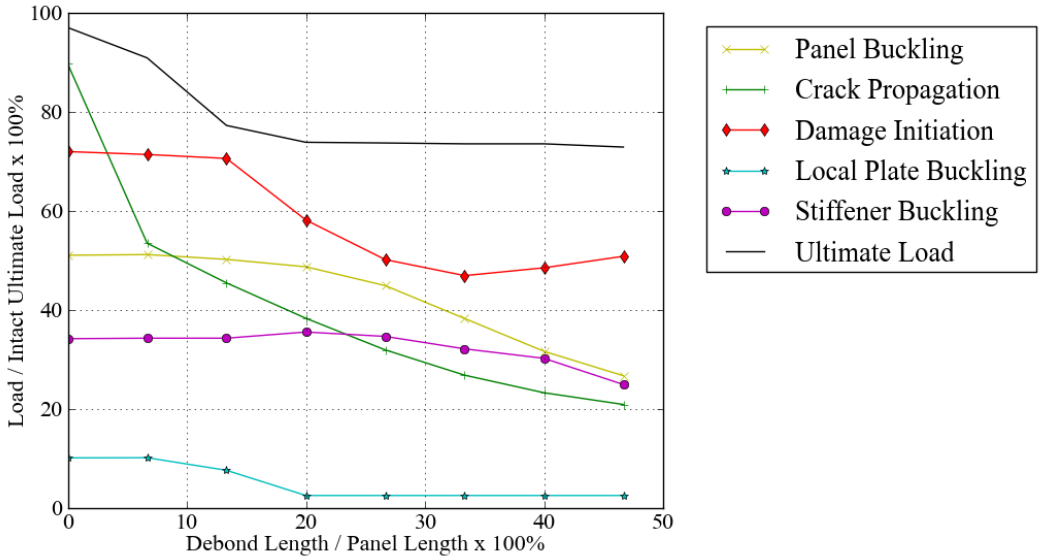

Figure 81: Failure Mechanism Map for Increasing Central Debond Size With Forced Imperfection

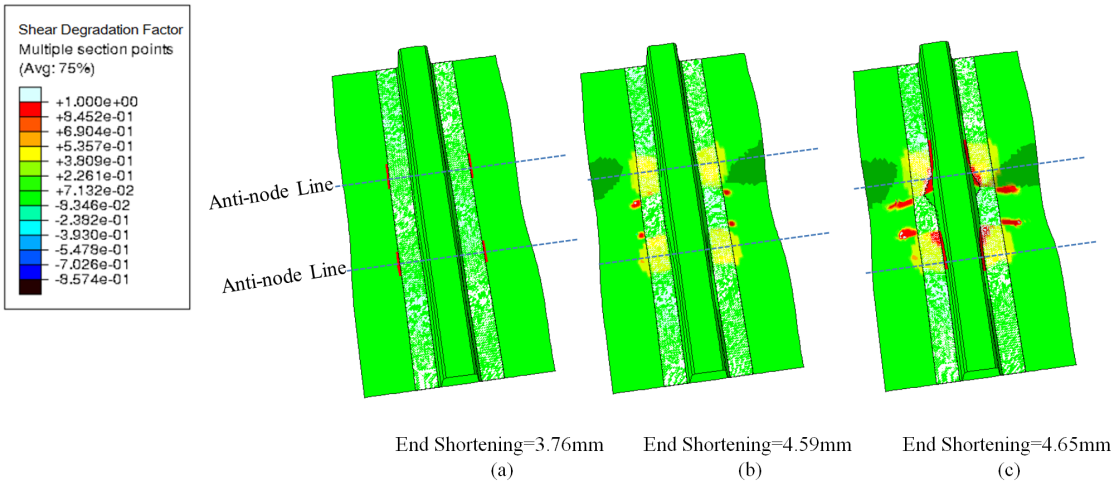

Figure 82: Shear Failure Development in the Intact Case and Forced Imperfection

between the two cases. However for debonds of 27% or greater both the nominal and forced imperfections form a negative inflection beneath the unsupported stiffener. The local plate buckling occurs at higher loads for the nominal case compared to the same debond size with a forced imperfection. The plate deformations beneath the flange, used to assess plate buckling, are shown in figure 83 for the intact cases and 40%, 300mm, debond for both a nominal and forced imperfection where the star shows the defined panel buckling point. The deflections for the intact case with forced imperfection remain negative, resulting in a negative central inflection, and shows a more rapid change in the gradient of the out-of-plane deflection of the plate against end shortening compared to the nominal case. For the debond cases there is a more rapid decrease in the out-of-plane deflection for the forced imperfection compared to the nominal imperfection. Therefore, the initial imperfection is shown to alter the plate deformations at lower loads resulting in a marked reduction in the plate buckling load for the forced imperfection, as expected.

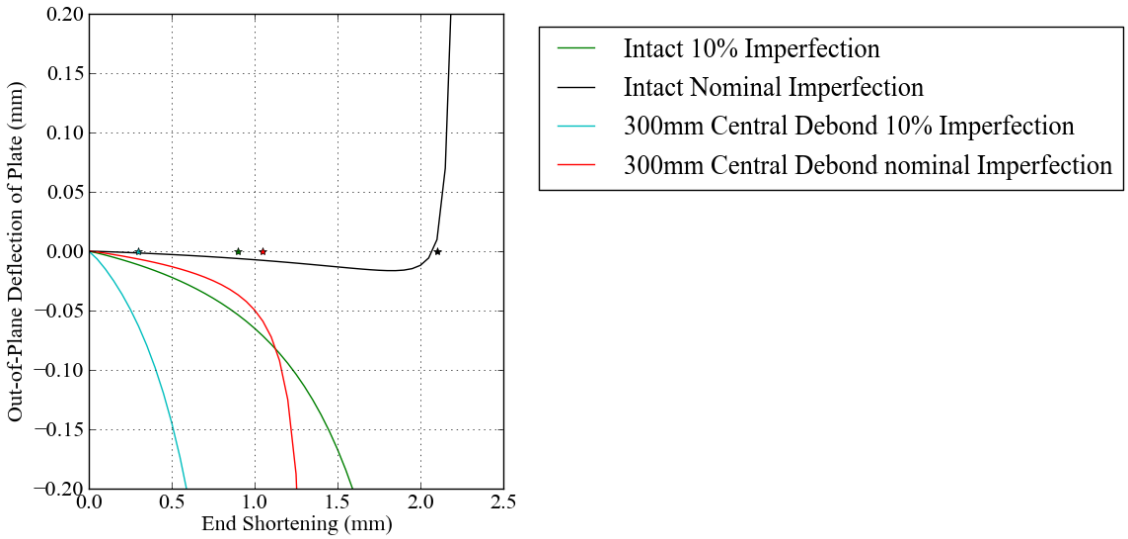

Figure 83: Comparison in Plate Deflection for nominal and forced imperfection

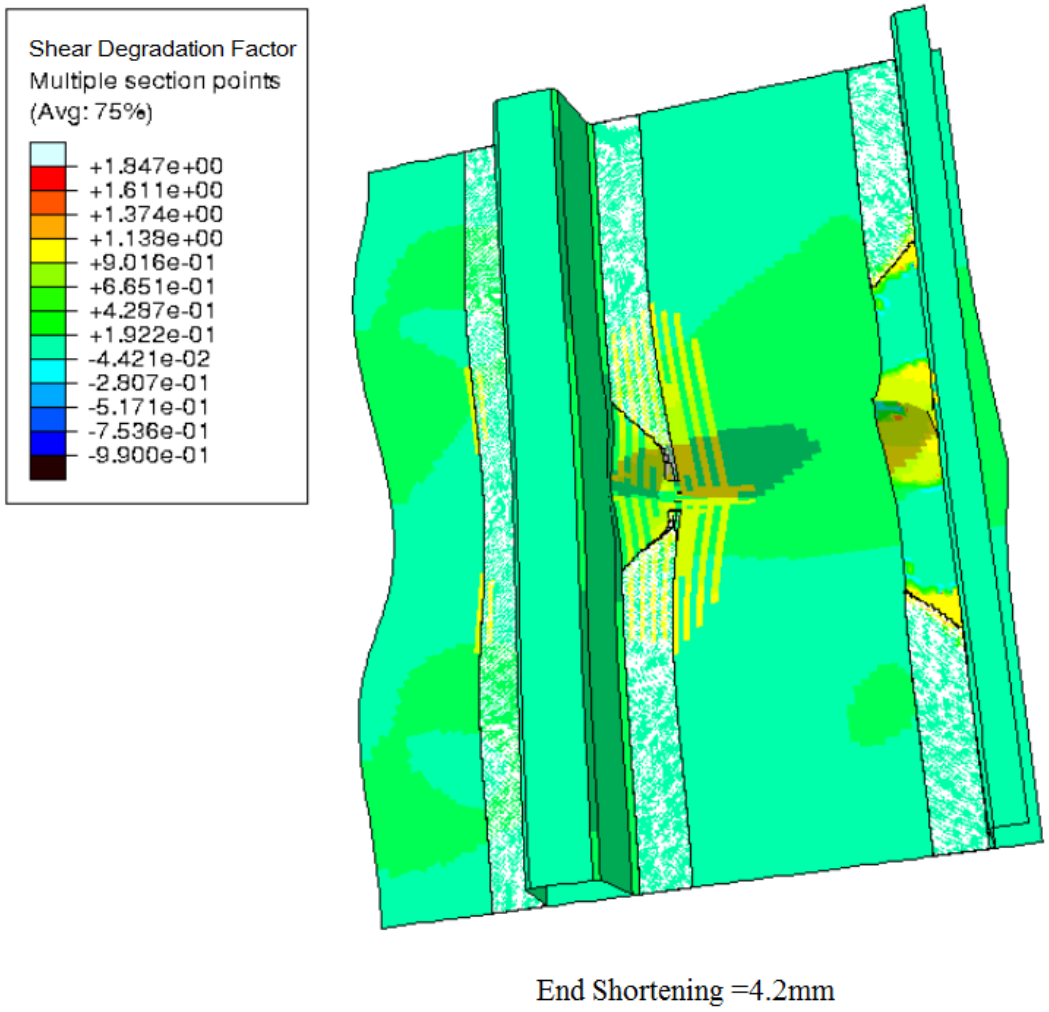

Figure 84: Shear Failure Development in the 3mm Debond Case

5.3 Effect of debond location

Debond position is investigated for small, 6.67% (50mm), medium, 20% (150mm), and large debonds, 40% (150mm). The location is represented as a ratio of the distance of the center of the debond from the plate end of the total plate length and the load is represented as a ratio of the intact ultimate strength with a nominal imperfection. The effect of debond position is compared from both a nominal and forced imperfection.

Figures 85 and 86 show the failure mechanism map for varying debond location for a small debond with a nominal and forced imperfections respectively. For small debonds, with both imperfections, there is a similar range in ultimate load showing up to a 5.1% reduction. For the nominal imperfection this reduction is due to the flange debond located over the anti-node line allowing increased displacement and therefore stresses in this area accelerating the material degradation. It is shown for both imperfections that as the center of the bond moves away from the central plane the onset of delamination growth occurs at reduced loading;the cracks initiate in the range of 100.4-60.0% for the nominal case and 90.0-52.2% for the forced imperfection case. The crack initiates from the initial debond on the outer edges of the flange however this debond does not propagate in these cases. The crack propagation for both imperfections is not a significant damage mechanism. There is significant deviation in local plate buckling for a forced imperfection due to the location change and its definition. Plate buckling is established based on the deflection of the plate beneath the flange in the center of the debond and is therefore dependent on the position relative to the buckled mode shape of the plate. As the center of the debond rests on the anti-node line a relative increase is seen in the load at which local plate buckling occurs. Similarly a relative decrease is observed as the center of the debond approaches the center of the buckled inflection which is more pronounced on the negative inflection (at the center of the plate).

Figures 87 and 88 show the failure mechanism maps for medium debonds with a nominal and forced imperfection respectively. Comparing these figures shows the damage and ultimate load have similar trends for the positive and negative inflections which occur either side of the anti-node line, located at 0.35. A more gradual change in mechanisms occurs compared to the small debonds with crack growth and ultimate failure occurring at increasing load as the debond moves towards the center of the positive inflection for both imperfection cases. There is a reduction of 26-29% in the ultimate load and crack propagation load as the debond passes from the positive to the negative inflection. Crack growth occurs at lower loads for the panels with a forced imperfection. This may be due to the more pronounced plate deflections illustrated in figure 83. The clamped end provides reduced opening moment at the crack tip suppressing crack growth for debonds between the clamped end and the peak of the positive inflection. The buckling load and damage initiation on the anti-node lines remains relatively unaffected by debond location.

For small and medium debonds the buckled mode shape is unaffected by the debond in all locations which is not the case for large debonds. For a nominal imperfection the buckling mode shape changes from two to three half sine waves in the plates adjacent to the debonded stiffener if the debond is moved from the center to the outer third of the plate. A reduction of 5% is observed in the ultimate load for a buckled mode shape of two half sine waves. This is due to a larger span between the anti-node lines which subsequently allows debonding to a larger width, more

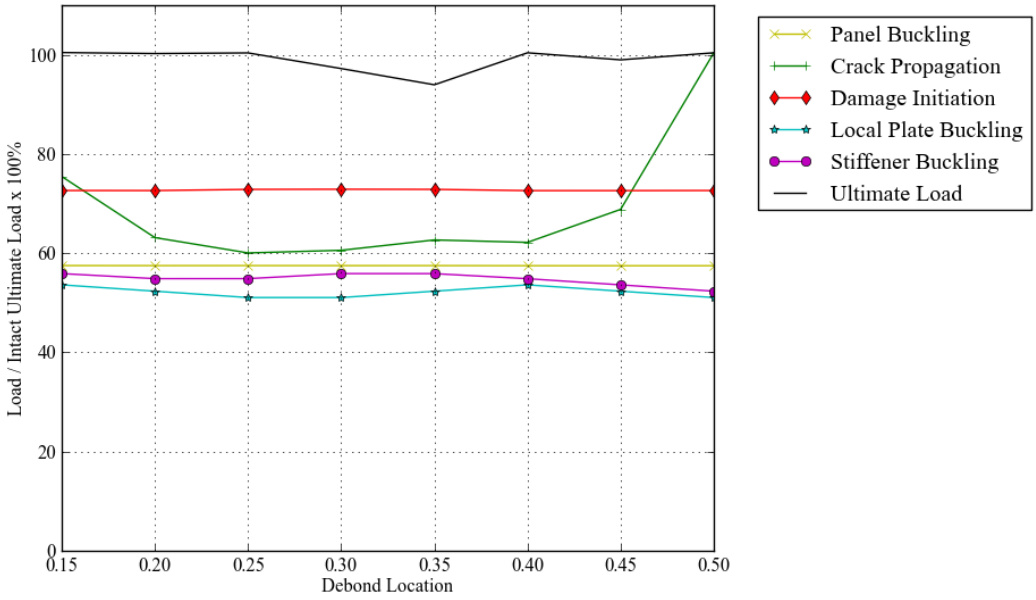

Figure 85: Failure Mechanisms for Offset small Debond with Nominal Imperfection

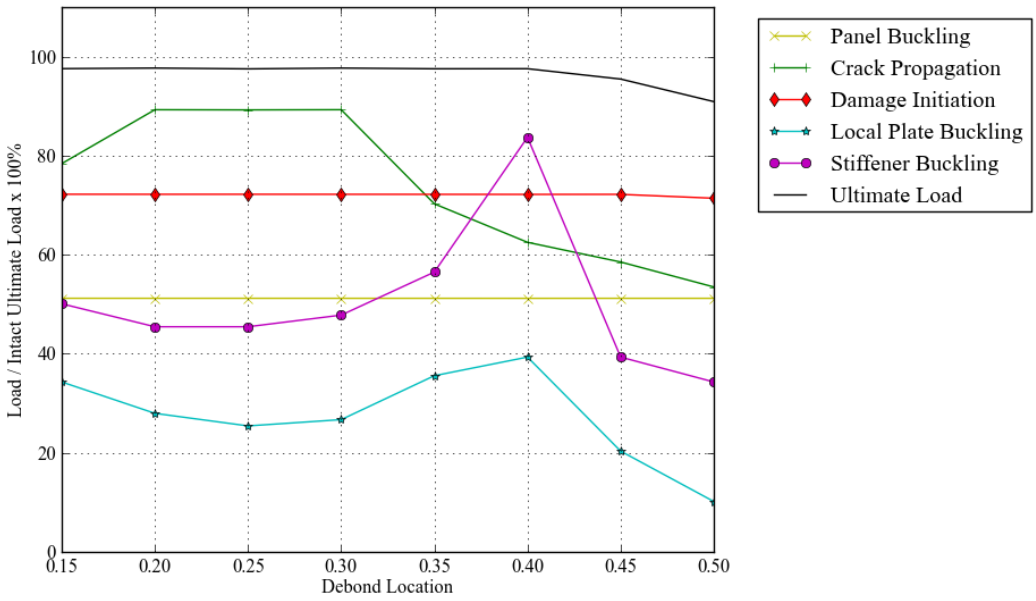

Figure 86: Failure Mechanisms for Offset Small Debond with Forced Imperfection

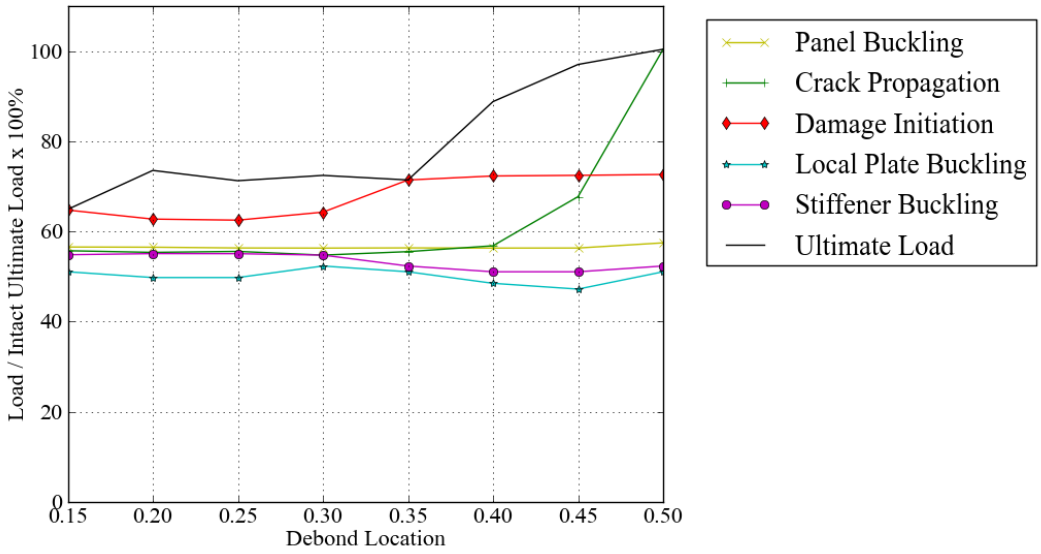

Figure 87: Failure Mechanisms for Offset Medium Debond with Nominal Imperfection

significant deflections and damage to the web and table of the debonded stiffener. Asymmetric buckling modes caused by two half sine waves in the damaged bay and three half sine waves in the adjacent intact bay also introduce torsional bending to the intact stiffener contributing to shear failure in the web of the supporting stiffeners and promoting stiffener buckling.

Figures 89 and 90 show the failure mechanism maps for large debonds at varying locations for nominal and forced imperfections respectively. The range in deviation in ultimate load for the locations is similar for both imperfections. Damage initiation and buckling load remain relatively constant. The largest difference is seen in the panel buckling, stiffener buckling and crack propagation load. For a nominal imperfection there is little dependence on debond location however the forced imperfection is shown to postpone crack propagation and plate and stiffener buckling for offset debonds as the debond moves into the positive inflection.

The effect of debond position relative to the buckling mode shape can be seen to mainly affect medium debonds, affecting both the crack propagation and ultimate load.

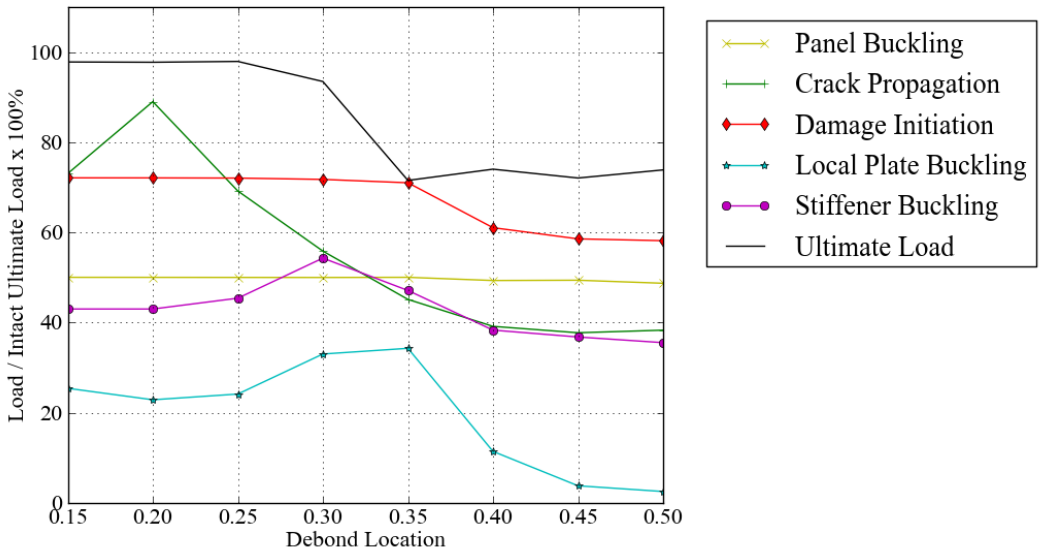

Figure 88: Failure Mechanisms for Offset Medium Debond with Forced Imperfection

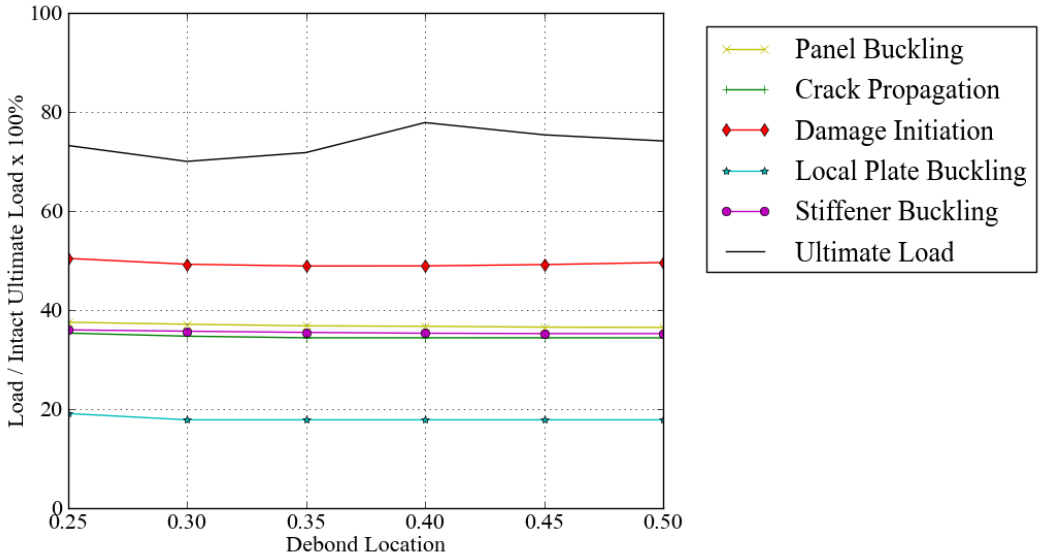

Figure 89: Failure Mechanisms for Offset large Debond with Nominal Imperfection

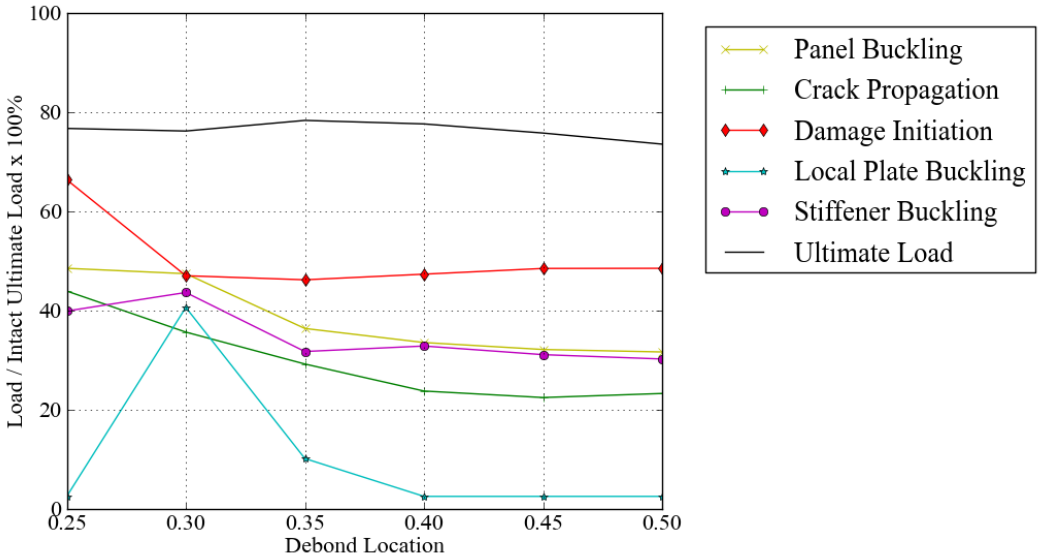

Figure 90: Failure Mechanisms for Offset Large Debond with Forced Imperfection

5.4 Stiffener Spacing

The effect of stiffener spacing is investigated for increased, 475mm, and reduced, 275mm, stiffener spacing compared to the reference case. For each panel the effect of central debonds with increasing size is investigated to assess their damage tolerance. The failure mechanism maps for increasing size of a central debond is shown in figure 91 and 92 for a stiffener spacing of 475mm and 275mm respectively. In both cases a nominal imperfection is seeded to ascertain the minimum energy configuration.

The intact ultimate strength is dominated by the stiffener second moment of area and is constant across the three spacings. The relationship between the ultimate strength and the debond size is similar for the three stiffener spacings; smaller debonds have little affect on the ultimate strength. At a critical debond size there is a marked drop in the ultimate strength followed by a plateau for larger debonds. This critical debond size varies depending on the stiffener spacing occurring between 13% and 20% for the smaller stiffener spacing, 27% and 33% for the reference case and a more gradual change is observed between 13% and 27% for the larger stiffener spacing.

The reference case and wide stiffener spacings show significant post-buckled strength with panel buckling occurring at 57.3% and 42.8% of the ultimate load respectively. For the widest stiffener spacing the intact case plate buckles into two half sine waves at 312kN, switching to three half sine waves with a positive inflection at the center of the plate at 434kN. Similar failure mechanisms are then observed as in the reference case with material failure and debonding initiating on the anti-node lines and propagating across the panel and stiffener debonding during the panel's final collapse. Whereas for the narrowest stiffener spacing panel buckling occurs at 99.9% followed by rapid collapse. For the narrowest stiffener spacing the ultimate strength is determined by stiffener buckling followed by material failure for the intact and crack propagation in the small damage cases. The panel's buckling mode may be affected by small debonds, 0-16%, causing switching between two and three half sine waves however, the ultimate load sees only a minor reduction compared to the intact case. For the reference and widest stiffener spacings the intact ultimate strength and small debond cases are driven by material failure which exacerbates the stiffener buckling leading to ultimate collapse. For all stiffener spacings, at the critical point, the buckling mode shape shows a significant deflection beneath the debond and has altered the preferred buckling mode of the plate resulting in mode I opening force at the crack tip and resulting in a significant reduction in the ultimate strength. For the narrowest spacing crack propagation leads to material failure and ultimate failure is due to debonding of the outer stiffener rather than stiffener buckling.

It is shown that for the reference and widest stiffener spacing that for small and medium debonds crack initiation does not propagate or diminish the ultimate strength of the panel significantly and that a 'no crack growth philosophy' results in conservative results.

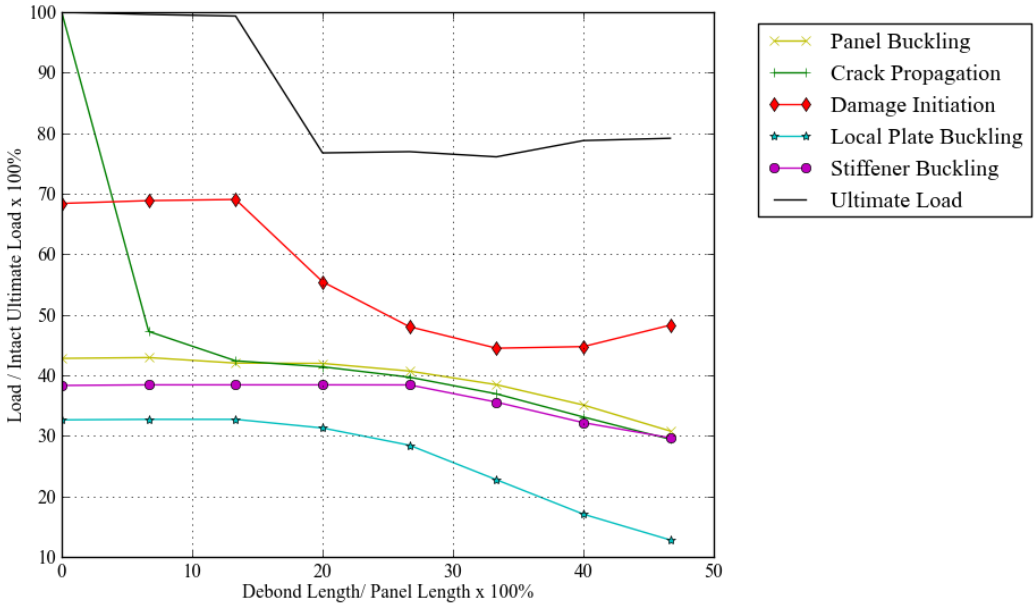

Figure 91: Failure Mechanisms for Increasing Central Debond for Nominal Imperfection and 475mm Stiffener Spacing

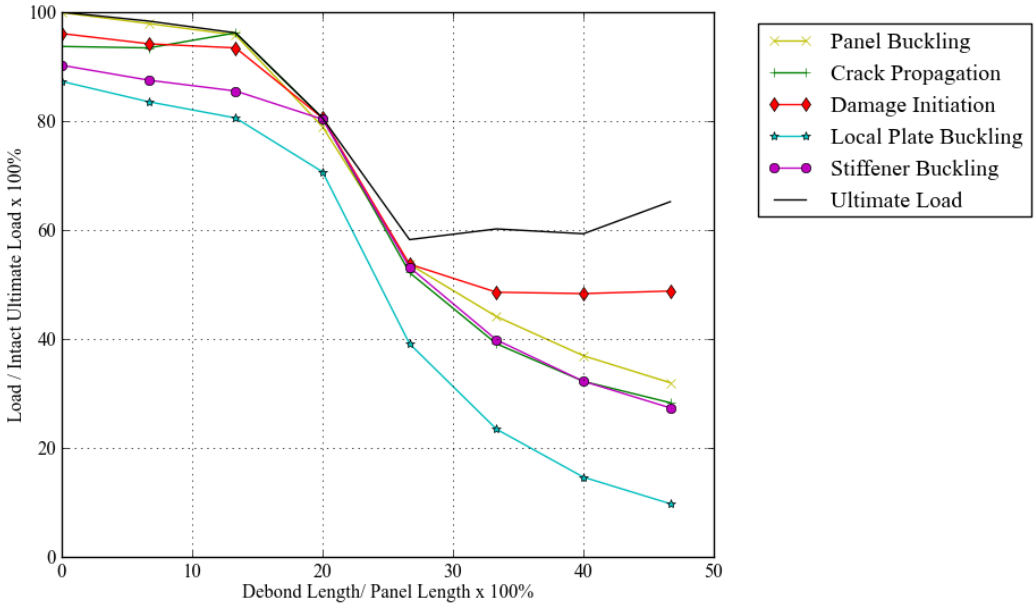

Figure 92: Failure Mechanisms for Increasing Central Debond for Nominal Imperfection and Stiffener Spacing 275mm

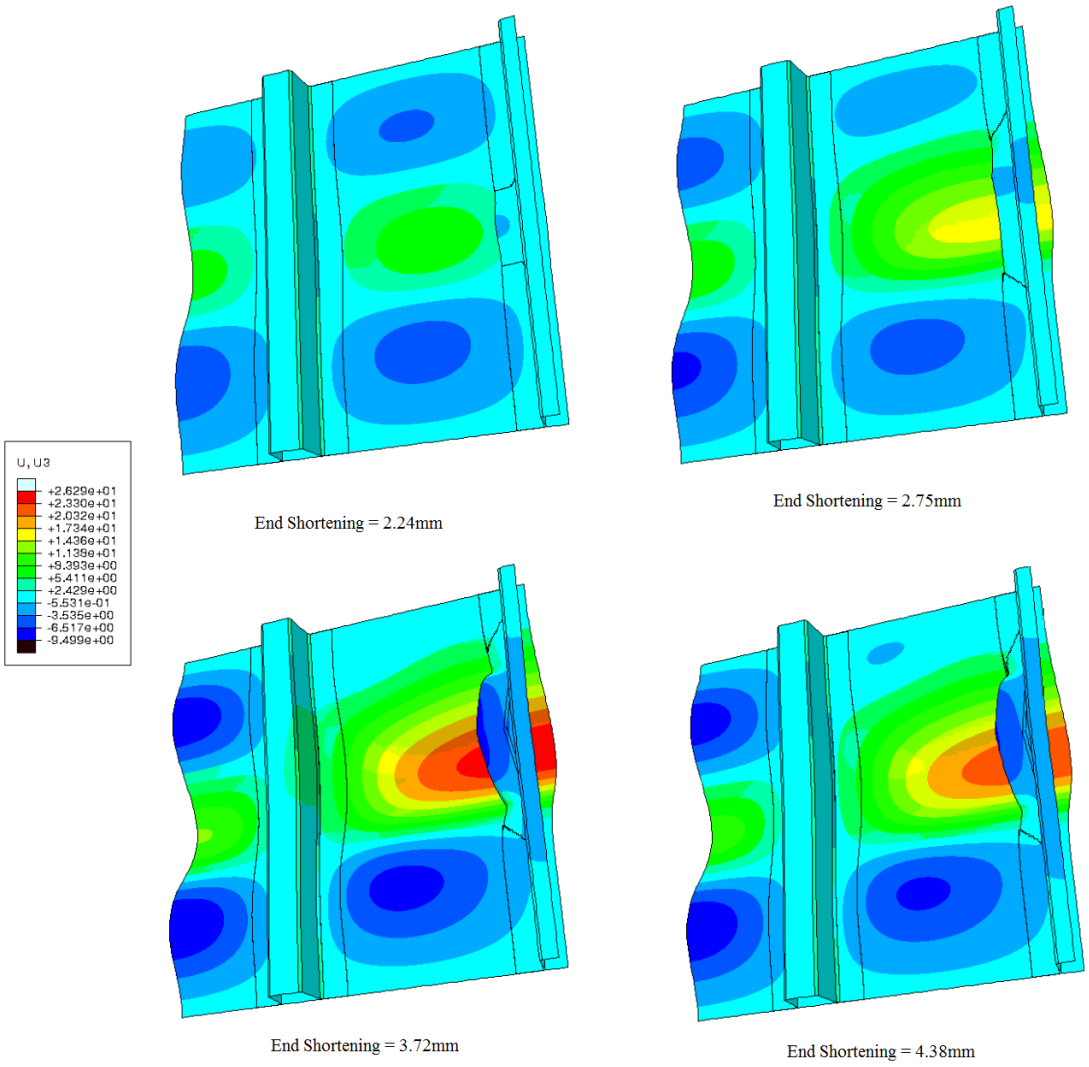

Figure 93: Plate deformations for 150mm, 20%, Debond for Nominal Imperfection and Stiffener Spacing 475mm

5.5 Stiffener Height

The effect of stiffener height is investigated for tall and squat stiffeners compared to the reference case. For each panel the effect of central debonds with increasing size is investigated to assess their damage tolerance.

For the intact case the failure mechanisms are similar to the reference case however stiffener debonding becomes more prominent for the squat stiffener and shear failure in the flange plate and web are critical for the tall stiffener. Figure 94 shows the effect of stiffener height on the failure mechanisms for the intact and large central debond cases. Considering the intact case there is a slight increase in local plate buckling, stiffener buckling, panel buckling and the damage initiation load as the stiffener height increases and a more pronounced increase in the ultimate load. Crack propagation is shown to increase from the squat to square stiffener but shows a decrease as the stiffener becomes tall. The increased second moment of area of the tall stiffener prevents the deformation of the stiffener causing an increased discrepancy in the stiffness between the plate and the top-hat and a reduction in the crack propagation for the tall relative to the square stiffener for the intact case. The crack propagation is stable and the panel can carry increased load during crack propagation.

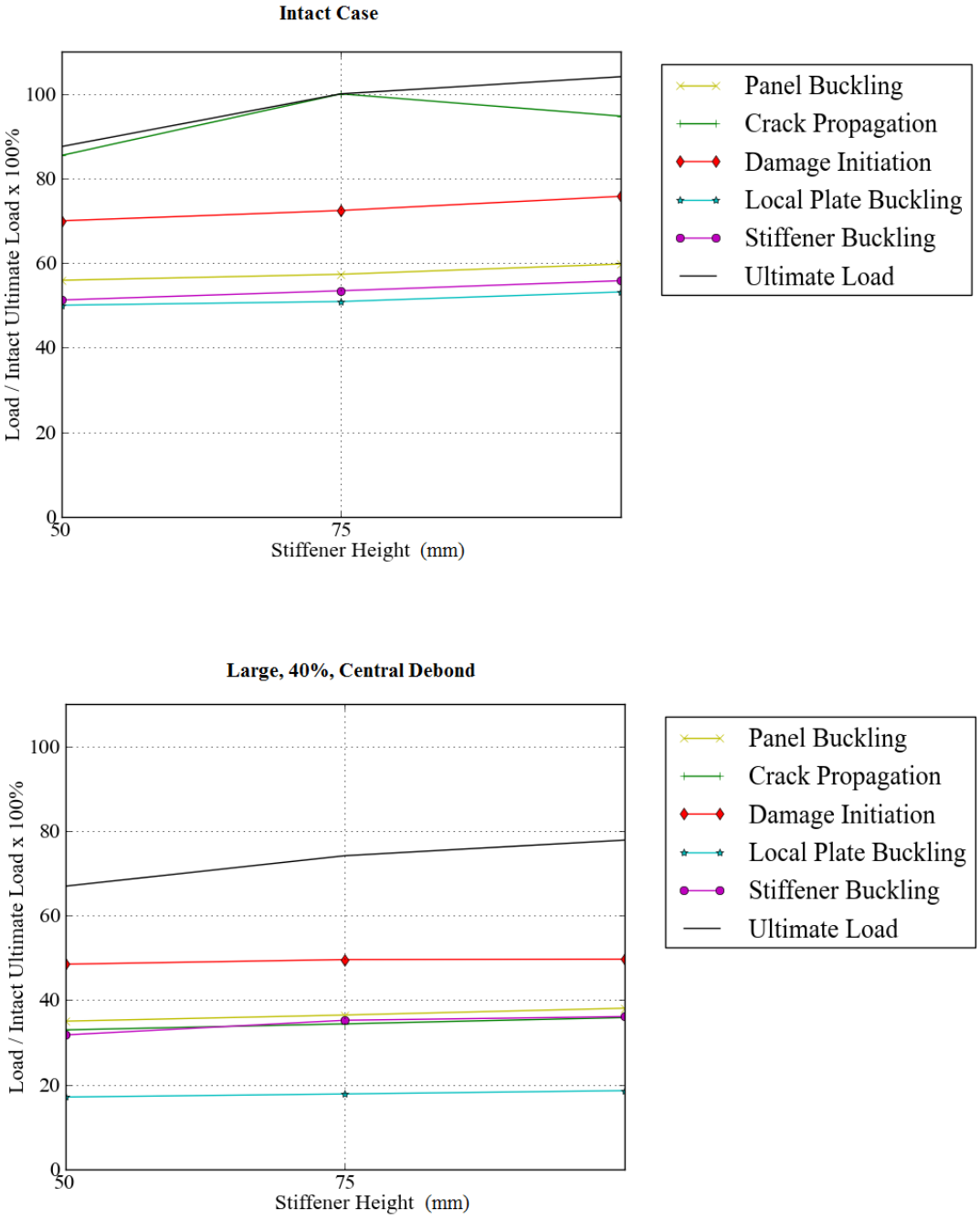

Figure 94: Assessment of Stiffener Height

Figure 95 shows the failure maps for squat, square and tall stiffeners with heights of 50mm, 75mm and 100mm for increasing central debond size. The pattern of failure mechanisms is similar between the stiffener ratios with a gradual reduction from the intact case to 27% debond, a marked reduction in ultimate strength between 27% and 33% and a plateau in debonds between 33% and 47%. The tall stiffener shows a more marked reduction in

the ultimate strength from the intact case to a debond size of 27% as crack propagation occurs at reduced loads compared to the square and squat cases. The three stiffener heights show a consistent trend of 75% ultimate load at the plateau. However the initial failure mechanisms such as local buckling, crack initiation, stiffener buckling and damage initiation occur at similar loads for these large damaged case.

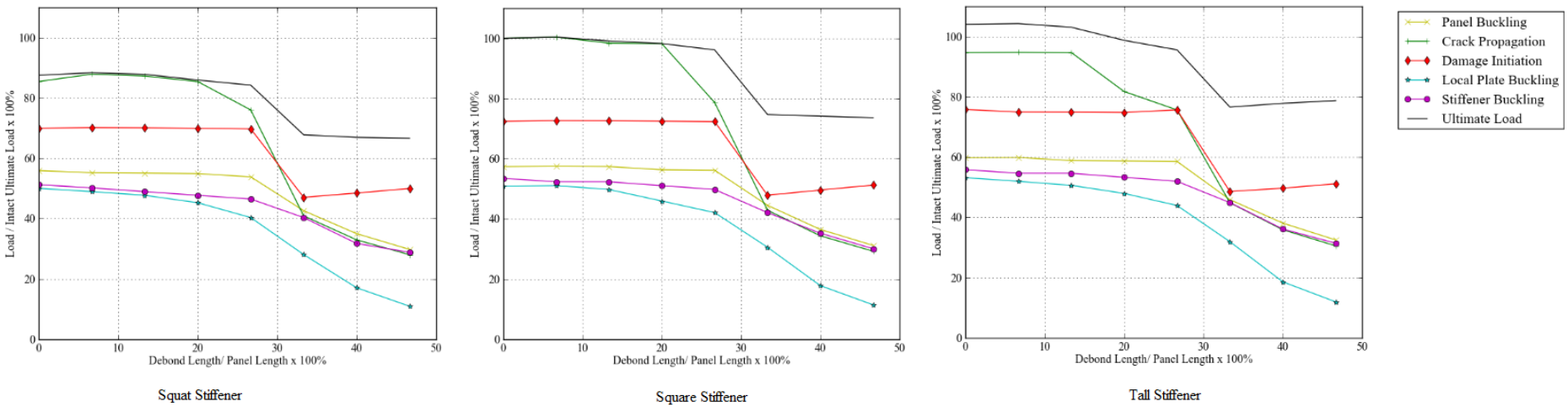

Figure 95: Failure Mechanisms for Increasing Central Debond for Squat, Square and Tall Stiffeners

5.6 Half Stiffener Debond

The effect of debonding half of the stiffener i.e. only one flange, is investigated using a full model containing three longitudinal stiffeners and a nominal imperfection. The failure map for increasing debond size for a central debond is shown in figure 96. The half debond shows the same overall trends in the failure map for increasing debond size; with limited reduction for debonds up to 27%. For large debonds the ultimate loads are seen to decrease by approximately 13% at the critical load and then plateau. This critical point corresponds to the mode switching of the negative inflection beneath the debonded flange causing increased mode I opening. In these cases the switch to the negative inflection is seen only on the debonded side whilst the intact bays on the right of the panel remain positive. The increase in this plateau load compared to the full stiffener debond is due to the restriction of the plate deformations by the second bonded flange of the central stiffener and may also be attributed to the asymmetry of the buckling mode shape. Debonding of the intact flange of the central stiffener is not observed in any of the cases and the failure criterion at the cohesive elements in this interface show only a nominal increase compared to the flanges of the supporting stiffeners. The failure criterion during crack propagation for a large debond is shown in figure 97.

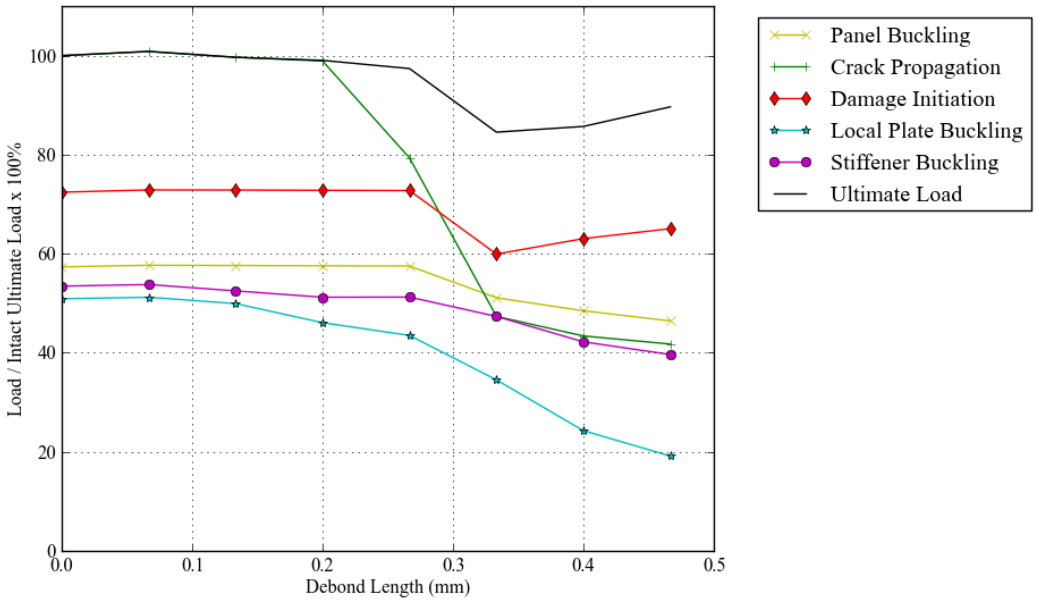

Figure 96: Failure Mechanisms for Half Central Debond for Increasing Debond Size

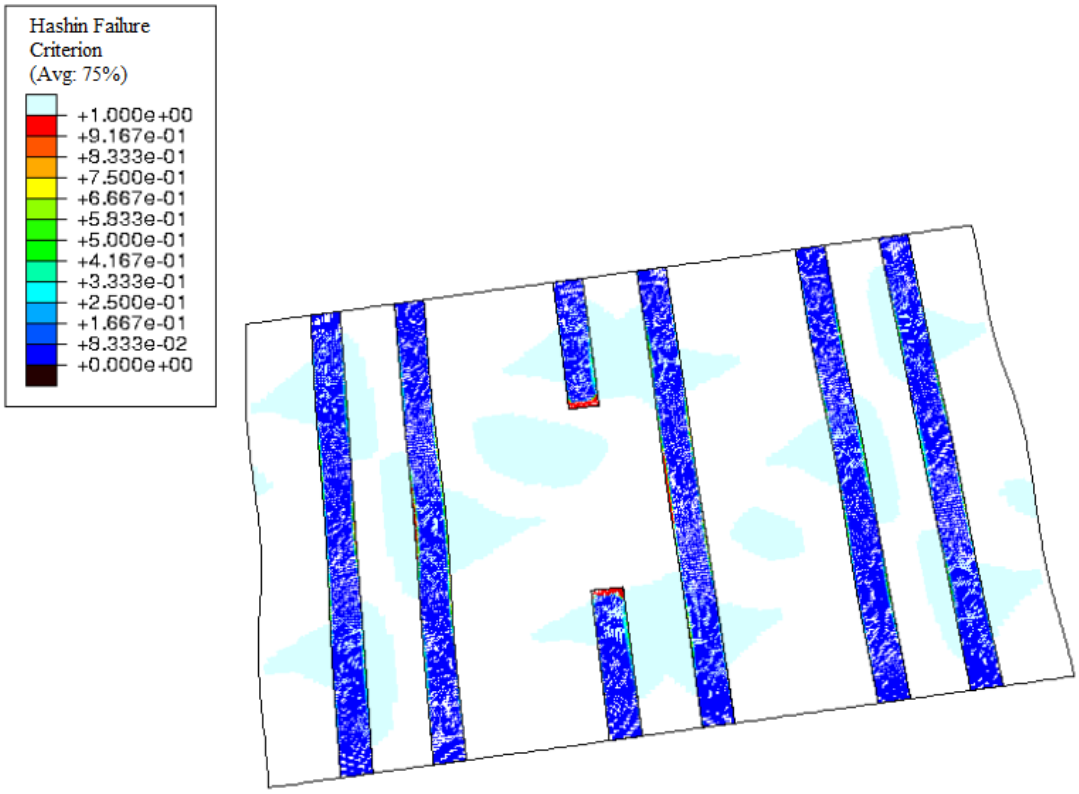

Figure 97: Failure Mechanisms for Half Central Debond for Increasing Debond Size

5.7 Comparison of Plate Thickness

The effect of plate thickness on the intact panel failure mechanisms is shown in figure 98 for plate thickness from 5mm to 17.5mm. For smaller plate thicknesses panel buckling is observed prior to damage initiation showing a marked change in stiffness of the panel as the plate buckles. These panels show considerable post-buckled strength with panel buckling occurring at 34% of the ultimate strength for a 5mm plate and 84% for a 10mm plate. A panel with plate thickness of 12.5mm or greater has uniform stiffness up to ultimate failure and does not exhibit panel buckling. Localised failure initiates in the center of the plate in the web of the stiffener following stiffener and plate buckling. Collapse of the panel is then rapid with failure induced in the plate, stiffener and bond at 99% of ultimate failure. There exists a post-buckled strength with regard to stiffener buckling although this is minimised at a plate thickness of 12.5mm and becomes more significant for increasing plate thickness. As the local plate and stiffener buckling is defined in terms of the change in out-of-plane deformation of the stiffener end shortening buckling can occur without significant deformation of the stiffener or plate itself. The out-of-plane deformations of the plate stiffener reference points are shown at 95% of the ultimate load for increasing plate thickness in figure 99. It is observed that without panel buckling the stiffener and plate deformations are less significant reaching a magnitude of only 0.24mm at 95% ultimate load compared to 0.9mm-2.9mm for the smaller plate thicknesses. It is therefore assumed that the buckling mode shape and interactions of the plate deformation and buckling modes have a reduced influence on the damage tolerance. The damage tolerance of a 15mm thick plate is investigated for comparison.

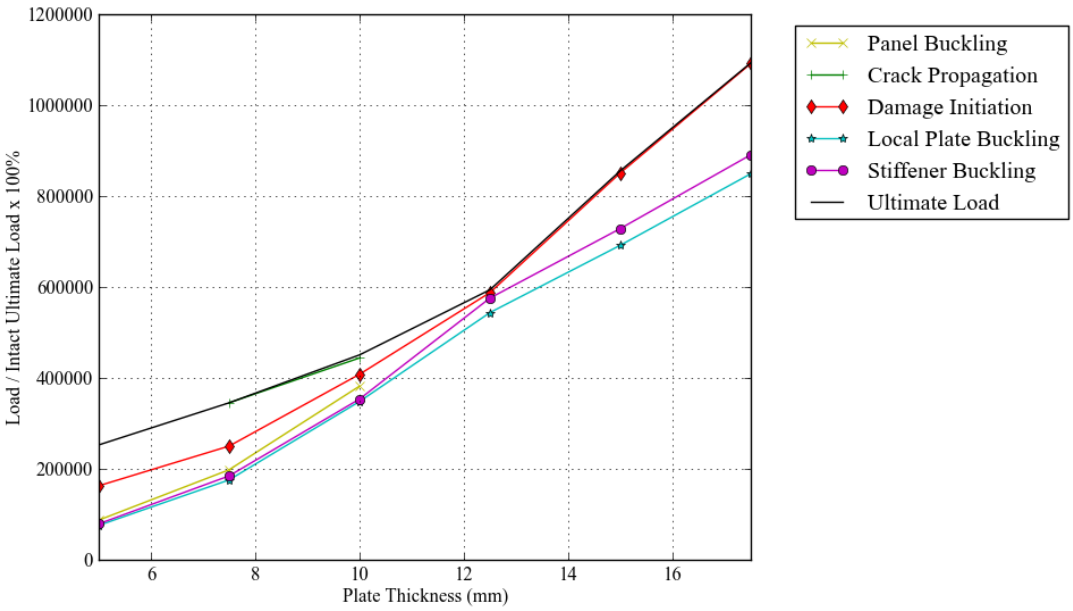

Figure 98: Failure Mechanisms for Increasing Central Debond for Increased Plate Thickness

The failure mechanism map for a central debond increasing in size is shown in figure 100 for a plate thickness

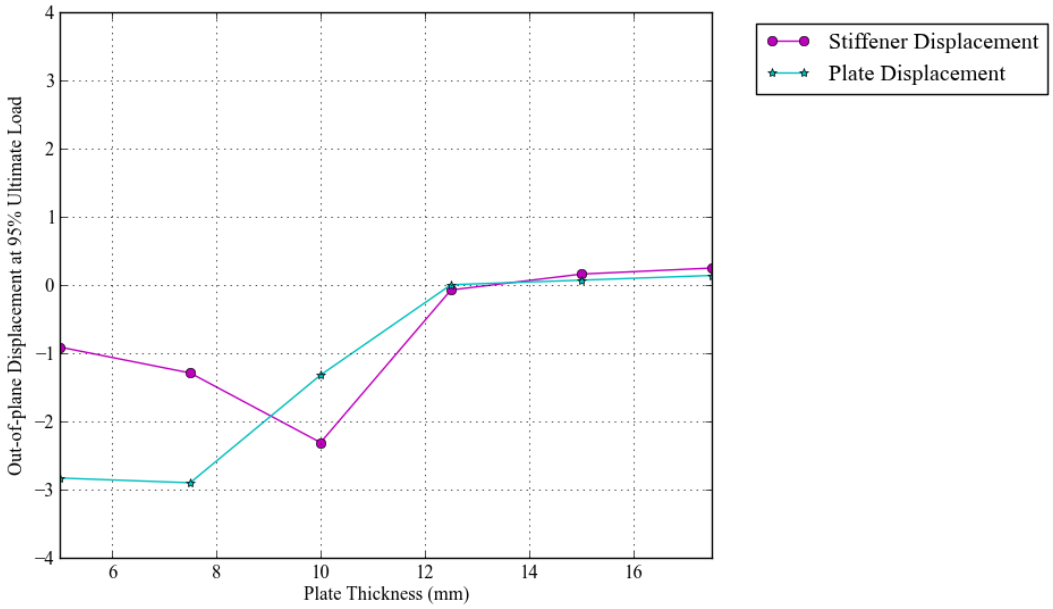

Figure 99: Stiffener and Plate Out-of-plane Displacement at 95% Ultimate Load for Increasing Plate Thickness

of 15mm. For small debonds, less than 15% of the panel length, there is only a limited deviation in the ultimate strength and damage mechanisms. For debonds greater than 15% there is a significant reduction in both the ultimate strength and failure mechanisms. At 33% debond there is a linear reduction in local plate buckling, damage initiation, crack propagation and ultimate load rather than the plateau observed for the reference case with thinner plate thickness. Debonds from 15-33% ultimate failure is due to the debonding of the outer, initially intact, stiffener whereas for debonds greater than 33% ultimate failure is driven by panel buckling as the debond grows to approximately 60% of the panel length. Between 53% and 60% the ultimate strength is seen to plateau and failure is due to buckling of the supporting stiffeners. This plateau occurs at increased debond length compared to the reference case, which has a smaller plate thickness. The increased second moment of area of the plate leads to reduced deflections during buckling and therefore reduced opening moment at the debond crack tip therefore a larger debond size is required to make crack propagation as significant.

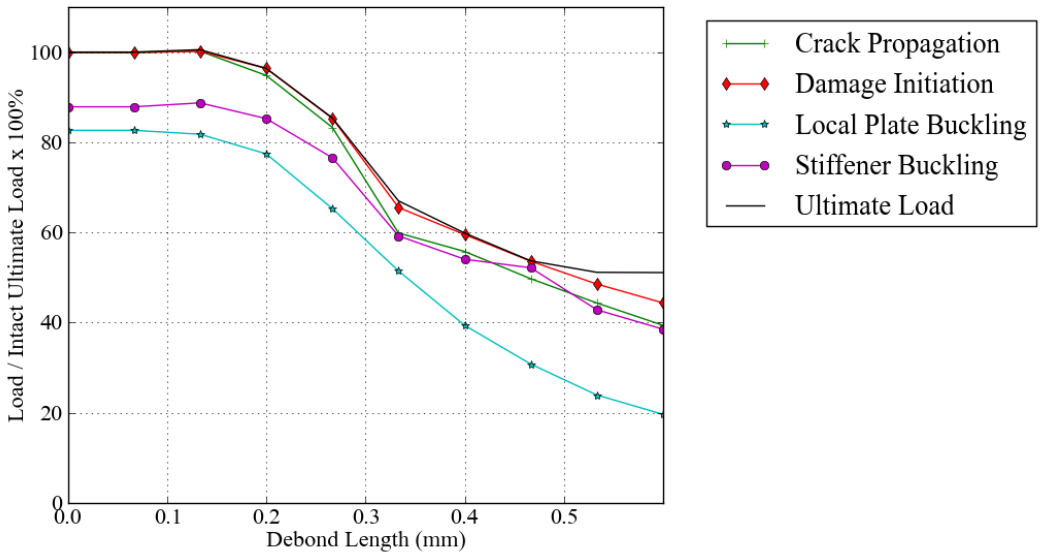

Figure 100: Failure Mechanism Map for 12.5mm Plate Thickness Increasing Debond Central Debond

5.8 Comparison of Stiffener Type

The effect of debonds in the study above is compared to the literature on open section stiffeners. Yap [23] investigated the effect of delamination size on T-stiffened panels. Yap found that the T-stiffened panels also exhibited a significant post-buckled strength; for the intact case the buckled load represented 55% of the ultimate load which is comparable to the top-hat-stiffened panel tested here where the reference case buckles at 57.3%. Yap has not stated the scale of the imperfection used in the T-stiffened study and it is assumed that a nominal imperfection was applied and is compared to the reference case with a nominal imperfection. Yap does not consider material degradation or failure and therefore, the effect of debond size on the ultimate load and damage failure mechanisms cannot be compared.

It is shown in this study, that for the top top-hat stiffened reference case local plate buckling becomes significant at a critical load of between 27% and 33% which is equivalent to the length of the half sine wave deformations for this panel. For debonds greater than this critical load debond crack propagation is driven by stiffener buckling. The effect of debond size was investigated by Yap [150] for 'T'-stiffeners. Yap's failure map for increasing debond size is shown in figure 101 for local buckling, global buckling and damage initiation; Yap has not defined the critical point determining local and global buckling. The T-stiffened panel is analysed in the context of a no-growth damage philosophy whilst considering a panel limit load which in this case is calculated at 66.6% of the ultimate load and is shown at 160kN. Yap found debonds representing 10%-22% of the panel length to be the most critical as local buckling resulted in debond crack opening below the limit load, 66% of ultimate load. The critical point occurs at 10% debonds when local and global buckling occurs simultaneously. Yap found that for debonds greater than 22% the crack front was no longer the critical region and that the neighbouring stiffener also became critical but that the debond crack failed to propagate due to the thinness of the stiffener flange. Yap found that skin buckling away from the stiffener was not enough to initiate debond crack growth as the deformed state of the stiffener had a larger influence on debond crack growth. In the T-stiffener panel the buckling of the plate and the T-stiffener is inherently linked. The flange increases the laminate thickness to 284% of the plate thickness buckling of the plate causes significant deformation in this web and trips the web of the stiffener. Top-hat stiffened panels have a different definition of global and local buckling due to the torsional rigidity of the stiffener, preventing stiffener tripping being coincident with global plate buckling. However section 5.2.2 has shown that top-hat stiffeners with a forced imperfection debond crack propagation may be initiated prior to stiffener buckling suggesting that manufacturing or material imperfections can cause debond crack propagation at reduced load depending on the debond location. No comparison to plate imperfection has been made by other authors.

This chapter has shown that location dependence is relative to the buckled peaks and is critical where the global buckling peak deforms away from the stiffener. This confirms trends seen by Orifici et al. [25], Yap [150] and Wiggenraad et al. [6] for open section stiffeners. It is shown here that local buckling affects the global buckling for debonds representing 40% of the panel length however location dependence is still observed in the debond crack propagation load although it has little influence on the ultimate failure load. Yap [150] showed for T-stiffeners that debonds greater than 10% of the panel form local buckling prior to global buckling and that the location along the stiffener became less critical. Local buckling would influence the subsequent global buckling mode shape and

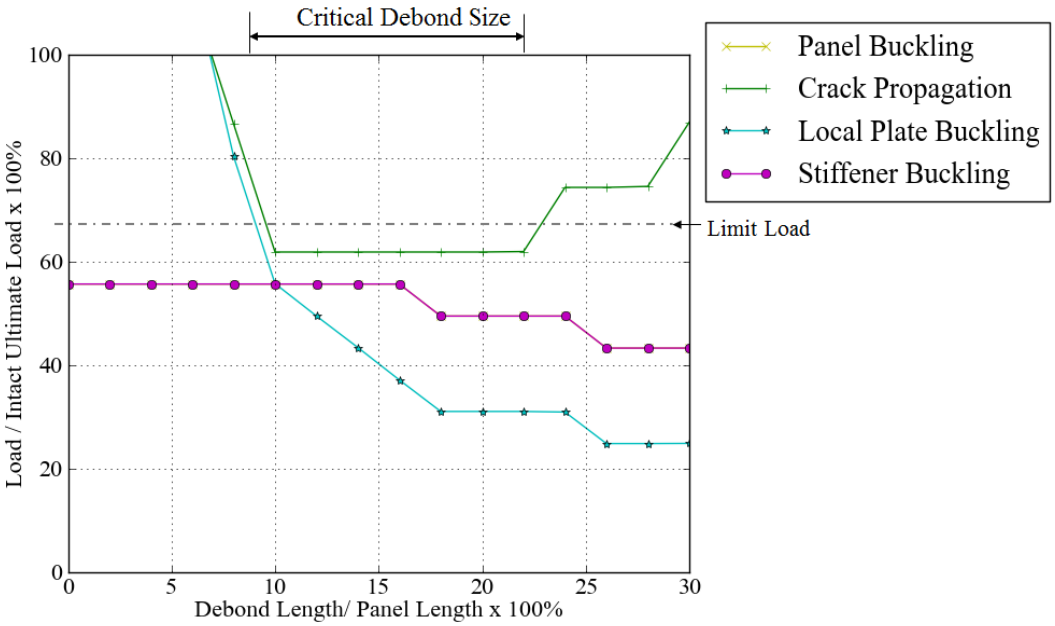

Figure 101: Yap [23]: Analysis of Debond Size

the onset of failure. It is shown here that this effect is less prominent in top-hat stiffened panels due to increased torsional rigidity preventing stiffener tripping.

The study of panel topology in this paper showed that stiffener height has little effect on the buckling load or damage tolerance which remains fixed as the ultimate strength increases with stiffener height. Stiffener spacing is shown to affect both the damage tolerance for large debonds and the critical debond size where the buckling mode shape shows a significant deflection beneath the debond and debond crack propagation becomes more prominent. Gadke et al. [149] also investigated the effect of top-hat stiffener panel topology on the damage tolerance with reference to the buckling load showing that geometric parameters could significantly affect the damage tolerance however where the damage tolerance was improved the load carrying capacity was decreased.

5.9 Applied Lateral Pressure

The damage tolerance is compared for a longitudinal compressive load combined with a small lateral pressure to initiate a post-buckled response. The lateral pressure is applied as a first step followed by increasing longitudinal compressive load. The failure mechanism maps are shown in figures 102 for increasing applied lateral pressure on an intact panel. The combined pressure is shown to have no effect on the ultimate load or damage mechanisms with the exception of stiffener buckling which shows a minor reduction at a pressure of 0.0030MPa, equivalent to 843.75N per stiffener. Similar trends are observed for small and medium central debonds, where the debond rests on the central positive inflection.

For large central debonds the failure mechanism map is shown in figure 103 for increasing applied lateral pressure. The smallest applied pressure tested was 1.25E-4MPa which is equivalent to an applied force of 35.16N per stiffener. An increase is observed in the load for all failure mechanisms and the ultimate load by between 12.5%-150.5%. As the pressure increases further a decrease is observed in the load at which local plate buckling and stiffener buckling occur as the increasing pressure acts to destabilise the unbonded area of both the plate and the stiffener. As a nominal pressure is applied, the buckled mode shape is affected altering the central inflection to a positive inflection, this is illustrated in figure 104 which shows the large central debond case for an applied pressure of 1.25E-4MPa compared to 0Mpa at an end shortening of 2.5mm. The inflection remains positive under a large central debond in contrast to both the equivalent nominal and forced imperfection cases.

Figure 106 shows a comparison of the failure mechanisms for a large central debond for a nominal imperfection, forced imperfection and nominal applied pressure cases. This figure shows that the damage tolerance is significantly improved with an increase in the ultimate strength of 23.5% for an applied pressure compared to both the equivalent nominal and forced imperfection cases and an increase of at least 34% for other damage mechanisms.

For a large central debond the failure of the nominal and forced imperfection follow the following failure mechanisms:

- Buckling of the plate to form a negative central imperfection
- Crack propagation initiating at the debond inner flange edge
- Enhanced plate deformation in the region of the growing debond
- Damage propagation initiating at the centre of the plate laterally across the plate
- Ultimate failure followed by debonding of the outer stiffener

Whilst the nominal pressure case for a large central debond follows the following failure mechanisms:

- Buckling of the plate to form a positive central imperfection
- Crack propagation at the debond inner flange edge
- Crack propagation beyond the anti-node lines

- Shear failure of the plate initiating at the anti-node lines and spreading laterally across the plate
- Ultimate failure followed by debonding of the outer stiffener

Both the lateral pressure and the inversion of the central buckled inflection alter the failure mechanisms. The lateral pressure, increases the plate, panel and stiffener buckling loads by stabilising the by providing a force that pushes the stiffener into the plate. This is in comparison to the nominal and forced imperfection cases, which provide a shape that separates the stiffener and plate. The inversion of the central buckled inflection also reduces the crack opening load and prevents buckling of the plate under the debond.

The failure mechanisms are altered by both the lateral pressure and the inversion of the central buckled inflection. The lateral pressure, increases the plate, panel and stiffener buckling loads by stabilising the plate compared to the nominal and forced imperfection cases. The inversion of the central buckled inflection also reduces the crack opening load and prevents buckling of the plate under the debond.

Similar trends are seen for medium debonds located over the negative inflection. The effect of an offset medium debond is shown in figure 105 for increasing pressure and the failure modes are compared to panels with a forced imperfection, nominal imperfection and applied pressure in figure 107.

The failure mechanisms for an offset medium debond with a nominal imperfection are:

- Buckling of the plate with positive central inflection
- Crack initiation at the debond inner flange edge
- Asymmetric crack propagation towards centre of the plate
- Buckled mode switch to two half sine waves
- Damage initiation in the centre of the plate on the anti-node line and propagate laterally
- Ultimate failure by debonding of the outer stiffener

The failure mechanisms for an offset medium debond with a forced imperfection are:

- Buckling of the plate with negative central inflection
- Crack propagation at the debond inner flange edge
- Damage initiation on the anti-node lines and propagate laterally
- Damage initiation in the centre of the plate on the anti-node line and propagate laterally
- Ultimate failure

The failure mechanisms for an offset medium debond with a nominal pressure are:

- Buckling of the plate with positive central inflection

- Crack initiation at the debond inner flange edge
- Symmetric crack propagation towards centre of the plate
- Damage initiation in the plate centrally below the debond and propagate laterally
- Asymmetric crack propagation towards the centre of the plate
- Further material damage propagation laterally across the plate
- Ultimate failure by debonding of the outer stiffener

The failure mechanisms for the nominal imperfection and nominal applied pressure case are similar however, a significant increase is observed in the load at which damage initiation occurs and the ultimate load by 15% and 7.6% respectively compared to the nominal imperfection offset case therefore showing an improved damage tolerance with nominal applied pressure. This improvement is due to the reduction of the out-of-plane deflections by the applied nominal pressure. The applied pressure causes changes to the buckling behaviour; in the central forced imperfection case the panel buckles into three half sine waves where the anti-node lines provide no limit to crack propagation, therefore the most crack growth is observed of the three panels. The nominal offset imperfection shows asymmetric crack growth as the clamped boundary condition inhibits out-of-plane deformation. The panel switches from 3 half sine waves to two half waves as the crack grows which provides limited impedance to the crack growth. The nominal pressure case remains in a three sine wave configuration with the anti-node lines acting to impede the crack growth and therefore improving the damage tolerance.

Therefore, for large debonds with significant plate deflections a nominal applied pressure can act to increase the damage tolerance of the panel, increasing the ultimate load by 23.5-24.5% compared to the nominal and forced imperfections respectively. For medium debonds a nominal applied pressure may increase the damage tolerance by 7.6-35.8% compared to the nominal and forced imperfections respectively where the debond rests over a negative inflection. Increasing the applied pressure by up to 0.003MPa shows there is little effect on the damage mechanisms and ultimate load of the panel. The effect of the applied imperfection of lateral load to initiate the non-linear response is shown to have a significant effect on the damage tolerance of the structure with a nominal imperfection providing a conservative result.

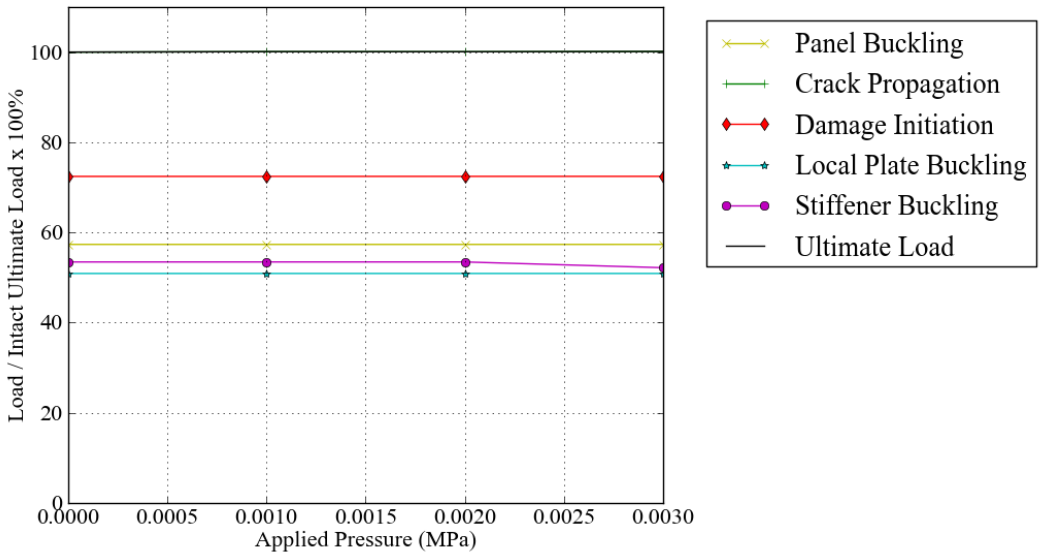

Figure 102: Effect of Combined Lateral Pressure on Intact Panel

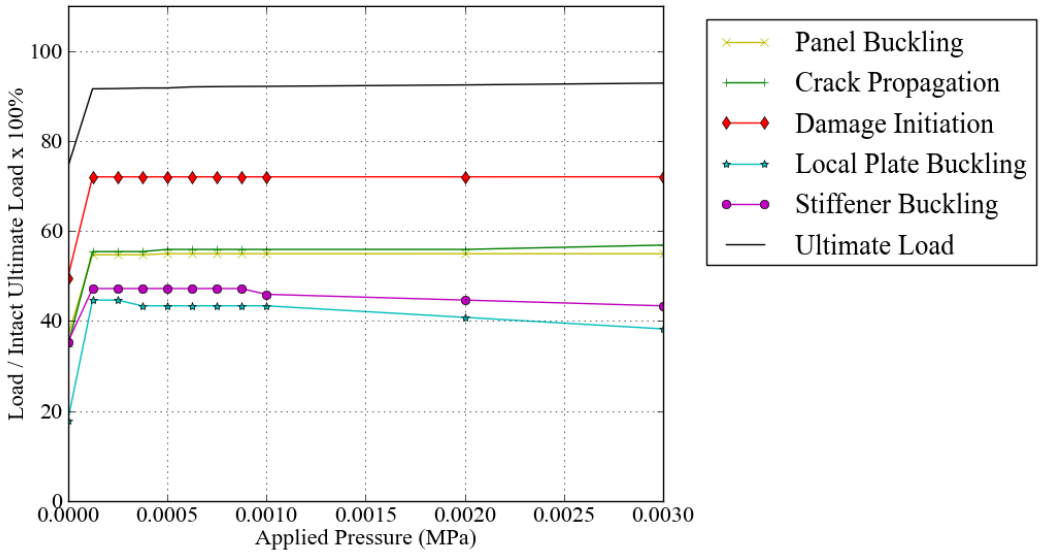

Figure 103: Effect of Combined Lateral Pressure on Large Central Damage Case

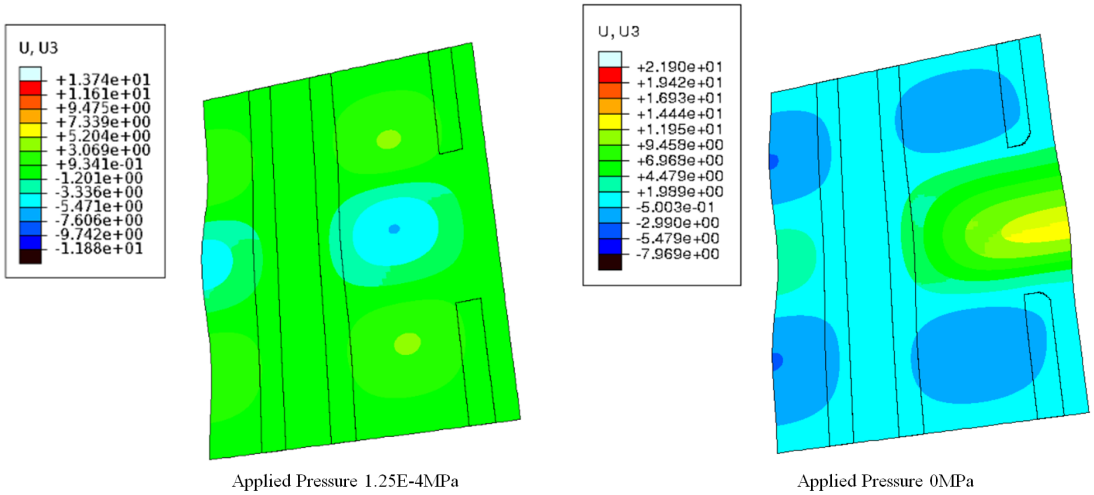

Figure 104: Comparison of Applied Pressure on Large Central Debond At 2.5mm End Shortening

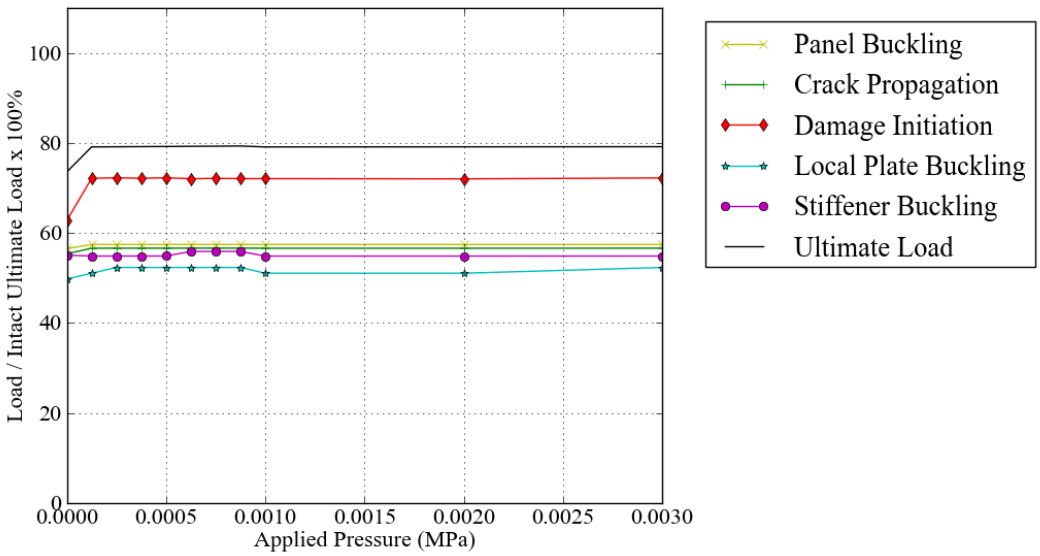

Figure 105: Effect of Combined Lateral Pressure on Medium Offset Damage Case

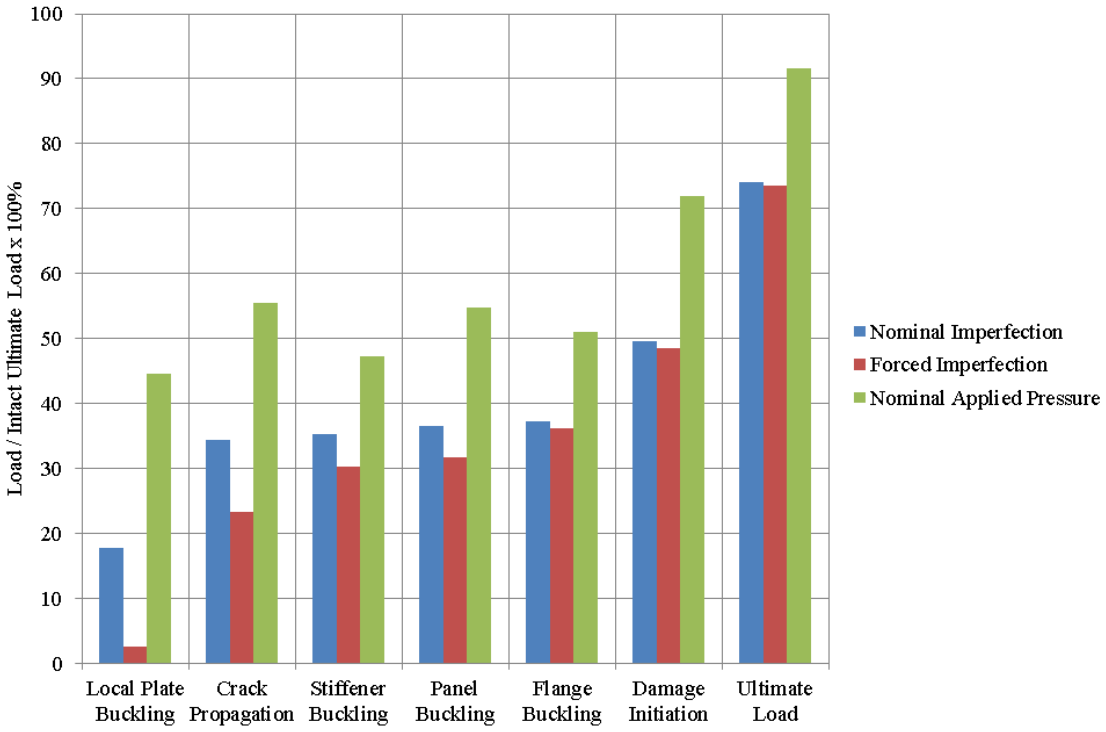

Figure 106: Comparison of Large Central Debond Failure Mechanisms

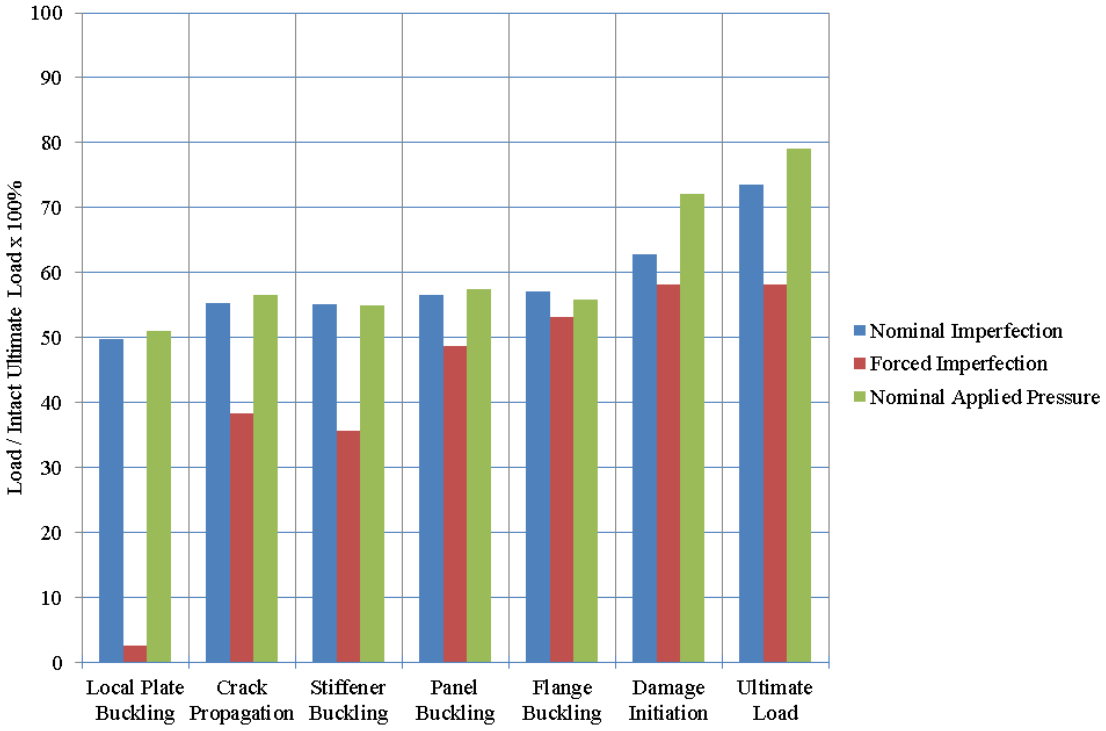

Figure 107: Comparison of Medium Debond Over Negative Inflection Failure Mechanisms

5.10 Summary

The results for the reference panel and modified topology are summarised in figure 108 which summarise the failure mode, debond size and residual strength factor for small, medium and large debond cases. The residual strength factor, RSF, is defined as the ratio of the damaged to intact ultimate fail load. The grey boxes are omitted as they represent nonsensical data whilst cases where crack propagation and stiffener debonding is a prominent failure mechanism is coloured blue. For each case small debonds show limited deviation to the failure mechanisms and ultimate failure compared to the intact case, medium debonds show deviation from the intact case and large debonds affect the buckling mode of the panel.

The analysis shows that the failure mode of the panel and interaction of failure modes changes as the debond size and location changes. Shear failure of the plate in the region of the anti-node lines is the dominant mode of failure for the intact case of the reference panel and small debonds with crack propagation becoming dominant for debonds greater than the critical debond size and location. For all stiffener spacings and locations there exists a critical debond size where debond initiation and growth becomes dominant. At this critical point the buckling mode shape shows a significant deflection beneath the debond and has altered the preferred buckling mode of the plate. This results in mode I opening force at the crack tip and in a reduction in stiffener buckling, significant crack growth and a significant reduction in the ultimate strength. For increasing debond size a plateau exists following the critical point where the ultimate strength remains at greater than 60% of the intact ultimate strength.

Debonding of the stiffener was not shown to be a critical failure mode and occurred during the collapse of the panel following significant material failure with the exception of large debonds aided by a forced negative inflection in the region of the debond.

The effect of the imperfection was assessed for a nominal imperfection shown to have no affect on the buckled mode shape and a forced imperfection scaled to represent those seen in large scale manufacture. Small debonds for both a nominal and realistic forced imperfection are largely location tolerant showing a 5% reduction in ultimate load. The crack propagation for both imperfections and all locations is not a significant damage mechanism. Medium debonds see a more gradual change in mechanism as the debond location changes with crack growth and ultimate failure occurring at increasing load as the debond moves towards the center of the positive inflection for both imperfection cases. Therefore the debond location relative to the plate's buckling mode has a significant impact on the effect of the debond; a positive inflection in the region of the debond pushes the debonded plate and flange together preventing mode I crack growth leading to an increase in damage tolerance. For debonds in the vicinity of the clamped end the deflections and therefore opening moment at the crack tip is reduced suppressing crack growth.

For large debonds the range in deviation in ultimate load and damage initiation load across the range of locations is similar for both imperfection scales. However whilst the nominal imperfection is location independent, the forced imperfections sees a gradual increase in the panel buckling, stiffener buckling and crack propagation load as the debond moves over the positive inflection. Crack propagation is postponed as the debond bridges the anti-node line inhibiting crack growth and effectively reducing the initial debond size. However mode switching into less damage

		Reference Case				Modified Topology				
		Location	**Nominal Imperfection**	**Forced Imperfection**	**Half debond**	**Wider stiffener spacing**	**Narrow stiffener spacing**	**Squat**	**Tall**	**Plate thickness ≥12.5mm**
Intact Case	**Failure Mode**		Material degradation on anti-node lines leading to panel buckling	Material degradation on anti-node lines leading to panel buckling		Material degradation on anti-node lines leading to panel buckling	Material degradation on anti-node lines leading to panel buckling	Debond crack propagation & material failure leading to panel buckling	Material degradation on anti-node lines leading to panel buckling	Crack propagation leading to debonding
Small Debond Case	**Failure Mode**	Largely Independent (change in RSF<6%)	Material degradation on anti-node lines leading to panel buckling	Material degradation on anti-node lines leading to panel buckling	Material degradation on anti-node lines leading to panel buckling	Material degradation on anti-node lines leading to panel buckling	Material degradation on anti-node lines leading to panel buckling	Material degradation on anti-node lines leading to panel buckling	Material degradation on anti-node lines leading to panel buckling	Material degradation on anti-node lines & debonding
	Debond Size	x<26%				x<13%	x<7%	x<27%	x<13%	x<13%
	Residual Strength Factor	RSF≥94%			RSF≥99%	RSF≥98%	RSF≥95%	RSF≥95%	RSF≥95%	RSF≥99%
Medium Debond Case	**Failure Mode**	Location dependent with reduction over negative inflection	Material degradation on anti-node lines leading to panel buckling	Material degradation on anti-node lines leading to panel buckling	Material degradation on anti-node lines leading to panel buckling	Material degradation on anti-node lines leading to panel buckling	Debond crack propagation leading to panel buckling	Material degradation on anti-node lines leading to panel buckling	Debond crack propagation leading to panel buckling	Debonding of outer stiffener
	Debond Size	26%≥X>33%				13%≥X>20%	7%≥X>27%	27%≥X>33%	13%≥X>33%	13%≥X>47%
	Residual Strength Factor	RSF≥71%			RSF≥85%	RSF≥76%	RSF≥58%	RSF≥77%	RSF≥75%	RSF≥52%
Large Debond Case (Buckling mode affected by debond)	**Failure Mode**	Largely Independent (change in RSF<6%)	Debond crack propagation leading to panel buckling	Debond crack propagation leading to panel buckling	Debond crack propagation leading to panel buckling	Debond crack propagation leading to panel buckling	Crack propagation leading to debonding	Crack propagation leading to debonding	Crack propagation leading to debonding	Debonding of outer stiffener
	Debond Size	x≥33%				x≥20%	x≥27%	x≥33%	x≥33%	x≥47%
	Residual Strength Factor	RSF≥71%			RSF≥85%	RSF≥76%	RSF≥58%	RSF≥77%	RSF≥75%	RSF≥52%

Figure 108: Summary of Damage Tolerance of Reference Panel

tolerant configurations means there is little variation in the ultimate strength. For large debonds with a forced imperfection the ultimate strength of the panel is driven by plate failure and following a significant amount of failure the supporting stiffener then debonds centrally at the peak load whereas for nominal imperfections debonding of the supporting stiffener occurs only during the panel's collapse. Plate buckling is shown to occur at much lower loads for all cases with a forced imperfection compared to those with a nominal imperfection. Examination of the central deflection has shown that the initial imperfection alters the plate deformations at lower loads resulting in a marked reduction in the plate buckling load for the forced imperfection case.

The plate buckling mode and length of the half sine wave introduced provides limits to the crack growth length which terminates at the anti-node lines unless mode-switching is present. A larger unsupported span leads to more significant deflections and damage to the web and table of the debonded stiffener causing ultimate collapse at a slightly reduces in load.

Asymmetric buckling modes introduced by large debonds have been shown to introduce torsional bending to the intact stiffener causing premature shear failure in the web resulting in stiffener buckling.

The investigation into the effect of stiffener spacing shows that the intact ultimate strength is dominated by the stiffener's second moment of area and is constant across the spacings studied. The relationship between the ultimate strength and the debond size is similar for the three stiffener spacings; smaller debonds have little effect on the ultimate strength, at a critical debond size there is a marked drop in the ultimate strength followed by a plateau in ultimate strength for larger debonds. This critical debond size varies depending on the stiffener spacing occurring between 13% and 33% of the panel length. The narrowest stiffener spacing exhibits limited post-buckled strength with panel buckling occurs at 99.9% of the ultimate load followed by rapid collapse. The ultimate strength is determined by crack propagation driven by plate buckling for both the intact and damage cases. The panels buckling mode is affected by the debond for small debonds (0-16%) switching between two and three half sine waves. For stiffened panels with significant post-buckled strength (medium and large stiffener spacings) the intact ultimate strength for small debond cases are driven by material failure which exacerbates the stiffener buckling leading up to ultimate collapse. Following the critical debond size the panel failure is dominated by crack propagation and stiffener buckling which follows plate buckling. It is shown that for the reference and widest stiffener spacing that small and medium debonds that crack initiation does not propagate or diminish the ultimate strength of the panel significantly and that a 'no crack growth philosophy' results in conservative results.

The investigation into the effect of stiffener height shows local plate buckling is independent of the stiffener height where as the stiffener buckling load, panel buckling and damage initiation load increase as the stiffener height increases and a more pronounced increase is observed in the crack propagation and ultimate load. The tall stiffener shows a more marked reduction in the ultimate strength from the intact case to a debond size of 27% of the panel length. The increased second moment of area of the tall stiffener prevents further deformation of the stiffener causing an increased difference in the stiffness between the plate and the top-hat and a reduction in the crack propagation for the tall relative to the square stiffener. The crack propagation is stable and the panel can carry increased load during crack propagation.

It is shown that increasing the plate thickness to 12.5mm changes the failure mechanism with limited post-buckled strength and results in catastrophic collapse, stiffener debonding and gross material failure. It is shown these panels are still damage tolerant to small debonds, less than 15% of the panel length and for debonds of less than 33% debonding of the outer stiffener is the main failure mode.

Debonds lying under one flange of the stiffener are shown to exhibit similar trends for debond size as full width debonds. It is shown that debonding of the other flange is not observed for any of the damage cases.

For both T-stiffeners and top-hat stiffeners the critical location of the debond corresponds with the position on the panel where the global buckling peak deforms away from the stiffener flange. For T-stiffeners it was shown that if the debond was large enough to form local buckling prior to global buckling the location along the stiffener became less critical. The formation of local buckling would influence the subsequent global buckling mode shape and the onset of failure was therefore independent of the debond location. For the top-hat stiffened panel only large debonds representing 40% of the panel length local buckling affects the global buckling of the panel however location dependence is observed in the crack propagation load although it is shown that this has little influence on the ultimate failure load.

Yap [23, 150] found that the peeling stress resulting from the skin buckling away from the stiffener was not enough to initiate crack growth and that for T-stiffeners the deformed state of the stiffener had a larger influence on the crack growth. Top-hat stiffened panels have a different definition of global and local buckling due to the torsional rigidity of the stiffener which prevents the stiffener tripping being coincident with global plate buckling. For top-hat stiffeners it is apparent that local buckling of the plate becomes a significant failure mechanism at a critical load between 27 and 33% for the reference case which is equivalent to the length of the half sine wave deformations for this panel and the stiffener spacing. For debonds greater than this critical load crack propagation is driven by stiffener buckling. However for a panel with a forced imperfection crack propagation may be initiated prior to stiffener buckling suggesting that manufacturing or material imperfections can cause crack propagation at reduced load depending on the debond location.

An applied nominal lateral pressure has little effect on the intact panel however is shown to increase the damage tolerance significantly for large debonds compared to cases without for both a nominal and forced imperfection.

6 Experimental Characterisation

Section 2.1 summarises the experimental work characterising the mechanical and interface properties of heavy weight woven glass vinylester. It is shown that there is a lack of a complete set of data relevant to modelling debond and delamination damage. Coupons were manufactured by a local fibre glass boat building, Composite Mouldings, to create typical marine composites. Material characterisation tests are conducted for tensile, compression, shear and flexure tests to establish the modulus and strength. Interface tests are conducted in mode I and mode II for a co-cured and post-cured and compared to assess the effect of the post-cured interface containing a chopped strand mat layer. Chopped strand mat (CSM) layer are often included in large composite post-cured joints to provide an infusion path between the two components. Testing is then conducted on a number of top-hat stiffened panels cut from a large scale infusion under four point bend. This test assesses the load deflection response of the sample as well as the crack propagation and failure mechanisms.

6.1 Mechanical Characterisation

The materials considered is a Scott Bader Crystic Resin VE679-03PA with a balanced woven roving of 600gsm typical of the marine industry for resin infusion based builds. The resin is a pre-accelerated, DCPD modified, vinylester resin, developed for use as an infusion resin which has Lloyd's Register approval. As the fabric is balanced the material is tested in a single direction parallel to the fibre direction. Test standards are not available for woven fabrics therefore uni-directional or multi-direction standards are used where appropriate or as a guide. Tensile, compressive and shear tests are conducted along with mode I and II tests to assess the interface properties for a co-cured and post-cured specimen with a CSM interface layer. This data provides a full set of the necessary characterisation data for a typical lay-up which is lacking in the literature.

6.1.1 Tensile Young's Moduli and Strength

Coupons were tested under tension to BS ISO EN 527-4:2009. Type 3 coupons are used as defined in the standard: 250mm in length and 25mm width with 150mm between the end tabs which are 50mm in length' two thicknesses are investigated, 7.5mm and 5mm. Two strain gauges are mounted to the front surface one parallel and one perpendicular to the loading direction.

The in-plane stress-strain curves for the two sample thicknesses are shown in figure 109. There is an initial hardening phase, as described by Cox [17] and Zhou and Davies [16], which is attributed to 'inelastic' straightening of the crimped in-plane tows which was visually observed during the experiments. This results in a bi-linear stress-strain relationship exhibited for the 5mm samples and to a lesser extent for the 7.5mm samples. The initial and final stiffness are shown in table 23. The coefficient of variation for each value is low, with a maximum of 6.68%, giving good confidence in the results.

It is observed that the 'knee', or change in stiffness occurs at approximately 82MPa for the 5mm samples and 64MPa for the 7.5mm samples. It was hypothesised by Zhou and Davies [16] that the 'knee' occurs at the typical

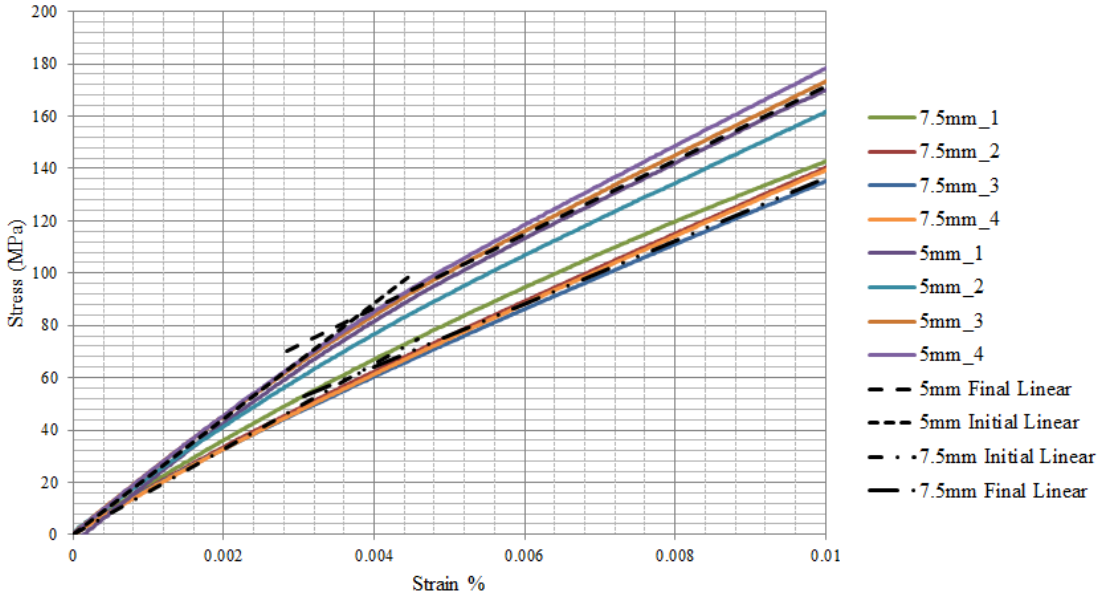

Figure 109: Tensile Stress Strain Relationship of 5mm and 7.5mm Coupons

	Number of Specimens	Average (MPa)	Coefficient of Variation
5mm initial slope	4	22100	6.68%
5mm final slope	4	14100	3.00%
7.5mm initial slope	4	16300	4.94%
7.5mm final slope	4	12000	2.61%

Table 23: Bilinear Moduli of 5mm and 7.5mm Samples in Tension

tensile stress of polyester. The experiments here show that the load at which the knee occurs is between 50 and 85MPa in the order of the tensile strength of the resin, 53-64MPa, as quoted by the manufacture ScottBader [172].

It is shown here that the reduction in stiffness is 36.4% to 26.0% for samples of 5mm and 7.5mm respectively. Ivanov et al. [173] reported that the meso-stress distribution and crack density is different for inner and outer layers of the laminate and this meso-stress distribution depends upon the stacking sequence, ply shift and the number of plies in the laminate. Therefore, the variation shown in figure 109 and table 24 are in part attributed to variation in the weave structure and ply stacking however, another more dominant factor is likely to be the number of plies in the sample, change in fibre volume fraction and the degree of compaction. It is suggested that the reduction in resin content could restrict the plastic deformation allowable between fibres and a more rapid coalescence of micro-cracks resulting in a reduced resistance to fibre straightening.

Welsh et al. [18] investigated 510gsm plain weave glass vinylester composite under biaxial tests and established an in-plane bi-axial failure envelope. Welsh also identified a non-linearity in the overall stiffness under tensile load representing a 'knee' and quoted the initial and final stiffness to be 27.4 and 19.2GPa which are stiffer than the results here, although the specific vinylester and manufacturing method are not stated. However a reduction of 29% in the stiffness is observed which is similar to the reduction estimated here giving confidence in the results.

	Number of Specimens	Average	Coefficient of Variation
Poisson's Ratio	6	.139	17.7%

Table 24: Poisson's Ratio

	Number of Specimens	Average (MPa)	Coefficient of Variation
Young's Modulus	5	31240	4.27%
Compressive Strength	5	272.5	8.46%

Table 25: Compression Tests Results

The Poisson's ratios were calculated between applied stresses of 100MPa and 200MPa and are shown in table 24.

6.1.2 Compressive Young's Moduli and Strength

Compressive tests are performed to BS ISO EN 14126:1999. Coupon type B1 is used with 110mm length, 5mm thickness, 10mm width and 10mm between the end tabs of 50mm in length. 2mm end tabs are manufactured from ± 45 biax with the fabric 0° direction aligned along the load direction. It was not possible to machine the tabbing flat however little deviation was observed in the thickness of both the tabbing and test laminates. Load, displacement, and strain gauge readings were recorded continuously until the specimen fractured. The compression modulus and strength were calculated using equation 22 where $\sigma_c^{''}$ is the compressive stress at $\varepsilon_c^{''} = 0.0025$ and $\sigma_c^{'}$ is the compressive stress at $\varepsilon_c^{'} = 0.0005$. Strain gauges were mounted on the front and back surfaces of the specimen and aligned with the loading direction. The average strain is calculated from the front and back surfaces of the coupon.

$$E_c = \frac{\sigma_c^{''} - \sigma_c^{'}}{\varepsilon_c^{''} - \varepsilon_c^{'}} \tag{22}$$

It is noted that the strain on the front and back gauges remained negative through the tests indicating that global buckling of the specimen did not take place in any of the samples. Samples where shear failure occurred at the tabbing-coupon interface were discarded. The results are summarised in table 25 and the load deflection curves are illustrated in figure 110. The Young's modulus and compressive strength have a coefficient of variation of 4.27% and 8.46% respectively showing low variation of the results and good confidence in repeatability for the tests given the inherent properties of the material.

The failure mode is recorded as localised crushing and buckling of the plies, shown in figure 111, with delaminations between the plies. The standard lists acceptable modes of failure for UD specimens including in-plane shear, complex, through-thickness shear, splitting and delamination. For woven laminates both in-plane and through-thickness shear are not applicable. Localised crushing and buckling of the plies is evident with delamination between the plies. As buckling is localised failure is deemed acceptable in these samples.

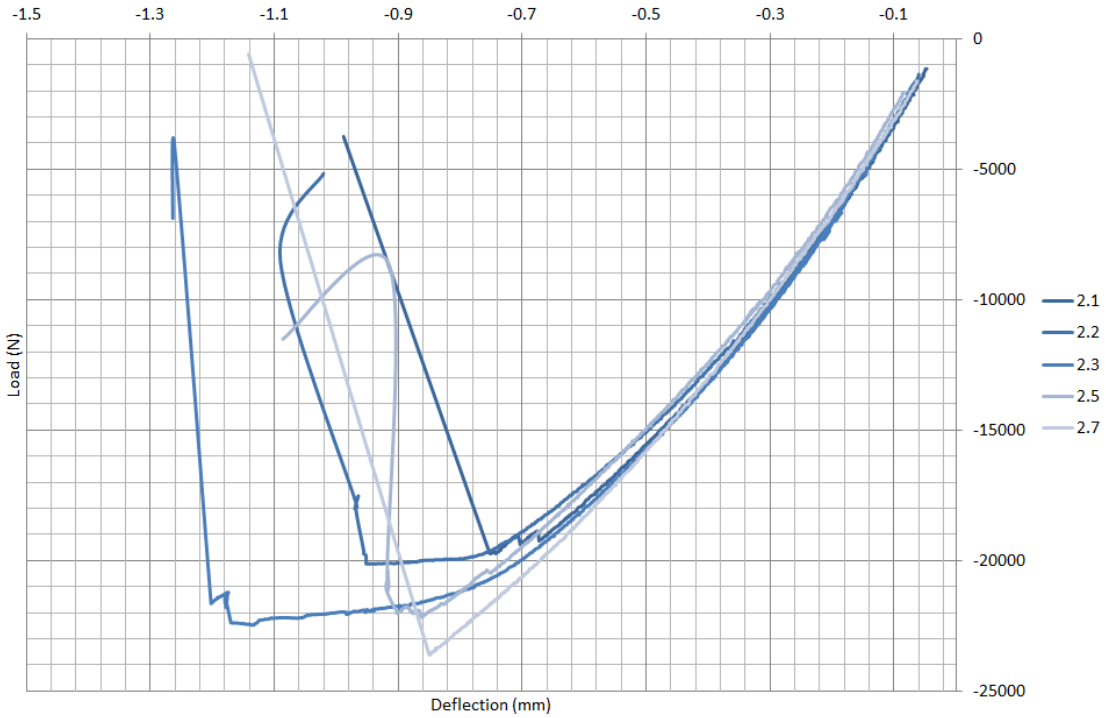

Figure 110: Compressive Test Load End Shortening Curve

	Number of Specimens	Average	Coefficient of Variation
Shear Strength	5	57.9MPa	2.54%

Table 26: Shear Tests Results

6.1.3 Shear Moduli and Strength

Shear tests are performed to BS ISO 14129:1997 with the exception of the specimen thickness. The standard requires for materials with layer thickness greater than 0.125mm that the laminate shall consist of 16 layers. It is required that the specimen fails at a load that can be applied by the grip pressure of the test rig. Therefore, a sample of 5mm was tested to ensure the manufacturing method and fibre volume fraction were similar to the other characterisation tests. Panels are manufactured at 45°to the loading direction with coupons of length 250mm, 5mm thickness and 25mm width. Strain is assessed by strain gauges parallel to and perpendicular to the loading direction. The in-plane shear strength and strain are calculated by $\tau_{12} = \frac{F_m}{2bh}$ and $\gamma_{12} = \varepsilon_x - \varepsilon_y$ where F_m is the load, b is the coupon width, h is the coupon thickness and ε_x and ε_y are the strains in the parallel and perpendicular directions. It is clear for the material tested the test does not represent a pure shear mode however it does provide the in-plane shear stress to strain relationship required for an anisotropic stiffness matrix.

The load defection curve is shown in figure 112 and the shear stress strain relationship is shown in figure 113. In both graphs the relationship is initially linear up to a shear strain of approximately 0.002 followed by a gradual curve. This non-linear behaviour is due to matrix yielding which is attributed to the 'scissoring' action of the

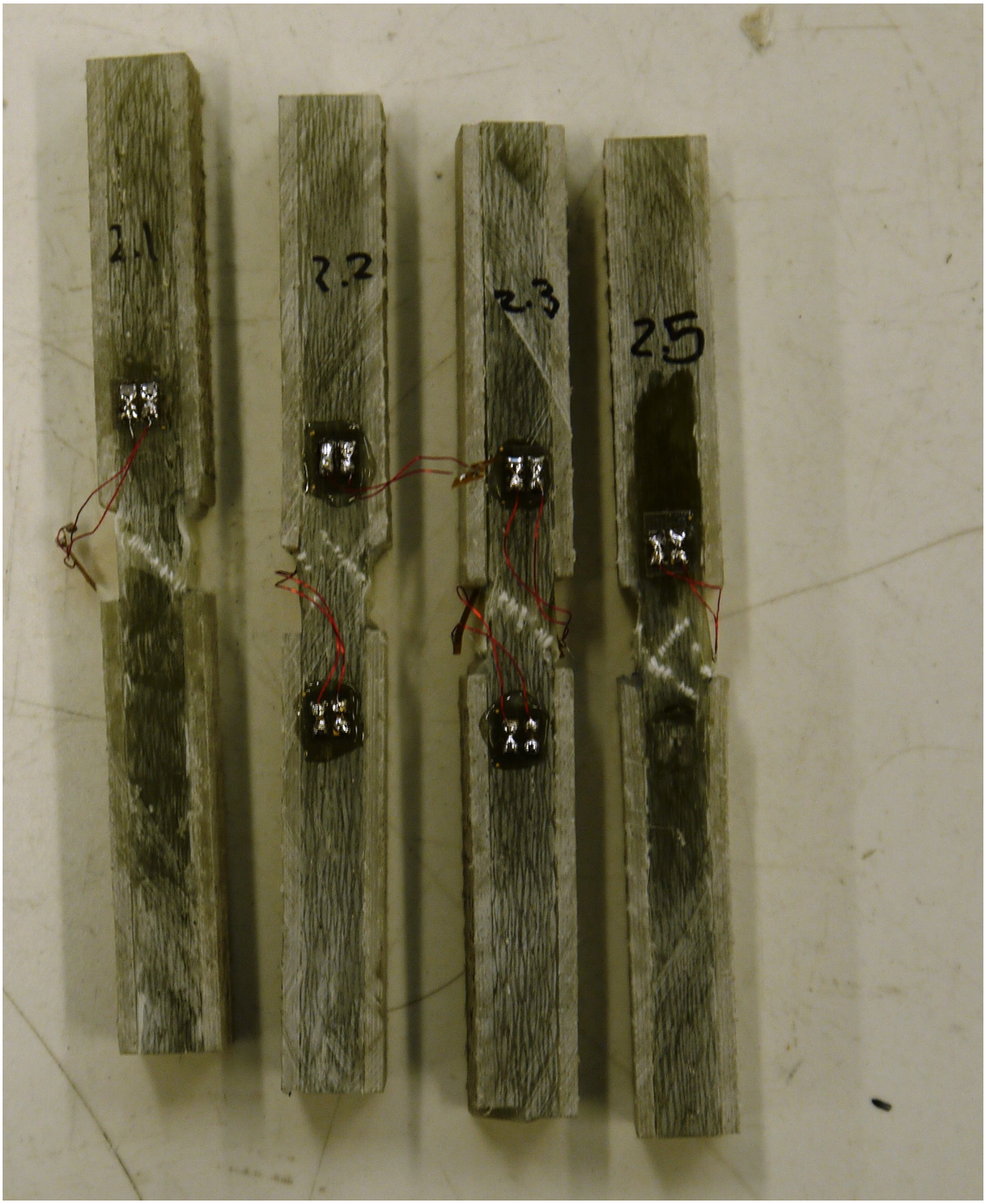

Figure 111: Failure of Coupons Under Compression

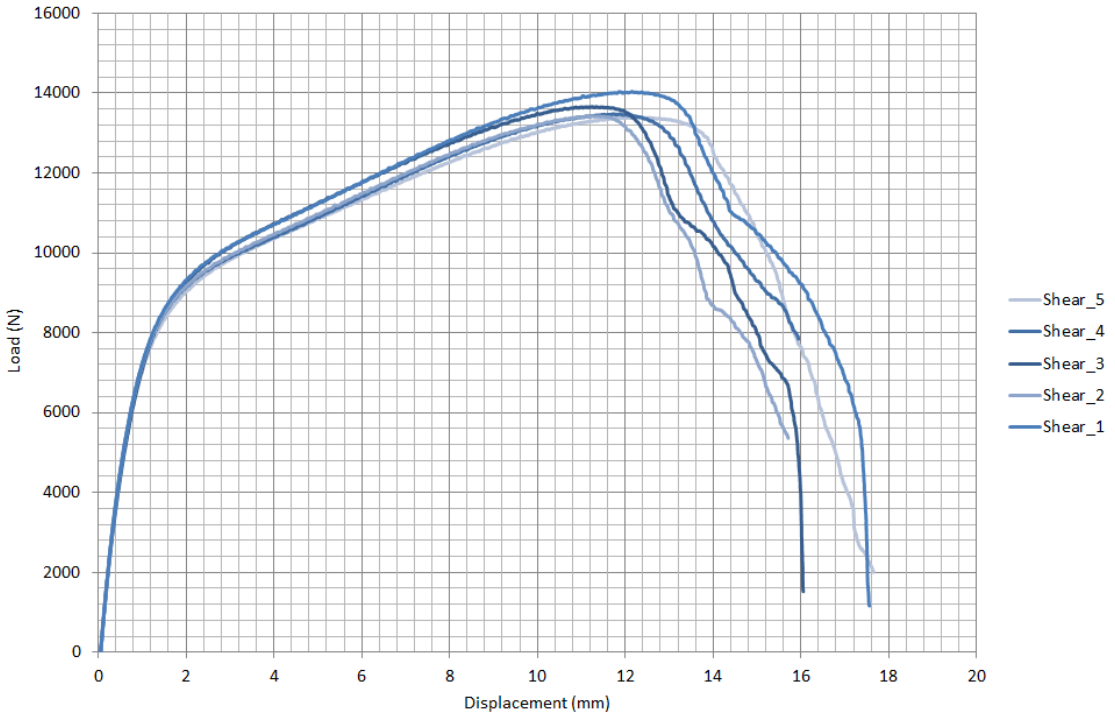

Figure 112: Shear Tests: Load Deflection Curve

fibres. A second linear region is observed at a shear strain greater than 0.013. Final failure is observed in the load deflection curve as the fibres straighten in the loading direction. The in-plane shear strength is shown in table 26 averaged from the 5 peak loads and is calculated at 57.9MPa with a coefficient of variation of 2.54% showing low variation.

The shear stress strain relationship may be approximated by a bi-linear approach using equations 23 and 24

$$y = 7000x \; x < 0.005, \tag{23}$$

$$y = 400x + 31.5 \; x \geq 0.005 \tag{24}$$

However, an initially elliptical relationship followed by a linear relationship provides an improved fit with the difference highlighted in figure 113:

$$y = \sqrt{48.9^2(1 - \frac{(x - 0.02)^2}{0.204^2})} - 10 \; x < 0.015, \tag{25}$$

$$y = 400x + 31.5 \; x \geq 0.015 \tag{26}$$

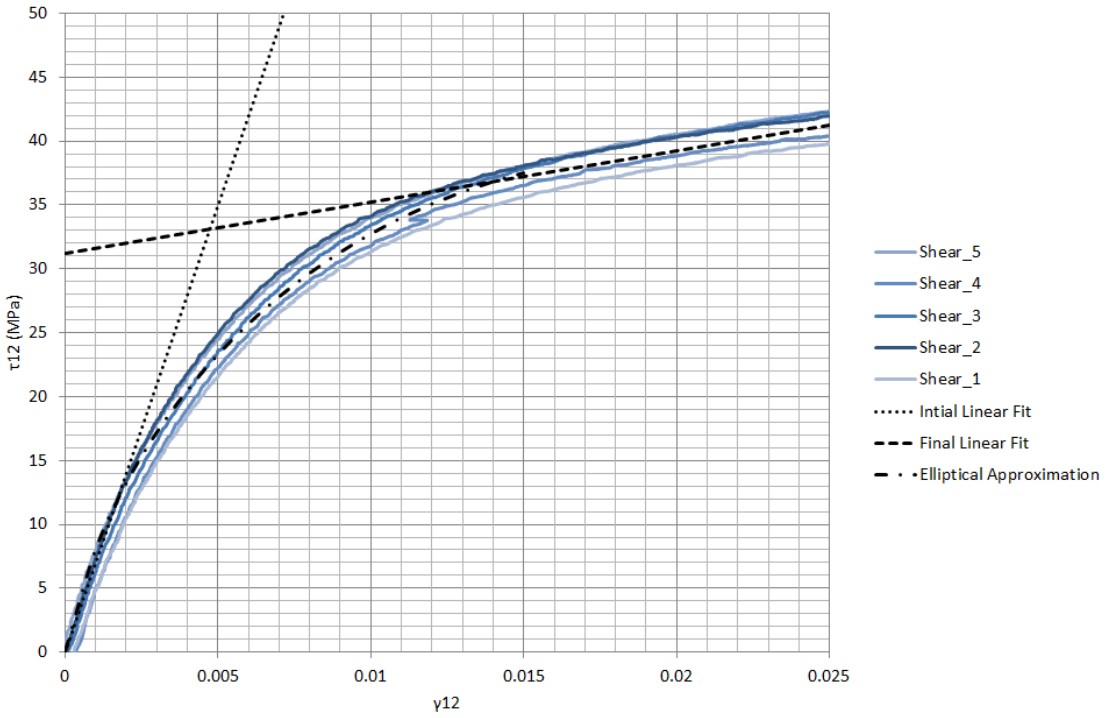

Figure 113: Shear Test:Shear Stress Against Shear Strain

6.1.4 Flexural Modulus

The flexural modulus was tested to standard BS ISO 14125:1998. 6 samples were tested under three point bending coupon width, b, is 15mm, thickness, h, 5mm and distance between the outer rollers, L, is 64.5mm. The flexural modulus is calculated from the following equation $E_f = \frac{l^3}{4bh^3}(\frac{\triangle P}{\triangle u})$ where P, the applied force, and u, the applied displacement, are calculated between the surface strains of 0.005 and 0.0025 as recommended in the standard. The beam was tested until failure which was observed on the upper surface adjacent to the roller. The load deflection curve for the six samples tested are shown in figure 114 along with the linear curve calculated between the surface strains of 0.005 and 0.0025 which broadly correspond to a applied loads of 200N and 400N. The average flexural modulus is 22634MPa with a low coefficient of variation of 1.8%. There is a non-linearity exhibited in the curves which initiates at roller displacements between 0.7mm and 1.4mm. It is suggested that this non-linearity in bending is associated with the straightening of the fibres in tension as presented in the tensile tests.

The flexural modulus for the flexure test and the associated flexural modulus calculated during the ENF tests in section 6.1.7 are compared in table 27 to those calculated from the tensile and compressive modulus using composite beam theory and those available in the literature. It is shown that the coefficient of variation for each sample is low, less than 6%. The results tested here are in the region of those presented by Dharmawan et al. [11] giving confidence in the results. However, there is a large variation between tested samples suggesting variation in the manufacturing process or material properties across the different tests.

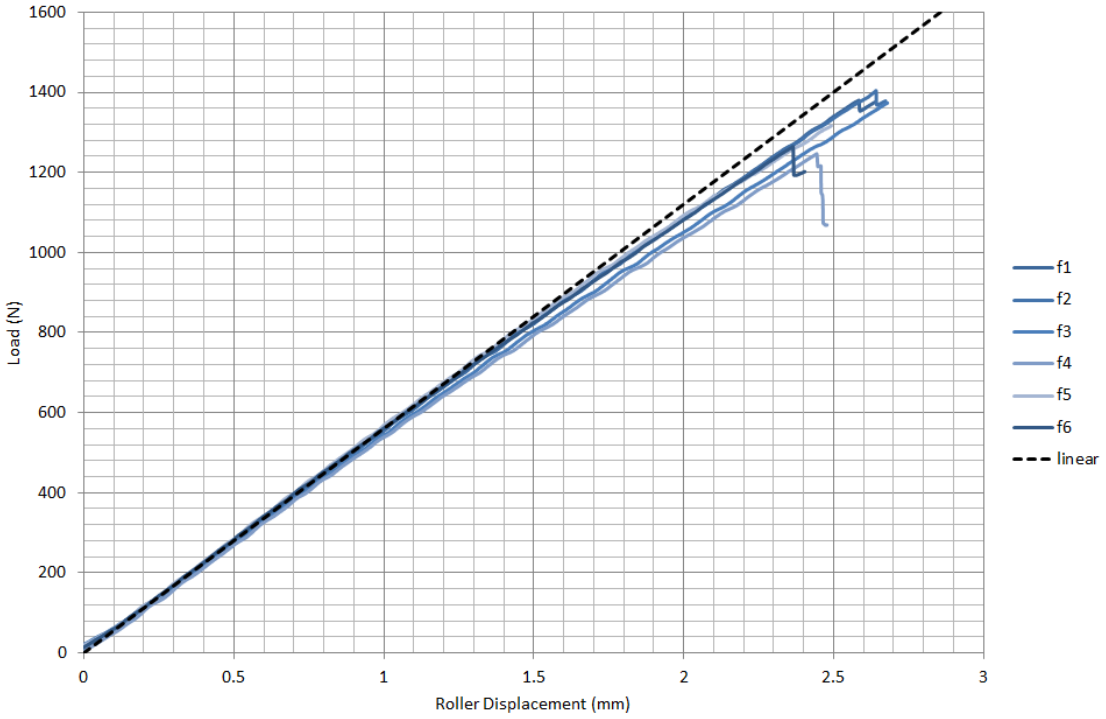

Figure 114: Experimental Flexure Test Load Roller Displacment Response

Source	Method	Average Flexural Modulus (MPa)	Coefficient of Variation
Yetman	Flexure test	22634	1.8%
Yetman	ENF test	24709	4.25%
Yetman	Calculation*	25053	-
Dharmawan	Flexure Test	27200	1.3%
Dharmawan	DCB (ASTM 5528-01)	26800	5.9%
Dharmawan	20% MMB (ASTM 6671-04)	26200	3.7%
Dharmawan	45% MMB (ASTM 6671-04)	20900	2.4%
Dharmawan	60% MMB (ASTM 6671-04)	22900	1.0%
Dharmawan	80% MMB (ASTM 6671-04)	21360	1.0%

Table 27: Flexural Modulus
*Calculated using composite beam theory and the experimentally determined tensile and compressive moduli

6.1.5 Mode I Strain Energy Release Rate Co-Cured

The mode I critical strain energy release rate is assessed by DCB tests conducted using BS ISO EN 7991:2001. The reference states that a minimum of 4 specimens are required. The coupon dimensions are not specified in the standard and are set to represent the full scale structure with a mid laminate crack; 2.5mm arm thickness for a total laminate thickness of 5mm. The initial crack length is approximately 30mm, the coupon width is 25mm and the coupon length 150mm. The sides of the specimen are spray painted white and marked at every 1mm from the end of the crack tip for 10mm and then every 5mm for a a total distance of 65mm from the crack tip as defined by the standard. A test block is adhered to the ends of the specimen, using araldite 2014, ensuring both the center of the hole for loading and the front of the load block are aligned on the upper and lower side.

The width and thickness are measured at three locations along the length, averaged and the initial crack length is measured on each sample prior to testing. Initial tests are conducted to create a pre-crack; the samples are loaded at at rate of 1mm/min until the crack is seen to propagate and a loaded drop is observed. The specimens are then unloaded fully at a rate of 5mm/min. The crack lengths are measured on both sides of the specimen to ensure the crack has propagated perpendicular to the coupon length. The sample is loaded again at a rate of 1mm/min monitoring the crack length using a DSLR camera until the crack reaches a length of 65mm from the initial crack tip. The load deflection response is synchronised with the crack length data observed visually, the sample is then unloaded. The sample is unloaded at a rate of 5mm/min.

The critical strain energy release rate is calculated using simple beam theory:

$$G_{IC} = \frac{4P^2}{E_s B^2}\left(\frac{3a^2}{h^3} + \frac{1}{h}\right) \tag{27}$$

BS ISO EN 7991:2001 describes three approaches for determining the initial critical strain energy release rate; the point on non linearity, 'NL', defined where the load deflection curve deviates from the initial compliance line, C_0, the first point at which the crack is observed to propagate, 'VIS', and 'MAX/5%' determined at the minimum of either the maximum load or the change in compliance of 5%. The initial crack initiation values are similar between the non-linear (NL), visual (VIS), and 5% stiffness change (5%) which are summarised in table 28. For each test there is an initial load drop followed by a further increase in load; the non-linear method is used to determine the initial critical strain energy release rate which corresponds to this initial peak in load and therefore gives the truest sense of the crack initiation load for this case with an average of 0.354KJ/m2 and a coefficient variation of 37.5%. The inherent variation of the weave structure contributes to the variation in the critical strain energy release rate as well as the degree of misalignment between the upper and lower weave structure relative to the Teflon layer. Martin [174] investigated the effect of the Teflon layer relative to the yarn locations in characterising the fracture toughness at initiation and showed that the lowest values of G_c were obtained in the specimens with the insert in the center of the yarn and the highest G_c with the insert at the edge of a yarn. The coefficient of variation is reduced significantly for the visible crack initiation, VIS, to 21.7%. The non 'visible' crack growth which causes a non-linearity in the load deflection curve is small in comparison to the tow width. Due to the slip-stick nature of

	4a_5 (KJ/m2)	4a_6 (KJ/m2)	4a_7 (KJ/m2)	4a8 (KJ/m2)	Average (KJ/m2)	Coefficient of Variation
NL	0.506	0.419	0.281	0.211	0.354	37.5%
VIS	0.494	0.453	0.418	0.279	0.411	21.7%
MAX/5%	0.507	0.635	0.281	0.276	0.425	41.6%

Table 28: Strain Energy Release Rates for Co-Cured Crack Initiation

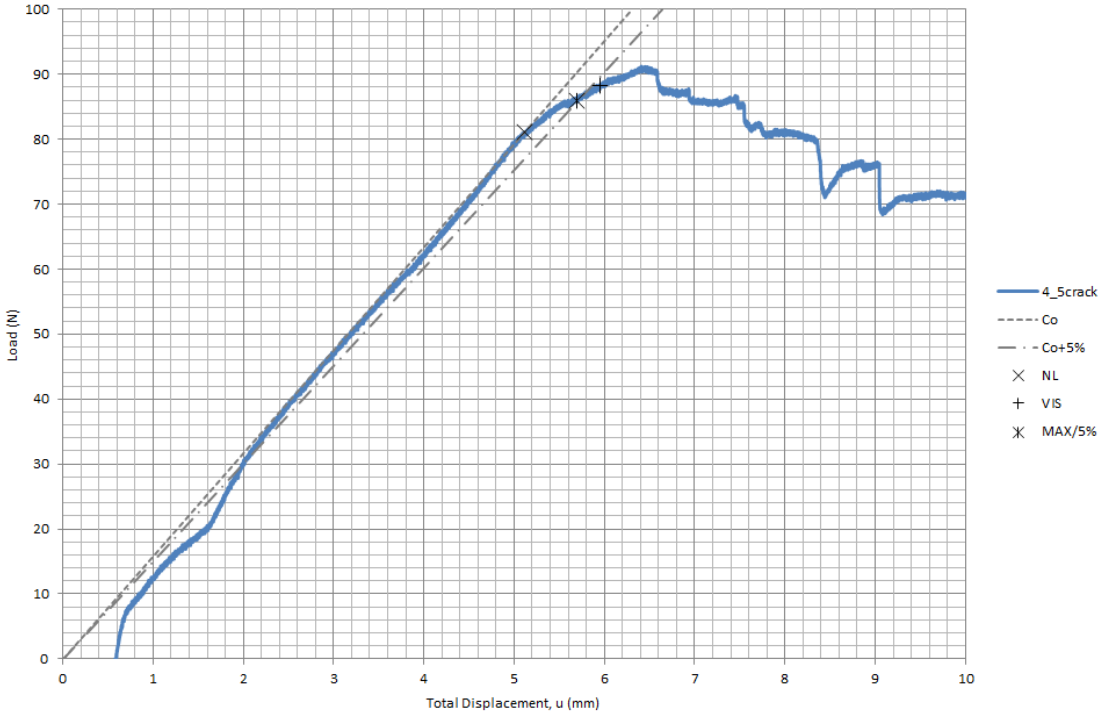

Figure 115: DCB Typical Load Deflection Curve

the crack growth it is likely that crack growth is more noticeable during the period of unstable crack growth with the crack arresting at the face of the next transverse tow. Therefore, there is less variability in the visible crack growth as it is less dependent on the variation in the relative Teflon and weave location. For all tests the 5% change in compliance occurs prior to the maximum load. The 5% change in compliance gives a standardised approach to characterising the non-linear response however the initial load drop is followed by a further increase in load and the critical load is sensitive to the specified compliance change, in this case 5%, resulting in a high degree of variation.

A typical load deflection curve shown in figure 115 illustrates the slip-stick nature of the crack propagation. Ebeling et al. [21] showed that the crack growth in woven fabric composites is dominated by fibre/matrix interface debonding following the undulating pattern of the yarns. Studies conducted on translucent specimens by Ebeling et al. [21] and Ebeling et al. [175] showed that the crack had multiple crack fronts, one for each warp yarn. During stable crack propagation the crack front was most advanced where the exposed yarns were aligned in the crack direction and lagged in the perpendicular direction. Once the crack front became unstable at a sudden load drop, the whole crack front jumps forward which was then immediately arrested at the next undulation and again forms

a continuous crack front.

It is also shown by [176] and other authors that the stacking method of woven fabrics leads to an inherent variability; the distribution of strands of one layer is unlikely to be in exact alignment with the distribution of strands of the adjacent layers. The relative movements of the fabric layers are affected by friction between fabric layers, local departure in strand perpendicularity, possible variation of strand count from place to place in the fabric and constraints on the relative lateral movement of the layer, during lamination. Therefore there is natural variation with scattered zones of different combinations of shifts which will cause the properties to vary from sample to sample. This variability is particularly apparent for interlaminar properties where the local roughness and variation in alignment and the weave structure lead to resin-rich areas which allow larger plastic yield zones to develop ahead of the crack tip [20, 21]. In mode I tests these variations due to alignment and the weave structure lead to an observed slip-stick technique.

To post-process this slip-stick propagation Mouritz et al. [177] determined the critical strain energy release rate from pre-determined values of the crack growth. However, Davies and Moore [178] discussed the problem in characterising the delamination resistance of uni-directional glass/Nylon-66 and defined the following key values which are illustrated in figure 116:

[1] Stable propagation value (where possible), 'STABLE'

[2] Value at onset of instability, 'INST.'

[3] Arrest value, 'ARREST'

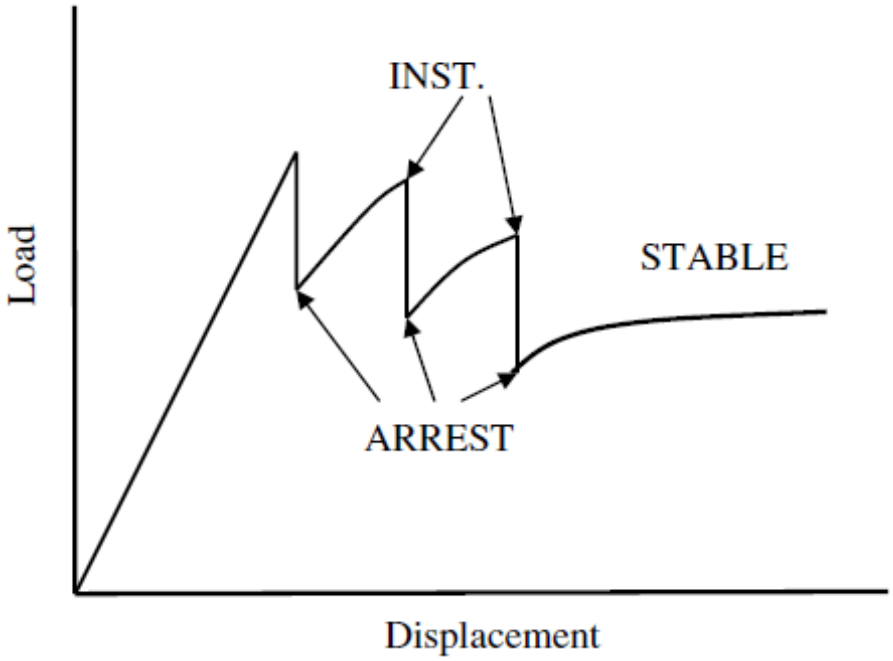

Figure 116: Unstable crack propagation Davies and Moore [178]

Authors such as Compston [12] and Dharmawan et al. [11] have used these definitions to determine the critical strain energy release rates of woven DCB specimens. These key values as defined by Davies and Moore [178] are considered here in the analysis of the crack propagation values where appropriate.

Figure 117 shows the crack propagation of a typical sample. The load line is illustrated along with the tow width which is determined visually and measured at 4.5mm. Crack growth is observed using these images synchronised to the corresponding load and extension. It is observed that cracks form under the cut tows which makes the determination of the crack length difficult to identify. Fibre bridging of the cut tows at the edge of the sample. The crack develops on the upper and lower side of the cut tow resulting in a sharp increase in the perceived critical strain energy release rate due to the increase in the surface area of the developed fracture surface. Examination of the fracture surface shows the cut tows are present only on one side of the specimen.

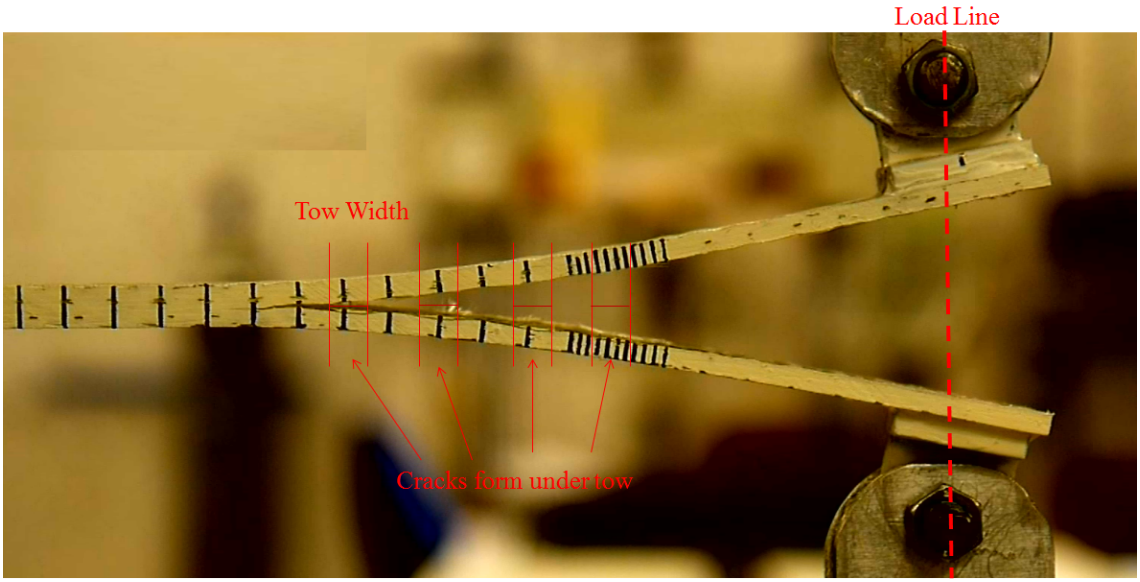

Figure 117: DCB Test Arrangement

Figure 118 illustrates the calculated strain energy release rate for crack displacement along with the load displacement plot. The grey areas correspond to where the crack tip is in the region of the cut tow. Increased peaks are observed as the crack front passes the tow and the tow bridges behind the crack tip, these increased instability points are marked in yellow. Instability points that correspond to no fibre bridging are marked in black and the arrest points are marked in red. For each specimen the three instability points and arrest points are calculated with respect to the bridging cut tows.

Figure 119 shows the critical strain energy release rate against crack length for the samples tested. Although there is significant variation across the values there is no obvious resistance curve, therefore all data points are included to ascertain the crack propagation values. The results for the strain energy release rate for the instability, bridging instability and arrest points are shown for the 4 samples tested in table 29 where a minimum of 3 points are averaged for each value. It is noted that coupon 4a_7 does not have an instability point as the coupon is cut to have a cut tow on alternate sides and therefore bridging occurs during all of the crack growth. The bridging of

the cut tows provides an artificial increase in resistance that would not be present in a pure mode I crack growth therefore the instability point without bridging is used for future modelling to provide a conservative result and to eliminate the increase in resistance of the bridging tows.

The variation in mode I crack initiation and propagation is more significant than the previous tests. Due to the nature of fabric there is an inherent variability in the alignment of the fabric and relative location of the adjacent plies. This variability is particularly apparent for interlaminar properties where the local roughness and variation in alignment and the weave structure lead to resin-rich areas which allow larger plastic yield zones to develop ahead of the crack tip [20, 21]. Naik et al. [176] and other authors have shown that the stacking method of woven fabrics leads to further inherent variability; local departure in strand perpendicularity, possible variation of strand count from place to place in the fabric and constraints on the relative lateral movement of the layer, during lamination. Therefore, there is natural variation which will cause the properties to vary from sample to sample which are particularly prominent for interlaminar properties.

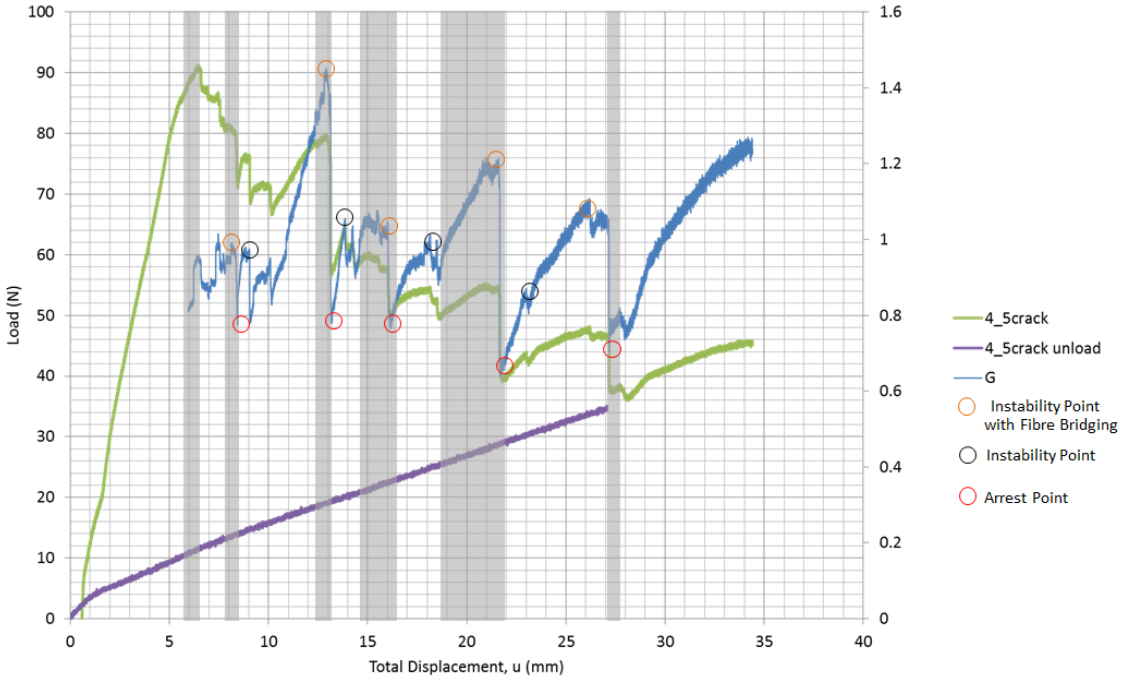

Figure 118: Load Deflection Response with Calculated Strain Energy Release Rate

	4a_5 (KJ/m2)	4a_6 (KJ/m2)	4a_7 (KJ/m2)	4a_8 (KJ/m2)	Average (KJ/m2)	Coefficient of Variation
Instability Point	0.984	0.920	-	1.006	0.967	14.5%
Bridging Instability Point	1.18175	1.056	1.16	1.12	1.07	14.0%
Arrest Point	0.734	0.744	.837	0.736	0.728	12.4%

Table 29: Strain Energy Release Rates for Co-Cured Crack Propagation

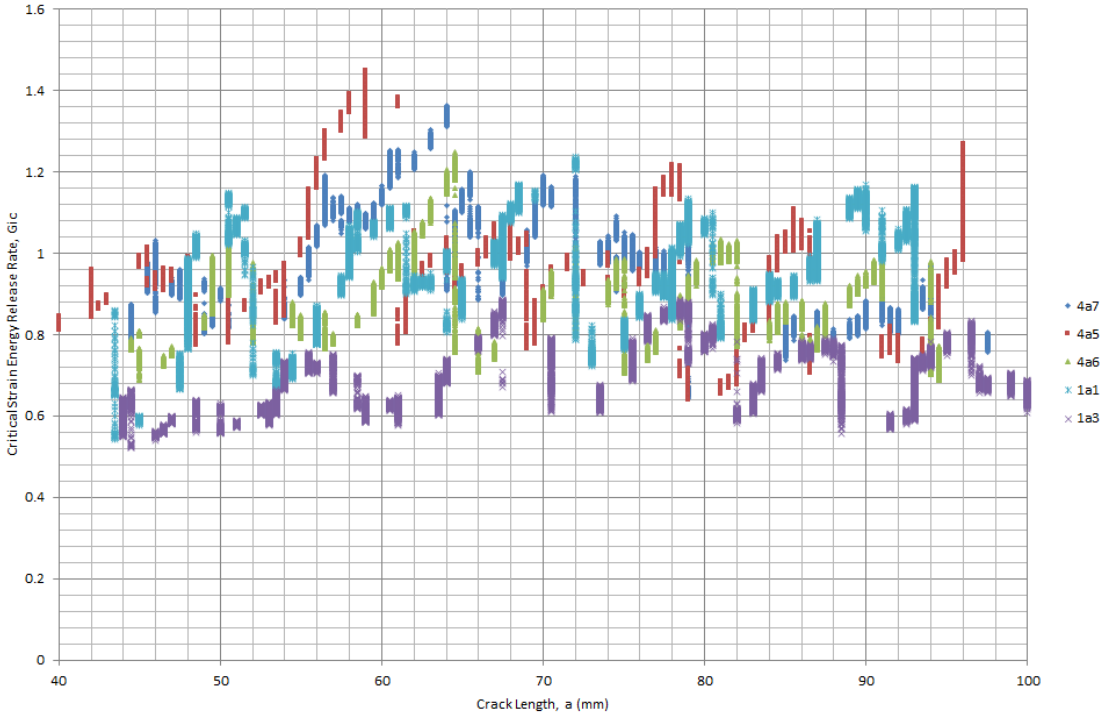

Figure 119: Strain Energy Release Rate Against Crack Length for Co-Cured DCB Coupons

Specimen width has been shown not to affect the fracture toughness of unidirectional composites[179] however it is evident from the study here that it is a critical parameter for woven composites. Further research is needed to determine size effects of woven fabric composites on fracture toughness. It is suggested that the result could be improved by eliminating these bridged tows by defining the edges of the specimen using Teflon strips to prevent adhesion of the cut tows.

The results of other authors for e-glass vinylester mode I tests are presented in table 30. Blake et al. [10] studied 800gsm woven E glass with a toughened Derakane 8084 matrix, the manufacturing method and weave type is not mentioned. Dharmawan et al. [11] studied 800gsm woven E glass with a Derakane 411-350 matrix however the manufacturing method is not mentioned. Compston [12] studied both Derakane 8084 and 411-45 using an E-glass woven 638gsm manufactured by hand lay up achieving a 50% fibre volume fraction. Table 30 shows there is significant variation across the samples and variation in the manufacturing and test procedures although it is evident that the results presented here are in the region of those reported by other authors.

6.1.6 Mode I Strain Energy Release Rate Post-Cured

The mode I DCB tests are repeated for the post-cured sample which contain a chopped strand mat, CSM, layer at the sub-laminate interface. The laminate is infused in 2 hits with the first 2.5mm sublaminate initially infused and a Teflon layer, chopped strand mat and woven roving plies post-cured onto the first sublaminate. The same three methods are used to calculate the crack initiation values with the results shown in table 31. There is a

	Dharmawan et al.	Compston	Compston	Blake et al.	Yetman
Material	Glass Derakane 411	Glass Derakane 8084	Glass Derakane 411	Glass Derakane 8084	Glass Scott Bader VE679-03PA
Manufacturing method	Unknown	Wet hand layup	Wet hand layup	Unknown	Resin Infusion
G_{IC} Initiation		0.577±0.111	0.227±0.048	0.239±0.105	0.371±0.111
G_{IC} Propagation	1.210±0.100	0.988±0.245	0.739±0.111	0.804	0.967±0.14

Table 30: Comparison of Co-Cured Mode I Fracture Toughness

	6a1 (KJ/m2)	6a2 (KJ/m2)	6a3 (KJ/m2)	6a4 (KJ/m2)	6a5 (KJ/m2)	Average (KJ/m2)	Coefficient of Variation
NL	0.317	0.200	0.290	0.308	0.247	0.272	17.8%
VIS	0.300	0.192	0.410	0.370	0.248	0.304	29.1%
MAX/5%	0.320	0.176	0.319	0.379	0.239	0.287	27.7%

Table 31: Strain Energy Release Rates for Post-Cured Crack Initiation

10.5% variation between the methods. Multiple load drops occur in these post-cured samples prior to the peak load resulting in a change in stiffness, prior to the crack becoming visible. The least variation is observed for the non-linear method in this case.

The strain energy release rate against crack length are shown in figure 120 for the 5 samples tested. A resistance curve is evident with an increase in strain energy release rate with crack length over the first 15-25mm and for samples 6a2-6a5 a plateau in the strain energy release rate is shown for a crack length of 60mm and greater. Good agreement is shown between samples 6a3-6a5 whilst higher strain energy release rate values are shown for samples 6a1-6a2. The linear increase is more pronounced for samples 6a1 with an increase in strain energy release rate for a crack growth of up to 30mm.

The strain energy release rate against crack length plots are shown in figure 120 for the 5 samples tested. For the post-cured samples a resistance curve is evident with an increase in strain energy release rate with crack length over the first 15-25mm. Samples 6a2-6a5 exhibit a plateau in the strain energy release rate for a crack length of 50mm and greater. Good agreement is shown between samples 6a3-6a5 whilst higher strain energy release rate values are shown for samples 6a1-6a2. The initial linear increase is more pronounced for samples 6a1 with an increase in strain energy release rate for a crack growth up to to a length of 68mm.

Unlike the co-cured samples a regular slip-stick behaviour is not shown in these samples due to the irregular interface. The data is therefore averaged in the plateau region for a crack length of greater than 60mm and shown in table 32. The results show there is similar variation about the average for each sample in the region of 11.5-17.3% however the coefficient of variation across the full data set is greater at 20.7%. This is largely explained by the difference between the samples in the relative alignment of chopped fibres parallel to the crack propagation direction introduced by the CSM layer. Fibres aligned to the loading direction provide a greater force, over a longer length

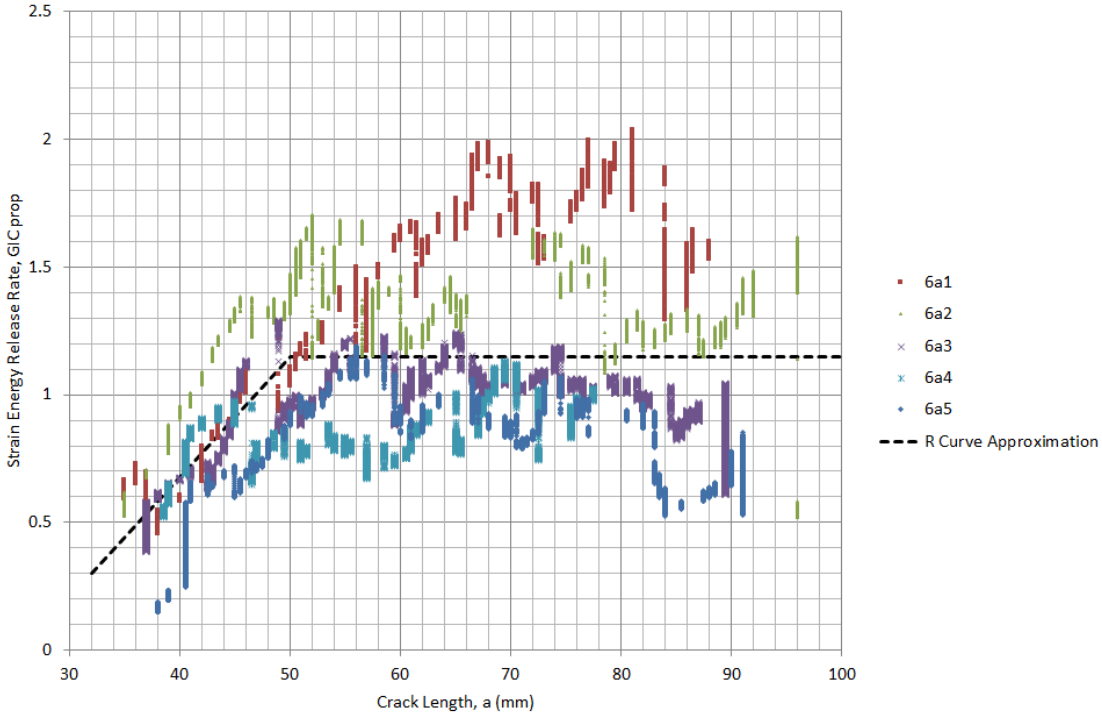

Figure 120: Strain Energy Release Rate Against Crack Length for Post-cured DCB Coupons

	Average SERR (KJ/m2)	Coefficient of Variation
6a1	1.51	17.27
6a2	0.139	11.5
6a3	0.954	12.52
6a4	0.865	12.66
6a5	0.765	16.8
All	1.15	20.7

Table 32: Analysis of Critical Strain Energy Release Rate for Post-cured Coupons

and acting in parallel with more fibres, resulting in higher critical strain energy release rates. Fibre bridging is apparent in all samples and occurs for approximately 30mm behind the crack tip. However, it is clear from the observations during the test that samples 6a1 and 6a2 have a higher degree of alignment in the CSM layer to the loading direction. Sample 6a1 shows that a number of fibres bridge the sub-laminates ahead of the Teflon layer and provide a resistive force prior to breaking at a visible crack length of 85-90mm.

6.1.7 Mode II Strain Energy Release Rate Co-Cured

The mode II strain energy release rate is calculated using the end notch flexure technique and ASTM D7905/D7905M-15. The experimental setup and dimensions are shown in figure 121. The specimen roller radius used was 10.0mm for all three rollers, the distance between rollers, L, is 50mm, width is 20mm, and thicknesses is 5mm and are measured for each specimen. A Teflon insert is used for the pre-crack as used in the DCB tests.

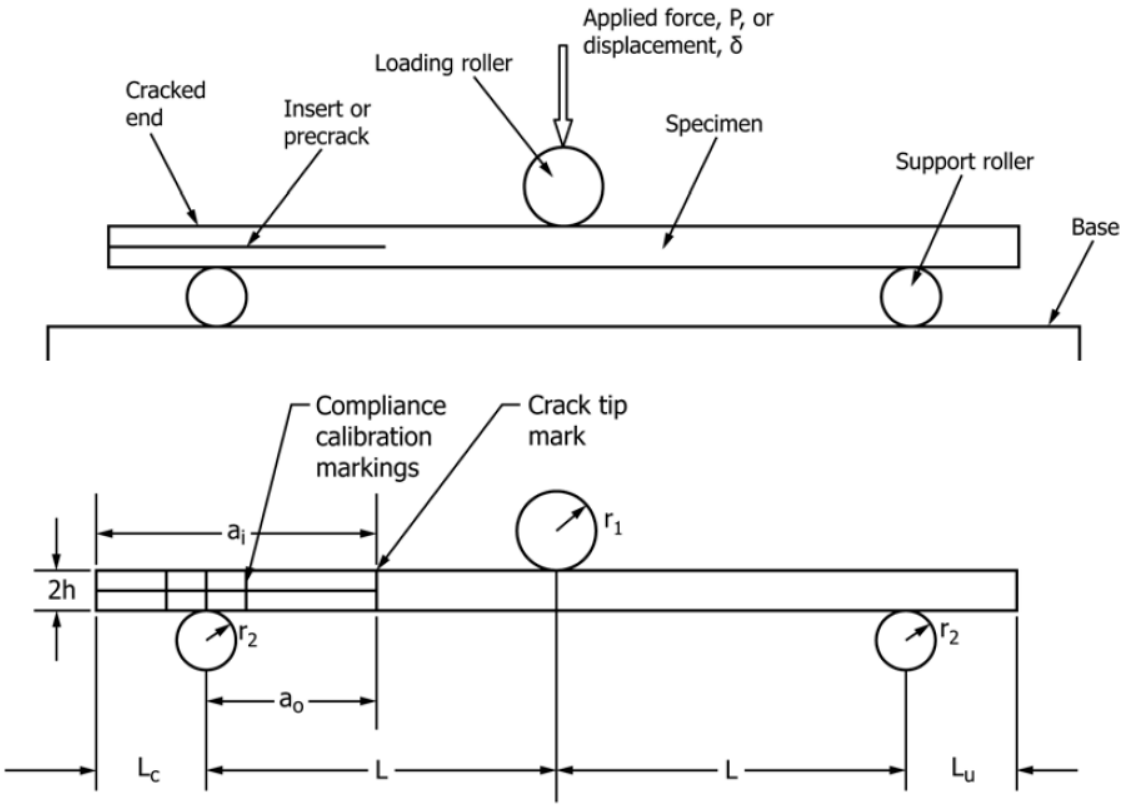

Figure 121: ENF experimental setup

Specimen ID	A NPC	m NPC	Pmax NPC	G_{IIC} NPC	A PC	m PC	Pmax PC	G_{IIC} PC
4a_4	4.47E-3	5.49E-8	463	.782	4.65E-3	5.75E-8	556	.957
4a_5	4.33E-3	4.45E-8	479	.688	4.37E-3	4.37E-8	581	.995
4a_6	4.63E-3	4.78E-8	467	.695	4.88E-3	4.95E-8	518	.886
4a_7	4.59E-3	4.39E-8	529	.879	4.76E-3	4.32E-8	541	.904
4a_9	5.06E-3	5.13E-8	432	.720	5.05E-3	5.44E-8	513	1.08
Average				.761				.936
Coefficient of Variation				10.5%				5.3%

Table 33: Co-cured ENF Experimental Data

The edges of the specimen were spray painted white to determine the crack tip and crack growth. The crack tip is marked and the 20mm, 30mm and 40mm crack lengths are marked. The compliance of the specimen for the three marked crack lengths are tested to 244N which represents approximately 50% of the peak load and is used to determine the compliance against crack length relationship. The parameters in equation 28 are obtained by means of a least square linear analysis where a is the crack length, C is the compliance and A and m are the intercept and gradient respectively.

$$C = A + ma^3, \tag{28}$$

The specimen is then loaded at a crack length of 30mm until the crack advances whilst monitoring the load and displacement. The unloading compliance is then used to determine the crack advancement for future tests. The peak load is used in equation 29 to establish the critical strain energy release rate where P_{max} is the peak load, B is the specimen width and a_o is the initial crack length.

$$G_{IC} = \frac{3mP_{max}^2 a_o^2}{2B} \tag{29}$$

The process is then repeated for the pre-cracked sample to re-establish the compliance relationship and determine the peak load for further crack advancement.

The results are tabulated in table 33 for the non pre-cracked (NPC) and pre-cracked (PC) samples. The non pre-cracked samples showed an average critical strain energy release rate of 0.761 with a coefficient of variation of 11.7% whereas the pre-cracked samples increased by 30% to 0.936 with a coefficient of variation of 5.3%. The coefficients of variation are considered to be low for both NPC and PC values.

The results of other authors for e-glass vinylester mode II tests are presented in table 34 and compared to the current results showing there is significant variation across the samples and variation in the manufacturing and test procedures. The results presented here for the mode II crack initiation are in the region of those reported by other authors however the mode II propagation results are significantly lower. Gill et al. [180] showed that the mode II fracture toughness of 5 harness satin carbon epoxy manufactured by resin transfer moulding were significantly affected by friction and mechanical interlocking between the delamination surfaces that were eliminated by mixed mode tests with 5% mode I. The variation observed between the crack propagation fracture toughness assessed here

	Dharmawan et al.	Compston	Compston	Blake et al.	Yetman
Material	Glass Derakane 411	Glass Derakane (8084	Glass Derakane 411	Glass Derakane 8084	Glass Scott Bader VE679-03PA
Manufacturing method	Unknown	Wet hand layup	Wet hand layup	Unknown	Resin Infusion
GII NPC		1.152±0.134	0.724±0.144	0.627±0.371	0.761±0.089
GII PC	4.550±0.400	5.461±0.413	4.102±0.470		0.936±0.050

Table 34: Comparison of Co-cured Mode II Fracture Toughness

and the comparable literature may be attributed to the level of compaction and degree of mechanical interlocking present in the tested samples or could be one of the many differing factors between the tests; manufacturing method, fibre volume fraction or differences in the mechanical properties of the component materials. However good repeatability is seen in the test results giving confidence for this specific configuration.

6.1.8 Mode II Strain Energy Release Rate Post-Cured

The mode II experiments described in the previous section are repeated for a post-cured specimen containing a layer of chopped strand mat at the cracked interface. The results are presented for these specimens in table 35. The non pre-cracked samples showed an average critical strain energy release rate of 1.12 with a coefficient of variation of 12.6% whereas the pre-cracked samples increased by 42% to 1.59 with a similar coefficient of variation of 12.3%. Both critical strain energy release rates are increased in the post-cured specimen relative to the co-cured specimen by 47.2% and 70.0% for the NPC and PC specimens respectively. For both the non pre-crack and pre-cracked specimen this is due to the introduction of the CSM which is likely to provide a path of least resistance for the resin during the infusion process. This results in a higher resin content at the interface between the sub-laminates and larger resin filled areas which allow larger plastic yield zones to develop ahead of the crack tip. The coefficient of variation is increased in the post-cured samples which is likely to be due to the variation in the chopped strand mat layer which provides a varied interface between the two sub-laminates.

Specimen ID	A NPC	m NPC	Pmax NPC	G_{IIC} NPC	A PC	m PC	Pmax PC	G_{IIC} PC
7a_1	0.002979	3.73E-8	732	1.32	0.002931	2.78	862	1.36
7a_2	0.002925	3.83E-8	600	0.91	0.003035	3.75	836	1.73
7a_3	0.002769	3.91E-8	651	1.09	0.002897	3.78	750	1.41
7a_4	0.002979	3.47E-8	675	1.04	0.002904	3.63	812	1.58
7a_5	0.002704	3.63E-8	695	1.16	0.002693	3.48	906	1.88
7a_6	0.002858	3.61E-8	704	1.08	0.002911	3.63	806	1.56
Average				1.12				1.59
Coefficient of Variation				12.6%				12.3%

Table 35: Post Cured ENF Experimental Data

6.2 Four Point Bend Tests of Top Hat Sections

In this section testing is conducted to establish the crack initiation and propagation through representative top-hat stiffened structures and to verify a model capable of representing delamination initiation and propagation under out-of-plane loading following damage progression and crack propagation. The plate is initially infused and in a second process the top-hat stiffener is cured onto the plate with an interface layer of chopped strand mat. The material properties determined in section 6.1 are used to verify the material model and the cohesive element properties are optimised to account for the chopped strand mat interface and fibre bridging present behind the crack tip.

The four point bend test configuration is applied, as shown in figure 122, until the specimen reaches ultimate failure; either by full delamination or loss of structural integrity of the laminate or stiffener occurs. The four point bend load position is established with the lower rollers positioned under the inner edge of the flange. This configuration minimises the risk of fibre failure on the upper surface of the laminate compared to a three point bend configuration. Load deflection data was recorded and delamination initiation and growth was observed and marked visually and audibly using a DSLR camera. The roller positions and stiffener dimensions are shown in figure 122 with stiffener dimensions as used in section 5. The plate and stiffener webs are a balanced glass-vinylester woven roving (VE679-03PA) aligned with the stiffener direction where the table of the stiffener contains an additional central glass-vinylester unidirectional ply (UE500). The plate, stiffener webs and stiffener table are 7.5mm, 3.75mm and 7.5mm thick respectively. Samples were taken from two stiffeners, stiffener A and B, and tested to assess the consistency of the manufacturing technique.

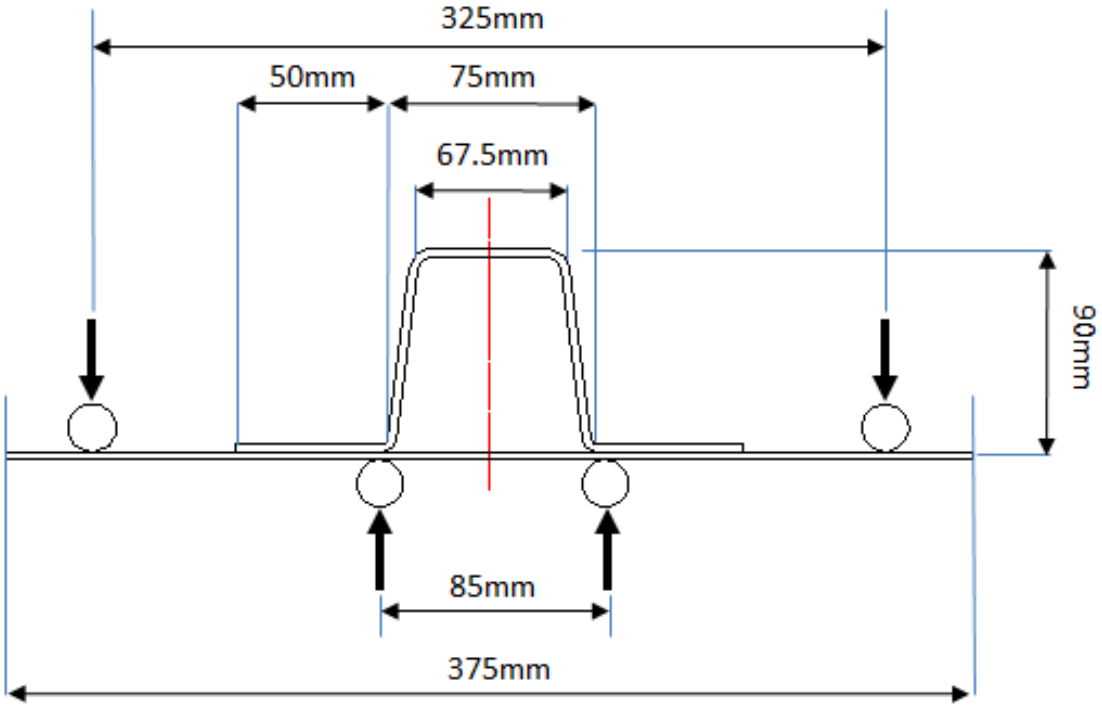

Figure 122: Four Point Bend Test Configuration

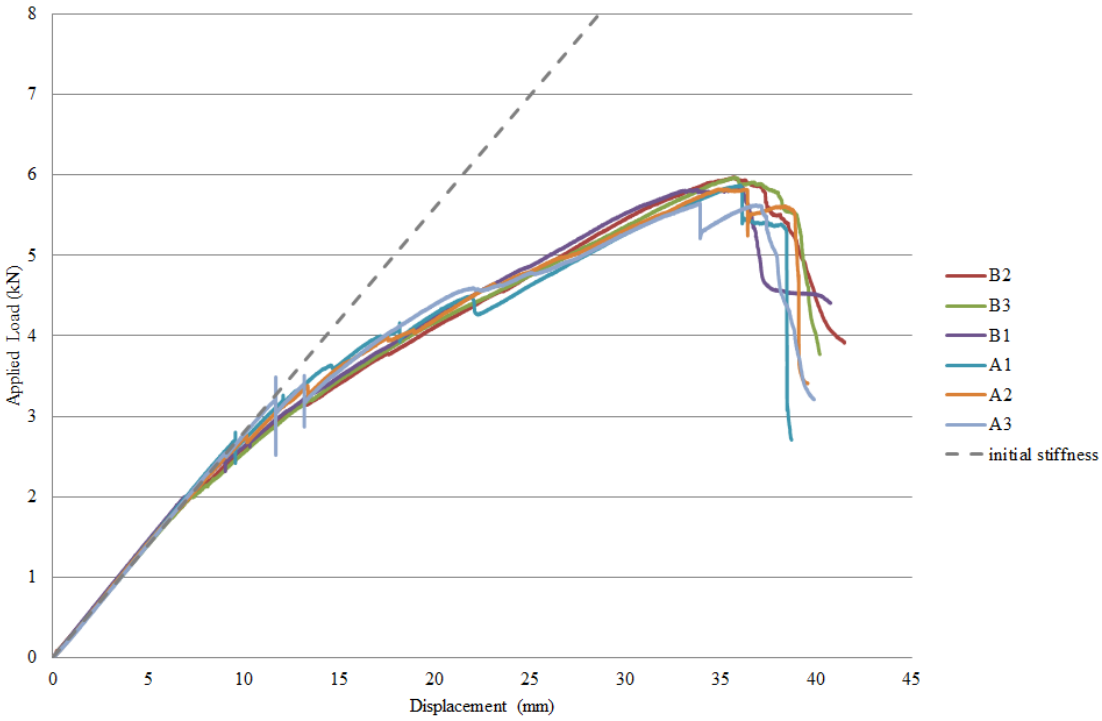

Figure 123: Four Point Bend: Test Data Load Displacement Curve for Stiffener A

Roller Displacement	Left Side Observations	Right Side Observations
6.3mm	audible cracking	
6.4mm		crack visible on the right outer flange edge
8.8mm		9mm crack on the right outer flange edge
9.24mm		15mm crack on the right outer flange edge
19.7mm	small Crack initiates at left inner curve	
22.5mm	crack visible on the left outer flange edge	
24.5mm	5mm crack at inner curve	
27.0mm	gradual debond of left flange edge	gradual debond of right flange edge
28.8mm	16mm crack on the left outer flange edge	
35.6mm	significant damage propagation on plate in contact with roller	

Table 36: Observations for Panel A3 During Four Point Bend Test

Roller Displacement	Left Flange Observations	Right Flange Observations
7.1mm	audible cracking	
9.5mm	crack initiates at inner curve	
15.5mm	crack visible on the left inner flange edge	
15.9mm		crack visible on the inner curve
19.5mm		crack visible on the right outer flange edge
20.4mm	crack visible on the left outer flange edge	
28.8mm	crack growth to 5mm on the left outer flange edge	crack growth to 12mm on the right outer flange edge
32.9mm	significant damage propagation on plate in contact with roller	

Table 37: Observations for Panel B3 During Four Point Bend Test

The load deflection curves for three specimens cut from stiffener A and B are shown in figure 123. The initial stiffness is shown to illustrate the change in stiffness with increasing displacement. For both stiffeners the three curves show good repeatability in the experimental set-up. Observation during loading of specimen A3 are described in table 36 and of specimen B3 in figure 37 which are typical of the results for each stiffener. To further illustrate the damage state of stiffener A the damage response of A3 at 35.6mm is shown in figure 124. The damage state for B3 is shown at 28.8mm roller displacement in figure 125.

For both samples cracking was audible at relatively low displacements and were frequent throughout loading as crack development was gradual and continuous. This initial audible crack is comparable to the change in stiffness present in the load displacement curve. Stiffener A and B illustrate similar failure mechanisms. Stiffener A illustrates a greater degree of asymmetry across the three samples with crack propagation dominant in the right hand flange plate interface. A level of variation is expected due to the inherent variability in the chopped strand mat at the interface which will provide variation in the strength. However, due to the similarity of mechanisms for the three tests for each stiffener respectively it is assumed that the asymmetry observed is representative of a geometric or infusion variation rather than interface variability caused by the chopped strand mat. There is a 1% difference in the average stiffness between stiffener A and B and a coefficient of variation across all tests of 1.4% showing low variability. This gives good confidence in the manufacturing technique and supplier.

6.3 Summary of Experimental Data

It was shown that there is a lack of complete experimental results for heavy weight marine composites with Lloyd's approval that includes the shear response and fracture properties. Fracture data for post-cured interfaces containing a chopped strand mat layer are also lacking in the literature. In this chapter experimental tests were conducted to provide a set of data to investigate mechanical, fracture and debonding in typical marine heavy weight glass

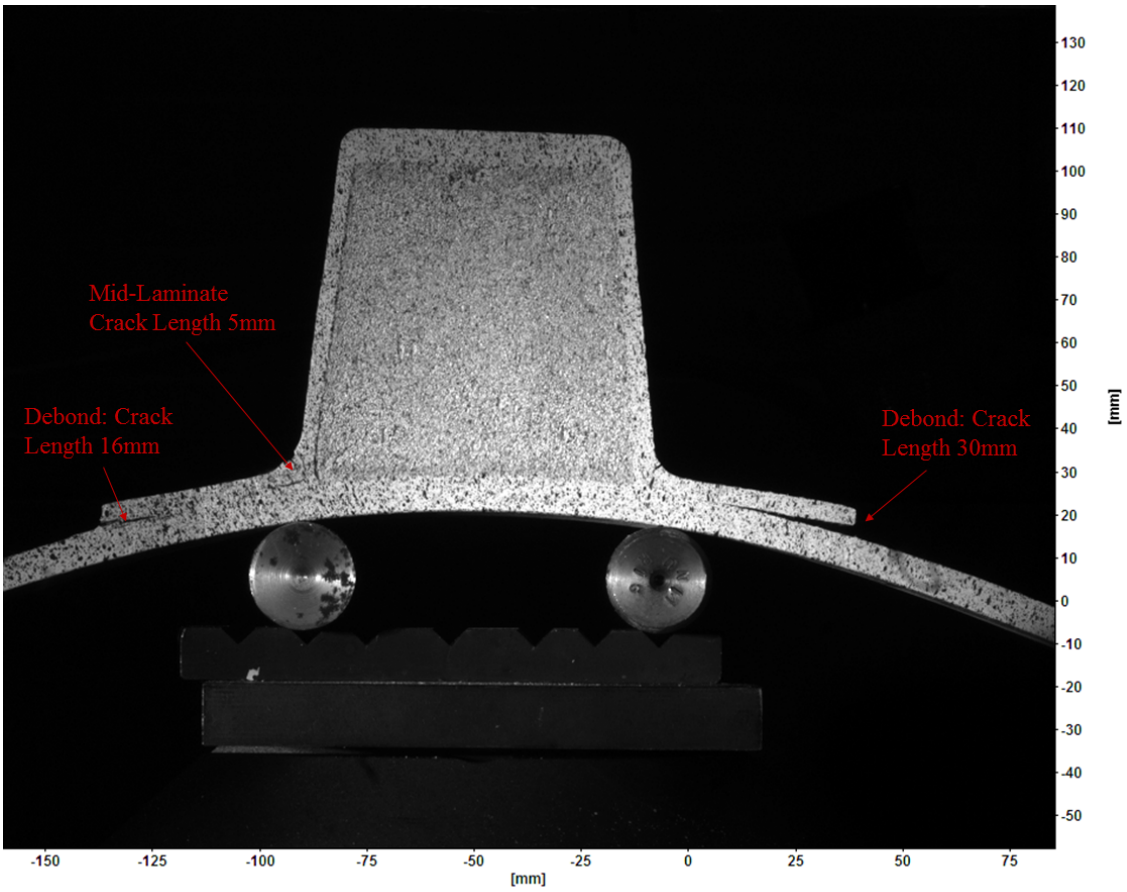

Figure 124: Four Point Bend: Test A2 at 35.6mm Displacement

vinylester as demonstrated in table 38. Tests are conducted on both co-cured and post-cured joints typical of the marine industry. It is shown that there is variation of the order of 10% in the flexural properties between laminate manufactured from the same material, methodology and manufacturer.

The mechanical properties are characterised using ISO standards for uni-directional and multi-directional composites where applicable. The non-linearities in tension and shear are characterised and material models developed to match the experimental data; a novel shear stress strain relationship for woven composites is developed. The mode I and II interfaces are characterised for the co-cured and post-cured samples. The mode I co-cured samples show a slip-stick release and the Mouritz method is used characterise data and determine crack propagation values with and without fibre bridging. The slip-stick mechanisms is not observed in the Mode I post-cured however samples show an R curve therefore propagation data is calculated in the stable region of this curve.

The fracture properties of both co-cured and post-cured samples were evaluated and a number of test parameters are discussed to improve the testing of woven roving samples and those containing a CSM layer. The Mouritz et al. [177] method was used to determine key critical strain energy release rates where slip-stick crack propagation was observed and key data was taken where fibre bridging was not present.

Further tests are recommended in order to fully assess the statistical significance of the CSM layer in mode

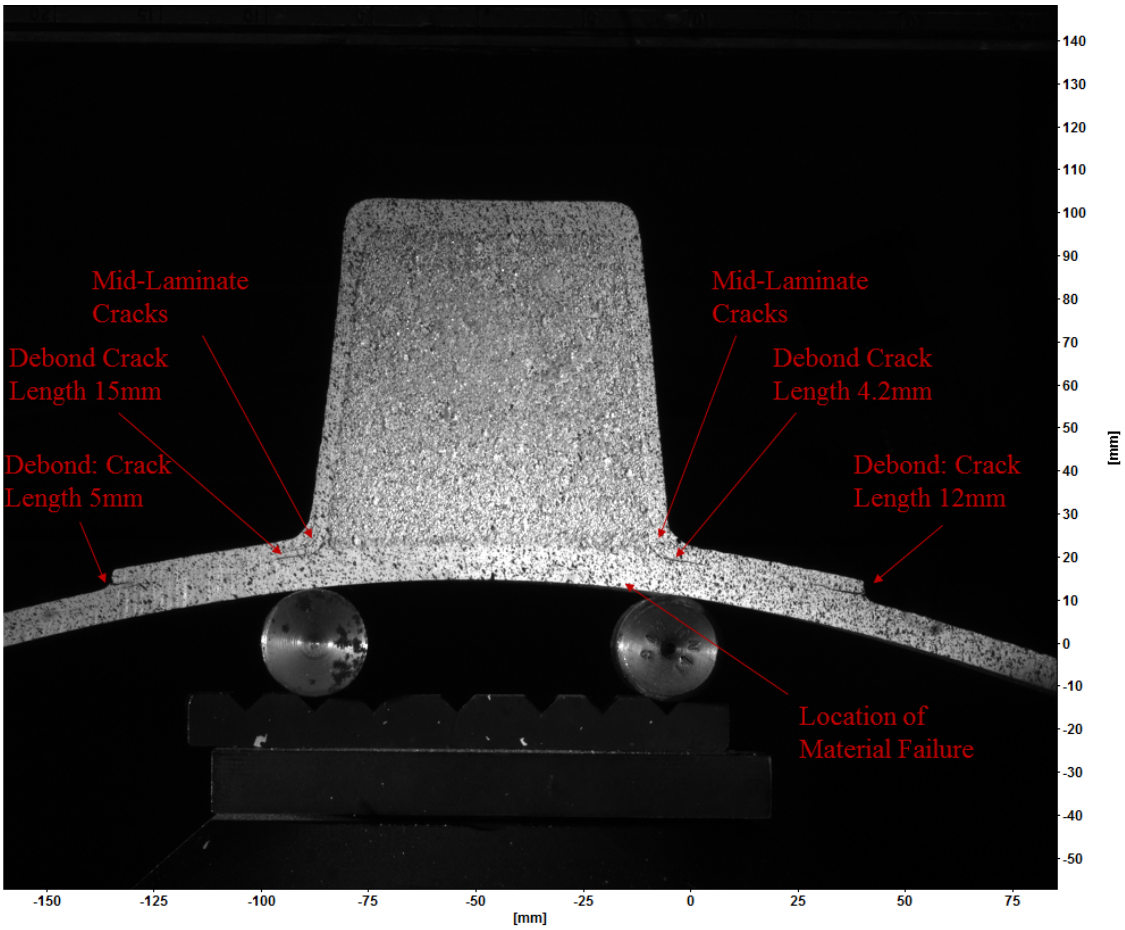

Figure 125: Four Point Bend: Test B1 at 28.8mm Displacement

I and II post-cured samples a greater number of samples should be assessed as the alignment of chopped strand tows resulted in a 98% variation between the samples with the most and least bridging observed. The width of the tested samples should also be addressed to be comparable to or greater than the CSM strand length. The average strain energy release rate are quoted however ideally a reliability approach is required for these interfaces due to the variability in the orientation of the CSM.

	Yetman	1 (warp/weft)	2	3	4	5	Units
Tensile Modulus	22100	29200/23900					MPa
Poisson's Ratio	.154	0.16/0.14					
Compressive Modulus	31200	31900/26900					MPa
Compressive Strength	272	363.4/336.4					MPa
Shear Modulus	.4-7	4.5/4.3					GPa
Shear Strength	57.9	47.3					MPa
Flexural Modulus	24000			24200			MPa
Co-Cured Mode I Strain Energy Release Rate NPC	.371			0.577	0.227	0.239	kJ/m2
Co-Cured Mode I Strain Energy Release Rate PC	0.967		0.804	1.210	0.988	0.739	kJ/m2
Co-Cured Mode II Strain Energy Release Rate NPC	.761		0.627		1.152	0.724	kJ/m2
Co-Cured Mode II Strain Energy Release Rate PC	.936			4.550	5.461	4.102	kJ/m2
post-cured Mode I Strain Energy Release Rate NPC	0.345						kJ/m2
post-cured Mode I Strain Energy Release Rate PC	1.15						kJ/m2
post-cured Mode II Strain Energy Release Rate NPC	1.12						kJ/m2
post-cured Mode II Strain Energy Release Rate PC	1.59						kJ/m2

Table 38: Summary of Experimentally Determined Material Properties

(1) Shivakumar [9] tested E-glass woven roving with a Dow Derakane 510A-40 brominated vinyl ester manufactured via VARTM

(2) Blake et al. [10] tested 800gsm woven E glass with a toughened Derakane 8084 matrix

(3) Dharmawan et al. [11] tested 800gsm woven E glass with a Derakane 411-350 matrix, data averaged if from multiple sources.

(4) Compston [12] tested Derakane 8084 using an E-glass woven 638gsm manufactured by hand lay up

(5)Compston [12] tested Derakane 411-45 using an E-glass woven 638gsm manufactured by hand lay up

[BLANK PAGE]

7 Case Studies

The material characterisation data from section 6 is used in this section to improve the assessment of the material model by investigating the effect of the tensile non-linearity for laminates in flexure and to improve the modelling parameters for the cohesive element response in fracture. The assessment of the cohesive interface strength is unclear in the literature and whilst it is shown to be less critical whilst modelling at the scale of the cohesive zone length by Alfano and Crisfield [95] it is critical to Turon's method for improving the efficiency whilst providing accurate results [87]. Therefore, the interface strengths are determined for glass vinylester composites using the experimental data determined in section 6. The four-point bend test on a post-cured top hat stiffened section is used to verify the modelling technique and identifying the key parameters to accurately assess the load deflection response and the failure mechanisms. A number of studies are then assessed using the determined modelling parameters and the damage tolerance model defined in section 3.4 and compared to the analysis in section 5 to determine the effect of the assumed parameters on the damage tolerance of debonded top-hat stiffened panels.

7.1 Modelling Laminate Flexure Test

An FEA model is built for the flexure test using a linear compressive and bi-linear tensile model as defined by the associated experimental tests previously. The model output is compared to a typical load per unit width and roller displacement response for an experimental coupon in figure 126. It is observed that the initial stiffness using the compressive and tensile experimental data provides a 10% increase compared to flexural stiffness determined experimentally as discussed previously. However, the non-linearity of the specimen is reasonably modelled suggesting that the flexural non-linearity is due to a similar mechanism of straightening of the tensile fibres as observed in the tensile tests.

Both the mode I and mode II tests rely on estimates of the flexural modulus, the effect of the non-linearity is assessed using typical mode I and mode II tests at the crack initiation load. The bi-linear model is used to assess the effect of the straightening of the crimped fibres.

An FEA analysis is conducted on the mode I test, modelling the opening arm at a crack length of 36mm at the experimental opening load of 70N, assuming a clamped end condition at the crack front. A bilinear model is used to model the tensile properties as recorded for the 5mm tensile tests. The longitudinal strain distribution illustrated in figure 127 shows that the transition strain of approximately 0.0035MPa is exceeded at the interface of the crack tip at the critical opening load. Therefore, it it is suggested that the straightening of the crimped fibres will contribute to micro-cracking at the crack tip, which is likely to affect the interface properties compared to non-crimped fabrics.

As the flexural modulus is critical in determining the strain energy release rate the effect of this non linearity is assessed with regard to the opening displacement. The stiffness of the beam is considered for a number of modelling assumptions and the end displacement of the beam under critical load are compared in table 39. The tensile modulus is tested as the linear stiffness defined as the failure stress over failure strain, 15152MPa, initial stiffness,

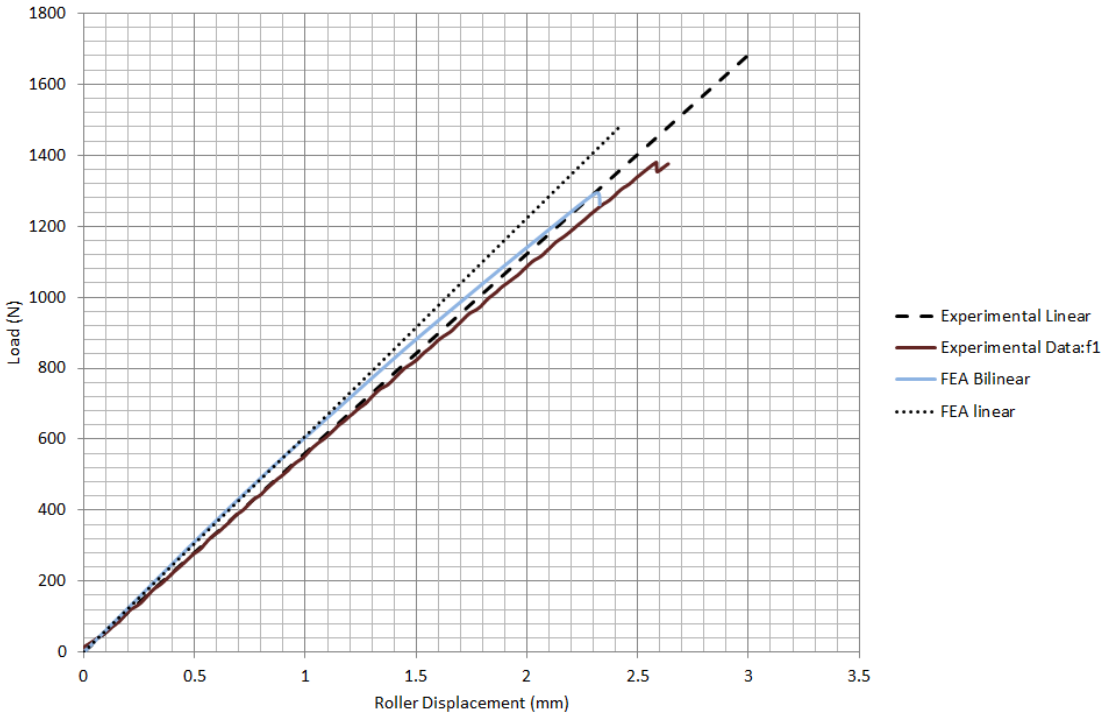

Figure 126: Flexure Test Typical Load Deflection Response

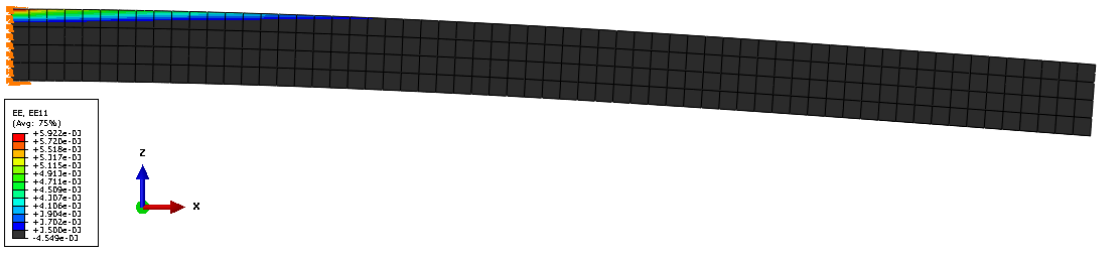

Figure 127: DCB Arm at Critical Opening Load

Model Description	Et	Ec	End Displacement (mm) at Critical Load	Error
Average Tensile Stiffness	15152	31200	1.91	20.3%
Initial Tensile Stiffness	20500	31200	1.61	0.9%
Bilinear Model	Bi-linear	31200	1.59	-

Table 39: Comparison of Beam Stiffness

20500MPa, and with a bilinear model. The percentage error is calculated using the bilinear model as a baseline. At the critical load at which the crack grows it is shown that the majority of the beam is below the initial tensile threshold therefore the flexural modulus is largely in the initial linear region and can be calculated to be equivalent for the critical loading at 25053MPa with 0.9% error. This is also confirmed by a linear load deflection curve prior to crack opening. This flexural modulus is then used for calculation of the strain energy release rates for mode I crack opening.

The experimental mode II tests show a distinct non-linearity in the load deflection curve prior to crack opening. The assessment of the bi-linearity of the tensile properties and micro-cracking at the interface are again assessed through analysis of a linear and bilinear model using cohesive elements at the interface. The longitudinal strain distribution is shown in figure 128 with tensile strains above 0.0035 shown. The load deflection curve is unaffected by the bi-linear model and therefore does not affect the compliance of the specimen during the tested loads. It is therefore assumed that non-linearity is due to matrix cracking ahead of the crack tip.

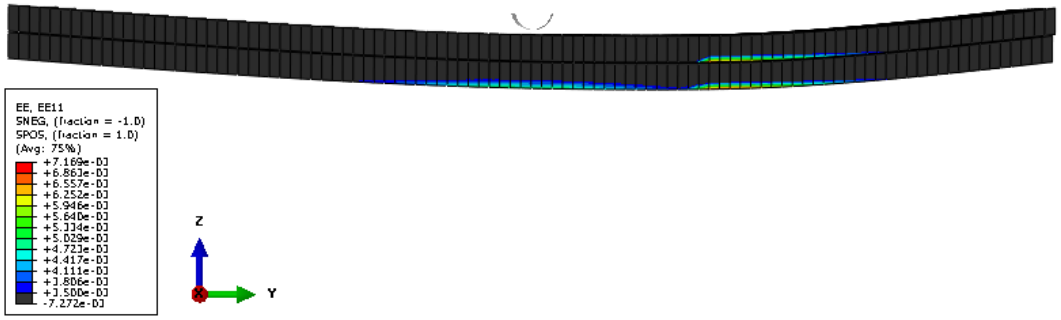

Figure 128: Longitudinal Strain at Critical Load for Experimental ENF Samples

7.2 Post-Cured Mode I and II Coupons

The DCB and ENF coupons are simulated to assess the appropriate interface strength and cohesive zone length and establish Turon's interface parameters. Mode I and II samples are modelled representing a post-cured pre-cracked sample, 6a2 and 7a6 respectively. As averaged properties are used in future modelling these samples are chosen as the critical strain energy release rates are closest to the average properties. The samples are modelled with a 5mm width to improve the efficiency of the model and results are scaled experimentally. The DCB sample has a crack length of 34mm and an average critical strain energy release rate of $1.39kN/m^2$ compared to the average for the sample set of $1.15kN/m^2$. The ENF sample has a crack length of 30mm, a critical strain energy release rate of $1.56kN/m^2$ compared to an average of the sample set of $1.59kN/m^2$. Both models use the mechanical properties as tested experimentally where the flexural modulus is 25053MPa. Initially a small mesh size is used which is assumed to be smaller than the cohesive zone length with a cohesive element size of 0.2mm and shell element size of 1mm. The effect of the interface parameter is assessed and chosen and the cohesive zone length is measured to ascertain the interface parameter in Turon's relationship. The interface parameter is then verified for increasing cohesive zone size and therefore mesh size.

The results are compared to the experimental and analytical results for varied values of the interface strength for the DCB in figure 129. The DCB test shows a significant R curve and therefore the peak load and crack propagation are not well modelled as the average critical strain energy release rate is used. The crack propagation of the analytical solution is well matched by the model giving confidence in the converged solution. Crack propagation is captured well by the mode I model for all interface strengths tested where interface strengths of 125MPa and larger are shown to provide a converged solution with a linear response until crack propagation is evident. As the interface strength reduces the response becomes less stiff prior to crack propagation and reduces the peak crack initiation load. It is noted by Alfano and Crisfield [95] that the variation of the maximum interfacial strength does not have a strong influence on the predicted properties but reducing the interface strength can aid convergence. Therefore, a minimum interface strength is selected that accurately models the crack propagation and stiffness. An interface strength of 125MPa is chosen which provides a linear response until crack propagation occurs. At this interface strength the cohesive zone length is 0.82 which is measured from the model as the distance over which the cohesive through thickness traction reaches the interface strength. The interface parameter is therefore calculated as 0.445. The interface strengths and cohesive zones are scaled with parameters shown in table 40 and the load deflection curves for each cohesive length are shown in figure 130. It is noted that increasing the cohesive zone lengths to 1.67mm and 5.0mm creates a slight deviation in the initial stiffness which is likely to be due to the convergence of the shell elements for this specific configuration. However, the peak load and crack propagation response are well modelled for both mesh sizes with a 5% increase in the peak load for the largest mesh size with all the key features represented.

The results are compared to the experimental and analytical results for varied values of the interface strength for the ENF samples in figure 131. It is shown that as the interface strength increases the load deflection response approaches the analytical solution which remains linear until the crack propagates. As the interface strength reduces

the stiffness of the coupon reduces at lower loads and the peak load is reduced. The experimental results show a degree of non-linearity indicating micro-cracking ahead of the crack tip and energy dissipation prior to crack propagation. The non-linearity is well represented by an interface strength of 50MPa however the peak load is under-estimated. To account for the energy dissipation prior to crack propagation the model is tested with a critical strain energy release rate of 1.71 representing 130% of the experimental measured energy and compared for a range of interface strengths. It is shown that an improved fit for the experimental data can be achieved by this method. However, without an assessment of the fit of reducing the interface strength on the quadratic stress criterion in comparison to the mixed mode curves the interface strength of 150MPa is chosen which provides a good estimate in comparison to the analytical response. At this interface strength the cohesive zone length is 1.00mm which is measure from the model as the distance over which the cohesive through thickness traction reaches the interface strength. The interface parameter is therefore calculated as 0.57. The interface strengths and cohesive zones are scaled with parameters shown in table 40 and the load deflection curves for each cohesive length are shown in figure 132. Good agreement is shown for cohesive zone lengths of 1mm and 1.67mm with the initial stiffness, peak load and crack propagation well modelled compared to the analytical solution. The 5mm cohesive zone model introduces a 1.7% error in the peak load but shows good agreement to the analytical solution.

Turon's method is therefore verified for this material for DCB and ENF samples with key parameters summarised in table 41.

Table 40: Double Cantilever Beam: Interface Strength (MPa) for Increasing Cohesive Zone Length

	1.0mm	1.67mm	5.0mm
t_{o_I}	113	88	51
$t_{o_{II}}$	150	116	67

Table 41: Interface Parameters for DCB and ENF Samples

	Mode I	Mode II
Cohesive Zone Length,l_{cz}, (mm)	0.82	1.00
Interface Strength,t_{o_i}, (MPa)	125	150
Interface Parameter, M	0.45	0.57
Critical Strain Energy Release Rate, G_i	1.15	1.59

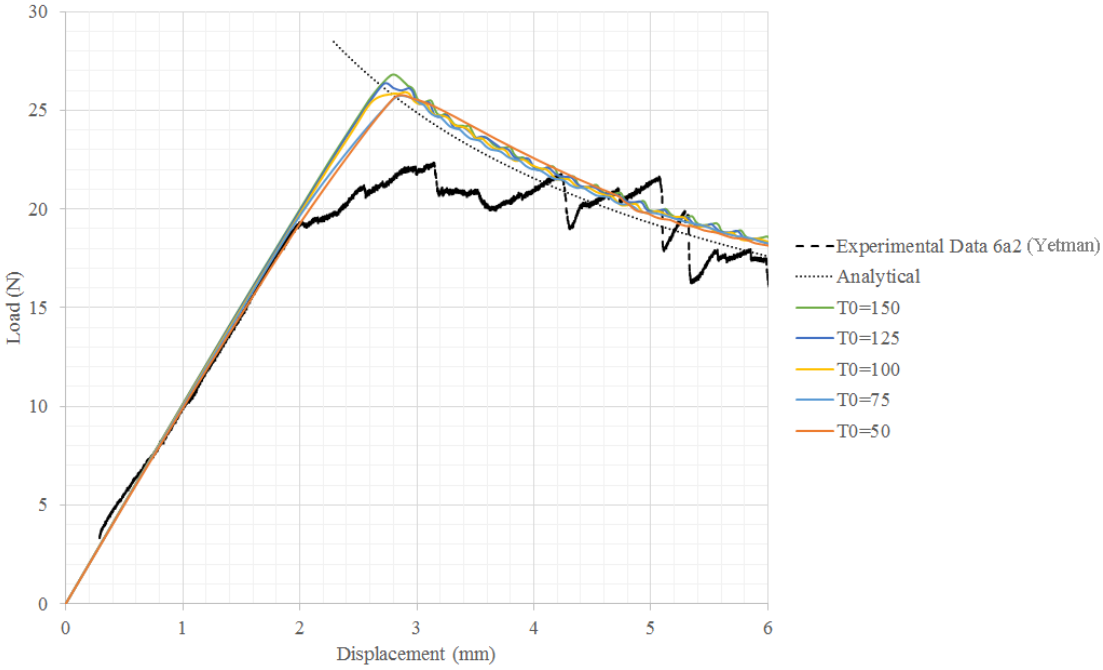

Figure 129: Double Cantilever Beam; Load Displacement Curve for Varying Interface Strengths

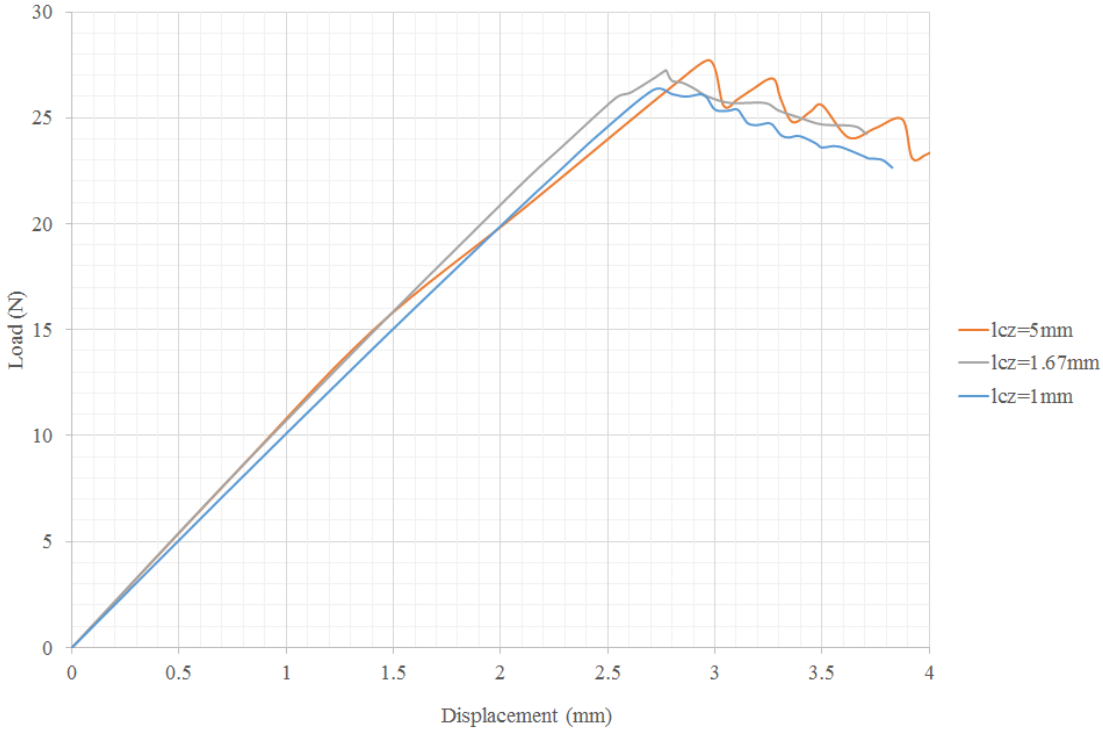

Figure 130: Double Cantilever Beam; Load Displacement Curve for Artificial Cohesive Zone Lengths

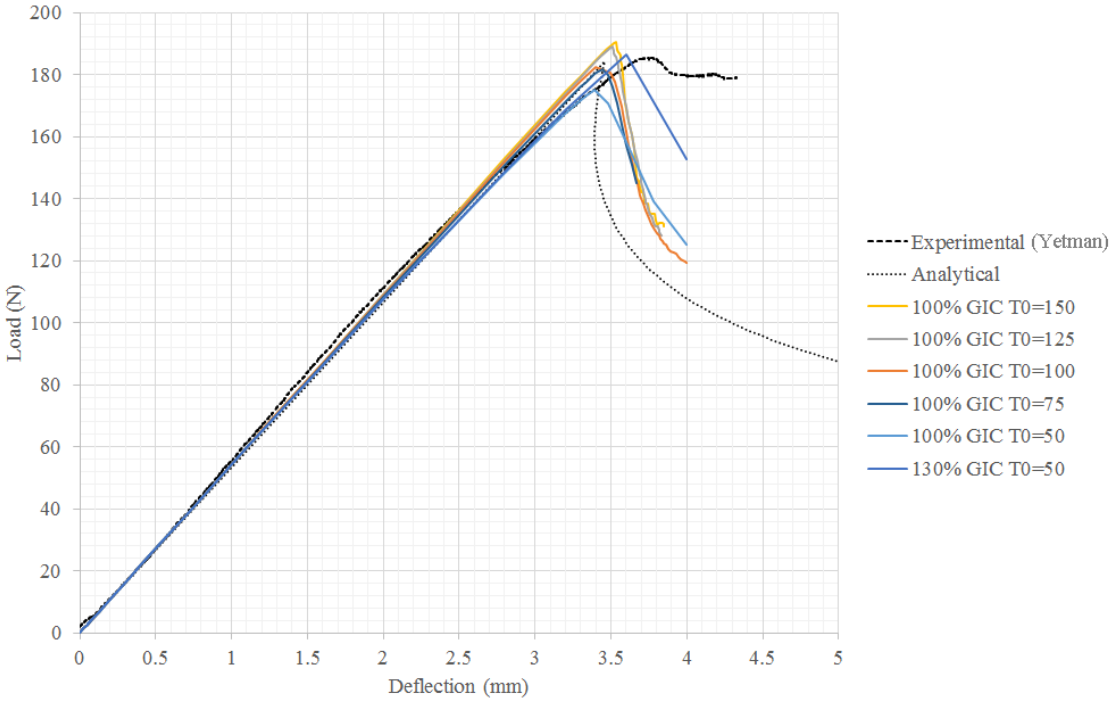

Figure 131: End Notch Failure; Load Displacement Curve for Varying Interface Strengths

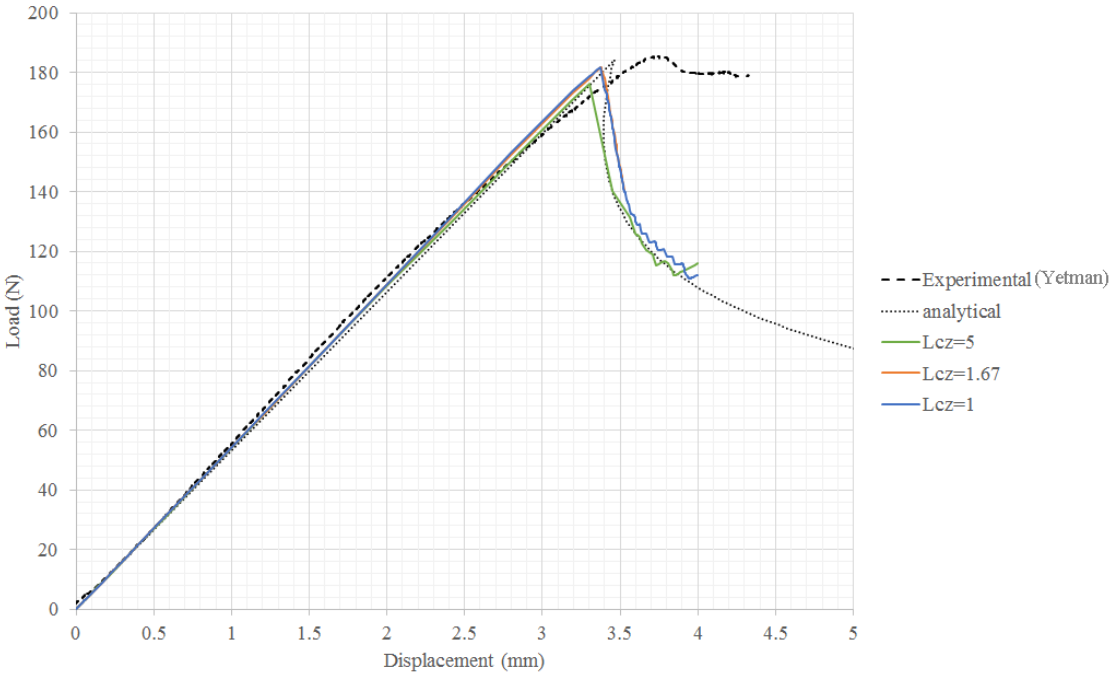

Figure 132: End Notch Failure; Load Displacement Curve for Artificial Cohesive Zone Lengths

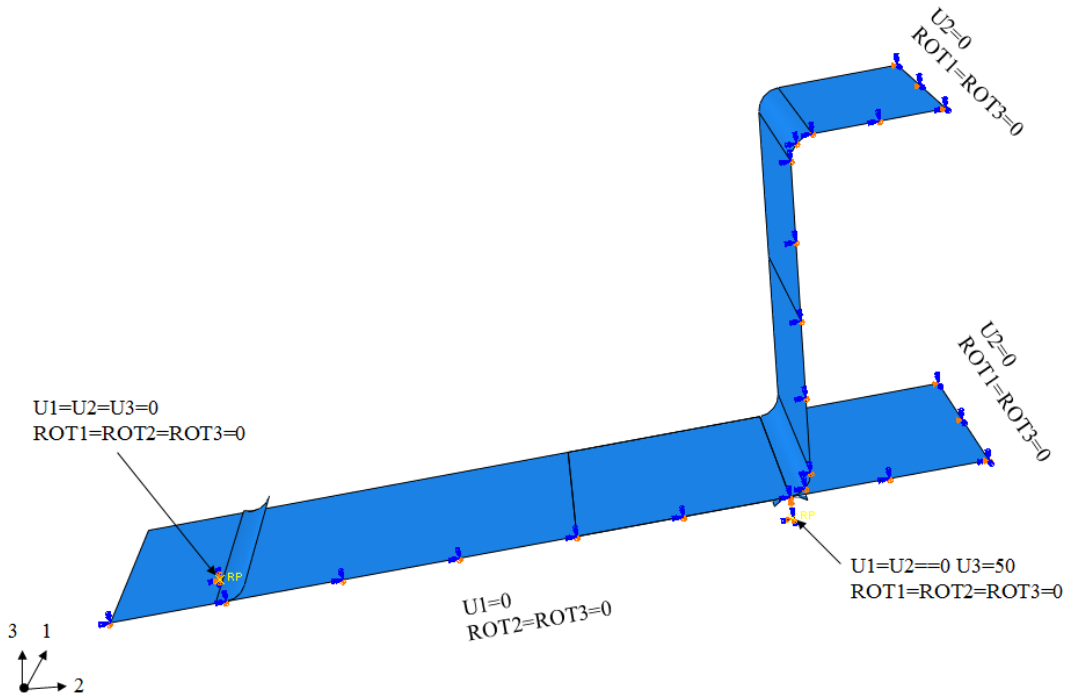

Figure 133: Four Point Bend: FEA Model Set-up

7.3 Top-Hat Stiffener Under Four Point Bend Loading

A quarter model of the top-hat four point bend configuration is created as shown in figure 133. Symmetric boundary conditions are applied to the inner 2-3 plane and 1-3 plane. The upper and lower rollers are fully constrained with the exception of a displacement load applied to the lower roller up to 50mm parallel to the vertical, '3', axis. The inner and outer rollers are positioned symmetrically about the center at 85mm and 325mm widths respectively. The stiffener geometry is as used in Configuration A discussed in section 5.

The material properties are given in table 42 for the assumed properties taken from the literature and the experimentally determined results. The assumed properties are taken from associated data where available. The Benzeggagh-Kenane exponent [69] is calculated at 1.17 using the least squares fitting method through similar available data which gives an R^2 value of 0.9242 showing a good fit.

The maximum shear stress observed is of the order of 10MPa which is within the initial linear region of the experimental results. Therefore the shear modulus is approximated to a linear stress-strain response with shear modulus of 7000MPa. Cohesive elements are used at the interface with a depth of 0.01mm.

A mesh convergence study is conducted, using the experimental material properties shown in table 42 for decreasing shell element size. Turon's method is used to determine the interface strength, with 3 cohesive elements within a cohesive zone length which is equivalent to the shell element size; the cohesive viscosity parameter is set to 1E-5. In this study material degradation is neglected. The load deflection curves for the full model are shown in figure 134 for decreasing shell element size. It is shown that the response converged for the initial stiffness and

Table 42: Material Properties

Property	Units	WRE580 Assumed Properties	Reference	UE500	Reference	WRE580 Experimental Results*
Tensile Young's Modulus, E_{11T}	MPa	26550	Averaged from Shivakumar [9]	26790	Manufacturer's Data	22100
Tensile Young's Modulus, E_{22T}	MPa	26550	Averaged from Shivakumar [9]	5850	Manufacturer's Data	22100
Tensile Young's Modulus, E_{33T}	MPa	2655	*	5850	Manufacturer's Data	2200*
Compressive Young's Modulus, E_{11C}	MPa	29400	Averaged from Shivakumar [9]	26790	Manufacturer's Data	31200
Compressive Young's Modulus, E_{22C}	MPa	29400	Averaged from Shivakumar [9]	5850	Manufacturer's Data	31200
Compressive Young's Modulus, E_{33C}	MPa	2940	*	5850	Manufacturer's Data	3400*
Shear Modulus, G_{12}	MPa	4400	Averaged from Shivakumar [9]	2200	Manufacturer's Data	7000
Shear Modulus, G_{13}	MPa	4400	*	2200	Manufacturer's Data	7000*
Shear Modulus, G_{23}	MPa	4400	*	2200	Manufacturer's Data	7000*
Poisson's Ratio, ν_{12}	-	0.16	Shivakumar [9]	0.272	Manufacturer's Data	0.154
Poisson's Ratio, ν_{13}	-	0.408	*	0.058	Manufacturer's Data	0.154*
Poisson's Ratio, ν_{23}	-	0.408	*	0.058	Manufacturer's Data	0.154*
Tensile Strength, S_{11T}	MPa	431	Averaged from Shivakumar [9]	482.0	Manufacturer's Data	444*
Compressive Strength, S_{11C}	MPa	350	Averaged from Shivakumar [9]	308.0	Manufacturer's Data	272
Tensile Strength, S_{22T}	MPa	431	Averaged from Shivakumar [9]	17.6	Manufacturer's Data	444*
Compressive Strength, S_{22C}	MPa	350	Averaged from Shivakumar [9]	87.8	Manufacturer's Data	272
Shear Strength, S_{12}	MPa	45.9	Averaged from Shivakumar [9]	24.2	Manufacturer's Data	57
Interface Strength, X_N	MPa	17.6	Determined from associated data			125
Shear Strength, $X_{T(ILSS)}$	MPa	23.2	Determined from associated data			150
Mode I Critical SERR, G_{IC}	kJ/m^2	1.21	Dharmawan et al. [11]	-		1.15
Mode II Critical SERR,G_{IIC}	kJ/m^2	4.55	Dharmawan et al. [11]	-		1.59
Benzeggagh-Kenane exponent, η_{BK}	-	1.17	Calculated from Dharmawan et al. [11]	-		1.17

* Values marked are assumed or calculated properties.

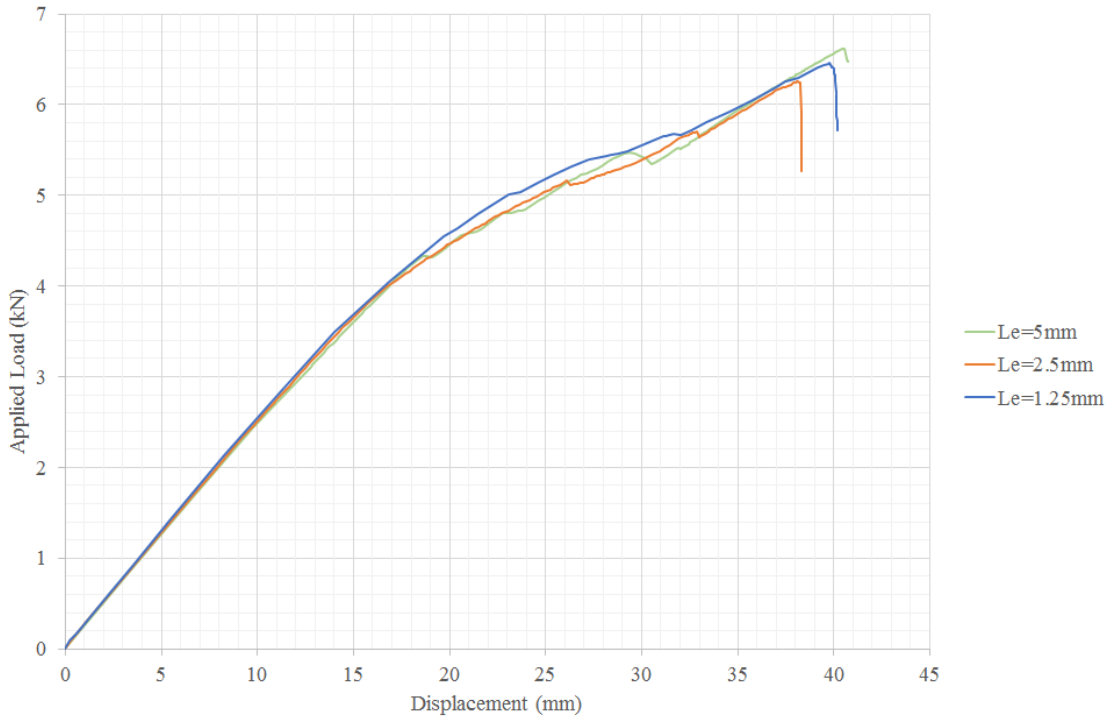

Figure 134: Four Point Bend: Mesh Convergence

non linearity between 25mm-31mm roller displacement for a mesh size of 3.3mm or less. Good correlation is shown between the three mesh sizes and therefore cohesive zone sizes. There is a 5.5% variation between the peak loads using an element size of 5mm and 2.5mm showing the calculation of the interface parameter could perhaps be improved although it provides a reasonable estimate foran acceptably larger mesh size. For this study a mesh size of 2.5mm is chosen which provides the most conservative response. Assessment of the mode mix shows the inner edge propagates under 86% mode II opening whereas the outer flange edge is mode I dominant with only 3% mode II.

A number of modelling parameters are compared in response to their load displacement curves as shown in figure 135. It is shown that the stiffness of the top-hat stiffened plate is underestimated with a 10% reduction compared to the experimental data. The measured lamina thickness is input into the model therefore, it is assumed that there is a discrepancy between the measured coupon flexural modulus and the top hat stiffened plate. The variation in flexural modulus is observed between the mode II and flexural testing and could be a result in variation in the manufacturing process as similar variation is commented on by Dharmawan et al. [11]. The initial non-linearity is captured reasonably well by the model where non-linearity occurs at a displacement of 14mm but is not conservative as non-linearity is observed experimentally at approximately 6.8mm for panel B and 9.0mm for panel A. However failure is predicted using the crack initiation values at a load of 3.61kN with complete debonding of the top hat stiffener. The crack propagation and ultimate failure is well modelled by the crack propagation strain energy release rates with final failure predicted by debonding at 6.2kN compared to the experimental value of 5.94kN which was

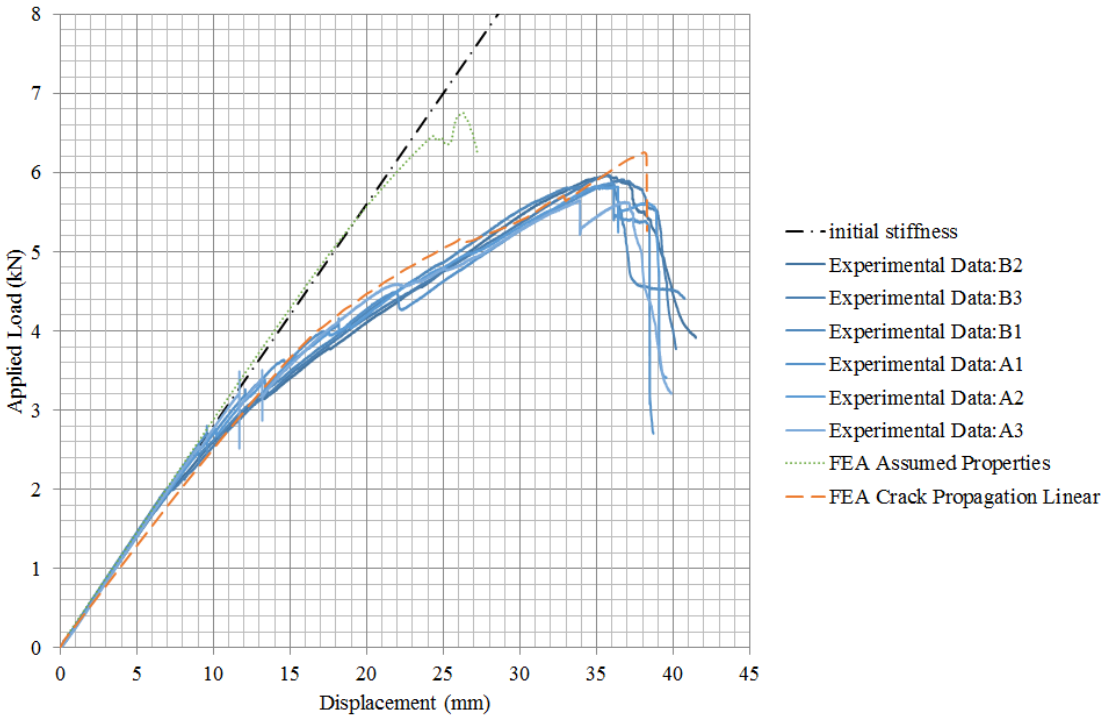

Figure 135: Four Point Bend: Comparison of Model

due to material failure under the rollers. The model is limited as it fails to capture crack initiation and propagation at the web flange curve of the top hat stiffener but the model provides a good approximation within its limitations.

The experimentally determined properties are compared to the assumed mechanical properties from the literature which are summarised in table 42. Figure 135 shows that the initial linear phase is well captured by the assumed properties gathered from the literature however the crack initiation, propagation and failure provide a non conservative result.

Crack length against roller displacement for the inner and outer flange edges are compared where crack initiation is determined when the stiffness of the cohesive element is degraded to 5% of the initial stiffness. Degradation of the cohesive elements begins at a deflection of 8.68mm when the cohesive strength criterion is exceeded however crack initiation is predicted on the inner and outer edge at a roller displacement of 12mm using the crack initiation model. This corresponds well to the experimental results with audible cracks heard at 6.4 and 7.1mm roller displacement. There is considerable scatter in the crack length data experimentally however, it is shown that crack initiated on the outer curve on one side of stiffener A earlier than predicted, which may have been caused by an imperfection at the joint, but the results for the other outer flange interfaces correlate well.

The shear stresses are assessed to determine whether the effect of non-linearities in the shear properties. The maximum shear stress is 13MPa observed in the flange area in the region of the crack tip and is therefore unlikely to be affected by non-linearity in shear. Figure 136 shows the stresses in the fibre direction aligned with the lateral plies, parallel with the y direction at 47.5mm roller displacement. At a roller displacement of 35mm the stresses are

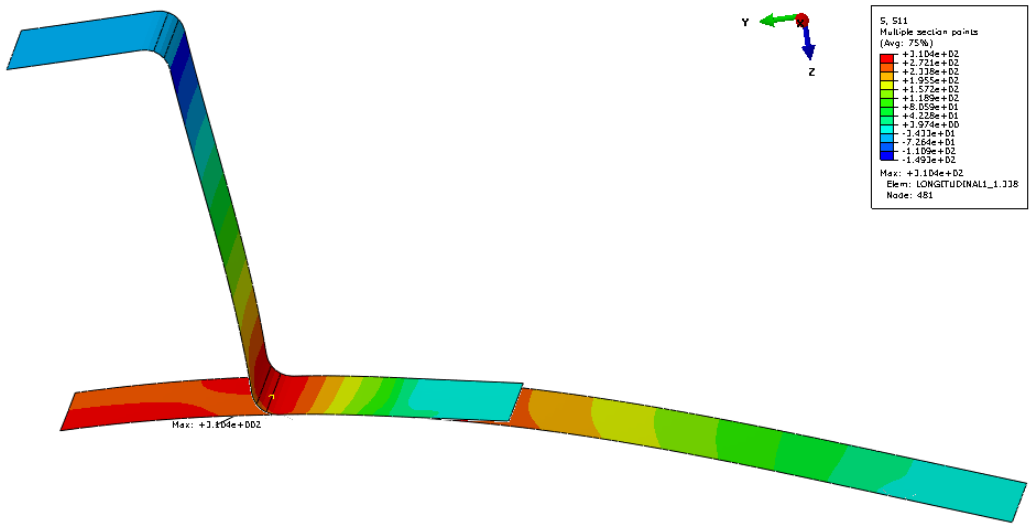

Figure 136: Four Point Bend: Stress Plot at 47.5mm roller displacement

approaching the failure stresses of the woven roving. The stress in the flange web curve is approaching the tensile stress of 444MPa however experimentally it is observed that mid-laminate cracks develop in this area relieving this tensile stress. Contact is not modelled between the roller and the plate and therefore failure in this area is not taken into account however in the experimental results it is assumed that accumulating damage under the rollers does not adversely affect the crack propagation or load-roller displacement response prior to failure.

In summary the method for modelling crack initiation and crack propagation for debonding of a top-hat stiffened plate is modelled with good agreement with the experimental results. Turon's method is used to artificially increase the cohesive zone length with reasonable agreement for increasing mesh size for the parameters identified. The specific fracture properties as tested are shown to be critical in assessing crack initiation and propagation with considerable error provided by data assumed from the literature for this configuration.

7.4 Analysis of Skin Stiffener Debonding of Top-Hat Stiffened Panels

The model used in section 5 is compared using the experimental data and parameters determined in section 6 and 7.2. To assess the effect of the material properties on the damage tolerance of the panel. The crack propagation values are used as determined experimentally to model the crack propagation and ultimate load. The reference panel is used as defined in section 3.3 and the effect of size of a central debond is assessed along with debond location for a nominal imperfection.

7.4.1 Analysis of Debond Size

The intact condition is used as the reference case with the effect of central debonds sized from 50mm to 350mm at 50mm spacings. The failure mechanism map is shown in figures 137 and 138 for the assumed and experimentally derived properties allowing direct comparison and illustrating the change in ultimate strength, crack propagation,

damage initiation, and panel, plate and stiffener buckling.

The intact case is assessed showing that the plate buckles into three half sine waves with a positive inflection at the center, local buckling and stiffener buckling occur at 73-75% of the ultimate load showing the panel has a significant post buckled strength. Damage initiation, in the form of shear failure, and crack initiation occur at 91% load on the anti-node lines with material failure being the dominant failure mode across the panel. The failure mechanism map shows similar trends to the assumed case reported in section 5.2.1 with two distinct phases for the data points shown.

For small debonds of 27% or less there is only minor deviation in the failure characteristics. Shear failure of the plate in the region of the anti-node lines and the center of the plate beneath the stiffener is the dominant mode of failure for the intact case and small debonds. Any crack propagation is nominal for these cases.

At 33% the debond exceeds the length of the half sine wave buckled mode and there is a significant reduction in the crack propagation load from 92% to 58% with a reduction in the ultimate strength to 76%. Crack propagation becomes the dominant failure mode which occurs prior to the damage initiation load and is largely coincident with the stiffener buckling. This change in mechanism is again caused by the inversion of the plate inflections, switching of the central inflection from positive to negative out-of-plane deflection. For increasing debond size a plateau exists where the ultimate strength remains greater than 75% of the intact ultimate strength. Ultimate failure is due to gross failure of the plate and buckling of the supporting stiffeners. The supporting stiffener is observed to debond only during the final collapse of the panel.

Comparing the results to those of section 5.2.1 shows similar trends despite the reduction in relative post-buckled strength of the panel.

7.4.2 Analysis of Debond Location

Debond position is investigated for small, 6.67%, medium, 20%, and large debonds, 40% using experimentally derived properties for comparison to the assumed properties used in section 5.3. The location is represented as a ratio of the distance of the centre of the debond from the plate end against the total plate length. Figures 139, 140 and 141 show the failure mechanism maps for small, medium and large debonds respectively for the experimentally derived material properties. The failure mechanism maps for small, medium and large debonds for the assumed properties are repeated to allow direct comparison in figures 142, 143 and 144 respectively.

For small debonds the debond location has little effect on the failure mechanisms and a slight increase for offset debonds. These are similar trends to those seen in section 5 with assumed material properties; for small and medium debonds the buckled mode shape is unaffected by the debond in all locations which is not the case for large debonds. For medium debonds representing 20% of the panel length the debonds location relative to the negative inflection is relevant with crack propagation initiated by a crack front resting on the negative inflection. The ultimate load reduced to approximately 75% of the ultimate load compared to 78% with the experimentally derived properties. Using the experimentally derived properties shows a more gradual effect then the assumed properties with only a 20% change in the ultimate load and a gradual reduction in ultimate load as the crack front approaches the

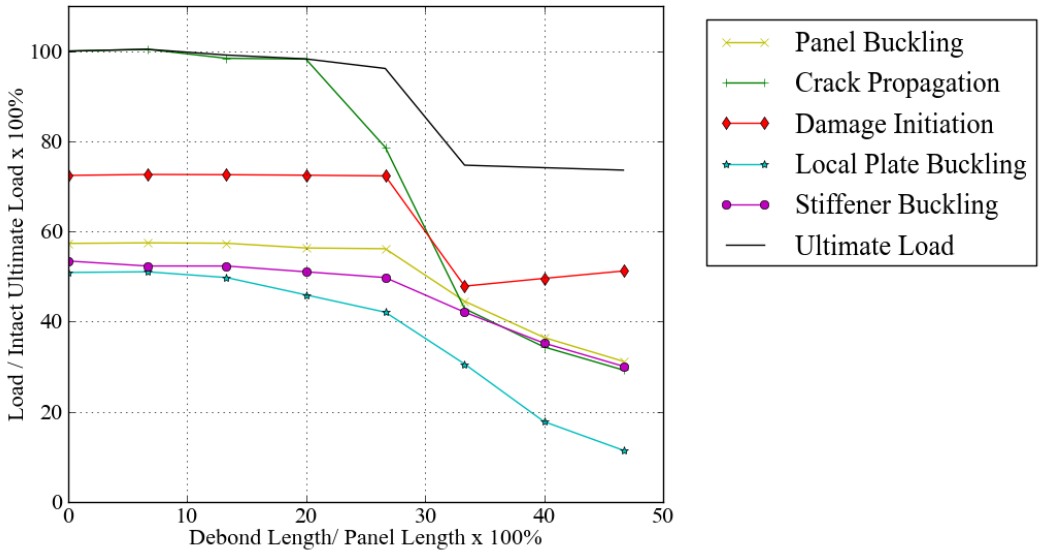

Figure 137: Failure Mechanism Map for Assumed Material Properties and Increasing Central Debond Size With Nominal Imperfection

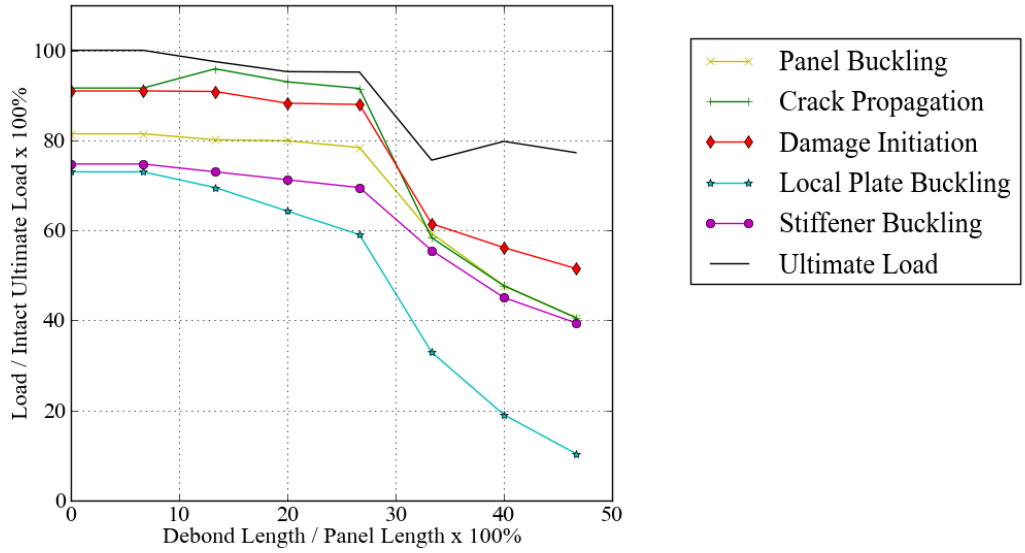

Figure 138: Failure Mechanism Map for Experimental Material Properties and Increasing Central Debond Size With Experimentally Determined Properties

anti-node line compared to approximately 30% in the previous study. This is due to the increased contribution of mode II opening at the crack front due to the reduction in the mode II critical strain energy release rate which leads to enhanced crack propagation for a crack front over the positive inflection and at the anti-node line. Debonding of the out stiffener is observed during final collapse of the panel following shear and compressive failure in the region of the anti-node lines and in the debonded plate.

For large debonds there is little dependency on location for this study and limited dependency in the previous study showing that the effect of debond position relative to the buckling mode shape can be seen to affect medium debonds only, affecting both the crack propagation and ultimate load. For large debonds the stiffener is observed to fully debond however final failure is initiated by the material failure of the plate prior to debonding of the outer, supporting stiffeners.

Therefore, the effect of the debonding of the top-hat stiffened panel using the experimental and assumed properties draws similar conclusions. The experimental properties show a reduction in the mode II critical strain energy release rate which is seen to affect the crack propagation for a crack front resting on a negative inflection and catastrophic stiffener debonding is observed during collapse.

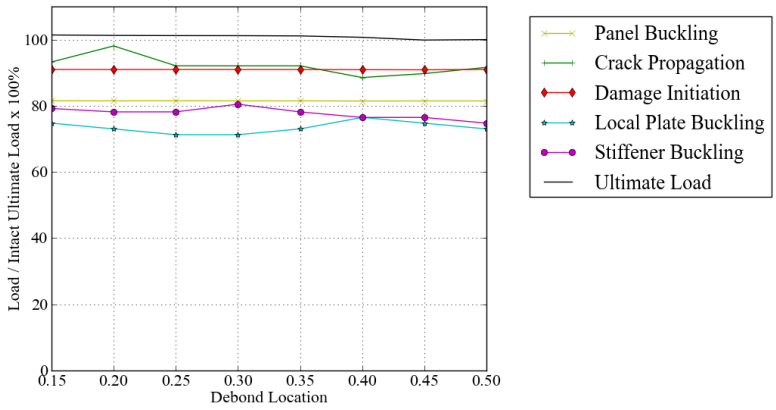

Figure 139: Failure Mechanisms for Experimental Material Properties and an Offset Small Debond with Nominal Imperfection

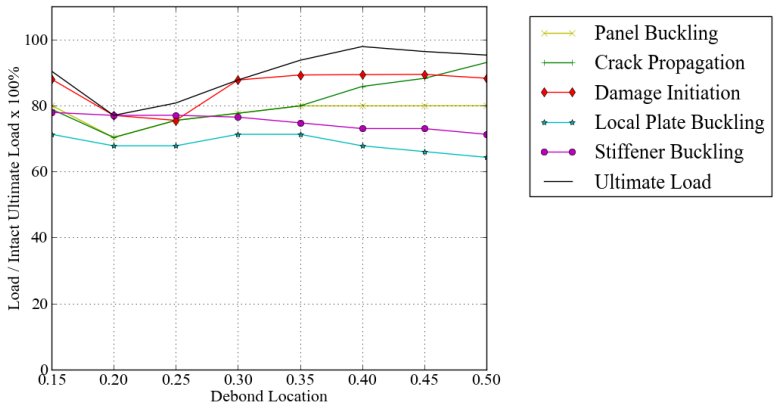

Figure 140: Failure Mechanisms for Experimental Material Properties and an Offset Medium Debond with Nominal Imperfection

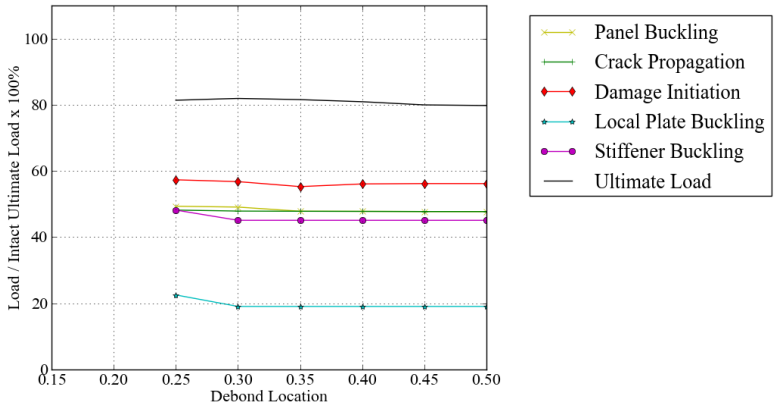

Figure 141: Failure Mechanisms for Experimental Material Properties and an Offset Large Debond with Nominal Imperfection

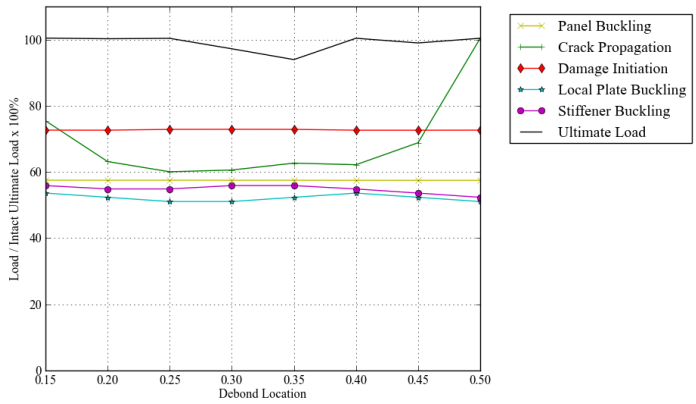

Figure 142: Failure Mechanisms for Assumed Material Properties and an Offset Small Debond with Nominal Imperfection

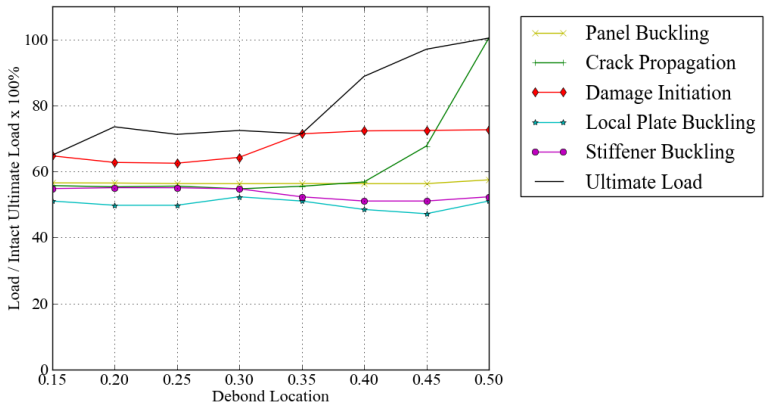

Figure 143: Failure Mechanisms for Assumed Material Properties and an Offset Medium Debond with Nominal Imperfection

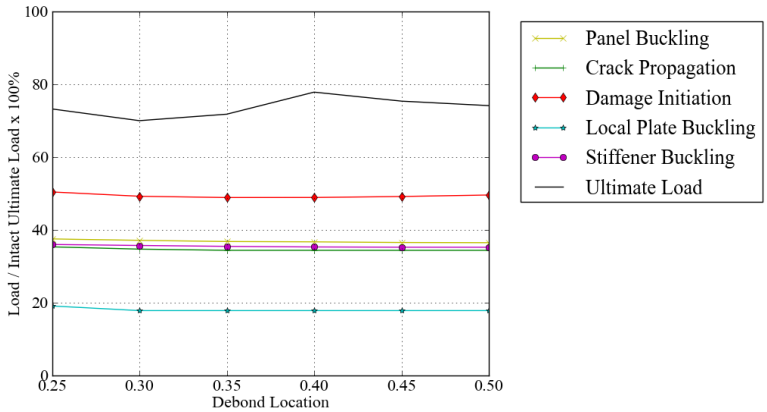

Figure 144: Failure Mechanisms for Assumed Material Properties and an Offset large Debond with Nominal Imperfection

7.5 Summary

In this section the effect of the non-linearities determined during material characterisation in section 6, on the flexural stiffness and the failure mechanisms of mode I and mode II crack propagation are investigated. It is shown the flexural response can be improved by modelling these non-linearities where the structure is loaded above 50% of its flexural strength. It is also shown that the critical strain at which crimped fibres straighten in tension is exceeded in the DCB and ENF samples tested resulting in additional micro-cracking at the interface however the flexural stiffness of the specimen is largely unaffected and therefore the strain energy release rate calculation is valid.

The mode I and II interfaces strengths are calculated using Turon's method and verified for increasing mesh size and verified against the experimental results for specific configurations. It is shown that micro-cracking ahead of the crack tip is evident for mode II crack opening and the interface strength is adjusted to improve the cohesive element model.

The modelling parameters are input into an FEA model representing the four point bend test on a post-cured top-hat stiffened panel, as tested in section 6.2. There is good agreement is shown between the load-deflection response and crack initiation and propagation within the limitations of the model. It is shown that there is a 10% variation in the flexural stiffness which is confirmed by the variation observed in the material characterisation tests and by other authors. Turon's method is used to artificially increase the cohesive zone length with reasonable agreement for increasing mesh size for the parameters identified. The as tested specific fracture properties are shown to be critical in assessing crack initiation and propagation with considerable error provided by data assumed from the literature for this configuration.

The determined interface parameters are then used in a final parametric study on the multi-stiffened panel containing simulated damage, which are comparable to the assumed properties. It is shown that debonding of the top-hat stiffened panel using the experimental and assumed properties draws similar conclusions. The experimental properties show a reduction in the mode II critical strain energy release rate which is seen to affect the crack propagation for a crack front resting on a negative inflection and catastrophic stiffener debonding is observed during collapse.

8 Conclusions

Top-hat stiffened shell structures are utilised across a number of applications to their ability to prevent lateral-torsional instability and panel buckling. In composite ships incidents such as accidental collisions, striking submerged objects or by severe wave slamming are commonly shown to lead to debond damage. It is imperative that once damage has occurred that it can be rapidly assessed and suitable precautions taken to ensure safety of the structure and its users, but this must be done cost efficiently to reduce expensive maintenance costs. At the design stage assessment of the effect of defects and damage leads to an optimised damage tolerant design which both avoids catastrophic failure and provides an efficient use of materials leading to optimised weight and fuel efficiency / load carrying capacity. Currently the UK-MoD post-damage procedure contains no readily available guidelines as to the residual capability of the structure and damage tolerance during the design phase is not considered. Therefore, the research in this thesis considers the damage tolerance of top-hat stiffened glass vinylester panels containing debond damage. The focus of the work is on typical top-hat stiffened panels in a marine environment through the verification of a numerical model, characterisation of materials and interfaces and the assessment of damage and design parameters on the damage tolerance.

The literature review has shown that many authors have investigated the damage progression of intact structures with good correlation with experimental results however, there is still limited research conducted on the residual capabilities of structures containing delaminations from prior damage. Research on damaged stiffened structures to date is primarily focused on airframe applications considering stiffeners with open cross sections and co-cured or co-bonded stiffeners which are not typical of marine structures. Top-hat stiffeners have been shown to have increased torsional rigidity in comparison to I-stiffeners or T-stiffeners and have an increased structural efficiency when compared to J-stiffened panels. However, the damage response of such panels is not well understood. The novel contribution of the numerical work is to model the effect of simulated debond damage on the ultimate strength of top-hat stiffened panels and multi-stiffened panels assessing the effects of damage and design parameters on the residual strength.

Analysis of the material data available in the literature for heavy weight glass vinylester woven roving typically used in large marine applications shows that a complete data set of mechanical and interface properties is lacking and that there can be significant variation between results from different manufacturing methods, component materials, layups and weave structures. Typical marine sub-component joints commonly use an interface layer of chopped strand mat between the initially cured plate and post-cured sub-component. These joints are not well characterised in the literature although it is shown that the chopped strand mat layer can have significant effect on the interface properties. Therefore the novel contribution of this experimental work is the full characterisation of typical materials providing a complete data set of mechanical characterisation and fracture data for both co-cure interfaces, typical of mid-laminate debonds, and post-cured interfaces which use an interface chopped strand mat layer at the interface, typical of sub-component joints.

The model is developed and verified against the literature in section 4. The developed model shows good correlation when compared to experimental data available in the literature for buckling and the collapse of plates

and stiffened panels, crack propagation in mode I and II coupons, delamination propagation and the post-buckled response of through width delaminated coupons and embedded delaminations in plates. The cohesive zone method is used to model both crack initiation and propagation and Turon's method is verified to allow the mesh size in the debond area to be increased. The WWFE recommendations are used in the verification cases to assess material failure and progressive damage. However as woven fabrics are used an analysis of failure criteria has shown that the Tsai-Wu failure criterion with an interaction parameter of -0.15 can represent bi-axial material failure in woven materials and the model is incorporated into a UMAT progressive collapse model.

In section 5 a parametric study is conducted on simulated debond damage on a multi-stiffened top-hat panel. The increased torsional rigidity of the stiffeners are shown to prevent stiffener tripping as a failure mode and therefore differences are observed in the trends of debond size and location compared to the previously investigated open section stiffeners. The complexities of the damage case are illustrated for a number of damage and panel parameters. Panel design parameters such as increasing the stiffener height and plate thickness are shown to decrease the damage tolerance of the panel and can result in catastrophic failure which should be designed against. However, for small and medium debonds it is shown that crack initiation does not propagate or diminish the ultimate strength of the panel significantly, for panels with a significant post-buckled strength, and that a 'no crack growth philosophy' results in conservative results. Location dependence is observed with respect to the buckled mode shape. The imperfection and particularly the nominal lateral pressure are shown to significantly affect the damage tolerance of the panels and therefore identifying the as-built geometry, residual stresses and loading conditions are critical in assessing the damage tolerance of a stiffened panel. However, the nominal imperfection case appears to give conservative results for the cases tested.

The mechanical and interface properties are characterised using ISO and ASTM standards for uni-directional and multi-directional composites where applicable in section 6. This provides a complete set of data and quantifies the fracture properties of post-cured laminates for the first time. The non-linearities in tension and shear are characterised and material models developed to match the experimental data. The mode I and II interfaces are characterised for the co-cured and post-cured samples. The mode I co-cured samples show a slip-stick release and the Mouritz method is used to characterise the experimental data and determine crack propagation values with and without fibre bridging. The slip-stick mechanisms is not observed in the Mode I post-cured however samples show an R curve therefore propagation data is calculated in the stable region of this curve. Further tests are recommended in order to fully assess the statistical significance of the CSM layer in mode I and II post-cured samples a greater number of samples should be assessed as the alignment of chopped strand tows resulted in a 98% variation between the samples with the most and least bridging observed. The width of the tested samples should also be addressed to be comparable to or greater than the CSM strand length. The average strain energy release rate are quoted however ideally a probabilistic approach is required for these interfaces due to the variability in the orientation of the CSM.

The final case studies conducted, in section 7, further verify and optimise the material model. An assessment is made on the effect of the non-linear tensile response on the flexural properties of the laminate. It is shown that the

flexural response can be improved by modelling these non-linearities where the structure is loaded above 50% of its flexural strength. It is concluded that this non-linearity does not affect the flexural modulus of the mode I and mode II samples and therefore the initial flexural strength may be used to determine the interface parameters. It is shown that the critical strain at which the crimped fibres straighten in tension is exceeded in the DCB and ENF samples tested resulting in additional micro-cracking at the interface. Mode I and II tests are simulated to ascertain appropriate interface strength and Turon's interface parameter to allow modelling of the specimens via cohesive elements and to ensure convergence as the cohesive elements increase in size. The four point bend test is modelled with good agreement verifying the material properties determined from coupon tests represent those of an as built large scale top-hat stiffened panel and verifying the material properties and interface parameters can appropriately assess the load-deflection response and crack initiation and propagation. Turon's method is used to artificially increase the cohesive zone length with reasonable agreement for increasing mesh size for the parameters identified. The as tested specific fracture properties are shown to be critical in assessing crack initiation and propagation with considerable error provided by data assumed from the literature for this configuration. These parameters are then used in a final parametric study on the multi-stiffened panel containing simulated damage and which are comparable to the assumed properties. It is shown that debonding of the top-hat stiffened panel using the experimental and assumed properties draws similar conclusions. The experimental properties show a reduction in the mode II critical strain energy release rate which is seen to affect the crack propagation for a crack front resting on a negative inflection and catastrophic stiffener debonding is observed during collapse. Therefore the novel contribution of these studies is the assessment of the effect on non-linearities on the flexural properties of DCB and ENF coupons and the assessment of interface properties for accurate modelling of post-cured glass vinylester laminates.

The research presented in this thesis assesses the performance capability of damaged joints and panels and meets the objectives defined in section 1 as follows:

[1] A comprehensive literature review is reported in section 2 which summarises the state of the art in modelling methods for composite structures, the effect of delaminations within composite structures, modelling of damage initiation and progression within such structures and a review of the available experimental data.

[2] The current state of the art in assessing the residual capabilities of composite stiffened structures is identified.

[3] A finite element model is developed and verified capable of representing idealised delamination damage within a composite structure. The model is verified incrementally incorporating each required response against both experimental data from the literature and experimental work conducted reported in section 7.

[4] An assessment of the effect of critical parameters on damage mechanisms and residual capability is conducted in section 5 and 7 which drawn conclusions about the failure mechanisms, residual strength and ultimate strength of damage and design parameters.

[5] Experimental assessment of the mechanical and interface properties of typical marine laminates and interfaces is conducted in section 6 which reports on the experimental assessment of the mechanical properties of heavy

weight marine composites and provides a consistent set of data for both mechanical and fracture properties. An experimental assessment of the crack initiation and propagation is conducted through representative stiffened top-hat structures and the experimental data is used to verify and compare numerical model with experimental data.

9 Recommendations for Future Work

This section builds on the work in this thesis and recommends future avenues for research.

Assessment of the literature on experimental data highlights the lack of literature for commonly used composite materials used in cheaper and larger structures. This is also highlighted in section 4 where verification cases require multiple sources to be used to acquire full data sets. Data is limited in this field for standard mechanical and characterisation tests including bi-axial tests and mixed mode interface strengths and fatigue. A lack of standardised materials and processes in composite materials and few published full multi-scale studies means there is a lack of complete sets of test data and material data sets used are often incompatible. In the marine industry Lloyd Register Special Service Craft Rules and ISO 12215 provide guidance for small craft design however in general there is a lack of standardised materials and techniques. To enable composite materials to be widely used standardised materials and shared data would aid industrial take up and reduced the cost of research and improve efficiency. Standards are also lacking for testing of mechanical and fracture properties in woven materials as highlighted by the results in section 6. For DCB testing of chopped strand mat layers at the interface requires current uni-directional standards leave interpretation into the post-processing of the results leading to further deviation across data sources. An assessment of the effect of the coupon width and a statistical approach to analysing fibre bridging and variability is also required.

For composite structures variation in manufacturing processes, component materials and tooling leads to variability in geometric and material parameters. The current study could be extended to incorporate manufacturing tolerance and inherent variability of marine and aerospace structures to determine the reliability of intact and damaged stiffened structures and the effect on their residual capabilities and damage mechanisms. Reliability techniques have been developed and successfully utilised on a number of composite structures relevant to the marine industry. However, reliability analyses fail to include delamination or debond damage which may initiate within the structure. Reliability methods are commonly applied to intact structures from a design perspective and have not been applied to damaged structures from a maintenance or damage tolerance assessment.

Large scale structural tests are also limited in the literature. This is partly due to the costs of large scale testing and also due to the complexities of capturing data from buckled panels. Extensive data is required to determine the exact boundary conditions applied and the mechanical properties of the as-built structure. Due to the complexity of the failure mechanisms of pre-damaged structures repetition of exact conditions is difficult to ascertain. Therefore more multi-scale approaches are required to ensure models are correctly verified and the materials are fully characterised to allow for sensitivity studies to be conducted numerically.

This thesis has verified the model in sections 4 and 7 through material characterisation tests, representative stiffened elements and stiffened elements models. To complete this verification a full panel test is required which was beyond the scope and budget of this research. This experimental data would complete the multi-scale study for this material and panel configuration.

The damage tolerance study present in section 5 has investigated simulated debond damage in a multi-stiffened top-hat panel. However, the model is limited to flat plates, longitudinal stiffeners, clamped boundary conditions,

in-plane loading conditions with limited range of lateral pressure and simulated debond damage. The next stage in this process is increasing the realism of the problem. The assessment of curved panels is shown to improve the damage tolerance for open-section stiffeners but has not been addressed for closed section stiffeners. A grillage analysis will improve the deformations of the panel in the region of a central debond and allow for multiple debonds and those under longitudinal and transverse stiffener joints. Combined bi-axial loading should also be considered for large grillage structures. Simulated damage is studied in section 5 however impact damage has shown to produce associated material damage and result in multiple delaminations which could be included with appropriate experimental data or knock down factors. Experimental data is critical in these studies to ensure delamination damage and material failure are representative of typical damage scenarios. To ensure damage modelling and residual strength calculations are conservative all typical delamination and material failure must be accounted for in the assessment. The effect of nominal and forced imperfections are assessed in section 5 and it is shown that the effect of the seeded imperfection can affect the damage tolerance of the panel. Therefore realistic imperfections from as built large scale grillage panels should be assessed to determine realistic panel imperfections for typical structures. This data would allow an assessment of realistic imperfections resulting from various manufacturing methods and cure cycles.

Future studies could also increase the complexity of the sub-components joints by assessing the effect of dropped plies, through thickness stitching and varying material processes. For each specific material and manufacturing process a multi-scale analysis is required to fully understand crack initiation, propagation and the effect of delamination and debonding.

10 Appendices

Appendix A: Fundamentals of Fracture Mechanics

In the 1920's Griffith [62] proposed his linear elastic theory of crack propagation, whereby a crack extension occurs when the energy available is large enough to overcome the resistance of the material. Irwin defined the strain energy release rate (SERR), G, as the amount of energy released if the crack were to advance by one unit length.

$$G = -\frac{\partial U}{\partial a}$$

U, elastic strain energy

a, crack length

G, strain energy release rate

When the strain energy release rate is greater than the surface energy of the material, the crack will advance. At the moment of crack propagation the strain energy release rate is equal to the critical strain energy release rate, G_c. The stability of crack growth can be calculated by computing the energy release rate, G, at different crack lengths, a, and calculating the derivative of the energy release rate with respect to the crack length, i.e $\frac{\partial G}{\partial a} \leq 0$ gives a stable crack growth.

Irwin [63] utilised linear elastic theory to develop the stress intensity approach. At the crack tip the stress intensity factor, K, determines the magnitude of the elastic stresses.

$$K = \sigma\sqrt{\pi a} f\left(\frac{a}{W}\right) \tag{30}$$

The stress intensity factor depends on the applied stress, σ, the characteristic length of the crack, a, and a parameter dependent on the crack and specimen geometry, $f\left(\frac{a}{W}\right)$. The term $f\left(\frac{a}{W}\right)$ accounts for the finite geometry of the specimen, where, a, represents half the crack length and W, the specimen width. Numerical approximations are available for a number of geometry specimen arrangements. Irwin [63] also showed that his critical stress intensity factor, K_c, is equivalent to the Griffith-Irwin energy balance approach. e.g. for tensile loading for plane stress the relationship is; $G_c = \frac{K_C^2}{E}$.

Irwin showed that the energy to create a new crack is insignificant for ductile materials when compared to the work done in plastic deformation. Therefore, linear elastic fracture mechanics is only applicable with a small plastic zone ahead of the crack tip. Rice [64] proposed the J-integral approach based on the linear elastic energy approach whereby the plastic response is modelled as a non-linear elastic response. As plastic deformation is irrecoverable it is required that no unloading may occur. The J-integral is a path independent line integral measuring the magnitude of the singular stresses and strains in the region of the crack tip and is equivalent to the strain energy release rate when subjected to monotonic loading under quasi static loading. The J integral is expressed in terms of the strain energy density, w, the displacement vector, u, and traction vectors, T, where the traction vector is defined in terms of the component stress, σ, and the unit vector normal to the path, Γ; $T_i = \sigma_{ij} n_j$

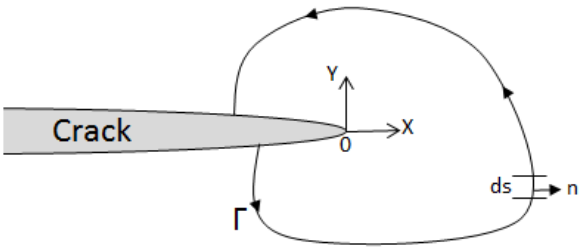

Figure 145: J integral configuration

$$J = \int_{\Gamma} w dy - \int_{\Gamma} T \frac{\partial u_i}{\delta x} ds \tag{31}$$

$$w = \int_0^{\varepsilon_{ij}} \sigma_{ij} d\varepsilon_{ij} \tag{32}$$

w, strain energy density

u, displacement vector at ds

n, unit vector normal to the contour path

σ_{ij}, stress field

ε_{ij} strain field

Γ, arbitrary contour around the crack tip

Appendix B: Implementation of the VCCT

A commonly used crack propagation algorithm, is the Abaqus kinematically compatible nodal release sequence, where the nodes at the crack front are released sequentially when the critical strain energy release rate is exceeded. The 2D case is illustrated in figure 146. Where $v_{1,6}$is the vertical displacement between nodes 1 and 6, $F_{v,2,5}$ is the vertical force between nodes 2 and 5, b is the width of the elements and d the length of the elements.

$$G_I = \frac{1}{2}(\frac{v_{1,6}F_{v,2,5}}{bd}) \tag{33}$$

The nodal connection between nodes 2 and 5 is released when the equivalent strain energy release rate calculated at the node, G_{equiv}, exceeds the critical equivalent strain energy release rate, G_{equivC}, i.e:

$$\frac{G_{equiv}}{G_{equivC}} \geq 1.0 \tag{34}$$

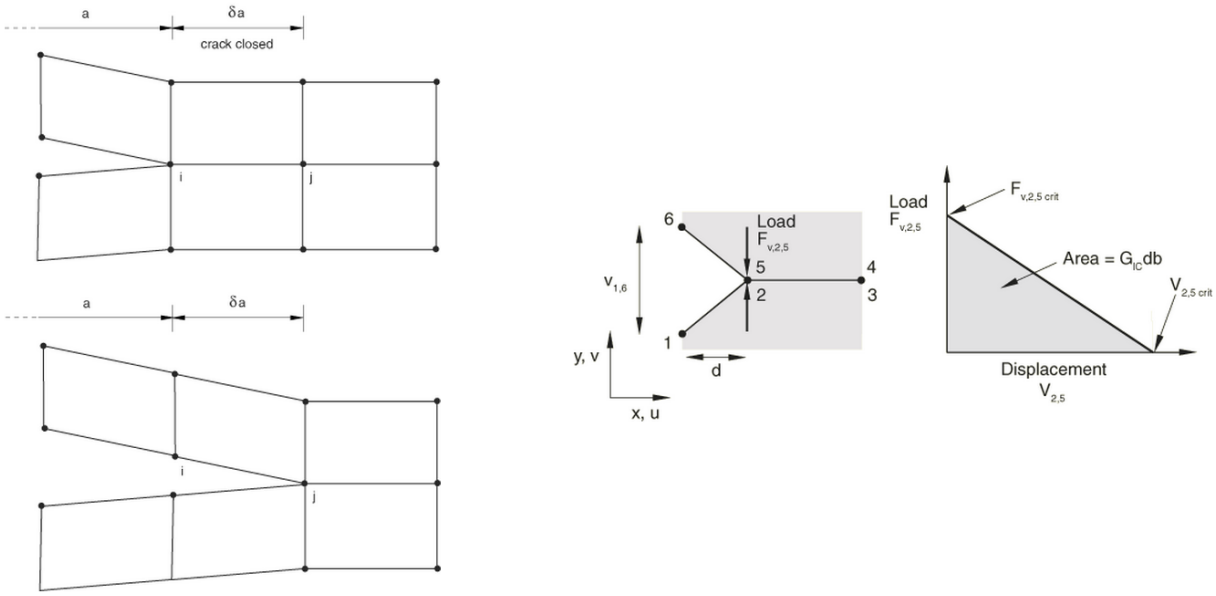

Figure 146: 2D VCCT nodal release(Abaqus 2010)

Similarly for modes II and III the strain energy can be calculated from the nodal displacements and forces in their respective opening directions.

It is possible for elements with quadratic shape functions to lead to interpenetration of the elements, as shown in figure 147, and therefore elements with linear shape functions are preferred for this method.

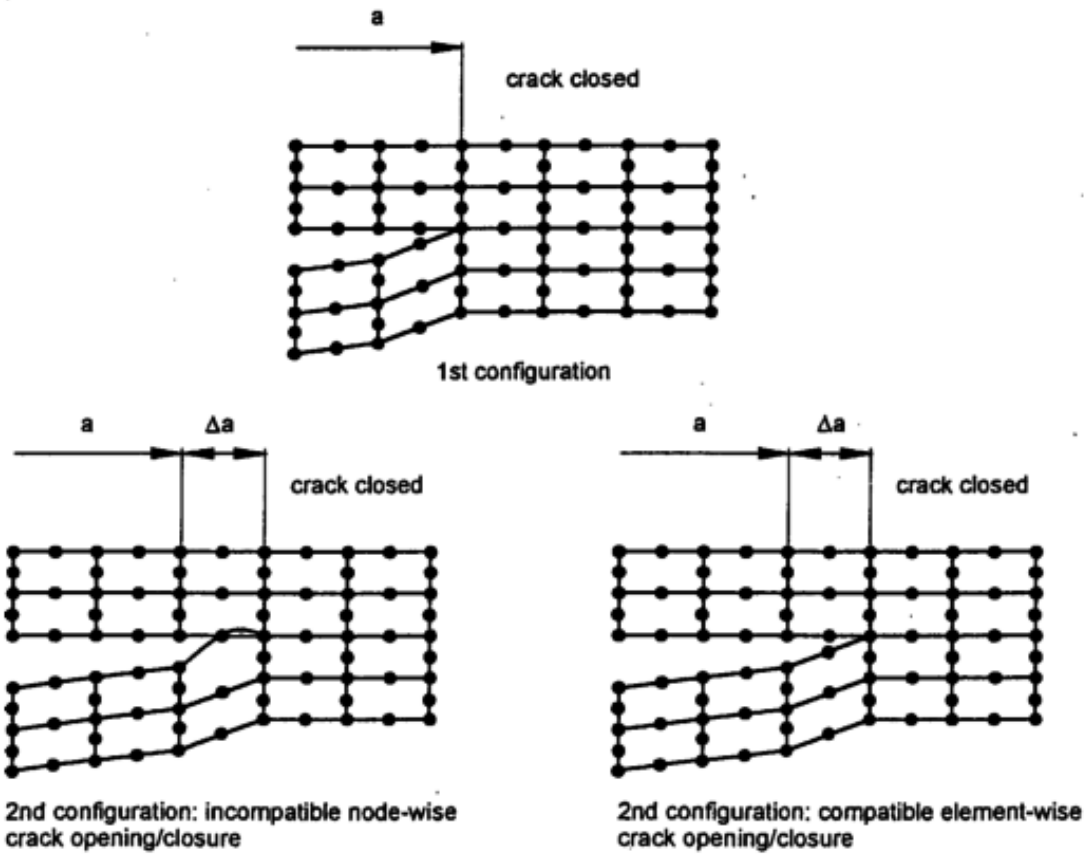

Figure 147: 8 node incompatible node-wise crack opening Krueger [71]

Appendix C: Implementation of Turon's Method for Cohesive Elements

The cohesive element constitutive equation assumes linear elastic behaviour with interfacial initial stiffness, E, until the damage initiation strain, ε_o, is reached followed by linear evolution of damage until the failure strain, ε_f, is reached. Where the tractions integrated to complete failure represents the fracture energy release rate, G_c.

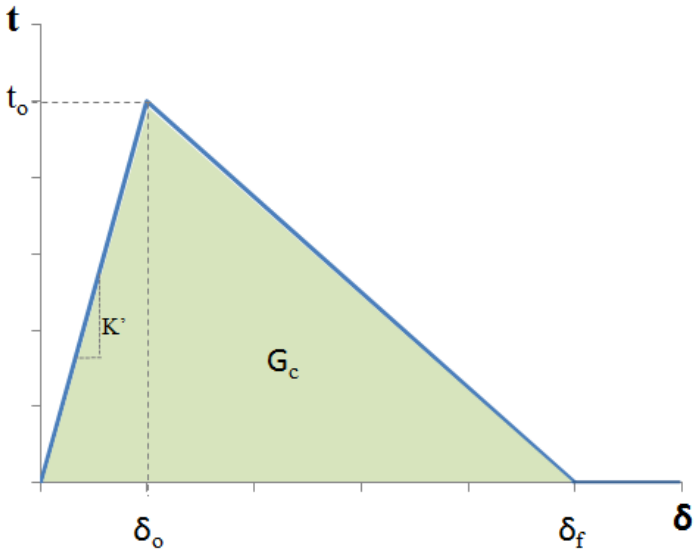

Figure 148: Constitutive linear softening relationship

The length of the cohesive zone, l_{cz}, is defined as the distance behind the crack tip where the maximum cohesive traction is obtained, $\delta_f - \delta_o$. It has been shown that for delaminations in slender bodies that the cohesive zone length is a material and structural property [88] and that for a polymeric composite is less than 1 or 2 mm . For accurate representation of the tractions ahead of the crack tip using finite element methods requires a fine discretisation is required with sufficient elements within the cohesive zones. Turon et al. [87] suggests that a minimum of 3 elements are required to accurately represent the cohesive zone. Therefore, this method becomes impractical for large structures due to the computational efficiency.

Alfano and Crisfield [95] showed that the interface strength does not have a strong influence on the predicted results and that reducing the damage initiation strain can improve the rate of convergence. Reducing the interface strength reduces the length of the cohesive zone and therefore the size of elements required in the cohesive zone also reduces improving the efficiency of the model. The fracture process ahead of the crack tip can be accurately modelled with a reduced interface strength however, the stress distribution in the region of the crack tip may be altered. Turon et al. [87] suggests that the interface strength can be calculated from the following equation:

$$t_{o_i} = \sqrt{\frac{ME_2Gc_i}{N_e l_e}}, \tag{35}$$

where l_e is the mesh size in the direction of crack propagation and N_e is the number of elements in the cohesive zone. By this method the cohesive zone length may be artificially increased therefore increasing the cohesive element

size in the vicinity of the crack tip and improving the efficiency of such models.

A method is proposed by Turon et al. [87] to determine the relationship between the cohesive zone length and the interface strength.

[1] An interface strength is used from the literature and an initial model is created using a mesh size smaller than the anticipated cohesive element size (assumed to be 1mm)

[2] The cohesive zone length is defined as the distance over which out-of-plane traction reaches the interface strength, t_{o_I}. This is approximately measured from the model using the nodal data of the traction ahead of the crack tip.

[3] The interface parameter, M, is calculated using the provided interface strength and cohesive zone length and equation 35

[4] Finally to create an efficient model an adjusted cohesive zone length is chosen and the interface strength is adjusted using equation 35.

Appendix D: Buckling of Stiffener Table

In order to assess the buckling point of the stiffener the deflection of the central table of the stiffener is assessed. The out-of-plane deflection against the end shortening is compared for increasing debond size in figure 149 for a wider stiffener spacing. For the intact case the deflection curve shows the stiffener exhibits a linear increase in out-of-plane deflection up to an end shortening of 4.6mm. A significant deviation is observed with a marked change in out-of-plane deflection observed at an end shortening of 5.2mm where the stiffener collapses. A similar trend is observed for the debond cases. The change in out-of-plane deflection with end shortening is shown against end shortening for increasing debond size in figure 150. A change in out-of-plane deflection with end shortening of greater than 0.05 is also chosen to represent the stiffener buckling point. Therefore using a consistent method is used to define buckling both in the stiffener and the plate. This is illustrated by a the marked circles in figures 149 and 150. This estimate is shown to give reasonable results when considering both the out-of-plane deflection results.

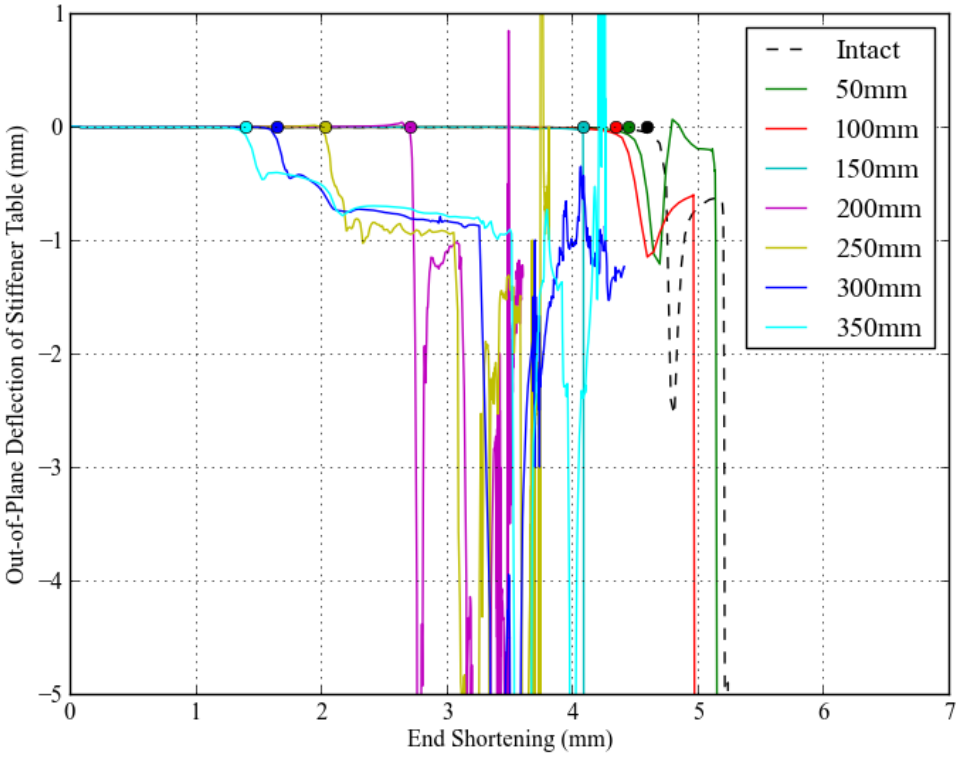

Figure 149: Out-of-Plane deflection of Stiffener Table for Increasing Central Debond for Nominal Imperfection and Stiffener Spacing 475mm

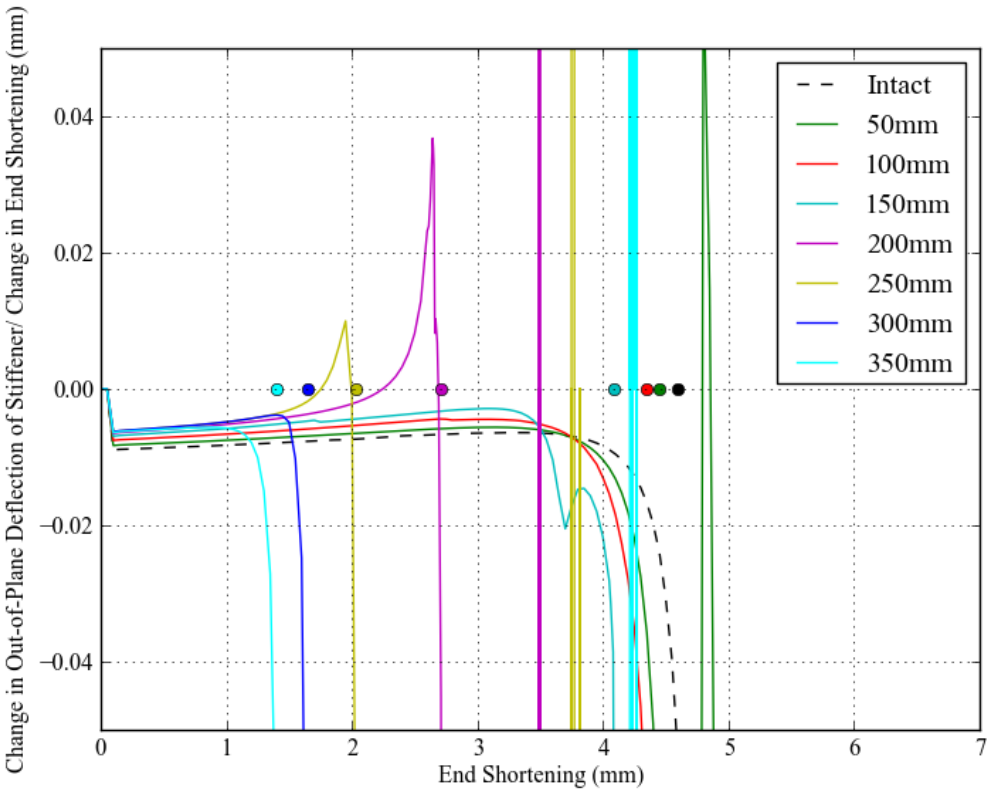

Figure 150: Change in Out-of-Plane deflection of Stiffener Table with Change in End Shortening for Increasing Central Debond for Nominal Imperfection and Stiffener Spacing 475mm

11 References

References

[1] C. Russell. Composites: long-term viability and benefits. *Reinforced Plastics*, 49(9):36–42, oct 2005.

[2] G. Schoeppner and S. Abrate. Delamination threshold loads for low velocity impact on composite laminates. *Composites Part A: Applied Science and Manufacturing*, 31(9):903–915, sep 2000.

[3] R. Trask. GFRP Repair Handbook. Technical report, 2000.

[4] R. M. Cripps, H. K. Jeong, H. Phillips, and R. A. Shenoi. A Generic Methodology for Postdamage Decisions. *Journal of Ship Production*, 22(1):21–32, 2006.

[5] C. Meeks, E. Greenhalgh, and B. Falzon. Stiffener debonding mechanisms in post-buckled CFRP aerospace panels. *Composites Part A: Applied Science and Manufacturing*, 36(7):934–946, jul 2005.

[6] J. Wiggenraad, E. Greenhalg, and R. Olsson. Design and analysis of stiffened composite panels for damage resistance and tolerance. In *5th world congress on computational mechanics; WCCM V, Vienna, July 2002*, pages 1–493. Vienna University of Technology, 2002.

[7] M. Arason, J. Kent, P. Murphy, C. Toole, and J. Hampshire. HMS Grimsby grounding incident: assessment of damage. Technical report, Qinetiq, 2006.

[8] C. Baley, P. Davies, Y. Grohens, and G. Dolto. Application of Interlaminar Tests to Marine Composites. A Literature Review. *Applied Composite Materials*, 11(2):99–126, mar 2004.

[9] K. N. Shivakumar. Carbon/Vinyl Ester Composites for Enhanced Performance in Marine Applications. *Journal of Reinforced Plastics and Composites*, 25(10):1101–1116, may 2006.

[10] S. P. Blake, K. a. Berube, and R. a. Lopez-Anido. Interlaminar fracture toughness of woven E-glass fabric composites. *Journal of Composite Materials*, 46(13):1583–1592, oct 2011.

[11] F. Dharmawan, G. Simpson, I. Herszberg, and S. John. Mixed mode fracture toughness of GFRP composites. *Composite Structures*, 75(1-4):328–338, sep 2006.

[12] P. Compston. Comparison of Interlaminar Fracture Toughness in Unidirectional and Woven Roving Marine Composites. *Applied Composite Materials*, pages 189–206, 1998.

[13] A. P. Mouritz, C. Baini, and I. Herszberg. Mode I interlaminar fracture toughness properties of advanced textile fibreglass composites. *Composites Part A: Applied Science and Technology*, 30:859–870, 1999.

[14] F. Dharmawan. Geometry and damage effects in a composite marine T-joint. *Composite Structures*, 66(1-4): 181–187, dec 2004.

[15] F. Dharmawan, H. C. H. Li, I. Herszberg, and S. John. Applicability of the crack tip element analysis for damage prediction of composite T-joints. *Composite Structures*, 86(1-3):61–68, nov 2008.

[16] G. Zhou and G. Davies. Characterization of thick glass woven roving/polyester laminates: 1. Tension, compression and shear. *Composites*, 26(8):579–586, aug 1995.

[17] B. N. Cox. On the tensile composites failure of 3D woven. pages 447–458, 1996.

[18] J. Welsh, J. Mayes, and C. Key. Damage initiation mechanics in glass fabric composites. *Proceedings of the 43rd AIAA/ASME/ ...*, 2002.

[19] J. Funk and J. Deaton. The Interlaminar Fracture Toughness of Woven Graphite/Epoxy Composites. 1989.

[20] B. Briscoe, R. Court, and D. Williams. The effects of fabric weave and surface texture on the interlaminar fracture toughness of aramid/epoxy laminates. *Composites Science and Technology*, 47(3):261–270, jan 1993.

[21] T. Ebeling, A. Hiltner, E. Baer, I. M. Fraser, and M. L. Orton. Delamination Failure of a Woven Glass Fiber Composite. *Journal of Composite Materials*, 31(13):1318–1333, jul 1997.

[22] F. Dharmawan, G. Simpson, I. Herszberg, and A. P. Mouritz. Influence of specimen thickness on Mode I fracture toughness of GFRP composites. In *Australian international aerospace congress*, 2005.

[23] J. Yap. The analysis of skin-to-stiffener debonding in composite aerospace structures. *Composite Structures*, 57(1-4):425–435, jul 2002.

[24] J. F. M. Wiggenraad, R. Aoki, M. Gädke, E. Greenhalgh, D. Hachenberg, K. Wolf, and R. Bübl. Damage propagation in composite structural elements-analysis and experiments on structures. *Composite structures*, 36(3-4):173–186, 1996.

[25] A. C. Orifici, I. Dezaratealberdi, R. Thomson, and J. Bayandor. Compression and post-buckling damage growth and collapse analysis of flat composite stiffened panels. *Composites Science and Technology*, 68(15-16):3150–3160, dec 2008.

[26] S. Suh. Compression behavior of stitched stiffened panel with a clearly visible stiffener impact damage. *Composite Structures*, 62(2):213–221, nov 2003.

[27] G.-H. Kim, J.-H. Choi, and J.-H. Kweon. Manufacture and performance evaluation of the composite hat-stiffened panel. *Composite Structures*, 92(9):2276–2284, aug 2010.

[28] E. Demuts, R. Whitehead, and R. Deo. Composite structures. *Composite structures*, 4:45–58, 1989.

[29] L. Sutherland. Effect of laminate thickness and of matrix resin on the impact of low fibre-volume, woven roving E-glass composites. *Composites Science and Technology*, 64(10-11):1691–1700, aug 2004.

[30] L. Sutherland. Impact characterisation of low fibre-volume glass reinforced polyester circular laminated plates. *International Journal of Impact Engineering*, 31(1):1–23, jan 2005.

[31] G. Belingardi and R. Vadori. Low velocity impact tests of laminate glass-fiber-epoxy matrix composite material plates. *International Journal of Impact Engineering*, 27(2):213–229, feb 2002.

[32] C. Prasad, D. Ambur, and J. Starnes. Response of laminated composite plates to low-speed impact by different impactors. *AIAA journal*, 32(6):1270–1277, 1994.

[33] E. Gellert, S. Cimpoeru, and R. Woodward. A study of the effect of target thickness on the ballistic perforation of glass-fibre-reinforced plastic composites. *International Journal of Impact Engineering*, 24:445–456, 2000.

[34] N. Cristescu, E. Malver, and R. Sierakowski. *Foreign object impact to composites*. ASTM International, 1975.

[35] R. Craven, L. Iannucci, and R. Olsson. Delamination buckling: A finite element study with realistic delamination shapes, multiple delaminations and fibre fracture cracks. *Composites Part A: Applied Science and Manufacturing*, 41(5):684–692, may 2010.

[36] F. Desplentere, S. Lomov, D. Woerdeman, I. Verpoest, M. Wevers, and a. Bogdanovich. Micro-CT characterization of variability in 3D textile architecture. *Composites Science and Technology*, 65(13):1920–1930, oct 2005.

[37] P. Badel, E. Vidalsalle, E. Maire, and P. Boisse. Simulation and tomography analysis of textile composite reinforcement deformation at the mesoscopic scale. *Composites Science and Technology*, 68(12):2433–2440, sep 2008.

[38] S. Srinivas and A. Rao. Bending, vibration and buckling of simply supported thick orthotropic rectangular plates and laminates. *International journal of solids and structures*, 6(11):1463–1481, nov 1970.

[39] J. N. Reddy. *Mechanics of laminated composite plates and shells: theory and analysis*. 2004.

[40] M. J. Hinton. Predicting failure in composite laminates: the background to the exercise. *Composites Science and Technology*, 58(7):1001–1010, jul 1998.

[41] M. J. Hinton and A. S. Kaddour. The second world-wide failure exercise: Benchmarking of failure criteria under triaxial stresses for fibre-reinforced polymer composites. *Polymer Composites*, 2007.

[42] M. J. Hinton. Evaluation of failure prediction in composite laminates: background to part B of the exercise. *Composites Science and Technology*, 62(3-4):1481–1488, mar 2002.

[43] A. S. Kaddour, M. J. Hinton, and P. D. Soden. A comparison of the predictive capabilities of current failure theories for composite laminates: additional contributions. *Composites Science and Technology*, 64(3-4): 449–476, mar 2004.

[44] P. D. Soden, A. Kaddour, and M. J. Hinton. Recommendations for designers and researchers resulting from the world-wide failure exercise. *Composites Science and Technology*, 64pp:589–604, 2004.

[45] A. Puck and H. Schürmann. Failure analysis of FRP laminates by means of physically based phenomenological models. *Composites Science and Technology*, 2002.

[46] J. Tsai. Constitutive model for high strain rate response of polymeric composites. *Composites Science and Technology*, 62(10-11):1289–1297, aug 2002.

[47] P. Zinoviev. The strength of multilayered composites under a plane-stress state. *Composites Science and Technology*, 58(7):1209–1223, jul 1998.

[48] R. Cuntze. The predictive capability of failure mode concept-based strength criteria for multidirectional laminates. *Composites Science and Technology*, 64(3-4):343–377, mar 2004.

[49] T. Bogetti. Predicting the nonlinear response and failure of composite laminates: correlation with experimental results. *Composites Science and Technology*, 64(3-4):329–342, mar 2004.

[50] P. Soden. A comparison of the predictive capabilities of current failure theories for composite laminates. *Composites Science and Technology*, 58(7):1225–1254, jul 1998.

[51] K. Misirlis. *Progressive Collapse Analysis of Composite Ship Hull Sections*. PhD thesis, Newcastle University, 2012.

[52] a. C. Orifici, I. Herszberg, and R. Thomson. Review of methodologies for composite material modelling incorporating failure. *Composite Structures*, 86(1-3):194–210, nov 2008.

[53] Z. Hashin. Failure criteria for unidirectional fibre composites. *Journal of Applied Mechanics*, 47:329–334, 1980.

[54] M. Owen and D. Rice. Biaxialstrength behaviour of glass fabric-reinforced polyester resins. *Composites*, 12 (1):13–25, 1981.

[55] T. Fujii, S. Amijima, and F. Lin. Study on Strength and Nonlinear Stress-Strain Response of Plain Woven Glass Fibre Laminates under Biaxial Loading. *Journal of Composite Materials*, 26(17):2493–2510, 1992.

[56] A. Puck, J. Kopp, and M. Knops. Guidelines for the determination of the parameters in Puck's action plane strength criterion. *Composites Science and Technology*, 62:371–378, 2002.

[57] F. K. Chang and K. Chang. A Progressive Damage Model for Laminated Composites Containing Stress Concentrations. *Journal of Composite Materials*, 21(9):834–855, jan 1987.

[58] a. Matzenmiller, J. Lubliner, and R. Taylor. A constitutive model for anisotropic damage in fiber-composites. *Mechanics of Materials*, 20(2):125–152, apr 1995.

[59] Y. S. N. Reddy and J. N. Reddy. An accurate prediction of failures in composite laminates using a layerwise model. *In Proc. Int. Conf. on Comp. Mat. ICCM-9*, 3:15–22, 1993.

[60] G. S. Padhi, R. A. Shenoi, S. Moy, and G. L. Hawkins. Progressive failure and ultimate collapse of laminated composite plates in bending. *Composite Structures*, 40(3-4):277–291, dec 1997.

[61] J. Blake. Progressive damage analysis of tee joints with viscoelastic inserts. *Composites Part A: Applied Science and Manufacturing*, 32(5):641–653, may 2001.

[62] A. Griffith. The phenomena of rupture and flow in solids. *Philosophical transactions of the royal society of london. Series A, containing papers of a mathematical or physical character*, 221:163–198, 1921.

[63] G. R. Irwin. Analysis of stresses and strains near the end of a crack traversing a plate. *Journal of Applied Mechanics*, 24:361–364, 1957.

[64] J. R. Rice. A path independent integral and the approximate analysis of strain concentration by notches and cracks. *Journal of applied mechanics*, 35(2):379–386, 1968.

[65] J. R. Reeder. *An evaluation of mixed-mode delamination failure criteria*. Number February. National Aeronautics and Space Administration, Langley Research Center, 1992.

[66] J. R. Reeder. 3D Mixed - Mode Delamination Fracture Criteria - An Experimentalist's Perspective. *NASA Langley research center, M/S 188E, Hampton VA*, pages 23681–2199, 2004.

[67] J. R. Reeder. A bilinear failure criterion for mixed-mode delamination. *Composite materials: testing and design (vol. 12). ASTM STP*, 11:303–322, 1993.

[68] S. Hashemi, A. J. Kinloch, and G. Williams. Mixed-mode fracture in fiber-polymer composite laminates. *Composite materials: Fatigue and fracture*, 3:143–168, 1991.

[69] M. Benzeggagh and M. Kenane. Measurement of mixed-mode delamination fracture toughness of unidirectional glass/epoxy composites with mixed-mode bending apparatus. *Composites Science and Technology*, 56 (4):439–449, 1996.

[70] A. D6671-01. Standard Test Method for Mixed Mode I Mode II Interlaminar Fracture Toughness of Unidirectional Fiber Reinforced Polymer Matrix Composites. Technical report, ASTM International, West Conshohocken, PA, USA, 2001.

[71] R. Krueger. Virtual crack closure technique: History, approach, and applications. *Applied Mechanics Reviews*, 57(2):109, 2004.

[72] I. Raju, J. Crewsjr, and M. Aminpour. Convergence of strain energy release rate components for Edge-Delaminated composite laminates. *Engineering Fracture Mechanics*, 30(3):383–396, 1988.

[73] D. J. Chen, W. S. Chan, and b. p. Wang. An Efficient Method to Simulate One-and Two-Dimensional Delamination Growth in Composite Laminates. *Journal of Reinforced Plastics and Composites*, 15(9):944–957, 1996.

[74] S. Zheng and C. Sun. A double-plate finite-element model for the impact-induced delamination problem. *Composites Science and Technology*, 53(1):111–118, jan 1995.

[75] N. Moes, J. Dolbow, and T. Belytschko. A finite element method for crack growth without remeshing. *International Journal for Numerical Methods in Engineering*, 46(1):131–150, sep 1999.

[76] T. Nagashima, Y. Omoto, and S. Tani. Stress intensity factor analysis of interface cracks using X-FEM. *International Journal for Numerical Methods in Engineering*, 56(8):1151–1173, feb 2003.

[77] Z. Suo. Singularities, interfaces and cracks in dissimilar anisotropic media. *Proceedings of the Royal Society of London. A. Mathematical and Physical Sciences*, 427(1873):331, 1990.

[78] C. Sun and C. Jih. On strain energy release rates for interfacial cracks in bi-material media. *Engineering Fracture Mechanics*, 28(1):13–20, 1987.

[79] J. L. Beuth. Separation of crack extension modes in orthotropic delamination models. *International Journal of Fracture*, 77(4):305–321, 1996.

[80] J. Hutchinson and Z. Suo. Mixed mode cracking in layered materials. *Advances in applied mechanics*, 29(63): 191, 1992.

[81] B. D. Davidson, S. J. Gharibian, and L. Yu. Evaluation of energy release rate-based approaches for predicting delamination growth in laminated composites. *International Journal of Fracture*, pages 343–365, 2000.

[82] B. D. Davidson and H. Hu. An Analytical Crack-Tip Element for Layered Elastic Structures. *journal of applied mechanics*, 62(2):294–306, 1995.

[83] B. D. Davidson. Prediction of energy release rate for edge delamination using a crack tip element approach. *composite materials: Fatigue and Fracture*, 5(ASTM STP 1230):155–175, 1995.

[84] Z. Yang, C. Sun, and J. Want. Fracture mode separation for delamination in platelike composite structures. *AIAA Journal*, 38(5):868–874, 2000.

[85] N. Sukumar, Z. Y. Huang, J.-H. Prévost, and Z. Suo. Partition of unity enrichment for bimaterial interface cracks. *International Journal for Numerical Methods in Engineering*, 59(8):1075–1102, feb 2004.

[86] D. Dugdale. Yielding of steel sheets containing slits. *Journal of the Mechanics and Physics of Solids*, 8(2): 100–104, may 1960.

[87] a. Turon, C. Dávila, P. P. Camanho, and J. Costa. An engineering solution for mesh size effects in the simulation of delamination using cohesive zone models. *Engineering Fracture Mechanics*, 74(10):1665–1682, jul 2007.

[88] Q. Yang and B. Cox. Cohesive models for damage evolution in laminated composites. *International Journal of Fracture*, 133(2):107–137, may 2005.

[89] C.-Y. Hui, J. A., S. J. Bennison, and J. D. Londono. Crack blunting and the strength of soft elastic solids. *Proceedings of the Royal Society A: Mathematical, Physical and Engineering Sciences*, 459(2034):1489–1516, jun 2003.

[90] G. R. Irwin and I. G. Analysis of stresses and strains near the end of a crack traversing a plate. *Journal of Applied Mechanics*, 24:361–364, 1957.

[91] G. Barenblatt. *Advances in Applied Mechanics Volume 7*, volume 7 of *Advances in Applied Mechanics*. Elsevier, 1962.

[92] J. R. Rice. *The mechanics of earthquake rupture*. 1979.

[93] M. L. Falk, A. Needleman, and J. R. Rice. *A Critical Evaluation of Cohesive Zone Models of Dynamic Fracture*. EDP Sciences, 2001.

[94] A. Hillerborg, M. Modéer, and P.-E. Petersson. Analysis of crack formation and crack growth in concrete by means of fracture mechanics and finite elements. *Cement and Concrete Research*, 6(6):773–781, nov 1976.

[95] G. Alfano and M. A. Crisfield. Finite element interface models for the delamination analysis of laminated composites: mechanical and computational issues. *International Journal for Numerical*, (March 2000):1701–1736, 2001.

[96] S. Hwang. Buckling behavior of composite laminates with multiple delaminations under uniaxial compression. *Composite Structures*, 53(2):235–243, aug 2001.

[97] Z. Kutlu and F.-K. Chang. Modeling Compression Failure of Laminated Composites Containing Multiple Through-the-Width Delaminations. *Journal of Composite Materials (USA)*, 26(3):359–387, 1992.

[98] S. Hwang. Failure of delaminated interply hybrid composite plates under compression. *Composites Science and Technology*, 61(11):1513–1527, sep 2001.

[99] H. Chai and C. Babcock. One dimensional modelling of failure in laminated plates by delamination buckling. *International journal of solids and structures*, 17(11):1069–1083, 1981.

[100] J. Whitcomb. Parametric Analytical Study of Instability-related Delamination Growth. *Composites science and technology*, 25(1):19–48, 1986.

[101] P. Larsson. On multiple delamination buckling and growth in composite plates. *International journal of solids and structures*, 27(13):1623–1637, 1991.

[102] I. Sheinman and G. Kardomateas. Delamination growth during pre-and post-buckling phases of delaminated composite laminates. *International journal of solids and structures*, 35(97):19–31, 1998.

[103] J. D. Whitcomb. Three-Dimensional Analysis of a Postbuckled Embedded Delamination. *Journal of Composite Materials*, 23(9):862–889, sep 1989.

[104] J. D. Whitcomb. Analysis of a Laminate with a Postbuckled Embedded Delamination, Including Contact Effects. *Journal of Composite Materials*, 26(10):1523–1535, jan 1992.

[105] K. Nilsson, L. E. Asp, J. E. Alpman, and L. Nystedt. Delamination buckling and growth for delaminations at different depths in a slender composite panel. *International journal of solids and structures*, 38, 2001.

[106] A. Riccio and E. Pietropaoli. Modeling Damage Propagation in Composite Plates with Embedded Delamination under Compressive Load. *Journal of Composite Materials*, 42(13):1309–1335, jul 2008.

[107] F. Elaldi. Structural Efficiency and Post-buckling Strength of J- and Hat-stiffened Composite Panels. *Journal of Reinforced Plastics and Composites*, 29(10):1590–1594, sep 2009.

[108] P. J. Minguet and T. K. O'Brien. Analysis of test methods for characterizing skin/ stringer debonding failures in reinforced composite panels. In *Composite materials: testing and design (vol. 12). ASTM STP*, pages 105–124. 1996.

[109] R. Krueger, M. Cvitkovich, T. K. O'Brien, and P. J. Minguet. Testing and analysis of composite skin/stringer debonding under multi-axial loading. *Journal of Composite Materials*, 34(15):1263, 2000.

[110] P. P. Camanho, C. G. Dávila, and S. T. Pinho. Fracture analysis of composite co-cured structural joints using decohesion elements. *Fatigue & Fracture of Engineering Materials & Structures*, 27(9):745–757, oct 2008.

[111] R. Krueger and P. J. Minguet. Analysis of composite skin stiffener debond specimens using a shell/3D modeling technique. *Composite Structures*, 81(1):41–59, nov 2007.

[112] A. Dodkins, R. A. Shenoi, and G. Hawkins. Design of joints and attachments in FRP ships' structures. *Marine Structures*, 7(2-5):365–398, 1994.

[113] R. A. Shenoi. An investigation into the performance characteristics of top-hat stiffener to shell plating joints. *Composite Structures*, 30(1):109–121, 1995.

[114] P. Junhou. Examination of key aspects defining the performance characteristics of out-of -plane joints in FRP marine structures. *Composites*, 27(2):89– 103, 1996.

[115] H. Phillips, R. A. Shenoi, and C. Moss. Damage mechanics of top-hat stiffeners used in FRP ship construction. *Marine Structures*, 12(1):1–19, jan 1999.

[116] H. C. H. Li, F. Dharmawan, I. Herszberg, and S. John. Fracture behaviour of composite maritime T-joints. *Composite Structures*, 75(1-4):339–350, sep 2006.

[117] a. C. Orifici, S. Shah, I. Herszberg, A. Kotler, and T. Weller. Failure analysis in postbuckled composite T-sections. *Composite Structures*, 86(1-3):146–153, nov 2008.

[118] J. Bertolini, B. Castanie, J. Barrau, and J. Navarro. An experimental and numerical study on omega stringer debonding. *Composite Structures*, 86(1-3):233–242, nov 2008.

[119] O. Eksik. Damage Mechanisms of Hat-Shaped GRP Beams. *Journal of Reinforced Plastics and Composites*, 23(14):1497–1514, sep 2004.

[120] O. Eksik, R. A. Shenoi, S. Moy, and H. K. Jeong. Finite Element Analysis of Top-Hat Reinforced Plastic Boat Structures. *Marine Technology*, 44(1):16–26, 2007.

[121] C. S. Smith. Elastic analysis of stiffened plating under lateral loading. *Trans. R. Inst. Naval Arch*, 108: 113–131, 1966.

[122] C. S. Smith and R. S. Dow. Compressive strength of deck strucutre in the hunt-class MCMV. Technical report, 1985.

[123] C. S. Smith. *Design of Marine Structures in Composite Materials*. Elsevier, 1990.

[124] J. A. Araico, I. O. D. Z. Alberdi, F. R. Arribas, J. A. Ansotegui, I. O. Ortiz de Zarante, and F. A. Rebollo. FEM Simulation of Potted-Ends on Compression Loaded Graphite-Epoxy Test Specimens. In *Proc. 2nd Int. Conf. Buckling and Postbuckling Behavior of Composite Laminated Shell Structures*, pages 2–5, 2008.

[125] B. Falzon, K. Stevens, and G. Davies. Postbuckling behaviour of a blade-stiffened composite panel loaded in uniaxial compression. *Composites Part A: Applied Science and Manufacturing*, 31(5):459–468, may 2000.

[126] C.-W. Kong, I.-C. Lee, C.-G. Kim, and C.-S. Hong. Postbuckling and failure of stiffened composite panels under axial compression. *Composite Structures*, 42(1):13–21, may 1998.

[127] A. C. Orifici, R. S. Thomson, A. J. Gunnion, R. Degenhardt, H. Abramovich, and J. Bayandor. Benchmark finite element simulations of postbuckling composite stiffened panels. In *11th Australian International Aerospace Congress*, 2005.

[128] A. Perret, S. Mistou, and M. Fazzini. Global behaviour of a composite stiffened panel in buckling. Part 1: Numerical modelling. *Composite Structures*, 93(10):2610–2618, sep 2011.

[129] K. N. Anyfantis and N. G. Tsouvalis. Post Buckling Progressive Failure Analysis of Composite Laminated Stiffened Panels. *Applied Composite Materials*, 19(3-4):219–236, mar 2011.

[130] W. L. Ko and R. H. Jackson. Compressive Buckling Analysis of a Hat-Stiffened Panel. *Dryden , Flight Research Center, Edwards, CA*, 1991.

[131] W. L. Ko and R. H. Jackson. Shear Buckling Analysis of a Hat-Stiffened Panel. *NASA TM-4644*, (November 1994), 1994.

[132] B. Falzon and G. I. Steven. Buckling mode transition in hat-stiffened composite panels loaded in uniaxial compression. *Composite Structures*, 37(2):253–267, feb 1997.

[133] B. Falzon. Capturing mode-switching in postbuckling composite panels using a modified explicit procedure. *Composite Structures*, 60(4):447–453, jun 2003.

[134] R. Zimmermann and R. Rolfes. POSICOSS-improved postbuckling simulation for design of fibre composite stiffened fuselage structures. *Composite Structures*, 73(2):171–174, may 2006.

[135] R. Degenhardt, R. Rolfes, R. Zimmermann, and K. Rohwer. COCOMAT-improved material exploitation of composite airframe structures by accurate simulation of postbuckling and collapse. *Composite Structures*, 73 (2):175–178, may 2006.

[136] C. Bisagni. Post-buckling optimisation of composite stiffened panels using neural networks. *Composite Structures*, 58(2):237–247, nov 2002.

[137] T. Mocker and H. Reimerdes. Postbuckling simulation of curved stiffened composite panels by the use of strip elements. *Composite Structures*, 73(2):237–243, may 2006.

[138] L. Lanzi and V. Giavotto. Post-buckling optimization of composite stiffened panels: Computations and experiments. *Composite Structures*, 73(2):208–220, may 2006.

[139] R. Rikards, H. Abramovich, K. Kalnins, and J. Auzins. Surrogate modeling in design optimization of stiffened composite shells. *Composite Structures*, 73(2):244–251, may 2006.

[140] R. Zimmermann, H. Klein, and A. Kling. Buckling and postbuckling of stringer stiffened fibre composite curved panels - Tests and computations. *Composite Structures*, 73(2):150–161, may 2006.

[141] J. Bertolini, B. Castanié, J.-J. Barrau, J.-P. Navarro, and C. Petiot. Multi-level experimental and numerical analysis of composite stiffener debonding. Part 1: Non-specific specimen level. *Composite Structures*, 90(4): 392–403, oct 2009.

[142] J. F. M. Wiggenraad. A seven-point bending test to determine the strength of the skin-stiffener interface in composite aircraft panels. *Aerospace*, 2000.

[143] A. C. Orifici, R. Thomson, I. Herszberg, T. Weller, R. Degenhardt, and J. Bayandor. An analysis methodology for failure in postbuckling skin-stiffener interfaces. *Composite Structures*, 86(1-3):186–193, nov 2008.

[144] A. Perret, S. Mistou, M. Fazzini, and R. Brault. Global behaviour of a composite stiffened panel in buckling. Part 2: Experimental investigation. *Composite Structures*, 94(2):376–385, jan 2012.

[145] a. Faggiani and B. Falzon. The use of a genetic algorithm to improve the postbuckling strength of stiffened composite panels susceptible to secondary instabilities. *Composite Structures*, 94(3):883–895, feb 2012.

[146] J. Sumpter. Final review of Project Support Tasking DNA1217 - damage tomerance in FRP ship's structures. Technical report, 1996.

[147] B. Falzon. Failure of thick-skinned stiffener runout sections loaded in uniaxial compression. *Composite Structures*, 53(2):223–233, aug 2001.

[148] A. Riccio, M. Giordano, and M. Zarrelli. A Linear Numerical Approach to Simulate the Delamination Growth Initiation in Stiffened Composite Panels. *Journal of Composite Materials*, 44(15):1841–1866, mar 2010.

[149] M. Gadke, B. Geier, and H. Goetting. Damage influence on the buckling load of CFRP stringer-stiffened panels. *Composite Structures*, 36(3):249, 1996.

[150] J. Yap. Influence of post-buckling behaviour of composite stiffened panels on the damage criticality. *Composite Structures*, 66(1-4):197–206, dec 2004.

[151] H. Suemasu, K. Kurihara, K. Arai, O. Majima, and T. Ishikawa. Compressive property degradation of composite stiffened panel due to debonding and delaminations. *Advanced Composite Materials*, 15(2):139–151, jan 2006.

[152] S. Lauterbach, A. C. Orifici, W. Wagner, C. Balzani, H. Abramovich, and R. Thomson. Damage sensitivity of axially loaded stringer-stiffened curved CFRP panels. *Composites Science and Technology*, 70(2):240–248, feb 2010.

[153] R. Vescovini, C. Dávila, and C. Bisagni. Failure analysis of composite multi-stringer panels using simplified models. *Composites Part B: Engineering*, 45(1):939–951, feb 2013.

[154] C. Bisagni and C. G. Dávila. Experimental investigation of the postbuckling response and collapse of a single-stringer specimen. *Composite Structures*, 108:493–503, feb 2014.

[155] X. Wang, W. Cao, C. Deng, P. Wang, and Z. Yue. Experimental and numerical analysis for the post-buckling behavior of stiffened composite panels with impact damage. *Composite Structures*, 133:840–846, dec 2015.

[156] A. C. Orifici, R. S. Thomson, R. Degenhardt, C. Bisagni, and J. Bayandor. A Finite Element Methodology for Analysing Degradation and Collapse in Postbuckling Composite Aerospace Structures. *Journal of Composite Materials*, 43(26):3239–3263, aug 2009.

[157] R. Juntikka and R. Olsson. Experimental and modelling study of hail impact on composite plates. In *International Conference of Composite Materials*, Edinburgh, 2009.

[158] P. Compston, J. Schiemer, and a. Cvetanovska. Mechanical properties and styrene emission levels of a UV-cured glass-fibre/vinylester composite. *Composite Structures*, 86(1-3):22–26, nov 2008.

[159] G. Duvaut and J. Lions. *Inequalities in mechanics and physics*. Springer, Berlin, 1976.

[160] J. Starnes. Postbuckling and failure characteristics of selected flat rectangular graphite-epoxy plates loaded in compression. *Structural Dynamics and Materials Conference*, 1981.

[161] Z. Kutlu and F.-k. Chang. Composite panels containing multiple through-the-width delaminations and subjected to compression. Part II: experiments & verification. *Composite structures*, 31(4):273–296, jan 1995.

[162] J. R. Reeder, J. R. C. Jr, and J. Crews. Mixed-Mode Bending Method for Delamination Testing. *AIAA Journal*, 28(7):1270–1276, 1990.

[163] P. P. Camanho, C. G. Davila, and M. F. De Moura. Numerical simulation of mixed-mode progressive delamination in composite materials. *Journal of Composite Materials*, 37(16):1415–1438, 2003.

[164] P. Liu, S. Hou, J. Chu, X. Hu, C. Zhou, Y. Liu, J. Zheng, a. Zhao, and L. Yan. Finite element analysis of postbuckling and delamination of composite laminates using virtual crack closure technique. *Composite Structures*, 93(6):1549–1560, may 2011.

[165] Y. Zhang and S. Wang. Buckling, post-buckling and delamination propagation in debonded composite laminates Part 2: Numerical applications. *Composite Structures*, 88(1):121–130, mar 2009.

[166] P. D. Soden. Lamina properties, lay-up configurations and loading conditions for a range of fibre-reinforced composite laminates. *Composites Science and Technology*, 58(7):1011–1022, jul 1998.

[167] L. E. Asp and K. Nilsson. On transition of delamination growth behaviour for compression loaded composite panels. *International journal of solids and structures*, 38(46-47):8407–8440, nov 2001.

[168] A. Turon, J. Costa, P. P. Camanho, and C. G. Dávila. Simulation of delamination in composites under high-cycle fatigue. *Composites Part A: Applied Science and Manufacturing*, 38(11):2270–2282, 2007.

[169] A. C. Swift. A numerical investigaiton of Mode I fracture toughness in woven glass reinforced plastic double cantilever beam specimens. Technical report, 1996.

[170] A. D. Morais and J. Silva. Mode II interlaminar fracture of filament wound angle-ply specimens. *Applied Composite ...*, pages 117–129, 2002.

[171] A. Green and W. Bowyer. The development of improved attachment methods for stiffening frames on large grp panels. *Composites*, 12(1):49–55, 1981.

[172] ScottBader. http://www.scottbader.com/grp-composites/selector/194/crystic-resin-ve679-03pa. URL `http://www.scottbader.com/grp-composites/selector/194/crystic-resin-ve679-03pa`.

[173] D. S. Ivanov, S. V. Lomov, S. G. Ivanov, and I. Verpoest. Stress distribution in outer and inner plies of textile laminates and novel boundary conditions for unit cell analysis. *Composites Part A: Applied Science and Manufacturing*, 41(4):571–580, 2010.

[174] R. Martin. Delamination characterization of woven glass/polyester composites. *Journal of Composites Technology and Research*, 19(1):20–28, 1997.

[175] T. Ebeling, a. Hiltner, E. Baer, I. M. Fraser, and M. L. Orton. Delamination Failure of a Single Yarn Glass Fiber Composite. *Journal of Composite Materials*, 31(13):1302–1317, jul 1997.

[176] N. K. Naik, K. S. Reddy, S. Meduri, N. B. Raju, P. D. Prasad, S. N. M. Azad, P. A. Ogde, and B. C. K. Reddy. Interlaminar fracture characterization for plain weave fabric composites. *Journal of Materials Science*, 37(14):2983–2987, 2002.

[177] A. P. Mouritz, C. Baini, and I. Herszberg. Mode I interlaminar fracture toughness properties of advanced textile fibreglass composites. *Composites Part A: Applied Science and Manufacturing*, 30(7):859–870, 1999.

[178] P. Davies and D. Moore. Glass/Nylon-6.6 composites: delamination resistance testing. *Composites Science and Technology*, 38:211–227, 1990.

[179] W. Johnson, J. Masters, T. O'Brien, T. O'Brien, and R. Martin. Round Robin Testing for Mode I Interlaminar Fracture Toughness of Composite Materials. *Journal of Composites Technology and Research*, 15(4):269, 1993.

[180] A. F. Gill, P. Robinson, and S. Pinho. Effect of variation in fibre volume fraction on modes I and II delamination behaviour of 5HS woven composites manufactured by RTM. *Composites Science and Technology*, 69 (14):2368–2375, nov 2009.